Computational modeling of healthy and epileptic hippocampal oscillations

Amélie Aussel

UNIVERSITÉ DE LORRAINE

École doctorale IAEM Lorraine

Computational modeling of healthy and epileptic hippocampal oscillations

THÈSE

présentée et soutenue publiquement le 14 Novembre 2019

pour l'obtention du

Doctorat de l'Université de Lorraine

(mention informatique)

par

Amélie Aussel

Composition du jury

Rapporteurs :	Daniel Wojcik, Prof., Nencki Institute, Warsaw, Poland Régine Le Bouquin Jeannès, Prof., LTSI - Univ. Rennes I, Rennes
Examinateurs :	Boris Gutkin, DR CNRS, LNC2 - ENS Ulm, Paris Patrick Hénaff, Prof., LORIA - Univ. Lorraine, Nancy Laure Buhry, MCF, LORIA - Univ. Lorraine, Nancy (codirectrice) Radu Ranta, MCF HDR, CRAN - Univ. Lorraine, Nancy (directeur)
Invité :	Louise Tyvaert, PUPH, CRAN - CHU Nancy - Univ. Lorraine, Nancy

Laboratoire Lorrain de Recherche en Informatique et ses Applications — UMR 7503

Mis en page avec la classe thesul.

Acknowledgments

The work described in this manuscript would have been much less fruitful and pleasant to fulfill without the help of the many people surrounding me.

Firstly, I would like to express my sincere gratitude to my advisors, Radu Ranta and Laure Buhry, for their continuous support of my Ph.D study and related research, as well as for our many discussions which helped me grow both on a scientific and human level. I'm glad I had you two as my supervisors, and I sincerely hope we have the chance to work together again in the future.

Besides my advisor, I would like to thank the rest of my thesis committee : Daniel Wojcik, Régine Le Bouquin Jeannès, Boris Gutkin and Patrick Henaff, for their insightful comments and encouragement, but also for the hard questions which incented me to widen my research from various perspectives.

I would also like to thank Louise Tyvaert, Olivier Aron and the other members of the epileptology department of the CHRU Nancy who helped me make my work as medically meaningful as possible.

Many thanks to the PhD students of the Neurorhythms and NeuroSysCo teams, and in particular Prisca, Sebastien, Nathalie and Harry, for the fun times together, for your listening and your advice, which helped me stay positive during these three years. I wish you all the best in your future lives and careers.

Finally, I am very grateful to my husband Georges, my mother, and all of my family and friends for their unwavering support and encouragements, as well as for reminding me to take care of myself when I would only care about my work. I couldn't have done this without all of you !

The pursuit of knowledge is a journey with no destination.
As long as people live, there is always something to learn.
And so we learn, we record, we speak,
Points connect, thus forming our history, our agency, our identity.
The world we live in is not for, or of, any individual - and so is knowledge.
And so I write and speak of all that I learned,
To plant seeds of knowledge to be harvested by those who follow me.
To you who have found my writings, read well these words
That they may help you build a bridge to a brighter future.

Octopath Traveler, Square Enix 2018

Summary

Résumé étendu

1 Notions de neurosciences

1.1 Neurones biologiques

Le cerveau humain comprend environ 10^{11} neurones, des cellules excitables électriquement dont l'activité coordonnée est le fondement de tout processus cognitif, perception et mouvement.

Un neurone typique est composé de trois parties : le soma, l'axone et les dendrites (Figure 1.1). Le soma (aussi appelé corps cellulaire) contient le noyau du neurone et possède une membrane capable de laisser des ions circuler vers l'intérieur ou l'extérieur de la cellule grâce à des canaux ioniques. La différence de concentration en ion de part et d'autre de la membrane d'un neurone donne lieu à une différence de potentiel appelée potentiel de membrane. Lorsqu'il est au repos, le potentiel de membrane d'un neurone est négatif (le potentiel à l'intérieur est inférieur au potentiel extérieur), mais selon les entrées qu'il reçoit sur ses dendrites, des mouvement d'ions peuvent l'augmenter (on parle de dépolarisation) ou le diminuer (on parle alors de repolarisation). Quand le potentiel de membrane d'un neurone dépasse un certain seuil, il emet un signal électrique appelé potentiel d'action, ou spike, qui se propage le long de son axone avant d'être communiqué aux dendrites d'autres neurones. Après qu'un neurone a émis un spike, son potentiel de membrane décroit en deçà de sa valeur au repos, ce qu'on appelle l'hyperpolarisation), puis retourne lentement à son état de repos. Tant qu'un neurone est hyperpolarisé, il ne peut pas émettre d'autre potentiel d'action et ne répond pas aux stimulations qu'il reçoit : cet intervalle de temps est appelé période réfractaire du neurone (voir 1.2).

1.2 De l'activité cellulaire à la cognition

A l'échelle microscopique, les neurones communiquent entre eux via des transmissions synaptiques : lorsqu'un potentiel d'action atteint l'extrémité de l'axone d'un neurone, cela déclenche la libération de molécules chimiques appelées neurotransmetteurs dans l'espace entourant la cellule, qui se lient par la suite aux récepteurs synaptiques présents sur les dendrites des neurones proches. Selon le type de neurotransmetteurs reçus de cette façon, des canaux ioniques spécifiques s'ouvrent sur les neurones post-synaptiques, ce qui conduit à l'augmentation ou la diminution de leur potentiel de membrane : dans le premier cas, la synapse est dite excitatrice, et dans le second elle est dite inhibitrice.

Dans une moindre mesure, les neurones peuvent aussi se transmettre leur activité électrique les uns aux autres à travers des jonctions communicantes (aussi appelées synapses électriques) connectant directement leur cytoplasmes, ou encore ils peuvent réagir au champ électrique généré par les neurones auxquels ils ne sont pas connectés (ce qu'on appelle un couplage éphaptique).

En s'activant ensemble, des petits groupes de neurones peuvent effectuer des tâches simples. A l'échelle macroscopique, les processus cognitifs requièrent la communication et la synchroni-

sation de grandes aires cérébrales, chacune étant associée à certaines fonctions. Ces interactions se font sous la forme d'émission de potentiels d'actions synchronisés à certaines fréquences, communément désignées sous le terme d'oscillations neuronales. Plus d'information à ce sujet peut être trouvée dans [Wang, 2010] et [Buzsaki, 2011].

Dans l'ensemble, le cerveau humain est organisé en différentes structures partageant des fonctions communes. La partie externe du cerveau, le cortex cérébral, peut être divisé en quatre lobes : le lobe frontal, le lobe pariétal, le lobe temporal et le lobe occipital. Les neurones formant les couches les plus superficielles du cortex, appelé néocortex, sont celles qui sont apparues le plus tardivement au cours de l'évolution, et sont à l'origine des fonctions cérébrales les plus avancées telles que le raisonnement ou la parole (voir Figure 1.3).

Sous le cortex cérébral se trouvent d'autres structures utiles telles que le tronc cérébral, le thalamus, l'amygdale, l'hippocampe, etc... qui assurent d'autres fonctions moins avancées évolutionnairement parlant telles que la respiration, le contrôle de la consommation alimentaire, les émotions ou la mémoire.

1.3 Mesures de l'activité neuronale

Il existe de nombreuses techniques pour mesurer l'activité neuronale, in vitro ou in vivo, et à différentes échelles.

Le mesure des potentiels de membranes ou des courants de membrane de neurones isolés peut s'effectuer in vitro à l'aide de techniques de patch-clamp par exemple. Au cours de ces expériences, une électrode constituée d'une micropipette remplie d'une solution électrolytique est mise au contact de la membrane d'un neurone, tandis qu'une seconde électrode est placée dans le bain entourant le neurone. Ces deux électrodes sont utilisées pour imposer au neurone une différence de potentiel (on parle alors de voltage-clamp, cf Figure 1.4) ou un courant (on parle alors de current-clamp) pendant que le courant ou le potentiel résultant est mesuré. Depuis leur première utilisation sur des axones de calamar géant dans les années 1940, ces techniques ont été massivement utilisées en électrophysiologie pour étudier les propriétés de divers canaux ioniques.

L'activité de neurones individuels peut également être mesurée in vivo à l'aide de microélectrodes, des électrodes bipotentielles constituées de verre, de silicium ou de metal, dont la pointe très fine (typiquement avec un diamètre de l'ordre de quelques microns) est insérée directement dans le corps cellulaire (quelques exemples de ce type d'électrodes sont présentés Figure 1.5). Des microélectrodes extracellulaires peuvent également être utilisées afin d'observer l'activité de quelques neurones voisins.

De la même manière, des éléctrodes plus grandes (avec un diamètre de l'ordre du millimètre) peuvent être insérées dans le milieu extracellulaire afin de mesurer l'activité électrique totale générée par tous les neurones environnants ainsi que celle propagée depuis les neurones plus lointains, qu'on appelle potentiel de champ local (Local Field Potential en anglais, souvent abrégé en LFP). Cette technique est appelée électroencéphalographie stéréotactique, ou sEEG. Dans certaines électrodes sEEG, il est possible d'insérer des fils électriques fin, formant un pinceau de microélectrodes à son extrémité, ce qui permet de combiner des mesures à l'échelle micro- et macroscopique.

La somme des activités de grandes populations de neurones peut aussi être mesurée à l'aide d'autres méthodes. La plus commune est l'electroencéphalographie de scalp (EEG de scalp ou EEG de surface), qui est non invasive et repose sur l'utilisation d'électrodes cupules posées sur la tête à l'aide d'un bonnet élastique ou de ruban adhésif. Afin de réduire l'impédence du contact électrique avec la peau et les cheveux dans une certaine mesure, un gel électrolytique est souvent

appliqué entre les électrodes et le scalp. Alternativement, il est possible d'insérer des grilles d'électrodes directement sous le crâne (sous la dure-mère) pour obtenir des signaux avec un meilleur rapport signal sur bruit (cette technique est appelée électrocorticographie ou ECoG).

L'activité neuronale génère également un faible champ magnétique (inférieur au champ magnétique terrestre d'environ neuf ordre de grandeur). Sa mesure peut s'effectuer à l'aide de magnétomètres très sensibles tels que les SQUIDs (superconducting quantum interference devices) placés autour de la tête, ce qui constitue la technique de magnétoencéphalographie (MEG). Comparée à l'EEG de surface, la MEG requiert un appareillage plus complexe et l'utilisation d'un blindage magnétique, et est donc plus coûteuse, et de plus elle ne permet de mesurer que la composante radiale du champ magnétique neuronal. Par ailleurs, elle est moins adaptée à la mesure d'activité issue de sources situées en profondeur à l'intérieur du cerveau que l'EEG. Cependant, elle présente l'avantage d'être moins déformée par le crâne, et offre aussi une meilleure résolution spatiale lorsqu'il s'agit de mesurer l'activité de petites régions à la surface du cerveau (pour une comparaison complète de ces deux techniques, voir [Malmivuo, 2011]).

Enfin, des techniques de mesures indirectes de l'activité neuronale in vivo existent également, telle que l'imagerie par résonance magnétique fonctionnelle (IRMf) ou la Tomographie par Emission de Positron (TEP). Dans un enregistrement par IRMf, les propriétés magnétiques différant entre le sang riche et pauvre en oxygène sont exploitées pour déduire la consommation en oxygène des neurones (augmentant avec leur activité) et obtenir une image cérébrale avec un contraste BOLD (pour blood-oxygen-level dependant, dépendant du niveau d'oxygène sanguin). De manière similaire en TEP, un autre corrélat de l'activité neuronale est étudié, généralement la consommation de glucose des neurones, mais la technique diffère en ce qu'elle repose sur l'injection d'une molécule adjointe d'un traceur radioactif (du fluorodesoxyglucose F18 souvent) et la mesure des émissions de positron en résultant dans le corps du patient. L'IRMf et la TEP peuvent être utilisées pour étudier l'activité cérébrale de régions bien plus profondes et avec une meilleure résolution spatiale que l'EEG de surface ou la MEG, mais leur résolution temporelle est bien inférieure. A l'échelle microscopique, il est aussi possible de mesurer des méthodes d'imagerie calcique pour observer l'évolution de la concentration en calcium intracellulaire à l'aide de molécules ayant des propriétés de fluorescence variant avec la présence d'ion Ca^{2+}.

2 Modèles computationnels de l'activité neuronale

Malgré toutes les méthodes existantes permettant de mesurer l'activité neuronale, il est toujours de nombreuses questions auxquelles ni les expériences in vitro ni celles in vivo ne peuvent répondre complètement, et dans de nombreux autres cas de telles expériences ne peuvent tout simplement pas être conduites pour des raisons techniques ou éthiques. En effet, les différentes méthodes de mesures apportent des informations à l'échelle micro ou macroscopique, mais ne permettent que rarement d'expliquer les liens entre ces différentes échelles. De plus, la plupart des techniques de mesures directes sont invasives et ne sont donc pas utilisées sur des sujets humains sains. Dans ce contexte, la modélisation mathématique des neurones est un outil puissant pour développer une meilleure compréhension des mécanismes neuronaux ou des processus cognitifs.

Différents modèles de neurones individuels et de groupes de neurones existent (voir par exemple le livre [Gerstner, 2014]), chacun ayant son propre degré de réalisme biologique et sa propre complexité algorithmique, et ils doivent donc être choisis avec soin selon le phénomène à étudier.

2.1 Formalisme de Hodgkin-Huxley

Les modèles de neurones biologiques les plus détaillés proviennent historiquement du travail de [Hodgkin and Huxley, 1952] sur les axones de calamar géant.

Leur modèle repose sur l'analogie entre un neurone biologique et un circuit électrique (voir Figure 1.7). La membrane du neurone est considérée comme un condensateur, et la variation de son potentiel de membrane V_m s'exprime en fonction de sa capacité C_m et des courants totaux résultants de stimulation extérieure (I_{stim}) et de ses courants transmembranaires (I_i) :

$$C_m \cdot \frac{dV_m}{dt} = -I_i + I_{stim} \tag{1}$$

où les courant transmembranaires (I_i) peuvent être décomposés en la somme d'un courant de fuite, d'un courant sodique et d'un courant potassique :

$$I_i = I_l + I_{Na} + I_K \tag{2}$$

Chacun de ces trois canaux ioniques peut être décrit comme une résistance dont la conductance varie quand le canal s'ouvre ou se ferme, et le courant ionique résultant peut alors s'exprimer en suivant les équations suivantes :

$$\begin{aligned} I_l &= g_l \cdot (V_m - E_l) && (3)\\ I_{Na} &= g_N a \cdot m^3 \cdot h \cdot (V_m - E_{Na})^4 && (4)\\ I_K &= g_K \cdot n^4 \cdot (V_m - E_K) && (5) \end{aligned}$$

où g_K, g_{Na} et g_l sont les conductances ioniques maximales, et E_K, E_{Na} and E_l sont les potentiels de repos des canaux potassiques, sodiques et de fuite respectivement, qui peuvent être vus comme un équilibre de Nernst entre l'intérieur et l'extérieur de la cellule. Les variables m et n décrivent l'activation des canaux potassiques et sodiques, et h décrit l'inactivation du canal sodique. Ces trois variables sont régies par des équations différentielles de la forme :

$$\frac{dx}{dt} = \alpha_x \cdot (1 - x) - (\beta_x \cdot x) \tag{6}$$

pour $x \in \{h, n, m\}$, où α_x et β_x sont des fonctions décrivant l'équilibre et les dynamiques des variables d'activation et d'inactivation. Au final, le modèle Hodgkin-Huxley standard comprend donc quatre équations différentielles ordinaires : $\frac{dV_m}{dt}$, $\frac{dm}{dt}$, $\frac{dh}{dt}$, et $\frac{dn}{dt}$.

Le modèle Hodgkin-Huxley d'origine a par la suite été étendu pour inclure d'autres canaux ioniques de façon similaire afin de représenter une plus grande variété de neurones. Il est aussi possible de définir plusieurs compartiments neuronaux suivant des équations similaires afin de prendre en compte la morphologie d'un neurone et les différentes propriétés de son soma, son axone et ses dendrites.

Les modèles dérivés de ce formalisme ont un haut degré de réalisme biologique, et en particulier ils permettent de reproduire fidèlement l'évolution temporelle du potentiel de membrane au cours d'un potentiel d'action, ainsi que les potentiels extracellulaires. Cependant, ils demandent des ressources informatiques importantes pour être simulés et ils sont difficiles à analyser mathématiquement, d'autant plus quand plusieurs compartiments sont modélisés.

2.2 Modèles intègre-et-tire et modèles à deux variables

Une possibilité pour modéliser l'activité neuronale avec une complexité moindre comparé aux modèles issus du formalisme de Hodgkin-Huxley consiste à ne considérer l'évolution du potentiel de membrane qu'entre les potentiels d'actions, sans modéliser précisément la forme de chaque spike.

Ce type de modèle se présente généralement sous la forme d'une ou deux équations différentielles décrivant l'activité neurale entre les spikes, complété d'un ensemble d'équations de "reset" appliquées lorsque l'activité neuronale dépasse un certain seuil, c'est-à-dire quand le neurone émet un potentiel d'action.

Une grande partie de ces modèles sont dérivé du modèle Intègre-et-Tire créé par Louis Lapique en 1907 (voir [Abbott, 1999]), qui a des équations de la forme :

$$\begin{aligned} C_m \cdot \frac{dV_m}{dt} &= I_{stim} \\ V_m &\leftarrow V_{reset} \text{ if } V_m > V_{threshold} \end{aligned} \tag{7}$$

Ce modèle tire son nom du fait que le potentiel de membrane V_m du neurone est approché par l'intégration de son courant d'entrée I_{stim}, jusqu'à ce qu'il atteigne un seuil $V_{threshold}$ où il émet un potentiel d'action (il "tire") et retourne à sa valeur de reset V_{reset}.

Ce modèle très simple peut être amélioré de différentes façons, par exemple en considérant qu'un neurone ne recevant aucune entrée devrait voir son potentiel de membrane revenir à sa valeur de repos (modèle "leaky integrate-and-fire"), ou en ajoutant une autre variable et une autre équation différentielle pour reproduire des dynamiques plus complexes (comme pour le modèle adaptatif exponentiel intègre-et-tire, voir [Brette and Gerstner, 2005]).

D'autres modèles à deux varaibles existent qui sont plus une simplification du modèle de Hodgkin-Huxley qu'une extension du modèle Intègre-et-tire, comme le modèle d'Izhikevich ([Izhikevich, 2003]), qui peut être décrit par les équations suivantes :

$$\begin{aligned} V_m' &= 0.04V_m^2 + 5V_m + 140 - u + I \\ u' &= a(bV_m - u) \\ \text{si } V_m \geq 30mV, \text{ alors } V_m &\leftarrow c \text{ and } u \leftarrow u + d \end{aligned} \tag{8}$$

où V_m représente le potentiel de membrane et u est la variable de rétablissement de la membrane, qui représente l'activation des courants ioniques K^+ et Na^+. Les valeurs numériques 0.04, 5 et 140 sont utilisées pour correspondre aux dynamiques d'initiation de spike de neurones corticaux, et les paramètres sans dimension a, b, c et d peuvent être choisis pour reproduire différentes types de comportements neuronaux.

D'autres exemples de modèles à deux variables sont les modèles de FitzHugh-Nagumo ([Nagumo et al., 1962]) et de Morris-Lecar ([Morris and Lecar, 1981]), et des modèles à trois variables existent également tels que le modèle de Hindmarsh-Rose ([Hindmarsh and Rose, 1984]).

2.3 Modèles de taux d'activation

Il est possible de simplifier encore davantage la description de l'activité d'un neurone en la considérant comme un processus stochastique et en modélisant uniquement l'évolution de la probabilité d'occurence d'un potentiel d'action.

Ces modèles de "taux d'activation" sont parfois proches des modèles de réseaux de neurones utilisés dans le domaine du machine learning, comme c'est le cas pour le modèle Linear-Nonlinear-Poisson (souvent abrégé en "modèle LNP"). Dans ce modèle, le taux d'activation d'un neurone est calculé en considérant une combinaison linéaire de ses entrées (étape linéaire) à laquelle on applique une fonction non-linéaire comme une sigmoide (étape nonlinéaire). Le timing des potentiels d'action du neurone est ensuite obtenu en le considérant comme un processus de Poisson dont le taux est le taux d'activation caluclé précédemment

Ce type de modèle peut être utilisé pour reproduire des résultats expérimentaux sur des processus visuels ou auditifs par exemple (voir [Simoncelli et al., 2004]), mais ils apportent des informations moins détaillées sur les mécanismes biologiques impliqués que les modèles présentés plus tôt.

2.4 Modèles de population

Enfin, pour modéliser des grands groupes de neurones de manière plausible biologiquement parlant sans avoir les contraintes computationnelles du formalisme de Hodgkin-Huxley, il est possible de considérer les dynamiques de populations de neurones au lieu de celles de neurones individuels. Pour ce faire, l'état de chaque population peut être décrit par quelques variables représentant l'état moyen de tous les neurones qu'elle contient.

Une telle approche a par exemple été développée dans le travail de [Wilson and Cowan, 1972], qui simplifie l'étude de l'évolution temporelle de la proportion de cellules actives dans deux populations (l'une excitatrice et l'autre inhibitrice) de neurones localisés spatialement en l'étude de deux équations différentielles couplées de la forme :

$$\begin{aligned} \tau \frac{dE}{dt} &= -E + (1 - rE) S_E[c_1 E - c_2 I + P(t)] \\ \tau' \frac{dI}{dt} &= -I + (1 - rI) S_I[c_3 E - c_4 I + Q(t)] \end{aligned} \tag{9}$$

où E et I sont la proportion de neurones excitateurs et inhibiteurs actifs respectivement, P et Q sont les entrées extérieures que chaque neurone reçoit, r est leur période réfractaire, et les variables de c_1 à c_4 représentent le nombre moyen de synapses par neurone au sein de et entre chaque population.

Ce type de modèle permet de simuler l'activité de grandes aires cérébrales et leur comportement est généralement facile à étudier à l'aide de méthodes d'analyse de plan de phase.

3 Variations de l'activité neuronale

Les oscillations neuronales peuvent varier en fonction de facteurs internes et externes tels que l'âge ou la maladie. Même au cours d'une seule journée, la fatigue, le niveau d'attention ou le sommeil peuvent grandement modifier l'activité cérébrale, par des mécanismes qui ne sont pas encore parfaitement compris à ce jour.

Dans les paragraphes qui vont suivre, nous allons décrire brièvement les deux processus d'intérêt pour le travail de cette thèse, c'est-à-dire le cycle veille sommeil et l'épilepsie.

3.1 Cycle veille-sommeil

Description des phases de sommeil

Les humains et la plupart des animaux font l'expérience du sommeil, un état caractérisé par une conscience altérée, un activité sensorielle relativement inhibée, une inhibition de presque tous les muscles de mouvements volontaires, et des interactions réduites avec leur environnement ([National Institute of Neurological Disorders and Stroke, 2019]). L'activité du cerveau change aussi au cours du sommeil, et différentes ondes cérébrales mesurées par EEG ont été utilisées pour distinguer plusieurs phases de sommeil.

Une première distinction peut être faite entre le sommeil à mouvements oculaires rapides (Rapid-Eye-Movement, ou REM) et le sommeil sans mouvements oculaires rapides (non-Rapid-Eye-Movement ou NREM). Le sommeil REM est caractérisé par des mouvements oculaires rapides derrière les paupières fermées, et l'activité cérébrale y est la plus proche de la veille. Cette phase de sommeil est également celle où peuvent se produire les rêves. Le sommeil NREM quant à lui peut être subdivisé en des phases N1, N2 et N3 qui font référence à la profondeur du sommeil (1 étant le plus léger et 3 le plus profond), et est caractérisé par des ondes cérébrales plus lentes et plus synchrones qu'au cours du sommeil REM. Le sommeil N3 est aussi appelé sommeil à ondes lentes.

Après l'endormissement, la première phase de sommeil qui intervient est la N1, caractérisée par des ondes theta (4-7Hz) et une absence d'ondes alpha (8-12Hz) sur les enregistrements EEG ([Miller et al., 2015]), qui dure environ 10 minutes avant de laisser place au sommeil N2, où des fuseaux de sommeil (des bouffées temporaires d'activité de fréquence 10-12Hz) et des complexes K (des brefs pics d'activité) apparaissent. Après environ 20 minutes de phase N2, la prochaine phase de sommeil apparaissant est la N3, où des ondes delta (0.5-4Hz) peuvent être enregistrées, suivies environ 30 minutes plus tard par du sommeil REM.

Ces phases se répètent dans un ordre similaire pendant toute la nuit en formant des cycles d'environ 90 minutes, comme on peut le voir sur l'exemple d'hypnogramme Figure 1.9, qui montre la classification des phases de sommeil obtenue par EEG, EOG (électrooculogramme) et EMG (électromyogramme) pendant une nuit.

Neurophysiologie du cycle veille-sommeil

De nombreuses régions du cerveau et de nombreux neurotransmetteurs sont impliquées dans l'alternance entre sommeil et veille.

Le maintien de l'état de veille est assuré par des groupes de cellules formant un chemin ascendant depuis le tronc cérébral jusqu'aux régions corticales via deux branches, l'une passant par le thalamus, et l'autre par l'hypothalamus et le cerveau antérieur. Ces neurones libèrent diverses substances associées à l'éveil comme l'Acétylcholine, la Sérotonine, l'Orexine, et bien d'autres (voir Figure 1.10 et [Schwartz and Roth, 2008] pour plus de détails).

Le besoin de sommeil s'accentue progressivement au cours des périodes d'éveil pour maintenir un équilibre entre veille et sommeil appelé homéostasie. Les mécanismes sous-jacents à cette homéostasie ne sont pas encore parfaitement compris, mais il a été montré qu'un nucléoside appelé adénosine y joue un rôle important. Plus précisément, sa concentration dans le cerveau antérieur basal augmente progressivement durant l'éveil, et il favorise l'endormissement (voir [Schwartz and Roth, 2008] ou [Steriade, 2003]). La régulation du cycle veille-sommeil dépend aussi du rhythme circadien, controllé par le noyau suprachiasmatique de l'hypothalamus.

Le sommeil quant à lui est maintenu par des neurones du noyau ventrolatéral préoptique (VLPO) produisant du GABA et de la galanine. Les régions impliquées dans l'éveil et le VLPO

s'inhibent mutuellement, c'est pourquoi la relation entre sommeil et veille est parfois décrite comme un système bistable.

Fonctions du sommeil

Le sommeil n'est pas qu'une période d'inactivité cérébrale et corporelle, mais sert également plusieurs buts (voir [Zielinski et al., 2016]). Il a été montré qu'il est impliqué dans la régulation de la température corporelle, ainsi que dans la modulation des réponses immunitaires. Concernant le cerveau lui-même, le sommeil est un facteur important du développement cérabral, et même chez l'adulte, il est nécessaire au maintien d'une bonne condition psychologique et de bonnes performances cognitives.

Le cycle veille-sommeil joue notamment un rôle très important dans les processus de formation et de consolidation de la mémoire (voir [Rasch and Born, 2013] pour une revue du sujet). Bien que ces processus ne soient pas parfaitement compris, une théorie répandue est que, au cours de la journée, les informations sont encodées dans une région cérébrale appelée hippocampe, formant la mémoire à court terme. Puis, durant le sommeil, l'hippocampe rejoue une partie de son activité de la journée, ce qui permet le transfert de l'information vers d'autres zones du cerveau pour créer la mémoire à long terme.

3.2 Epilepsie

Outre les processus physiologiques tels que le cycle veille-sommeil, de nombreuses maladies peuvent aussi altérer l'activité cérébrale, et l'une des plus fréquentes est l'épilepsie.

Définition de l'épilepsie

L'épilepsie est une affection qui est caractérisé par un risque élevé de générer une activité cérébrale excessive et/ou anormale au cours d'épisodes temporaires appelés crises. Ces crises peuvent avoir des effets divers selon la position et la taille de la zone cérébrale affectée, par exemple des mouvements involontaires, une sensation de peur injustifiée ou une perte de conscience.

La International League Against Epilepsy (ILAE) a proposé la définition pratique de l'épilepsie suivante dans [Fisher et al., 2014] :

"L'épilepsie est une maladie neurologique caractérisée par l'une des conditions suivantes :

— 1. Au moins deux crises non provoquées (ou réflexes) intervenant à plus de 24h d'intervalle
— 2. Une crise non provoquée (ou réflexe) mais une probabilité de nouvelle crise similaire au risque général de récurrence après deux crises non provoquées (au moins 60%), pour les dix années suivantes
— 3. Diagnostic d'un syndrome épileptique"

Dans cette définition une crise "non provoquée" désigne une crise qui survient alors qu'une personne n'est exposée à aucun facteur facilitateur tel que la fièvre ou le sevrage de l'alcool.

Une épilepsie peut être considérée comme "résolue" lorsqu'un patient n'a pas eu de crise pendant au moins 10 ans, sans avoir pris de traitement anti-épileptique pendant 5 ans, mais cela ne signifie pas qu'il est impossible qu'une crise survienne à nouveau plus tard (c'est pourquoi l'ILAE propose de ne pas utiliser le terme "guérie").

Une classification détaillée des différents types de crises est proposée par l'ILAE dans [Fisher et al., 2017] (voir Figure 1.11 pour la dernière mise à jour de 2017). Dans cette classification, trois facteurs principaux sont pris en compte :

— la zone épileptogène : le ou les groupes de neurones qui initient les crises, et plus précisément s'ils se situent dans un hémisphère unique du cerveau (crise focale, autrefois appelée "partielle"), ou dans les deux hémisphères (crise généralisée ou bilatérale)
— l'état de conscience du patient au cours des crises : si le patient reste conscient et attentif au cours de la crise
— : les symptômes moteurs du patient : pas de symptôme (crise non motrice), les muscles devenant faibles (crise atonique), des mouvements saccadés (crise clonique), des brèves contractions musculaires (crise myoclonique), ou des spasmes épileptiques (c'est-à-dire des mouvements de flexion et d'extension du corps répétés). D'autres mouvements automatiques ou involontaires comme des frottements des mains ou une mastication peuvent aussi survenir.

Même dans le cas de crises non motrices, un patient peut ressentir différents changements dans ses sensations, ses émotions ou ses fonctions autonomes, par exemple des vagues de chaleur ou de froid, de la fièvre, une accélération du rythme cardiaque, etc. (typiquement pour des crises focales), ou des pertes d'attention, avec un regard fixe (on parle alors de "crises d'absences", qui sont typiquement des crises généralisées).

Les épilepsies peuvent aussi être classifées en fonction de leurs causes. Une épilepsie est dite idiopathique quand elle est causée par des anormalités génétiques, ou symptomatique quand elle est la conséquence d'une maladie, d'une tumeur ou d'une autre source identifiable. Les épilepsies de causes inconnues sont dites cryptogéniques. Parmi les épilepsies symptomatiques, il se peut que l'affection à l'origine de la maladie ne soit plus présente.

Données épidémiologiques

L'épilepsie est la quatrième affection neurologique la plus répandue au monde (après la migraine, les AVC et la maladie d'Alzheimer), d'après [Hirtz et al., 2007], et elle se classe deuxième en terme de charge économique selon [Murray and al., 2012].

La prévalence et l'incidence de l'épilepsie sont respectivement une mesure de la proportion de personnes souffrant d'épilepsie et la proportion de personnes nouvellement diagnostiquée chaque année dans une population, et ont été rapportées dans de nombreuses études ces dernières années.

Dans [Fiest et al., 2017], une méta-analyse de telles études est présentée, qui rapporte une prévalence de l'épilepsie active d'environ 6.38 pour 1000 personnes, et une incidence de 61.44 pour 100,000 personnes-années. La prévalence de l'épilepsie au cours de la vie (c'est-à-dire la proportion de personnes qui souffriront d'épilepsie à un moment donné de leur vie) est estimée à 7.60 pour 1000 personnes. La prévalence de l'épilepsie ne semble pas varier significativement en fonction de la tranche d'âge ou du genre, mais son incidence est plus importante chez les enfants et les personnes âgées que dans le reste de la poputation.

Quant à la proportion de chaque type d'épilepsie, la distribution des types de foyers épileptogènes et les étiologies chez environ 1000 patients adultes, elle est rapportée chez [Picot et al., 2008]. Dans l'ensemble, cette étude indique que les épilepsies focales sont plus courantes que les épilepsies généralisées. Parmi les épilepsies focales, 72.5% sont symptomatiques et 27.5% sont cryptogéniques, tandis que parmi les épilepsies généralisées, 94.5% sont idiopathiques et 5.5% sont cryptogéniques ou symptomatiques. Peu d'études rapportent la position du foyer épileptique parmi les épilepsies focales, mais selon l'étude de [Manford, 1992] (sur environ 250 patients), le lobe temporal serait la zone épileptogène la plus commune, suivie par le cortex moteur et le lobe frontal, bien que dans de nombreux cas la zone exacte à l'origine des crises ne peut pas être déterminée (voir Table 1.1).

Diagnostic et traitement

Après qu'un patient a rapporté avoir eu des crises, l'épilepsie est le plus souvent diagnostiquée en enregistrant son activité cérébrale avec un EEG de surface à la recherche d'activités épileptiques typiques (ictale ou interictale). Ce premier test s'accompagne d'un examen neurologique qui aide à déterminer les régions impliquées dans la génération des crises. Des tests sanguins, et des examens IRM ou TEP peuvent aussi être pratiqués pour rechercher la cause de la pathologie, par exemple pour repérer des anomalies génétiques ou des signes de lésions ou d'infections ([Foundation, 2013]).

Afin de diminuer les crises ou de les faire disparaître, le traitement le plus fréquent est la prescription de médicaments antiépileptiques (antiepileptic drugs, ou AED). Cependant, trouver l'AED approprié parmi la multitude de molécules existantes peut prendre beaucoup de temps, et en fonction du type et l'étiologie de l'épilepsie, 30 à 40% des patients ont des crises qui ne peuvent pas être contrôlées à l'aide de médicaments ([Engel, 2014]). Les épilepsies du lobe temporal, où l'hippocampe est souvent impliqué, sont les plus courantes parmi ces épilepsies pharmaco-résistantes ([Engel, 2014]).

D'autres thérapies comme les régimes cétogènes (un régime alimentaire incluant beaucoup de gras et peu de glucides), ou la stimulation du nerf vagal ont aussi commencé à se développer récemment, mais leurs résultats sont limités (jusqu'à 50% de contrôle des crises, d'après [Engel, 2014]).

Pour les patients pharmaco-résistants, le traitement offrant le plus de chance de supprimer complètement les crises consiste à retirer la zone épileptogène de leur cerveau. Avant une résection chirurgicale, des électrodes sEEG peuvent être implantées pour quelques jours dans le cerveau du patient afin de définir la zone épileptogène aussi précisément que possible. Cependant, cette opération n'est pas applicable à tous les patients, elle peut avoir de nombreux effets secondaires indésirables, et de plus tous les patients ne sont pas libérés de leur crises par la suite (voir [Spencer et al., 2005]).

Dans l'ensemble, il est encore nécessaire d'améliorer les traitements de l'épilepsie et la compréhension de cette maladie en général.

Interactions entre l'épilepsie et le cycle veille-sommeil

L'épilepsie est d'autant plus difficile à comprendre qu'elle intéragit avec d'autres processus physiologiques tels que le cycle veille-sommeil. En effet, la plupart des patients ne souffrent de crise que pendant la veille ou pendant des phases de sommeil spécifiques ([Crespel et al., 1998]), pour des raisons largement méconnues.

Réciproquement, les observations in vivo des structures cérébrales internes impliquées dans le cycle veille-sommeil chez l'homme sont généralement dérivées des enregistrements intracrâniens obtenus chez des patients épileptiques, qui ne sont pas nécessairement représentatifs du fonctionnement d'un cerveau sain.

Une région qui pourrait être intéressante à étudier dans ce contexte est l'hippocampe, puisqu'il est l'une des principales régions impliquées dans les épilepsies chez l'adulte ou les épilepsies pharmacorésistantes, alors que même son fonctionnement sain n'est pas parfaitement compris.

4 Objectifs de la thèse

Dans ce travail, nous cherchons à apporter une meilleure compréhension de différents facteurs influençant l'activité cérébrale, à savoir le cycle veille-sommeil et l'épilepsie. Cette étude est

ramenée à une seule région, l'hippocampe, qui présente des dynamiques intéressantes en lien avec ces deux phénomènes.

Concernant le cycle veille-sommeil, nous investiguons la génération de rythmes hippocampiques typiquement associés au processus de mémorisation, à savoir les complexes sharp-wave ripples (observés durant le sommeil profond), et les oscillations theta-gamma (observées durant la veille). Concernant l'épilepsie, nous nous concentrons sur la génération des crises ainsi que des fast ripples.

Ensemble, ces oscillations couvrent une large bande de fréquences différentes. A partir de là, la principale question à laquelle nous cherchons à répondre est : quels sont les mécanismes contrôlant ces rythmes ? De nombreuses hypothèses existent qui impliquent soit des changements dans les dynamiques des neurones individuels ou dans leurs interactions synaptiques et leur organisation en tant que réseau, mais elles sont difficiles à vérifier expérimentalement à cause du manque de données in vivo chez l'humain. En conséquence, pour répondre à cette question, nous avons construit un modèle computationnel de l'hippocampe complet et étudié individuellement l'influence de chacun de ses paramètres, avant de le comparer à des données cliniques.

Ce travail a été effectué au Loria au sein de l'équipe de recherche Neurosys, et au CRAN au sein de l'équipe Espace. Nous avons collaboré avec le CHRU Nancy où les mesures sEEG intracraniennes que nous avons utilisées pour valider notre modèle ont été obtenues sur des patients épileptiques dans le cadre de leur procédure de résection chirurgicale.

5 Structure du manuscrit

Ce manuscrit comporte six chapitres. Le présent chapitre a présenté le contexte général de ce travail, ainsi que des informations générales sur le sommeil et l'épilepsie. Dans le second chapitre, nous présenterons une partie des connaissances actuelles sur l'hippocampe, son anatomie, sa physiologie et ses oscillations neuronales typiques, et nous passerons également en revue différents modèles de l'activité hippocampique existants.

Dans le chapitre 3, nous décrirons notre modèle computationnel de l'hippocampe. Nous justifierons les choix de nos paramètres de modélisation en apportant une analyse de sensibilité de notre système et nous montrerons comment reproduire différents types d'oscillations saines.

Puis dans le chapitre 4, nous montrerons comment des changements fonctionnels peuvent permettre de reproduire des oscillations typiques du sommeil profond ou de la veille. Nous étudierons plus en détail le rôle des dynamiques individuelles des neurones et de la connectivité fonctionnelle du réseau en lien avec une modulation cholinergique. Nous comparerons aussi les rythmes obtenus avec des enregistrements sEEG.

Le chapitre 5 suivra une logique similaire, mais cette fois le modèle de l'hippocampe sera modifié pour reproduire et expliquer des rythmes épileptiques. Nous étudierons l'influence de trois des principales anomalies observées dans l'hippocampe épileptique, à savoir la sclérose hippocampique, le bourgeonnement des fibres moussues et les anomalies génétiques.

Enfin, dans le chapitre 6 nous résumerons nos résultats, et nous suggèrerons des améliorations possibles qui pourraient être apportées à notre modèle dans des travaux futurs.

6 Conclusions générales

L'hippocampe peut présenter différents rythmes oscillatoires au cours du cycle veille-sommeil, chacun d'eux étant impliqué dans des processus cognitifs. Par exemple, les oscillations theta-gamma, qui consistent en un couplage d'ondes theta (4-12Hz) et gamma (40-100Hz), sont pro-

duites au cours de la veille et sont utiles aux tâches de navigation spatiale et de mémoire à court terme ([O'Keefe and Recce, 1993], [Axmacher et al., 2010]), tandis que les complexes sharp-wave ripples, qui consistent en des oscillations rapides (120-200Hz) se produisant au cours d'ondes lentes ($\leq$ 0.5Hz), sont produites au cours du sommeil lent profond et de repos et jouent un rôle important dans la consolidation de la mémoire ([Girardeau and Zugaro, 2011], [Buzsáki, 2015]). Des modèles existent pour expliquer la génération de chacun de ces rythmes individuellement : pour les sharp-wave ripple, voir [Taxidis et al., 2012] ou [Traub and Bibbig, 2000], et pour les oscillations theta-gamma, voir [Pastoll et al., 2013], [Fukai, 1999], ou [Bartos et al., 2007]. Cependant, les mécanismes impliqués dans la génération et les transitions entre l'ensemble de ces rythmes ne sont pas encore parfaitement compris.

Cette question est d'autant plus importante qu'une altération des rythmes hippocampiques est impliquée dans l'épilepsie du lobe temporal médian phamaco-résistante, une forme d'épilepsie affectant environ 0.6 personne sur 1000 ([Asadi-Pooya et al., 2017]) et qui ne peut pas être contrôlée par les traitements médicamenteux existants. Comme pour les rythmes physiologiques, des modèles ont été développés pour reproduire des crises d'épilepsie (des épisodes d'activité neuronale excessive, voir la revue de [Stefanescu et al., 2012]) ou des pointes intercritiques (de brefs pics d'activité synchrone, voir par exemple [Demont-Guignard et al., 2009]), mais ces modèles ne parviennent pas à expliquer entièrement les liens entre les conditions neuropathologiques de l'hippocampe, des processus physiologiques comme le cycle veille-sommeil, et les oscillations qui en résultent.

Dans ce contexte, l'objectif principal de cette thèse est d'apporter une meilleure compréhension de diverses oscillations hippocampiques, tant physiologiques que pathologiques, incluant notamment les oscillations theta-gamma, les complexes sharp-wave ripple, les crises d'épilepsie et les pointes intercritiques. Pour ce faire, nous avons développé un modèle computationnel de l'hippocampe tenant compte de divers mécanismes auparavant décrits dans des travaux séparés, et avons analysé son activité oscillatoire en variant différents paramètres représentant les propriétés structurelles ou fonctionnelles du réseau, ainsi que des modifications pathologiques typiquement observées chez des patients épileptiques, en nous appuyant sur des techniques bien définies telles que des plans d'expérience ou une analyse de sensibilité de Sobol' afin d'évaluer quantitativement l'importance de chaque paramètre. Le modèle comprend également une estimation du potentiel de champ local (LFP) généré par ses neurones, afin d'être comparable à des enregistrements cliniques.

Nos résultats montrent que la connectivité fonctionnelle de l'hippocampe est un facteur crucial dans le contrôle de la fréquence de ses oscillations rapides notamment. De plus, concernant l'épilepsie, le bourgeonnement des fibres moussues semble avoir un fort effet épileptogène tandis que la sclérose hippocampique aurait au contraire un effet protecteur. Au final, nos résultats apportent un nouvel éclairage sur les mécanismes impliqués dans la génération des oscillations hippocampiques, qui pourraient ouvrir la voie à de futures applications cliniques.

List of Figures

List of Abbreviations

ACh : Acetylcholine
AED : Antiepileptic drug
AMPA : α-amino-3-hydroxy-5-methyl-4-isoxazolepropionic acid

CA : Cornus Ammonis
CAN : Calcium-Activated Nonspecific
CCH : Carbachol

DG : Dentate Gyrus
DOE : Design of Experiment

EC : Entorhinal Cortex
ECoG : Electrocorticography
EEG : Electroencephalography
EMG : Electromyogram
EOG : Electrooculogram

fMRI : Functional Magnetic Resonance Imaging

GABA : γ-aminobutric acid

HS : Hippocampal Sclerosis
HCN : Hyperpolarization-activated cyclic nucleotide–gated
HFO : High Frequency Oscillations
HYP : Hypersynchronous

IED : Interictal Epileptiform Discharge
ILAE : International League Against Epilepsy

LFP : Local Field Potential
LIF : Leaky Integrate-and-Fire
LVF : Low Voltage Fast

MEG : Magnetoencephalography
MRI : Magnetic Resonance Imaging

NREM : Non-Rapid-Eye-Movement
NMDA : N-Methyl-D-Aspartate

O-LM : Oriens Lacunosum-Moleculare

PET : Positron Emission Tomography
PV : Parvalbumine

REM : Rapid-Eye-Movement
RMS : Root-Mean-Square

SD : Standard Deviation
sEEG : Stereotactic Electroencephalography
SNR : Signal-to-Noise Ratio
SPW-R, SWR : Sharp-Wave Ripple

VLPO : Ventrolateral Preoptic Nucleus

Chapter 1

Introduction

1.1 Basics of neuroscience

1.1.1 Biological Neurons

The human brain comprises about 10^{11} neurons, electrically excitable cells whose coordinated activities are at the core of all cognitive processes, perceptions and behaviors.

A typical neuron is made of three main parts : the soma, the axon and the dendrites (Figure 1.1). The soma (also called cell body) contains the neuron's nucleus and has a membrane capable of letting ions flow in and out of the cell through ionic channels. The gradients in concentrations of ions on each side of a neuron's membrane give rise to a voltage difference called membrane potential. In its resting state, a neuron's membrane potential is negative (intracellular with respect to extracellular potentials), but depending on the inputs it receives on its dendrites, ion flows can increase it, which is called depolarization, or decrease it, which is called hyperpolarization. When a neuron's membrane potential increases above a certain threshold, it emits an electrical signal called action potential or spike which propagates through its axon, and is then sent to other neurons' dendrites. After a neuron has emitted a spike, its membrane potential decreases and gets lower than its resting potential, before slowly going back to its resting state. As long as a neuron is hyperpolarized, it cannot emit any other action potential and will not respond to any input it receives : this period of time is called the refractory period of the neuron (see 1.2).

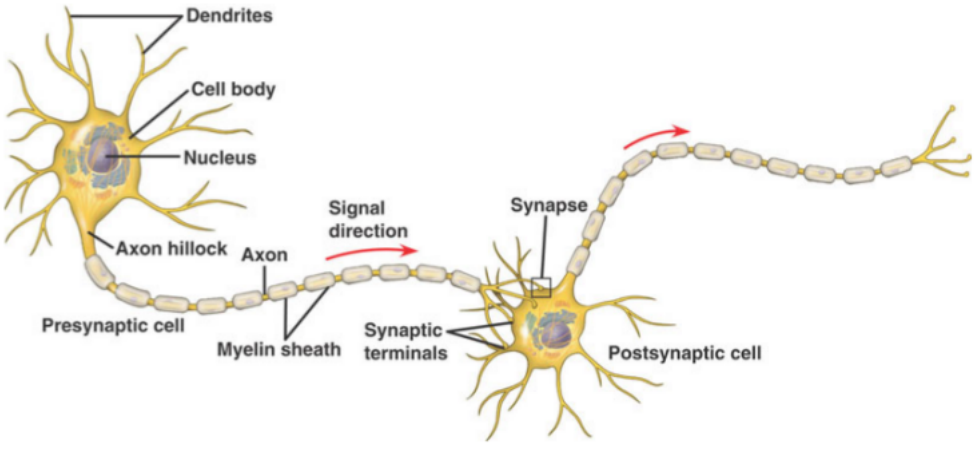

FIGURE 1.1 – Anatomy of a neuron and its regions. (Source : [Cheung, 2008])

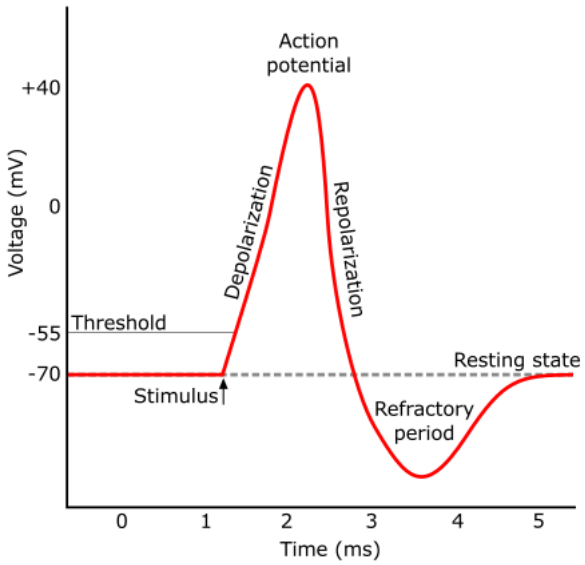

FIGURE 1.2 – A typical voltage trace of an action potential showing the polarisation phases. (Source : Wikimedia Commons)

1.1.2 From single neuron activity to cognition

At the microscopic level, neurons communicate with each other through synaptic transmissions : when an action potential reaches the end of a neuron's axon, it triggers the release of chemicals called neurotransmitters in the extracellular space, which bind onto synaptic receptors on nearby neurons' dendrites. Depending on the type of neurotransmitter received this way, specific ionic channels on the post-synaptic neuron open, which can lead to an increase or decrease of its membrane potential : in the former case, the synapse is said excitatory, and in the latter it is said inhibitory.

To a lesser extent, neurons can also communicate their electrical activity to each other through gap junctions, also called electrical synapses, connecting cells cytoplasms directly, or they can react to the electrical field generated by neurons to which they are not connected, which is called ephaptic coupling.

By working together, small groups of neurons can perform simple tasks. At the macroscopic level, cognitive processes require the communication and synchronization of large brain areas, each associated with a specific function. These interactions take the form of temporary synchronized activation at specific frequencies, commonly referred to as neural oscillations. In general, neural oscillations, or brainwaves, can be defined as any rhythmic or repetitive patterns of neural activity. More information on this topic can be found in [Wang, 2010] and [Buzsaki, 2011].

Overall, the human brain is organized in different structures sharing common functions. The outer part of the brain, the cerebral cortex, can be divided in four lobes, the frontal, parietal, temporal and occipital lobe, and into two hemispheres, left and right. The most superficial layers of neurons in the cortex, called the neocortex, are those which appeared the latest in the evolutionary history of the brain, and are able to perform the most advanced functions such as reasoning or speech (see Figure 1.3).

Underneath the cerebral cortex lie other structures like the brainstem, the thalamus, the amygdala, the hippocampus, etc... which perform older evolutionary functions such as breathing, control of food intake, emotions or memory.

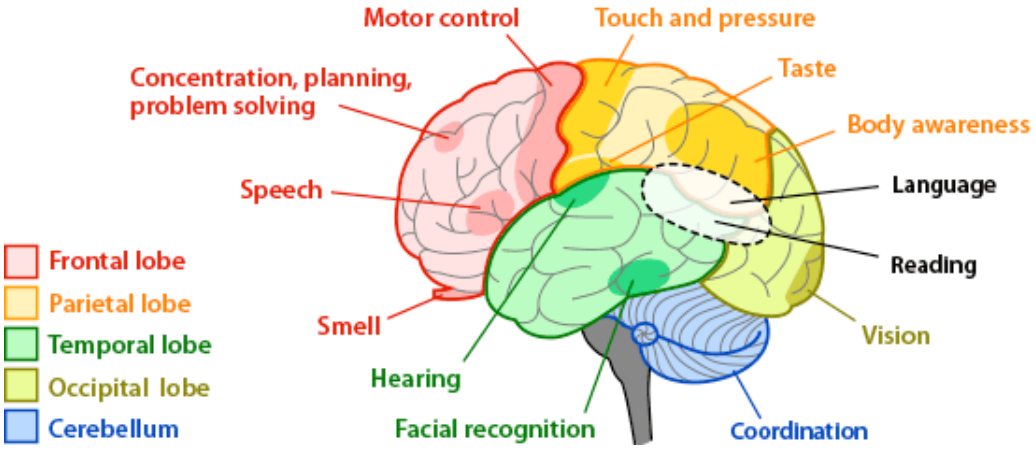

FIGURE 1.3 – Diagram of the four lobes of the human cerebral cortex and the cerebellum, with their associated functions (Source : [Kazilek, 2011])

1.1.3 Measures of neural activity

Different techniques exist to record neural activity, in vitro or in vivo, and at different scales.

Recordings of single neurons membrane potential or membrane currents can be performed in vitro with patch-clamp techniques for example. During such experiments, an electrode consisting in a micropipette filled with an electrolitic solution is put in contact with the membrane of a neuron, while another electrode is placed in the bath surrounding the neuron. These electrodes are used to impose a voltage (voltage-clamp technique, see Figure 1.4) or a current (current-clamp technique) to the cell while the resulting current or voltage is measured. Since their first use in the late 1940s on giant squid axons, these techniques have been used extensively in electrophysiology to study the properties of various ion channels.

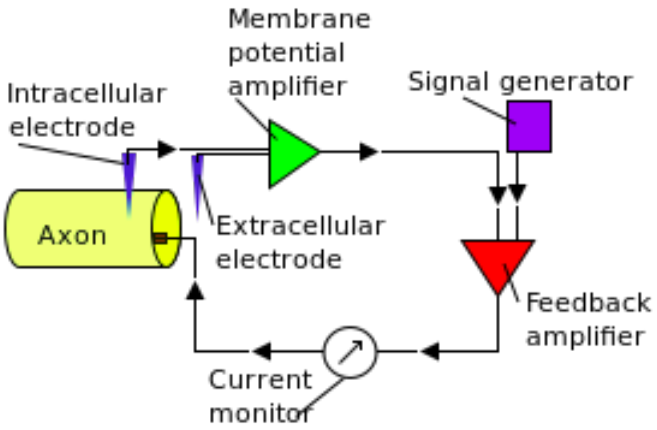

FIGURE 1.4 – Schematic drawing of a voltage-clamp circuit. (Source : Wikimedia Commons)

Single neuron activity can also be recorded in vivo by what is called a microelectrode, a biopotential electrode made of glass, silicon or metal, with an very thin tip (typically with a diameter of a few microns) inserted directly into the cell body (a few examples of such electrodes are shown on Figure 1.5). Extracellular microelectrodes can also be used to observe the activity of the few surrounding neurons.

Similarly, when larger electrodes are inserted in the extracellular space (with a diameter of about 1mm), the electrical activity generated by all nearby neurons or propagated from distant ones, called Local Field Potential (LFP), can be recorded. This technique is called stereotactic electroencephalography, or sEEG. In some sEEG electrodes called Behnke-Fried electrodes (Figure 1.6), small wires can be inserted, forming a bunch of microelectrodes at its tip, thus enabling both micro- and macro- measurements.

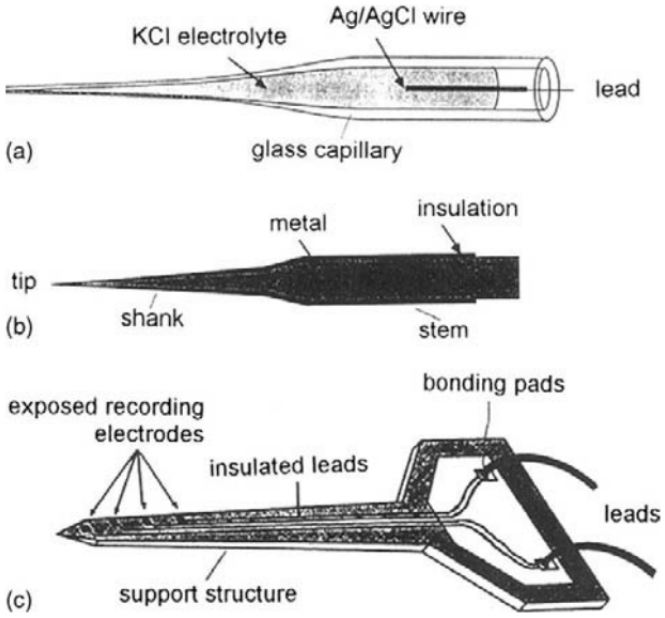

FIGURE 1.5 – Biopotential microelectrodes : (a) a capillary glass microelectrode, (b) an insulated metal microelectrode, and (c) a solid-state multisite recording microelectrode. (Source : [Mendelson, 2012])

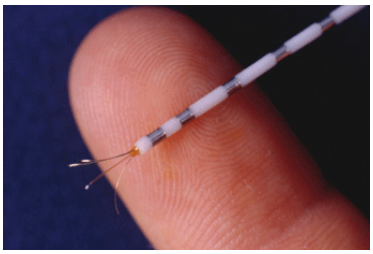

FIGURE 1.6 – Illustration of a Benhke-Fried electrode (Source : [Sirven, 2011])

The summed electrical activity of large populations of neurons can be recorded through different other techniques. The most common one is scalp electro-encephalography (scalp EEG or surface EEG), which is non-invasive and uses cup electrodes attached to the head with an elastic cap or adhesive tape. To reduce the impedance of the electrical contact with the skin and hair to some extent, an electrolytic gel is often placed between the electrode and the scalp. Alternatively, arrays of electrodes can also be inserted directly under the skull (below the dura mater) to obtain measurements with a better signal to noise ratio (this technique is called electrocorticography or ECoG).

Neural electrical activity also generates a weak magnetic field (about nine orders of magnitude smaller than the earth's static magnetic field). Its measure, relying on very sensitive magnetometers such as SQUIDs (superconducting quantum interference devices) placed all around the skull, constitutes the magneto-encephalography (MEG) technique. Compared to surface EEG, MEG recordings require more complex instrumentation and magnetic shielding and are therefore more expensive, and it can only be used to record radial components of the neural magnetic field. Also, MEG is less adapted than scalp EEG for measuring the activity of sources situated deep inside the head. However, it presents the advantage of being less distorted by the skull and can also offer better spatial resolution for the recording of small regions of the brain (see [Malmivuo, 2011] for a thorough comparison of these two techniques).

Finally indirect measures of neural activity in vivo exist as well, such as functional Magnetic Resonance Imaging (fMRI), and Positron Emission Tomography (PET). In fMRI recordings, the different magnetic properties of highly and lowly oxygenated blood are used to infer the oxygen consumption of neurons (increasing with their activity) and obtain what is called a BOLD (blood-oxygen-level dependent) contrast on the image. Similarly in PET, a metabolic correlate of neural activity is studied, usually the glucose uptake of neurons, but the recording technique is quite different and relies on the injection of a radioactive tracer molecule (flurodeoxyglucose F18 usually) and the measure of the resulting positron emissions in the patient's body. fMRI and PET can be used to infer neural activity from regions deep inside the brain with high spatial resolution, but their temporal resolution is much poorer than in scalp EEG or MEG. At a microscopic scale, it is also possible to perform Calcium Imaging to observe the evolution of intracellular calcium concentration by using molecules that change their fluorescence properties in presence of Ca^{2+} ions.

1.2 Computational models of neural activity

Despite all the methods available to record neural activity, there are still many questions that neither in-vitro nor in-vivo experiments can fully answer, and many other cases in which such experiments can simply not be performed due to technical or ethical issues. Indeed, the different recording techniques provide some information either at the microscopic scale, for example regarding membrane potentials and chemical changes, or at the macroscopic scale, regarding oscillatory patterns of brain structures and behavior, but rarely explore the links between these scales and the activity of relatively small neuronal populations. Furthermore, many of the direct recording techniques are invasive and therefore they are not performed on healthy human brains. In this context, mathematical modeling of neurons is a powerful tool to gain insight into a neural mechanism or a cognitive process.

Different models of individual neurons and groups of neurons exist (see for example in [Gerstner, 2014]), which come with different degrees of biological realism and computational burden, and should be chosen carefully depending on the phenomenon to be studied. The main types of computational models will be presented in this section.

1.2.1 The Hodgkin-Huxley formalism

The most biologically detailed models of neurons historically come from the work of [Hodgkin and Huxley, 1952] on giant squid axons.

This model relies on an analogy between a biological neuron and an electrical circuit (see Figure 1.7). The membrane of the neuron is seen as a capacitor, with the rate of change of its

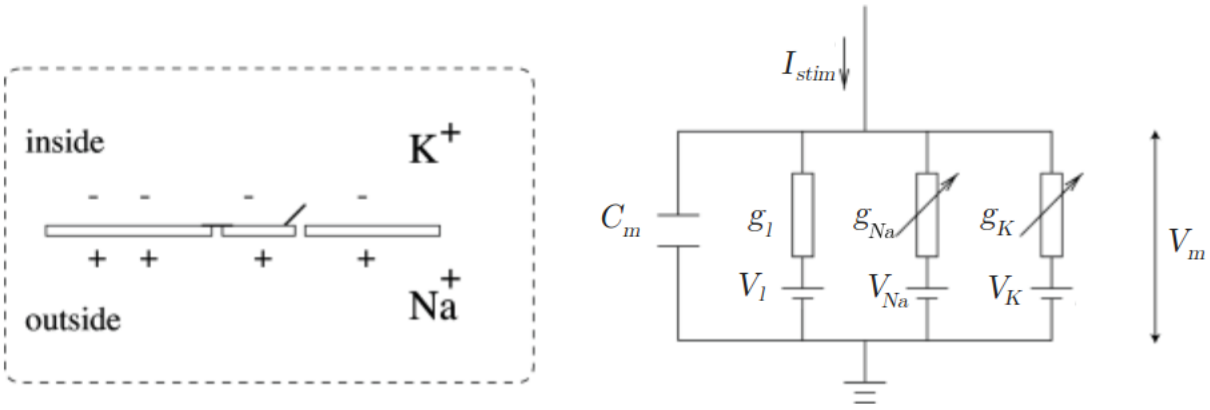

FIGURE 1.7 – Schematic diagram for the Hodgkin-Huxley model, adapted from [Gerstner, 2014]

potential V_m expressed a function of its membrane capacitance C_m and its total input currents resulting from external stimulation (I_{stim}) or transmembranal ionic currents (I_i) :

$$C_m \cdot \frac{dV_m}{dt} = -I_i + I_{stim}, \tag{1.1}$$

where the total transmembranal ionic current (I_i) is the sum of a leak, sodium and potassium components :

$$I_i = I_l + I_{Na} + I_K. \tag{1.2}$$

Each of these three ion channels can be described as a resistor with a conductance varying as the channel opens and closes, and the resulting ionic current can then be expressed by using the following equations :

$$I_l = g_l \cdot (V_m - E_l), \tag{1.3}$$
$$I_{Na} = g_N a \cdot m^3 \cdot h \cdot (V_m - E_{Na})^4, \tag{1.4}$$
$$I_K = g_K \cdot n^4 \cdot (V_m - E_K), \tag{1.5}$$

where g_K, g_{Na}, and g_l are the maximum ionic conductances, and E_K, E_{Na}, and E_l are the resting potentials of the potassium, sodium, and leak channels respectively, which can be seen as a Nernst equilibrium potential between the intracellular and extracellular space. m and n are variables describing the activation of the potassium and sodium channels, and h is a variable describing the inactivation of the sodium channel. These three variables are governed by a set of ordinary differential equations in the form :

$$\frac{dx}{dt} = \alpha_x \cdot (1 - x) - \beta_x \cdot x, \tag{1.6}$$

for $x \in \{h, n, m\}$, where α_x and β_x are functions describing the steady-state and temporal dynamics of the activation and inactivation variables. Therefore, the standard Hodgkin-Huxley model comprises four ordinary differential equations : $\frac{dV_m}{dt}$, $\frac{dm}{dt}$, $\frac{dh}{dt}$, and $\frac{dn}{dt}$.

The original Hodgkin-Huxley model has then been extended to include more ion channels in a similar manner to be able to represent a large variety of neurons. It is also possible to define several neural compartments with similar equations to take into account the morphology of a neuron and the different properties of its soma, axon and dendrites.

Models derived from this formalism have a high degree of biological realism, and in particular they are able to faithfully reproduce the temporal course of membrane potentials during action potentials, as well as extracellular potentials. However, this comes at the cost of a high computational burden and difficulties to mathematically analyze the system, and even more so when multiple compartments are involved.

1.2.2 Integrate-and-Fire and two-variable models

One possible way to model neural activity with a reduced complexity compared to the Hodgkin-Huxley models is to consider the evolution of membrane potential only between action potentials, without modeling the exact shape of each spike.

Such models usually come in the form of one or two differential equations describing neural activity between spikes, complemented by a set of "reset equations" applied when neural activity reaches a predefined threshold, i.e. when the neuron spikes.

A large proportion of these models are derived from the Integrate-and-Fire model by Louis Lapique in 1907 (see [Abbott, 1999]), which has simple equations of the form :

$$\begin{aligned} C_m \cdot \frac{dV_m}{dt} &= I_{stim}, \\ V_m &\leftarrow V_{reset} \text{ if } V_m > V_{threshold}. \end{aligned} \tag{1.7}$$

This model draws its name from the fact that the neuron membrane current V_m is approximated by the integration of its input current I_{stim} until it reaches a threshold $V_{threshold}$ where it fires and returns to its reset value V_{reset}.

This simple model can be improved in many ways, for example by considering that without inputs the membrane potential of a neuron should go back to its resting state (leaky integrate-and-fire model), or by adding another variable and differential equation to reproduce more complex dynamics (adaptive exponential integrate-and-fire model, see [Brette and Gerstner, 2005]).

Other two-variables models exist which are more a simplification of the Hodgkin-Huxley formalism than an expansion of the integrate-and-fire model, such as the Izhikevich model ([Izhikevich, 2003]), which can be described by the following equations :

$$\begin{aligned} V_m' = 0.04V_m^2 + 5V_m + 140 - u + I, \\ u' = a(bV_m - u), \\ \text{if } V_m \geq 30mV, \text{ then } V_m \leftarrow c \text{ and } u \leftarrow u + d, \end{aligned} \tag{1.8}$$

where V_m represents the membrane potential and u represents a membrane recovery variable, which accounts for the activation of K^+ and Na^+ ionic currents. The values 0.04, 5 and 140 are used to fit the spike initiation dynamics of a cortical neuron, and the dimensionless parameters a, b, c and d can be chosen to reproduce different types of neural behaviors.

Other examples of two-variable models are the FitzHugh–Nagumo ([Nagumo et al., 1962]) and Morris–Lecar models ([Morris and Lecar, 1981]), and models with three variables also exist such as the Hindmarsh–Rose model ([Hindmarsh and Rose, 1984]).

Such models can reproduce some features of single neuron activity with a low computational burden, but have overall less precise spike dynamics than the Hogkin-Huxley models, which can lead to differences for example when stimulating a neuron with correlated inputs (see [Feng, 2001]), and also they are not appropriate to represent detailed channel properties. Therefore

the choice between a Hodgkin-Huxley and a simplified model can be seen as a tradeoff between biological realism and computational simplicity.

1.2.3 Rate models

It is possible to simplify even more the description of a single neuron activity by considering it as a stochastic process and modeling only the evolution of the probability of occurrence of an action potential.

These "rate models" are sometimes close to the artificial neural networks used in the field of machine learning, such as the Linear-Nonlinear-Poisson (LNP) model. In this model, the firing rate of a neuron is computed by considering a linear combination of its inputs (linear step) through a non-linear function such as a sigmoid (nonlinear step). The timing of the spikes of the neuron is then obtained by considering the neuron as a Poisson process with the previously calculated firing rate.

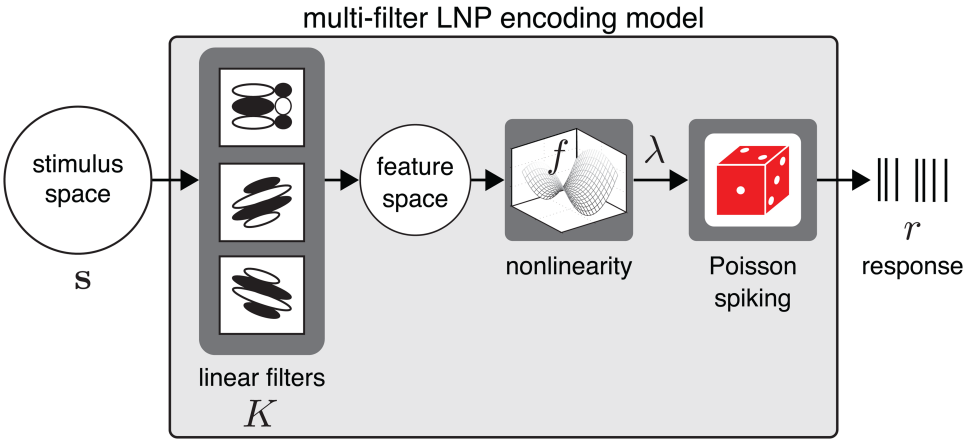

FIGURE 1.8 – Schematic diagram for Linear Non-linear Poisson model, taken from [Williamson et al., 2015]

These models can be used to reproduce experimental findings on visual and auditory processes for example (see [Simoncelli et al., 2004]), but provide less detailed explanations of the underlying biological mechanisms involved compared to the models presented previously.

1.2.4 Population models

Finally, to model a large group of neurons in a rather biologically plausible way without the computational burden of the Hodgkin-Huxley formalism, it is possible to consider populations of neurons instead of individual neuron dynamics. To do so, the state of each population can be described only by a few variables which represent the average state of all the neurons inside it.

Such an approach was for example developed in the work of [Wilson and Cowan, 1972], which simplifies the study of the temporal evolution of the proportion of active cells in two interacting populations (one excitatory and one inhibitory) of spatially localized neurons into the study of two coupled differential equations of the form :

$$\tau \frac{dE}{dt} = -E + (1 - rE)S_E[c_1E - c_2I + P(t)], \tag{1.9}$$
$$\tau' \frac{dI}{dt} = -I + (1 - rI)S_I[c_3E - c_4I + Q(t)],$$

where E and I are the proportions of active excitatory and inhibitory cells respectively, P and Q the external inputs they each receive, r their refractory period, and c_1 to c_4 represent the average number of synapses per cell made between and within each population. For other population models, see for example [Jansen and Rit, 1995] or [Wendling et al., 2002].

Such models make possible to simulate the activity of large brain areas (such as the synchronization of cortical areas) and their behavior are usually easy to predict through phase plane analysis methods.

1.3 Variations of neural activity

Neural oscillations can vary depending on internal and external factors, such as age or illnesses. Even over the course of a single day, fatigue, attentional level and sleep can drastically change brain activity, through mechanisms that are not fully understood yet.

In the following paragraphs, we will shortly describe the two processes of interest for the course of this work, i.e. the sleep-wake cycle and epilepsy.

1.3.1 The sleep-wake cycle

Functions of sleep

Sleep is not simply a period of body and brain inactivity, but serves many purposes (see [Zielinski et al., 2016]). It has been shown to be involved in the regulation of body temperature, as well as the modulation of immune responses. Regarding the brain itself, sleep is a key factor in neural development, and even in adults, it is needed for the maintenance of good psychological conditions and cognitive performances.

The sleep-wake cycle is a very important process for memory formation and consolidation in particular (see [Rasch and Born, 2013] for a review). Though the exact mechanisms involved are not fully understood, one common theory is that during the day, information is encoded in a brain region called the hippocampus, forming short-term memories. Then during sleep, the hippocampus replays some of its daily activity, which help transfer information to other brain regions to create long-term memory.

Description of sleep stages

Humans and most animals experience sleep, a state characterized by altered consciousness, relatively inhibited sensory activity, inhibition of nearly all voluntary muscles, and reduced interactions with surroundings ([National Institute of Neurological Disorders and Stroke, 2019]). Brain activity also changes during sleep, and different brain waves measured with EEG have been used to distinguish between different stages of sleep.

One first distinction can be made between Rapid-Eye-Movement (REM) and non-Rapid-Eye-Movement (NREM) sleep. REM sleep is characterized by eye movements behind the close eyelids, and brain activity closest to wakefulness. This stage is also the one that enables dreaming. NREM sleep can be further divided into stages N1, N2 and N3 which refer to the depth of sleep (1 being

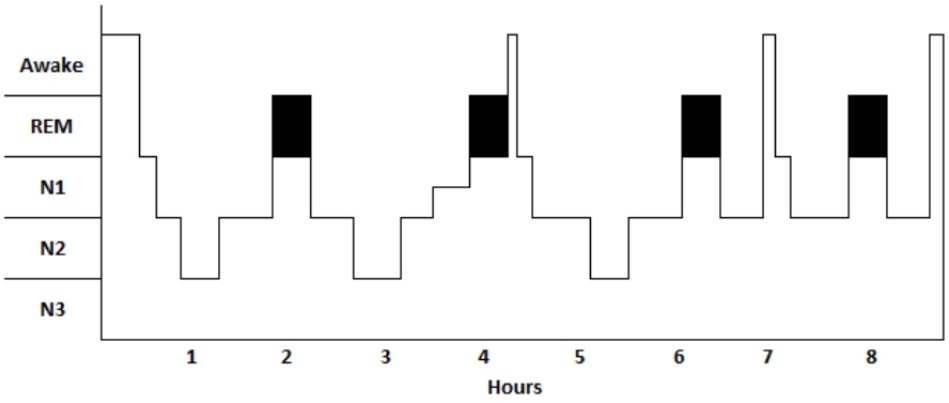

FIGURE 1.9 – Example of a normal hypnogram showing the progression of sleep stages during the night for an individual's sleep, from [Miller et al., 2015]. The y-axis represents sleep stages (evaluated in 30-second epochs) including : REM (Rapid Eye Movement) ; Stage 1 (N1) ; Stage 2 (N2) ; Stage 3 (N3 or SWS). The x-axis represents time during the night in hours.

the lightest and 3 the deepest), and is characterized by slower, more synchronous brain waves than REM sleep. NREM stage N3 is also called slow-wave sleep.

After falling asleep, the first stage of sleep occurring is N1, characterized by theta (4-7Hz) waves and an absence of alpha waves (8-12 Hz) on the EEG recording ([Miller et al., 2015]), which lasts for around 10 minutes before turning to stage N2, where sleep spindles (transient bursts of activity of frequency 10-12Hz) and K-complexes (brief peaks of activity) appear. After about 20 minutes of stage N2, the next stage occurring is N3, where delta waves (0.5-4Hz) can be seen, followed about 30 minutes later by REM sleep.

These stages repeat themselves in a similar order during the whole night in cycles of about 90 minutes, as can be seen on the hypnogram Figure 1.9, a graph showing the scoring of sleep stages using EEG, EOG (electrooculogram), and EMG (electromyogram) measures throughout one night.

Neurophysiology of the sleep-wake cycle

Many brain regions and many neurotransmitters are involved in the alternation of sleep and wakefulness.

The maintenance of the awake state is promoted by groups of cells that form an ascending pathway from the brainstem to cortical regions going through two branches, one in the thalamus, and one in the hypothalamus and forebrain. These neurons release a wide variety of substances associated with arousal, such as Acetylcholine, Serotonine, Orexin, and many others (see Figure 1.10 and [Schwartz and Roth, 2008] for more details).

The need for sleep gradually increases during periods of wakefulness to maintain a balance between sleep and wakefulness called sleep homeostasis. The exact mechanisms underlying this homeostasis are not yet fully understood, but the nucleoside called adenosine has been shown to play important role in it. More precisely, its concentration in the basal forebrain increases progressively during wakefulness, and has a sleep-inducing effect (see [Schwartz and Roth, 2008] or [Steriade, 2003]). Sleep-wake regulation also depends on the circadian rhythm, controlled by the suprachiasmatic nucleus of the hypothalamus.

Sleep itself is maintained by neurons of the ventrolateral preoptic nucleus (VLPO) which

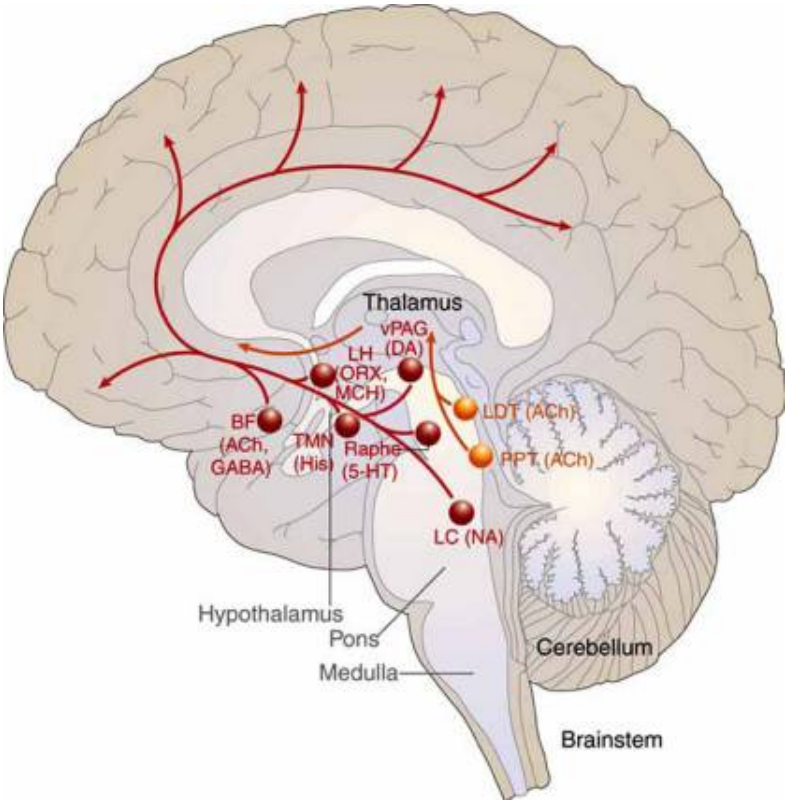

FIGURE 1.10 – A schematic drawing showing key components of the ascending arousal system, from [Schwartz and Roth, 2008]. BF : Basal Forebrain, LH : Lateral hypothalamus, vPAG : ventral periaqueductal grey matter, TMN : tuberomammillary nucleus, LDT : laterodorsal tegmental nucleus, PPT : pedunculopontine, LC : locus coeruleus. Inside the parenthesis are indicated the neurotransmitters involved : ACh : Acetylcholine, GABA : Gamma-Aminobutyric acid, 5-HT : Serotonine, ORX : Orexin, MCH : Melanin-concentrating hormone, NA : Noradrenaline, DA : Dopamine, His : Histamine.

produce GABA and galanin. The regions involved in arousal and the VLPO mutually inhibit each other, which is why the relationship between sleep and wakefulness is sometimes described as a bistable circuit.

1.3.2 Epilepsy

Besides physiological processes such as the sleep-wake cycle, brain activity can also be altered by many diseases, one of the most frequent being epilepsy.

Definition of epilepsy

Epilepsy is a disease which is characterized by a high risk of generating excessive and/or abnormally synchronous neural activity in one's brain during transient episodes called seizures. These seizures can have various effects depending on the location and size of the affected brain zone, ranging from involuntary movements to out of place fear sensations and loss of consciousness.

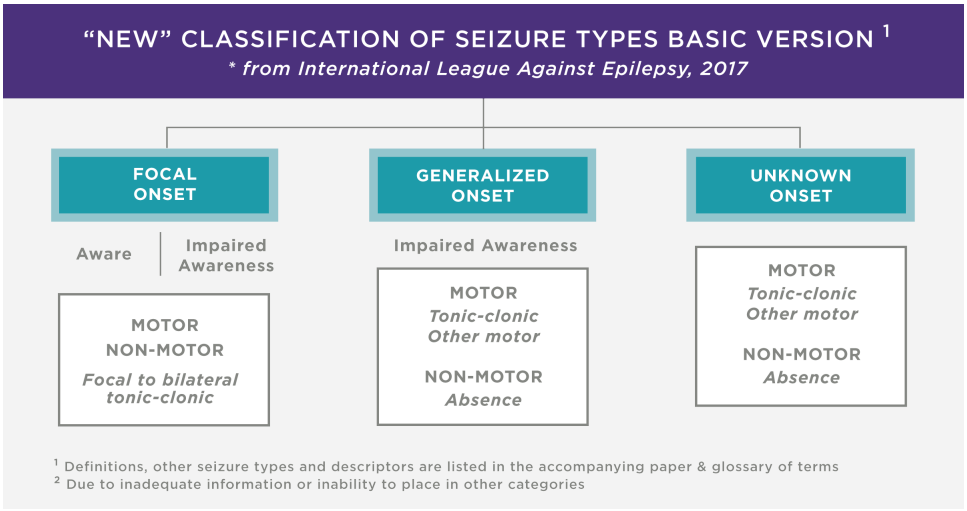

FIGURE 1.11 – Classification of seizures types according to the ILAE in 2017.

The International League Against Epilepsy (ILAE) proposed the following practical definition of epilepsy in [Fisher et al., 2014] :

"Epilepsy is a disease of the brain defined by any of the following conditions :

— 1. At least two unprovoked (or reflex) seizures occurring 24 h apart

— 2. One unprovoked (or reflex) seizure and a probability of further seizures similar to the general recurrence risk (at least 60%) after two unprovoked seizures, occurring over the next 10 years.

— 3. Diagnosis of an epilepsy syndrome"

In this definition, "unprovoked" seizures means that seizures occurring when a person is exposed to a facilitating factor such as fever or alcohol withdrawal are not considered.

An epilepsy can be considered "resolved", for example when a patient has been seizure-free for at least 10 years, without taking any seizure medication for at least 5 years, but it doesn't mean that it will never come back later (which is why the ILAE proposes not to use the term "cured").

A detailed classification of seizure types has been proposed by the ILAE in [Fisher et al., 2017] (see Figure 1.11 for the latest update from 2017). In this classification, mainly three factors are taken into account :

— the onset of the seizure : the group(s) of neurons which initiate the seizure, and more precisely whether they lie within a single hemisphere (focal onset, previously referred to as "partial onset"), or in both hemispheres of the brain (generalized or bilateral onset). A focal onset seizure initiated by several distinct groups of neurons is sometimes called complex, and it is termed "secondarily generalized" or "focal to bilateral" if after the seizure initialization neurons on both hemispheres start to produce epileptiform activity ;

— the patient's awareness during a seizure : whether the patient stays awake and aware during a seizure or not ;

— the patient's motor symptoms : no symptoms (non-motor seizure), muscles becoming weak (atonic), muscles becoming tense or rigid (tonic), jerking movements (clonic), brief muscle twitching (myoclonic), or epileptic spasms (body flexes and extends repeatedly). Other involuntary automatic movements such as rubbing of hands or chewing can also occur.

Even in the case of non-motor seizures, a patient can feel different changes in sensation, emotions, or autonomic functions, for example waves of heat or cold, fear, heart racing, etc. (typically for seizures with focal onset), or losses of awareness, sometimes with staring (these are referred to as "absence seizures", and are typically generalized onset seizures).

Epilepsies can also be classified depending on their causes. An epilepsy is said idiopathic when it is caused by genetic abnormalities, or symptomatic when it is the consequence of a disease, infection, tumor or any other identifiable brain abnormalities. Epilepsies with unknown causes are called cryptogenic. Among symptomatic epilepsies, cases where the brain abnormality is due to a previous event that is no longer present are termed "remote symptomatic" (in opposition with acute symptomatic epilepsies).

Epidemiological data

Epilepsy is the fourth most common neurological disorder (the first three being migraine, stroke and Alzheimer disease), as reported in [Hirtz et al., 2007], and it ranks second in terms of economical burden according to [Murray and al., 2012].

The prevalence and incidence of epilepsy respectively measure the proportion of people suffering from epilepsy and the proportion of newly diagnosed patients every year in a given population, and have been reported in many studies throughout the years.

In [Fiest et al., 2017], a meta-analysis of such studies is presented, which reports a prevalence of active epilepsy of about 6.38 per 1,000 persons, and an incidence of 61.44 per 100,000 person-years. The lifetime prevalence of epilepsy (that is, the proportion of people that will suffer from epilepsy at some point in their life) is estimated at 7.60 per 1,000 persons. The prevalence of epilepsy doesn't seem to differ significantly by age group or sex, however, incidence is higher in children and elderly people than in the rest of the population.

As for the proportion of each epilepsy type, [Picot et al., 2008] reports on the distribution of seizure onset types as well as etiologies in about 1000 adult patients. Overall, this study indicates that focal onset seizures are more common than generalized onset ones. Among focal onset epilepsies, 72.5% were symptomatic and 27.5% cryptogenic, whereas for the generalized epilepsies 94.5% were idiopathic and 5.5% cryptogenic or symptomatic. Fewer studies exist which report the location of focal epilepsies onset zones, but according to [Manford, 1992] (on about 250 patients), the temporal lobe would be the most common, followed by the motor cortex and the frontal lobe, though in many cases the exact seizure onset zone cannot be determined (see Table 1.1).

Diagnosis and treatments

After a patient has reported having seizures, epilepsy is most commonly diagnosed by recording its brain activity through surface EEG in search of typical epileptic patterns (ictal or interictal). This first test is accompanied with a neurological examination to help determine the regions involved in the seizure generation. Blood tests and MRI or PET scans can also be performed to search for the etiology of the pathology, for example to look for genetic disorders, or signs of lesions or infections ([Foundation, 2013]).

So as to reduce seizures or make them disappear, the most frequent treatment is the prescription of an antiepileptic drug (AED). However, finding the appropriate AED among the many existing molecules can take a long time, and depending on the type and etiology of the epilepsy, 30% to 40% of patients have seizures that cannot be controlled by medication ([Engel, 2014]).

TABLE 1.1 – Distribution of proposed sites of seizure onset in focal epilepsies

Proposed onset zone	Distribution %
Localized to a single ILAE site	**19.6**
Motor Cortex	12.2
Supplementary motor	2.4
Lateral temporal	1.2
Parietal	3.9
Overlapping neighboring ILAE regions	**43.1**
Frontal	11.8
Central	8.2
Frontotemporal	3.5
Temporal	15.7
Posterior cortex	3.9
Lateralized only	**1.2**
Unlocalized	**36.1**

Temporal lobe epilepsies in particular, which usually involve the hippocampus, are the most common type of pharmaco-resistant epilepsies ([Engel, 2014]).

Other therapies such as ketogenic diet (a specially high-fat, low-carbohydrate diet), or vagal nerve stimulation have also started to develop recently, but with limited results (up to 50% of seizure control, according to [Engel, 2014]).

In pharmaco-resistant patients, the best opportunity for complete freedom from seizures still lies in a surgery to completely remove the seizure onset zone from their brain. Before the surgical resection, sEEG electrodes can be implanted in the patient's brain for a few days so as to define the seizure onset zone as precisely as possible. However, this procedure cannot be applied to all patients, it has many potential adverse effects, and not all patients become seizure-free after it (see [Spencer et al., 2005]).

Overall, there is still need for improved treatments of epilepsy, and better understanding of this disease in general.

Interactions between epilepsy and the sleep-wake cycle

Epilepsy is all the more difficult to understand that it interacts with other physiological brain processes such as the sleep-wake cycle. Indeed, most patients experience seizures only during the day or during specific stages of the sleep ([Crespel et al., 1998]), for largely unknown reasons.

Conversely, in vivo observations of the internal brain structures involved in the sleep-wake cycle are mostly derived from intracranial recordings made in epileptic patients, which might not be fully representative of their healthy dynamics.

One of the brain regions that could be very interesting to study in this context is the hippocampus, as it is the main cause of adult and drug-resistant epilepsy, yet even its healthy functioning is far from being completely understood.

1.4 Objectives of this thesis

In this work, we want to provide a better understanding of the different factors influencing brain activity, focusing more particularly on the sleep-wake cycle and epilepsy. This study is

narrowed down to a single region, the hippocampus, as it shows some interesting dynamics related to these two phenomena.

Regarding the sleep-wake cycle, we investigate the generation of hippocampal rhythms typically associated with memory processes, i.e. sharp-wave ripple complexes (observed during slow-wave sleep) and theta-nested gamma oscillations (observed during wakefulness). Regarding epilepsy, our focus is put on epileptic seizures as well as fast ripples and interictal discharges.

Altogether, these oscillations cover a wide range of frequencies. From then, the main question we try to answer is : what are the mechanisms controlling these rhythms ? Many hypotheses exist that involve either changes in individual neuron dynamics or their synaptic interactions and organization as a network, but these are hard to verify experimentally due to the low availability of in vivo human data. Therefore, to complete this work, we devise a computational model of the whole hippocampus and study each of these parameters individually, before comparing it with clinical data.

Our work was carried out at Loria within the Neurorhythms research team (former name Neurosys), and the CRAN within the NeuroSysCo team (former name Espace). We collaborated with the CHRU Nancy where intracranial sEEG measurements we used to validate our model were obtained on epileptic patients undergoing resective surgery.

1.5 Structure of the manuscript

This manuscript comprises six chapters. The current chapter has set the general context of this work, and some background information on sleep and epilepsy. In the second one, we will present some of the current knowledge on the hippocampus, its anatomy, physiology and its oscillatory patterns, as well as review existing models of hippocampal activity.

In Chapter 3, we will describe our computational model of the hippocampus. We will justify the choices of our modeling parameters by providing a parameter sensitivity analysis of our system and we will show how to reproduce different types of healthy oscillations.

Then in Chapter 4, we will show how functional changes can make the model produce either typical wakefulness oscillations or slow-wave sleep ones. In particular, we will investigate the role of single-neuron dynamics as well as network functional connectivity in relation with cholinergic modulation. We will also compare the rhythms we obtain with real sEEG measurements.

Chapter 5 will follow a similar logic, but this time the hippocampus model will be altered to reproduce and explain epileptic rhythms. We will study the influence of three of the main abnormalities commonly observed in epileptic hippocampus, i.e. hippocampal sclerosis, mossy fiber sprouting and genetic defects.

Finally, Chapter 6 will summarize our results, and suggest possible improvements that could be made to our model in future works.

Chapter 2

Literature Review

2.1 The Hippocampus

2.1.1 Neuroanatomy of the Hippocampus

The hippocampus is a structure located inside each mesio-temporal lobe in mammals, which gets his name from its resemblance with a sea-horse (Figure 2.1 and Figure 2.2). It is composed of two U-shaped regions, the Cornus Ammonis, also called hippocampus proper, and the Dentate Gyrus. The Cornus Ammonis itself is divided into different subregions named CA1, CA2, CA3 and CA4 (sometimes called the hilus), which differ mostly by the synaptic connectivity they make or receive (Figure 2.3). The CA2 and CA4 regions are often ignored in discussions about the hippocampus due to their small size.

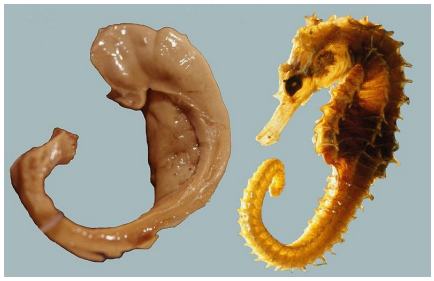

FIGURE 2.1 – Comparison of a dissected human hippocampus and fornix (left) to a specimen of Hippocampus leria (right). Source : Hungarian neuroscientist László Seress' 1980 preparation, Wikimedia Commons.)

Different types of neurons can be found in each of these regions. In all the Cornus Ammonis, most of the excitatory neurons are pyramidal cells, which are characterized by a long cone-shaped dendritic tree. Interneurons on the other hand represent between 10 and 15% of the total cell number, and are more diverse and comprise (but are not limited to) basket cells, O-LM cells, chandelier cells or axo-axonic cells, bistratified cells etc. (see [Freund and Buzsáki, 1998] for a detailed review). In the Dentate Gyrus, there are no pyramidal cells, but instead smaller round shaped excitatory neurons called granule cells can be found, as well as mossy cells, while interneurons are mostly similar to the Cornus Amonnis ones. An estimation of the number of principal neurons in each structure in human can be found in Table 2.1, while the structure and proportions of CA1 interneurons can be found in Figure 2.4, classified in different categories depending on the shape of the neurons or the proteins they express.

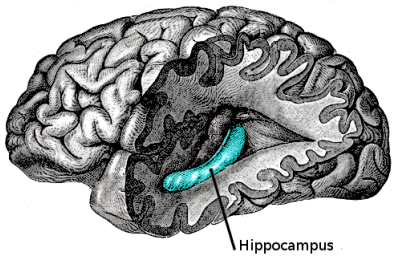

FIGURE 2.2 – Positioning of the human hippocampus inside the temporal lobe. Source : Wikimedia Commons.

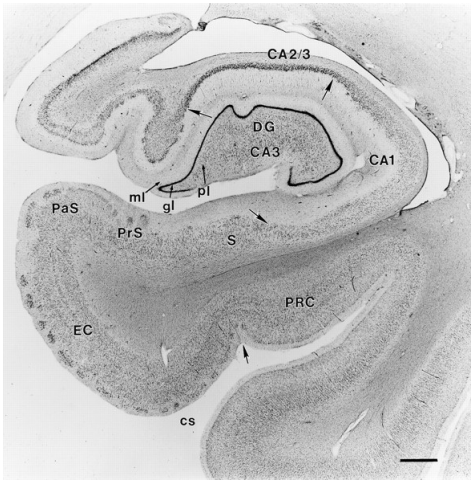

FIGURE 2.3 – Coronal section from a healthy brain through the right rostral hippocampal formation stained with thionin. Arrows mark the borders between regions. CA1 and CA2/3 refer to the CA fields of the hippocampus. DG, Dentate gyrus ; ml, molecular layer of the dentate gyrus ; gl, granule cell layer ; pl, polymorphic layer ; S, subiculum ; PrS, presubiculum ; PaS, parasubiculum ; EC, entorhinal cortex ; cs, collateral sulcus ; PRC, perirhinal cortex. Scale bar, 1 mm. Source : [Rempel-Clower et al., 1996]

TABLE 2.1 – Number of principal neurons in each region of the human hippocampal formation (in millions). Sources : [West et al., 1994], [West and Slomianka, 1998]

Region	Pyramidal cell	Granule cells
Dentate Gyrus	-	18
CA3	2.8	-
CA1	14	-
Subiculum	6	-
Entorhinal cortex	8	-

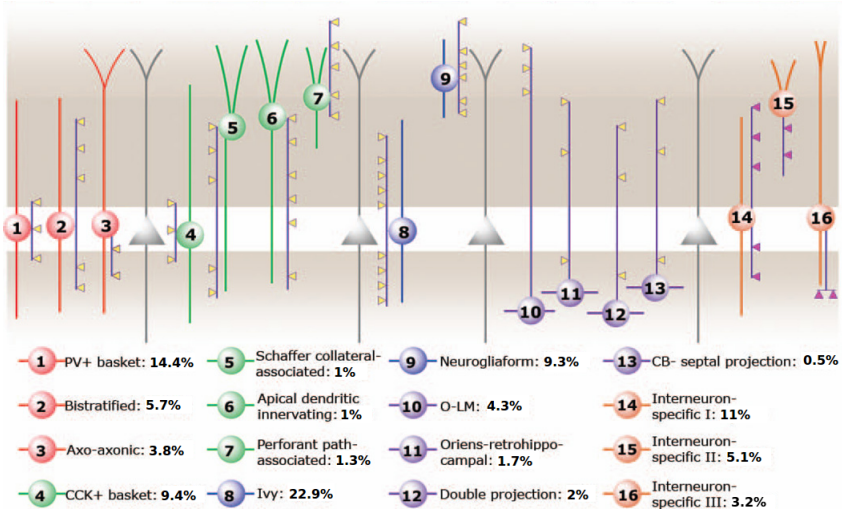

FIGURE 2.4 – Diagram of interneuron types in the rat CA1 region. The dendrites and somata of the interneurons are the same color, and the axon is shown in purple with color coded boutons. Pink boutons specify synapses made only onto other interneurons. The legend below the diagram gives the names and proportions of each interneuron type. Red : PV+ cells, Green : CCK+ cells, Blue : Neurogliaform family, Purple : SOM+ cells, Orange : Interneuron-specific cells. Figure adapted from : [Bezaire and Soltesz, 2013].

Each hippocampal region can then be seen as an organized structure composed of different layers, each of them containing specific neuron's somas or dendritic arborizations. In the Cornus Ammonis, one can distinguish in that way the stratum oriens (containing the soma of some interneurons), the stratum pyramidale (containing the soma of pyramidal cells) and the stratum lacunosum moleculare and stratum radiatum (which contains respectively the distal and proximal dendrites of pyramidal cells). In the Dentate Gyrus, the soma of the granular cells are located inside the stratum granulosum, while their apical dendrites are located in the molecular layer. The first segments of the axons of the granular cells, called mossy fibers, are located in the polymorphic layer (this layer also contains basket cells).

2.1.2 Internal connectivity, afferent and efferent connections

The hippocampus receives most of its glutamatergic synaptic inputs through its neighboring structures, the Entorhinal Cortex and the Subiculum, which convey information coming from various cortical sources, such as sensory areas (including visual cortices) and the prefrontal cortex, as well as from other structures of the limbic system. From there, neural activity follows what is usually called the "trisynaptic pathway", a set of unidirectional excitatory synapses going from the Entorhinal cortex layer II to the Dentate Gyrus (these connections form the so called perforant path), from the Dentate Gyrus to CA3, from CA3 to CA1 (through what it called Schaffer collaterals) and finally from CA1 back to the Subiculum and the Entorhinal Cortex's deeper layers. Fewer connections are also made from the Entorhinal Cortex directly to CA3 (from neurons in layer II) and CA1 (from layer III) ([Andersen et al., 2007], see Figure 2.5).

The hippocampus also receives some glutamatergic inputs directly from some subcortical regions such as the amygdala ([Felix-Ortiz and Tye, 2014]) and different thalamus nuclei, namely, the supramammillary nucleus, which projects to the Dentate Gyrus, and nucleus reuniens,

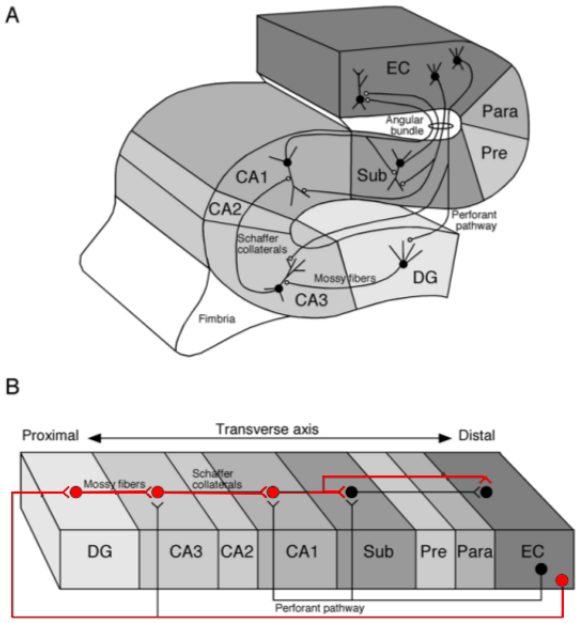

FIGURE 2.5 – Diagram of the excitatory synaptic connections between subregions of the hippocampal formation, adapted from [Andersen et al., 2007], with the trisynaptic pathway appearing in red.

which projects to the CA1 region, and are thought to amplify the synaptic transmissions received by these regions, (see [Vertes, 2015]), as well as GABA-ergic (inhibitory), cholinergic and glutamatergic (excitatory) inputs from the medial septum ([Wainer et al., 1985], [Huh et al., 2010]).

As for hippocampal efferent projections, most of them go through the entorhinal or perirhinal cortices ([Agster and Burwell, 2013]), which in turn contact other regions of the brain such as the frontal and temporal cortices ([Muñoz and Insausti, 2005]), and through the fornix, which then contacts thalamic nuclei ([Raisman et al., 1966]). Synaptic connections also exist from one hippocampus to the controlateral one, especially from the dentate gyri and CA2/CA3 regions ([Andersen et al., 2007]).

This anatomical organization underlies the hippocampal functions detailed in the following section.

2.1.3 Functions of the Hippocampus

As was explained in Chapter 1, the hippocampus has been reported to play a major role in memory formation and consolidation. According to the two-step memory formation theory, during the day the hippocampus receives information from the rest of the brain and stores it in the CA3 and CA1 regions, which is the basis of short-term memory. Conversely during the night, the information previously stored is transmitted from the hippocampus back to the neocortex to consolidate it into long-term memory. This theory is supported by the fact that hippocampus surgical removal is associated with a loss of recent memories and a loss of the ability to make new ones, but no loss of older memories, suggesting that only short-term memory is stored in the hippocampus (see [Scoville and Milner, 1957] for the first report on this phenomenon, on the famous "H.M" patient). Sleep has also been shown to enhance memory performance, while

sleep deprivation decrease it (for a review on this subject in human and animals, see [Stickgold, 2005]). According to the multiple trace theory ([Nadel et al., 2000], [Nadel et al., 2007]), episodic memory (which is the memory of autobiographical events) could also actively depend on the hippocampus for the retrieval of precise details, while only semantic memory (which refers to general world knowledge) encoded in multiple neocortical circuits could be fully retrieved in the case of hippocampal damage.

The hippocampus and entorhinal cortex also play a role in spatial navigation. As reported by ([O'Keefe and Dostrovsky, 1971],[Brun, 2002]), some neurons in these two structures present an activity which depends on one's position in one's environment. In the hippocampus, some neurons called place cells fire preferentially when the subject is in one precise location of its environment, whereas in the Entorhinal cortex, grid cells fire in a spatially regular pattern. Some neurons called head-direction cells have also been discovered in the Entorhinal cortex, which show an increased firing rate when one's head is facing in a specific direction. After having been first discovered and described in animals, this spatial dependant neural activity have then been observed in human, either through indirect methods (fMRI in [Doeller et al., 2010]), and more directly with sEEG recordings ([Jacobs et al., 2013]). Together, these different cell types enable the brain to build an efficient mental representation of one's environment and perform spatial navigation. Similarly, the hippocampus has been shown to include "time cells", neurons that fire at successive moments in temporally structured experiences ([Eichenbaum, 2014]).

As a part of the limbic system, the hippocampal formation (and more precisely, its ventral part), has also been shown to be involved in fear and anxiety behaviors ([McHugh et al., 2004], [Adhikari et al., 2010]) and social interactions ([Felix-Ortiz and Tye, 2014]).

Overall, the hippocampus acts as a hub which integrates information from multiple brain areas so as to build temporally, spatially, and even emotionally structured representations of one's experiences. This region is then all the more important to study that pathologies like mesial temporal lobe epilepsies may disturb these functions and lead to many cognitive impairments, such as memory deficits, language impairments or attention deficits (see [Rastogi et al., 2014] or [Uslu et al., 2019]).

2.2 Oscillatory patterns of the Hippocampus during the sleep-wake cycle and their modeling

2.2.1 Theta-nested gamma oscillations

The hippocampus multiple functions are each characterized by specific neural activity patterns.

In awake animals, it has been demonstrated that spatial navigation as well as short-term memory encoding is accompanied by theta-nested gamma oscillations, which consists in low frequency oscillations (theta, 5-10Hz) coupled with high frequency ones (gamma, 30-100Hz), as shown on Figure 2.6.

Theta oscillations are most prominent in the CA1 region, but they also occur in CA3 and in the Dentate Gyrus ([Buzsáki, 2002]). It has been hypothesized that the generation of this rhythm could be caused by medial septum cholinergic and GABA-ergic inputs acting as a "pacemaker" for the hippocampus ([Bland and Bland, 1986], [Hangya et al., 2009]), but it could also be generated by hippocampal pyramidal neurons themselves, as they present a specific ion channel called Calcium-Activated Nonspecific cationic channel (CAN channel, see description in [Partridge and Swandulla, 1988]), which enable sustained activity in the theta frequency range ([Egorov et al.,

2002], [Giovannini et al., 2017]), or by O-LM interneurons which spike preferentially at a theta frequency ([Gloveli et al., 2004]).

The gamma oscillations on the other hand are thought to be produced by the interaction between hippocampal pyramidal cells and various types of interneurons, in the CA3 and CA1 region in particular ([Csicsvari et al., 2003], [Klausberger and Somogyi, 2008], [Gloveli et al., 2004]). As part of these gamma rhythms, hippocampal place cells and grid cells corresponding to recently crossed locations fire at a specific phase of theta oscillations ([Lisman and Jensen, 2013]). This precise spatiotemporal firing is what enables a faithful representation of an animal's trajectory. The same type of oscillations could also be involved in short-term memory processes, as a way to maintain information even as the related input is fading.

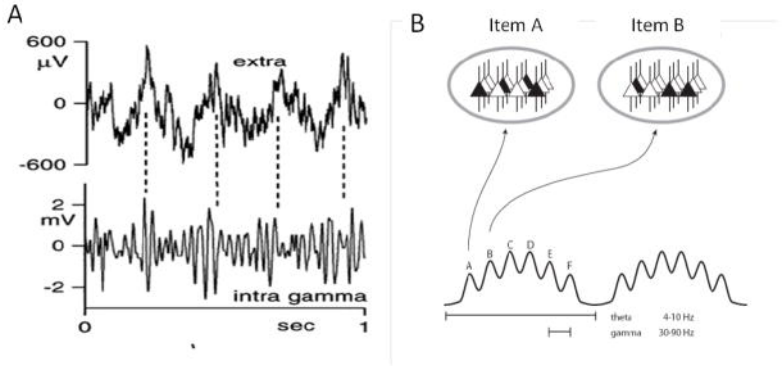

FIGURE 2.6 – Illustration of theta-nested gamma oscillation, from [Lisman and Jensen, 2013]. (A) Simultaneous extracellular (top) and intracellular (bottom) recordings from the hippocampus. (B) Schematic of the theta-gamma code. The ovals at top represent states of the same network during two gamma cycles (active cells are black and constitute the ensemble that codes for a particular item). Different ensembles are active in different gamma cycles.

Multiple computational models have been proposed to reproduce and explain theta and gamma oscillations, as well as the formation of place cells or grid cells firing patterns.

In [Wulff et al., 2009] for example, a small model of the CA1 region is proposed to study the role of intrahippocampal networks on the coupling of theta and gamma oscillations, in relation with an experiment on genetically modified mice lacking a GABA-A receptor subunit on their parvalbumin positive (PV+) interneurons. The model, consisting of 21 single compartment Hodgkin-Huxley neurons of different subtypes (pyramidal cells, PV+ basket cells and O-LM cells), is used to compare the oscillations generated by a "wild-type" network where basket cells receive strong inhibitory inputs from themselves and from O-LM cells and a genetically modified network where these synaptic interactions are removed. Both the experimental procedure and the computational model demonstrate the importance of the synaptic inhibition on CA1 basket cells in the generation of theta-nested gamma oscillations, as without GABA-A receptors on basket cells, CA1 theta (but not gamma) oscillations are reduced in amplitude, and the phase coupling of theta and gamma rhythms is reduced as well.

In [Tiesinga et al., 2001], a larger model is described to better understand the generation of different oscillatory rhythms in the CA3 region, and their link with the concentration of a cholinergic agonist, carbachol (CCH). So as to reproduce the various effects of CCH on 500 pyramidal cells and 100 interneurons, a more complex, two-compartmental neuron model is used (also derived from Hodgkin-Huxley formalism), which enables a study of each neuron channel and synapse property individually. Overall, this network is capable of exhibiting different CCH-

induced rhythms, such as delta, theta and gamma oscillations, and proposes an explanation to the transitions between them : CCH-theta rhythms caused by subthreshold membrane oscillations transition to CCH-delta bursts when CCH concentration increases due to changes in potassium channel properties, while an even greater concentration of CCH results in an increased activation of both pyramidal cells and interneurons and the apparition of CCH-gamma oscillations.

Simpler models have also been developed, for example in [Keeley et al., 2017], where a leaky integrate-and-fire (LIF) model is compared with a reduced population rate model in order to study the generation of gamma oscillations of different frequencies in the CA1 region. In this article, one population of pyramidal cells and two populations of interneurons with different synaptic time constants are considered. Simulation results from the LIF model show that the population of excitatory neurons can fire at a frequency ranging from slow to fast gamma depending on which interneuron population it is more strongly connected with, while the strength of the synaptic coupling between the two interneuron populations determine whether intermediate firing frequencies can be reached. The population rate model can reproduce most (though not all) of the behaviors seen with the LIF network, but it can also help understand them in terms of bifurcations in the parameter space.

Regarding place cells and grid cells, more functional and abstract models exist such as the oscillatory inference model presented in [Burgess et al., 2007], which expresses the firing rate of grid cells as a sum of sine waves with phase and frequencies depending on the animal's speed and the distance it traveled in a "preferred" direction specific to that cell. The combination of cells with different preferred directions enables the formation of hexagonal grid maps such as the ones seen in experiments. This model also simulates inputs from place cells coming to grid cells, which helps reset their phase and correct errors that might accumulate in the grid field over time.

Attractor models are another main type of grid cells or place cells model. In [Pastoll et al., 2013] for example, about 4000 excitatory and 1000 inhibitory exponential integrate-and-fire neurons are modeled and connected with each other in accordance with their positioning on a torus (which here reflects their preferred direction, and not their spatial position). The network receives both a theta stimulation and a stimulation current which corresponds to a simulated animal movement (for each neuron this input is proportional to the speed of the movement along its preferred direction). This model is capable of reproducing gamma oscillations coupled to the theta cycles, and grid fields similar to those seen in experiments. The grid firing pattern of interneurons in particular is highly dependent on the connectivity of the network, i.e. the distance at which excitatory and inhibitory connections are made preferentially.

More example of grid cells and place cells computational models can be found in [Giocomo et al., 2011].

2.2.2 Sharp-Wave Ripple complexes

Memory consolidation is thought to rely on a specific hippocampal oscillatory pattern, called Sharp-Wave Ripple complex (SPW-R).

This pattern consists in a large amplitude LFP deflection (Sharp-Wave) in CA1 stratum radiatum, on which a high-frequency is superimposed (Ripple, 120-200Hz) in the CA1 pyramidal layer ([Buzsáki, 2015]). Sharp-Wave ripple complexes usually last around 100ms, and occur mostly during slow-wave sleep as well as awake resting states, last around 100ms, and seem to be able to arise and propagate anywhere along the septotemporal axis of the hippocampus ([Patel et al., 2013]). A complete review of this phenomenon can be found in [Buzsáki, 2015].

During these oscillations neurons and place cells "replay" the activity they had during the day ([Wilson and McNaughton, 1994]), spiking in the same order or in a reversed order (Figure

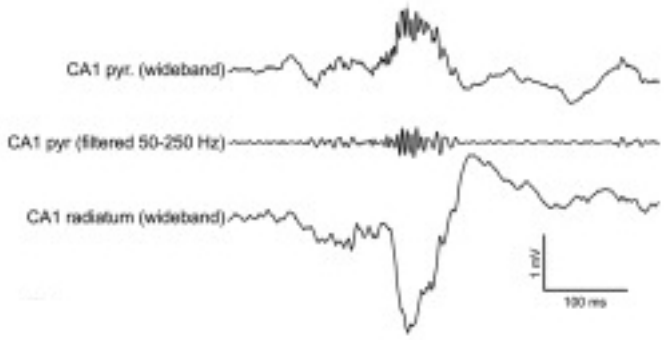

FIGURE 2.7 – Illustration of a sharp-wave ripple complex, taken from [Buzsáki, 2015]. Raw traces of wide-band LFP (1–625 Hz) recorded simultaneously from the CA1 pyramidal layer and the mid str. radiatum, together with a band-pass filtered (50–250 Hz) trace of the pyramidal layer signal.

2.8, [Diba and Buzsáki, 2007]), but in a time-condensed manner, which may help transferring new information and episodic memory traces to cortical areas. Regarding spatial memory, experiments indicate that Sharp-Wave Ripple complexes help stabilizing place fields ([Roux et al., 2017]), and that disturbing them through optogenetic methods reduces animal's performance in spatial memorization tasks ([Girardeau and Zugaro, 2011]).

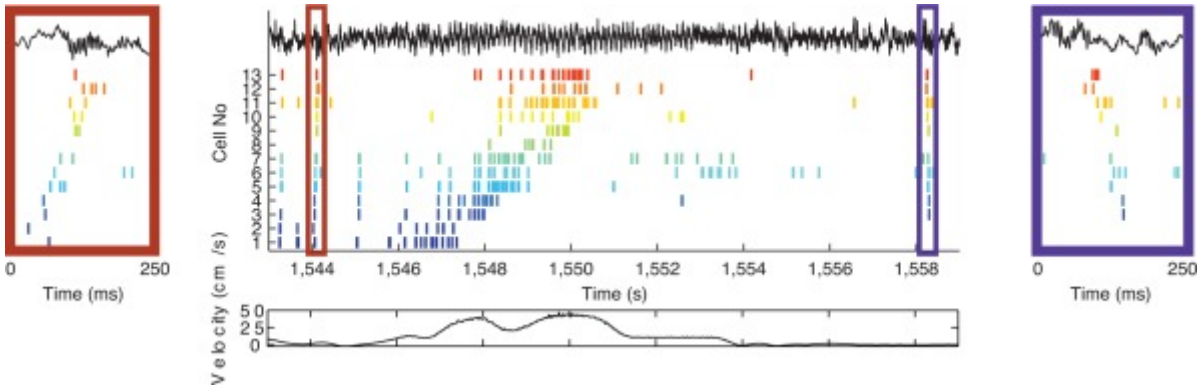

FIGURE 2.8 – Illustration of place cells replay during SPW-Rs, from [Buzsáki, 2015]. Place cell sequences experienced during behavior are replayed in both the forward and reverse direction during awake SPW-Rs. Spike trains for place fields of 13 CA3 pyramidal cells of a rat running on a track are shown before, during and after a single traversal. Sequences that occur during track running are reactivated during SPW-Rs both before and after the run, when the rat stays immobile. Forward replay (left inset, red box) occurs before traversal of the environment and reverse replay (right inset, blue box) after. The CA1 local field potential is shown on top and the animal's velocity is shown below.

Sharp-Wave Ripples are usually considered as a consequence of the activity of the CA3 region, where strong recurrent excitation gives rise to synchronized excitatory bursts, sometimes called CA3 ripples, and transferred via Schaffer collaterals. However, CA3 high frequency oscillations could arise from various dentate gyrus or entorhinal cortex inputs, in the fast gamma frequency

range in particular ([Sullivan et al., 2011]). During SPW-Rs, CA1 pyramidal neurons are strongly activated and synchronized, and so are some types of interneurons like basket cells, but other types of interneurons like O-LM cells get relatively silent ([Csicsvari et al., 2003]). The fast pacing of ripples could be the result of synaptic interactions between CA1 pyramidal cells and interneurons, between CA1 interneurons, or axo-axonic electrical coupling of cells through gap junctions (as presented in [Stark et al., 2014], where the first hypothesis is favored).

Similarly to theta-nested gamma oscillations, many computational models have been developed throughout the years so as to better understand sharp-wave ripple complexes.

Among these, the fast oscillation model from [Traub et al., 1999] was quite influential. This model includes about 3000 pyramidal cells with more than 60 compartments, linked to each other by axo-axonic gap junctions so as to form either a tree-like or a random graph, and was able to produce bursts of activity in the ripple frequency range (100-200Hz), independently of the presence of excitatory chemical synapses. These ripples appeared in the presence of a Poisson background input applied to the neurons, provided that the gap junction coupling was strong enough, and their frequency was mostly determined by the structure of the network, i.e. the mean path length between two interconnected neurons. Later on, this model was developed further, for example in [Traub and Bibbig, 2000] where a population of interneurons was also included.

Models including only chemical synapses and no axo-axonic gap junctions were also able to reproduce sharp-wave ripple oscillations, such as the CA3 and CA1 model from [Taxidis et al., 2012]. In this study, each of the two hippocampal regions was represented by an array of 1000 pyramidal cells (two compartmental Pinsky-Rinzel) and 100 fast spiking interneurons (single compartment Hodgkin-Huxley), connected with AMPA and GABA-A synapses so that each neuron receives the same number of synapses as was reported in electrophysiological studies. The isolated CA3 model produced bursts of activity at a theta frequency, while the isolated CA1 interneuron population generated gamma activity. Putting all the populations together gave rise to sharp-wave ripple oscillations in CA1, with a stronger activation of interneurons than pyramidal cells. The frequency of the oscillations could be modified by changing synaptic properties : for example, increasing the maximum conductance of GABA synapses slowed down the oscillations, while increasing the decay time of AMPA synapses had the opposite effect.

In [Omura et al., 2015], the focus is put on how to explain the variability of SPW-Rs amplitudes with a network with heterogeneous synaptic properties. A model of CA3 is proposed, comprising 10000 excitatory and 2000 inhibitory adaptive threshold integrate-and-fire neurons, where the weight of synaptic connections between excitatory neurons is drawn from a lognormal distribution. Such distribution made it possible to reproduce not only the frequency of SPW-Rs but also the firing rates and amplitude variability observed experimentally, which was not the case with other distributions (such as a truncated Gaussian function).

The transition between theta-nested gamma oscillations and sharp-wave ripple complexes is not yet fully understood, but it has been theorized in [Hasselmo, 1999] that these could depend on the level of neuromodulators present in the hippocampus, and Acetylcholine (Ach) in particular (see Figure 2.9). This idea is supported by an experiment presented in [Zylla et al., 2013], where the activation of cholinergic receptors shifted hippocampal oscillations from ripple to gamma frequency range. In [Brunel and Wang, 2003], the factors influencing the frequency and synchrony of the fast oscillations generated by a integrate-and-fire neuron network are studied. In a network consisting only of inhibitory neurons, the oscillatory frequency can be approximated analytically and is mostly governed by synaptic rise time constants, and can reach the ripple frequency band. When a population of excitatory cells is added, the frequency of the oscillations decreases depending on the balance of relative speeds of excitatory and inhibitory synapses, down to a gamma frequency range.

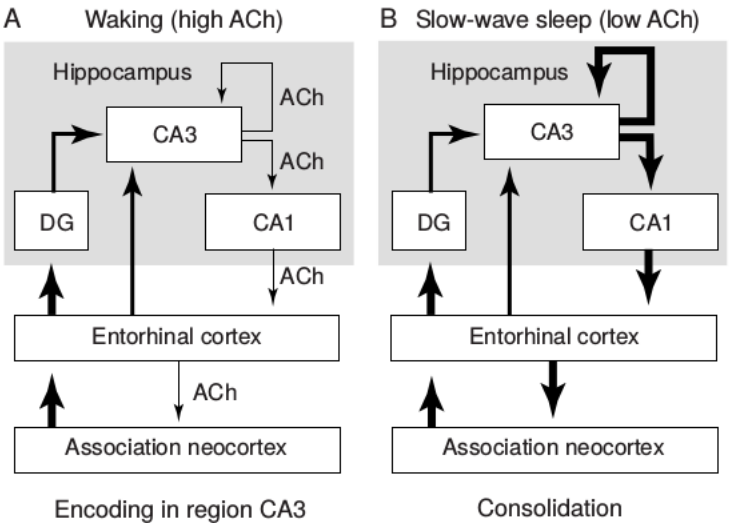

FIGURE 2.9 – Two-stage model of long-term memory formation by [Hasselmo, 1999]. Panels A and B represent synaptic connectivity from the neocortex to the hippocapal formation during active waking and slow-wave sleep respectively. Connections suppressed by Ach are represented with thin arrows and connections less sensitive to the modulation by Ach are represented with thick arrows.

Overall it can be seen that many different models exist to explain each aspect of healthy hippocampal activity, each of them relying on different cellular or network mechanisms, which is why in the course of this thesis we think that building a single model capable of reproducing all the types of hippocampal rhythm and taking into account the influence of several mechanisms could be beneficial for a better global understanding of this brain structure.

2.3 Modifications of the hippocampus in mesial-temporal lobe epilepsy

2.3.1 Anatomical and physiological modifications

In patients suffering from mesial temporal lobe epilepsy, physiological hippocampal rhythms like theta-nested gamma oscillations or sharp-wave ripple complexes still occur, but other pathological activity patterns are present which drive the symptoms and cognitive impairments associated with this disease. Many structural and functional modifications have been observed in the epileptic hippocampus, which may be a cause or a consequence of its abnormal activity.

Firstly, a very common histopathology seen in the epileptic hippocampus is hippocampal sclerosis (HS), which consists in severe neuronal cell loss and gliosis. All the different CA subfields may be affected, as well as the Dentate Gyrus, to various levels depending on the patient. The International League Against Epilepsy (ILAE) proposed a classification of the different types of HS in [Blümcke et al., 2013] (see Figure 2.10).

The most common type of HS (60 to 80% of reported cases) is ILAE-Type 1, which is sometimes called typical HS, and affects all regions of the hippocampus. ILAE types 2 and 3 show preferential cell loss in the CA1 and CA4 regions respectively, with less severe neuronal loss in other regions (the reported proportions of cell loss in each region for each HS type can be found in Table 2.2). The last type called "no-HS" corresponds to about 20% of patients, which

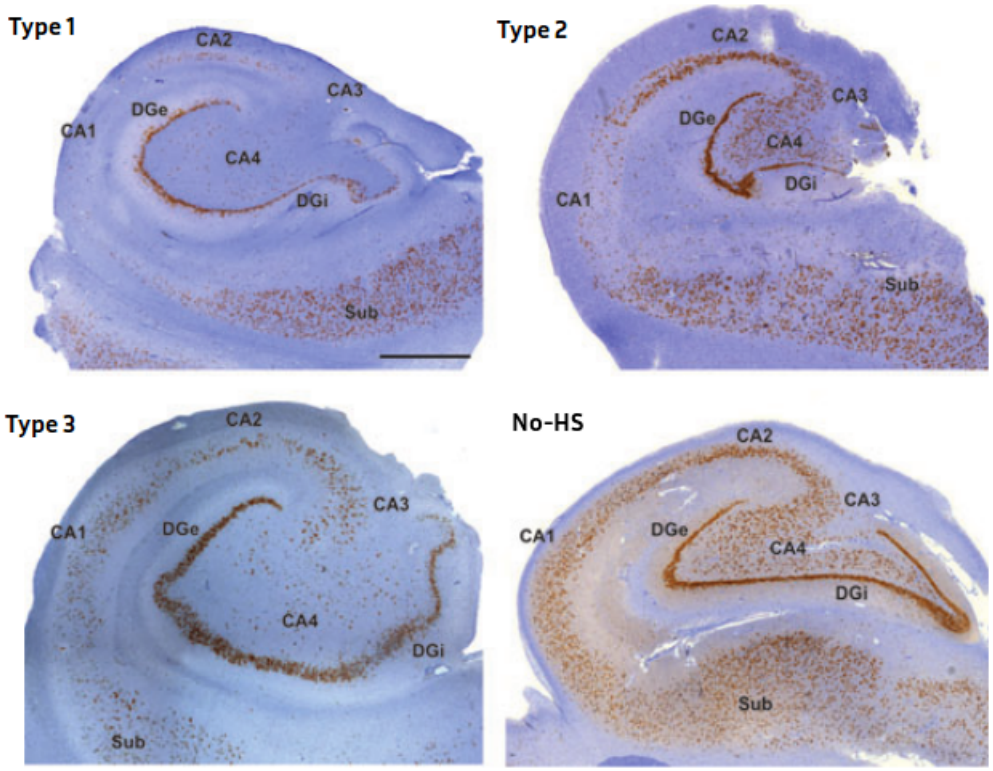

FIGURE 2.10 – Illustration of the different ILAE hippocampal sclerosis types observed in temporal lobe epilepsies, adapted from [Blümcke et al., 2013]. All stainings represent NeuN immunohistochemistry, i.e. the presence of a biomarker characteristic of neural nuclei. DGe/DGI, external/internal limbs of dentate gyrus ; Sub, subiculum. Scale bar in the first panel = 1,000μm (applies also to the other panels).

Region	Type 1	Type 2	Type 3
CA1	>80%	80%	<20%
CA3	40-90%	<20%	30%
DG	50-60%	<20%	35%

TABLE 2.2 – Typical proportion of cell loss in different hippocampal sclerosis patterns

only present gliosis and no neuronal loss. HS is often associated with granule cell dispersion, a broadening of the granule cell layer in the dentate gyrus.

Interestingly, while HS involves loss of pyramidal neurons and granule cells, the number of GABA-ergic cells in the epileptic hippocampus is mostly preserved (as mentioned for example in [Babb et al., 1989], but see also [Fritschy et al., 1999]), which could lead to an hypersynchronizability of the hippocampus. Similar patterns of cell loss are also observed in the entorhinal cortex in epilepsy models of rats ([Drexel et al., 2012]) as well as in humans ([Vismer et al., 2015]).

Hippocampal sclerosis is observed in most experimental models of acquired epilepsy, such as electrical kindling ([Cavazos and Sutula, 1990]) and kainate-acid administration ([Bouilleret et al., 1999]), or after brain injuries. HS may appear as a consequence of inflammation following an initial injury, calcium ions accumulation to an excitotoxic level during seizure episodes ([Sendrowski and Sobaniec, 2013]), or systemic hypoxia during status epilepticus (in this case, the varying vulnerability of hippocampal cells would also depend on their containing calcium binding proteins, see [Freund et al., 1992]).

Another major abnormality seen in the epileptic hippocampus is mossy fiber sprouting, the growth of granule cell axons (mossy fibers) and the multiplication of excitatory synaptic contacts they make with surrounding or more distant neurons (see Figure 2.11). This phenomenon is seen in almost every animal model of epilepsy, presumably as a consequence of mossy cell loss and granule cell deafferentation (see [Noebels et al., 2012] for a review of this phenomenon).

In [Schmeiser et al., 2017], mossy fiber sprouting patterns are described depending on HS type : usually no sprouting is observed in no-HS hippocampus, whereas in HS types 1, 2 and 3, increased mossy fiber density is found especially in CA1. In HS types 1 and 3 also, fewer mossy fiber projections are found going from the dentate gyrus to CA3 and CA4, which could be linked to the cell losses in these regions. This work also reports granule cell dispersion is more prominent in ILAE HS types 1 and 2 compared to no-HS, with the width of the granule cell layer being larger by about 50 μm.

Inside the Dentate Gyrus itself, mossy fiber sprouting is associated with the generation of mono-synaptic excitatory connections between granule cells : approximately 500 new synapses are created that way for each granule cell ([Buckmaster et al., 2002]), which gives an overall connection probability of 0.7% between any pair of cells ([Scharfman et al., 2003]). This recurrent excitation is often seen as a potential cause of epileptic activities ([Cavarsan et al., 2018]). New synapses from granule cells to inhibitory interneurons can also be formed ([Sloviter et al., 2005]), but according to [Buckmaster et al., 2002] these are less numerous (only 5% of newly formed synapses).

Among other anatomical and physiological hippocampal features linked to epilepsy, hippocampal neurons' ion channels can be altered as well, either due to genetic mutations, or after plasticity in acquired epilepsy syndromes (see [Lerche et al., 2012]). More precisely, genetic alterations of sodium, potassium, HCN or chloride channels subunits can be observed on mice with

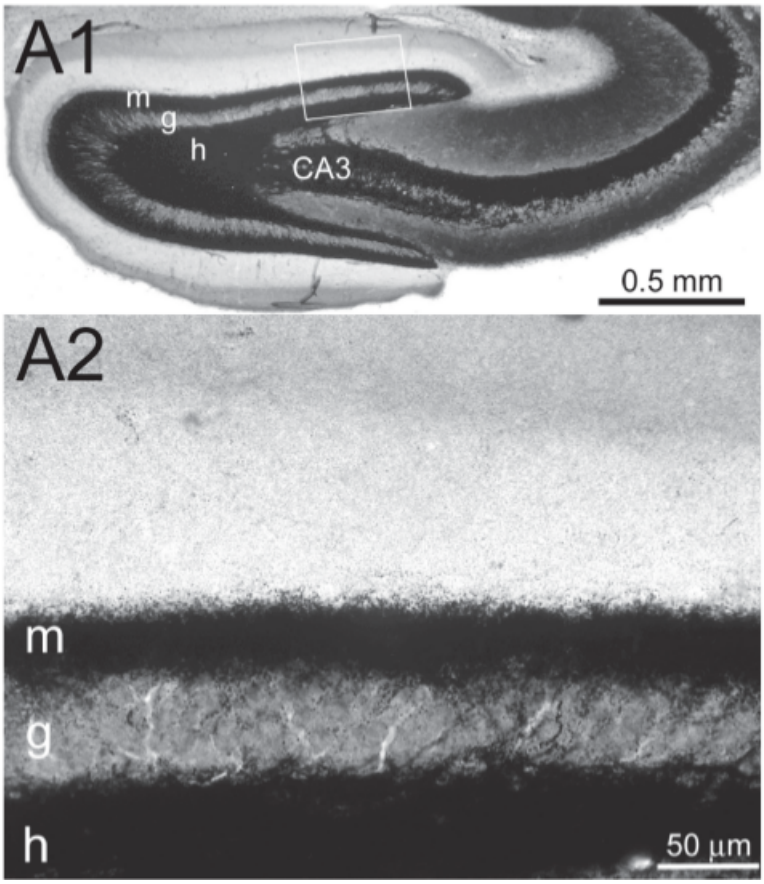

FIGURE 2.11 – Illustration of mossy fiber sprouting in epileptic pilocarpine-treated rats, from [Noebels et al., 2012]. A1- Timm staining of the dentate gyrus (h=hilus, g=granule cell layer, m=molecular layer) and CA3 region. A2- Magnified view of boxed region in A1 shows a dense band of black Timm-staining in the inner molecular layer, made of sprouted mossy fibers.

spontaneous epilepsy phenotypes, while in acquired temporal lobe epilepsies the HCN channel currents can be either reduced or enhanced, potassium current can be reduced, and persistent sodium current can be enhanced, for example. Synaptic receptors of AMPA, GABA and NMDA types can be modified too ([Lerche et al., 2012], [Fritschy et al., 1999]). Finally, glial cells are also involved in different types of temporal lobe epilepsy, as impaired astrocytes alter the regulation of potassium as well as glutamate (for example) in the extracellular space, which lead to neuronal hyperexcitability (see [Heinemann et al., 2000] and [Coulter and Steinhauser, 2015]).

2.3.2 Pathological hippocampal rhythms

Apart from (but probably related to) anatomical and functional modifications, the epileptic hippocampus generates different abnormal rhythms which will be discussed in this section.

Of course, the best known of these pathological oscillatory patterns is the epileptic seizure. In mesial temporal lobe epilepsy, the most common seizure onset types are the hypersynchronous (HYP) and low voltage fast (LVF) types, though other patterns also exist (see [Engel, 2001], [Weiss et al., 2015] and Figure 2.12). HYP onsets are associated with high amplitude ictal discharges seen on depth electrodes with a frequency less than 2Hz, while LVF onsets consists in low amplitude faster oscillations with a frequency higher than 12Hz and are more likely to propagate outside the seizure onset region. During seizures, other oscillatory patterns can appear and vary between brain regions, as developed in [Osorio et al., 2016] for surface electrodes. On a smaller scale, [Gonzalez-Sulser et al., 2012] shows that in a rat epilepsy model, LFP discharges originating from small groups of neurons either in CA3 or in the DG occur during seizures and propagate through excitatory synaptic transmissions, mostly glutamatergic.

In temporal lobe epilepsies, seizures occur predominantly during waking (see for example [Crespel et al., 1998] for a study on humans) and REM sleep ([Sedigh-Sarvestani et al., 2014] for a rat model), which indicates there could be a facilitating effect of theta oscillations on seizure occurrence. According to [Lopim et al., 2016], the frequency of seizure occurrence is also reduced correlated with the severity of hippocampal sclerosis.

The epileptic hippocampus generates pathological rhythms outside of seizure episodes as well, mainly pathological high frequency oscillations (HFOs) and interictal epileptiform discharges (IEDs), shown in Figure 2.13.

HFOs regroup all types of oscillations in the 100Hz-500Hz frequency range, but in the context of mesial temporal lobe epilepsy usually refer to one particular pattern called fast ripples, events similar to sharp-wave ripple complexes but of shorter duration and capable of reaching higher frequency([Bragin et al., 1999]). After having been observed only in areas ipsilateral to seizure onsets at first, fast ripples have then been shown to occur also in contralateral hippocampus and entorhinal cortex as well ([Staba et al., 2002]), and their occurrence rate is correlated with hippocampal sclerosis ([Staba et al., 2007]). Fast ripples can have a peak frequency close to that of physiological ripples, in which case they are hard to differentiate, except when fast ripple involve regions or groups or neurons which do not produce physiological ripple, such as the Dentate Gyrus ([Engel et al., 2009]). Pathological HFOs and increases in the >100Hz frequency range occur during both REM and NREM sleep, but are also seen during ([Jirsch, 2006]) or just before seizures ([Weiss et al., 2015], [Jiruska et al., 2010]) as a marker of increased neuronal synchronization in the mesial temporal lobe.

On the other hand, Interictal Epileptiform Discharges (sometimes also called interictal spikes) are defined as events on EEG recordings with short duration (20-70ms) and clearly distinguishable from background activity ([Gloor, 1975]), and are commonly used to diagnose epilepsy and define seizure onset zones before resection surgeries ([Engel, 2012]). Their exact morphology can vary

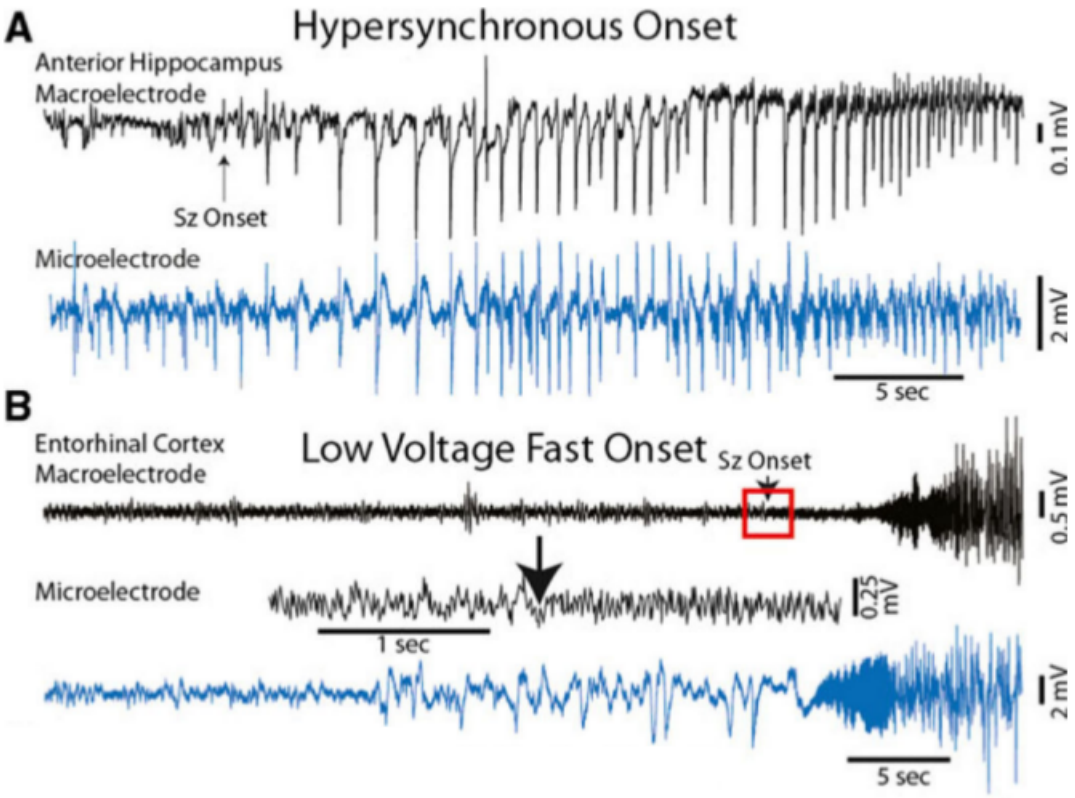

FIGURE 2.12 – Different ictal EEG onsets recorded by clinical electrodes (black) and microelectrodes (blue) positioned in mesial temporal limbic structures, taken from [Weiss et al., 2015]. (A) The hypersynchronous (HYP) onset pattern. (B) The low voltage fast (LVF) onset pattern. Red box indicates expanded time epoch of macroelectrode recording shown directly below.

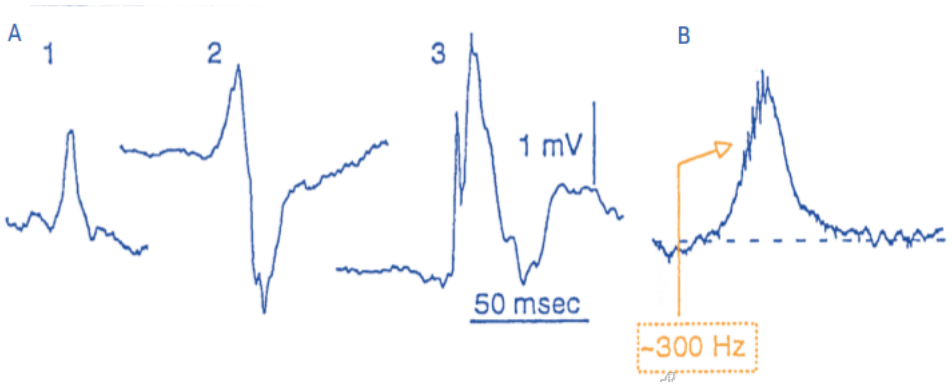

FIGURE 2.13 – Examples of interictal events in a Kainate Acid-treated rat, adapted from [Engel, 2001]. A1–3, Interictal spikes. B, HFO (Fast ripple). The numbers within dashed boxes show the frequency of oscillations indicated by arrows.

greatly at the inter-individual and intra-individual levels ([Gaspard et al., 2014]), but they are characterized by an increased energy in the 10-70Hz frequency band which provides the basis for automatic detection techniques (see for example [Gaspard et al., 2014] and [Janca et al., 2014]). IEDs occur during all stages of the sleep-wake cycle, but are more numerous in NREM sleep ([Gelinas et al., 2016]), and many studies show that they are associated with memory impairments : those occuring during wakefulness disturb working memory ([Krauss et al., 1997]) and more precisely memory maintenance and retrieval ([Kleen et al., 2013]), while those occuring during NREM sleep impair memory consolidation ([Gelinas et al., 2016]) by inducing abnormal hippocampal-cortical coupling.

2.3.3 Models of the epileptic hippocampus

Computational models are powerful tools to study possible mechanisms underlying epilepsy and the generation of epileptiform activity. We will now present a few of these models, focusing either on individual neuron properties, the balance between excitation and inhibition, or the topology of synaptic connections (others models can be found for example in the review from [Stefanescu et al., 2012]).

In [Cressman et al., 2009], a full Hodgkin-Huxley type model as well as a reduced model (with a sigmoid fit to membrane currents) are proposed to study the role of sodium and potassium concentration dynamics in the generation of epileptiform activity, which involves simulating the behavior of a single neuron in a bath containing these ions in different concentrations. This model suggests that potassium dynamics may play a very important role in epileptogenesis, as a broad range of potassium bath concentration can give rise to seizure-like activity, a situation that can be described as a Hopf bifurcation and the apparition of a stable periodic orbit in internal potassium concentration in the model's reduced form. It should be noted that not all of the neuron's possible behaviors obtained with the full model could be reproduced with the reduced model, though.

The role of another membrane current, the hyperpolarization activated current (h-current), is discussed in [Dyhrfjeld-Johnsen, 2008]. This current had been shown to be significantly upregulated in CA1 dendrites in different types of hippocampal epilepsies (such as those induced by childhood fever-induced seizures), but its exact role on epileptogenesis was not clear. The authors investigated this issue by simulating the behavior of a single pyramidal cell with three different existing models (multicompartmental Hodgkin-Huxley type) after an increase of their dendritic h-current conductance density, and showed that it resulted in a hyperexcitability of the neuron, but to various degrees depending of the model.

The work of [Cressman et al., 2009] accompanies that of [Ullah et al., 2008], where a network of 100 pyramidal cells and 100 interneurons is represented with single compartment Hodgkin-Huxley neurons, and the dynamics of sodium and potassium concentrations are further studied connected to glial modulation and synaptic interactions. This network is able to reproduce seizure-like activity when presented a perturbing stimulus, provided that its recurrent excitatory connections are strong enough. The exact synaptic strength and stimulus needed to reach such state is lower when the extracellular potassium concentration is high, which is coherent with the idea that abnormal glial buffering could play a role in seizure generation.

The work of [Demont-Guignard et al., 2009] also mentions the neuronal hyperexcitability induced by abnormal potassium channels and h-channels, but focuses more on the effect of varying several synaptic conductances (AMPA, NMDA and GABA) on interictal spike generation, in a CA1 network consisting of 2500 pyramidal neurons (two-compartments Hodgin-Huxley), 312 basket cells and 312 O-LM cells (single comportment Hodgkin-Huxley). The results of this work

suggest that AMPA conductance plays a prominent role in determining the characteristics of interictal spikes : it is the main factor increasing their amplitude (though NMDA conductance increases it GABA conductance decreases it to a lesser extent), and only a specific range of AMPA conductances enables NMDA and GABA conductance to increase their duration. This model is also interesting as it provides an estimation of the local field potential generated by the network, obtained by approximating each pyramidal neuron as a current dipole, with a dipolar moment proportional to the difference of membrane potential between its somatic and dendritic compartment.

In [Wendling et al., 2002], the role of the varying strength of synaptic interactions is also explored, this time using a population model including 4 groups of neurons present in the CA1 region : pyramidal cells, excitatory interneurons, and two groups of inhibitory interneurons. These two groups of inhibitory interneurons have different dynamics, to represent both fast interneurons contacting pyramidal cells somata, and slower interneurons contacting their dendrites. Different typical epileptic activity can be reproduced by changing the coupling between these different populations, and though all types of synaptic coupling influence the resulting rhythms, changing only the dendritic inhibition coming from slow interneurons is enough to reproduce various transitions of activity observed in sEEG data.

The role of the number and topology of synaptic connections is investigated for example in [Netoff, 2004], where the activity of a ring-shaped hippocampal network (corresponding to the CA3 or CA1 region) is simulated with different number of synapses per neuron, proportions of long-range versus short-range synaptic connections and synaptic strength. Increasing the proportions of long-range connections in particular enables the network to evolve from a normal activity to a seizure-like activity and then to a bursting activity, whatever the neuron model used (Hodgkin-Huxley, Integrate-and-fire or Poisson).

Similar questions are also studied in a Dentate Gyrus model by [Morgan and Soltesz, 2008] (taken from the mossy fiber sprouting and sclerosis models of [Santhakumar et al., 2005] and [Dyhrfjeld-Johnsen et al., 2007]). In this work, the number of synaptic connections in a network of about 50000 multi-compartmental Hodgkin-Huxley neurons is progressively increased by following different rules (Hebbian-like connectivity, scale-free connectivity, repetition of small motifs, etc...), which proves to greatly influence the hyperexcitability of the network. In particular, the presence of small hubs of highly interconnected neurons seems to be a key feature for the generation of epileptiform activity.

To conclude, similarly to healthy hippocampal oscillations, many models exist to reproduce epileptic activity, each focusing on a specific aspect or mechanism, but these models cannot fully explain the links between neuropathological conditions of the hippocampus, physiological processes such as the sleep-wake cycle, and the resulting oscillations. In this work, we would like to provide a different approach and include those different mechanisms, from cell level to network level, in a single model so as to be able to analyze their effects jointly.

2.4 Tools for analyzing and predicting the behavior of neural network models

For a computational model of neural activity to be truly useful, it is necessary to be able to interpret its behavior, and then find out the factors influencing it. We will now present a few methods that can be used to address this issue.

2.4.1 Typical model outputs

Spike timing and coherence measures

Technically, any variable of a model can be stored and plotted to visualize its activity over time. In single neuron models, membrane potentials or ionic channels conductances can be used, but in models including multiple neurons, visualizing the timing of their spikes is usually more meaningful.

This information is often represented on a raster plot (also called rastergram) such as the one shown on Figure 2.14 : each spike happening in the network is indicated as a dot with x-coordinate corresponding to its timing and y-coordinate corresponding to the index of the neuron that fired it. Most of the models presented in the previous sections include a raster plot as a qualitative, easy to interpret visualization of their activity.

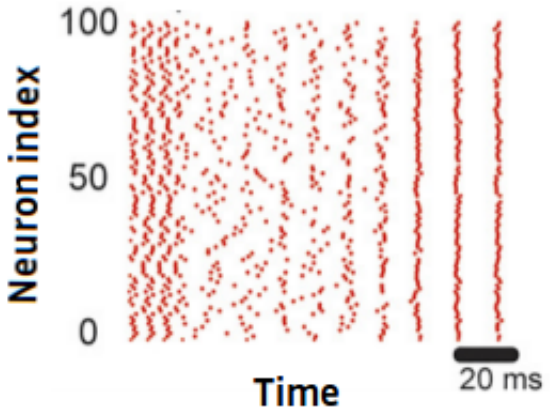

FIGURE 2.14 – Example of a raster plot, adapted from [Keeley et al., 2017]

More quantitative analysis can be done by computing the firing rate of a population of neurons, or the synchrony of their spike trains. Several methods exist to obtain the latter information, such as the coherence measure from [Wang and Buzsáki, 1996], the spike-train distance measure proposed in [Victor and Purpura, 1997], or the event synchronization measure from [Quiroga et al., 2002].

Local Field Potentials

The previous methods provide some useful insights on a neural network's activity, however the individual spike trains of a large number of neurons is not commonly obtained experimentally, and therefore the validation of a model must often be done in comparison with LFP measurements.

In a model comprising multicompartmental neurons, the LFP generated by the network can be computed with high realism ([Einevoll et al., 2013]). Considering the extracellular medium as a three-dimensional continuum, the extracellular potential ϕ generated by a single neuron follows the equation :

$$\phi(\mathbf{r}_e, t) = \frac{1}{4\pi\sigma} \sum_{n=1}^{N} \frac{I_n(t)}{|\mathbf{r}_e - \mathbf{r}_n|} \tag{2.1}$$

where $\mathbf{r}_e$ is the measurement point (the tip of the electrode), $\mathbf{r}_n$ the position of the n-th compartment of the neuron, I_n the transmembrane current of this compartment, and σ is the conductivity of the extracellular medium (see Figure 2.15). The LFP generated by a whole network of neurons at the point $\mathbf{r}_e$ is then simply the sum of the contributions of each neuron individually. Here the conductivity σ is supposed isotropic, but the formula can be easily adapted to account for a more complex extracellular medium.

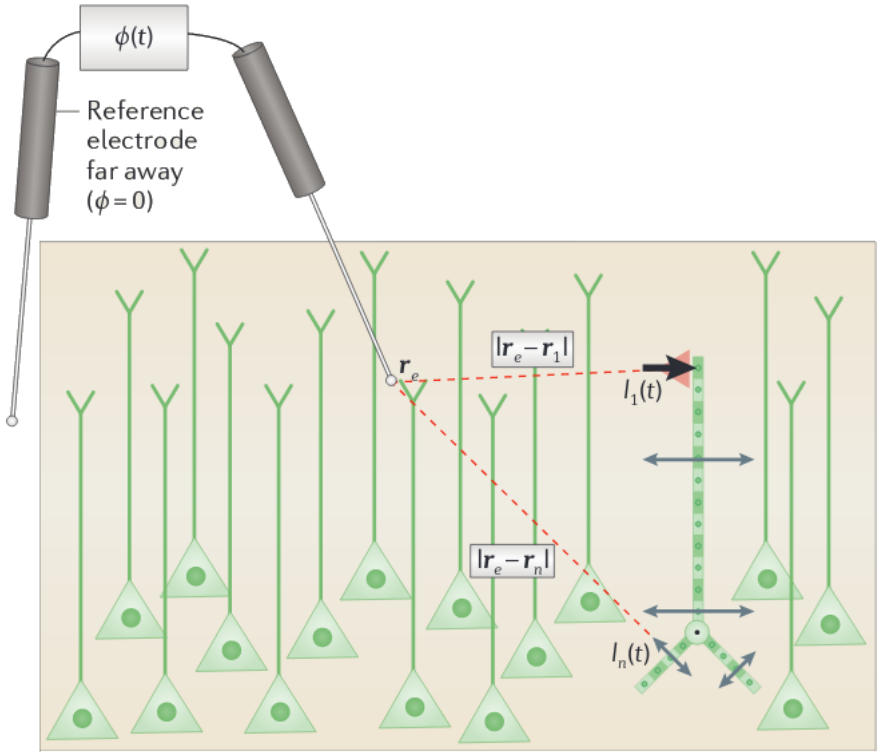

FIGURE 2.15 – Illustration of the LFP calculation from multicompartment neurons, adapted from [Einevoll et al., 2013]

However, simulating neurons with a detailed morphology is highly time-consuming, and therefore it is common to approximate neurons as current dipoles with the source located at the soma and the sink located at the neuron's dendrites ([Pettersen et al., 2012]) to reduce the computational burden of the model while keeping a good estimation of the LFP (see Figure 2.16). Further simplification can be made by considering only synaptic currents and no other membrane currents in the calculation of the LFP, as synaptic activity is often the most important contribution to the extracellular field (see [Buzsaki et al., 2012]).

This forward calculation of the LFP is not applicable to single compartment neurons as is, because a cell must remain electrically neutral by current conservation law, but different LFP proxies exist to work around this problem if necessary (notably the weighted sum of neuron's membrane potentials or synaptic currents). In [Mazzoni et al., 2015], a realistic LFP (obtained with a model with multicompartmental neurons) is compared with several of these proxies in a LIF model, showing that proxies can reproduce almost 90% of the variance of the more realistic LFP. Interestingly, this work also shows that synaptic contacts made onto pyramidal cells

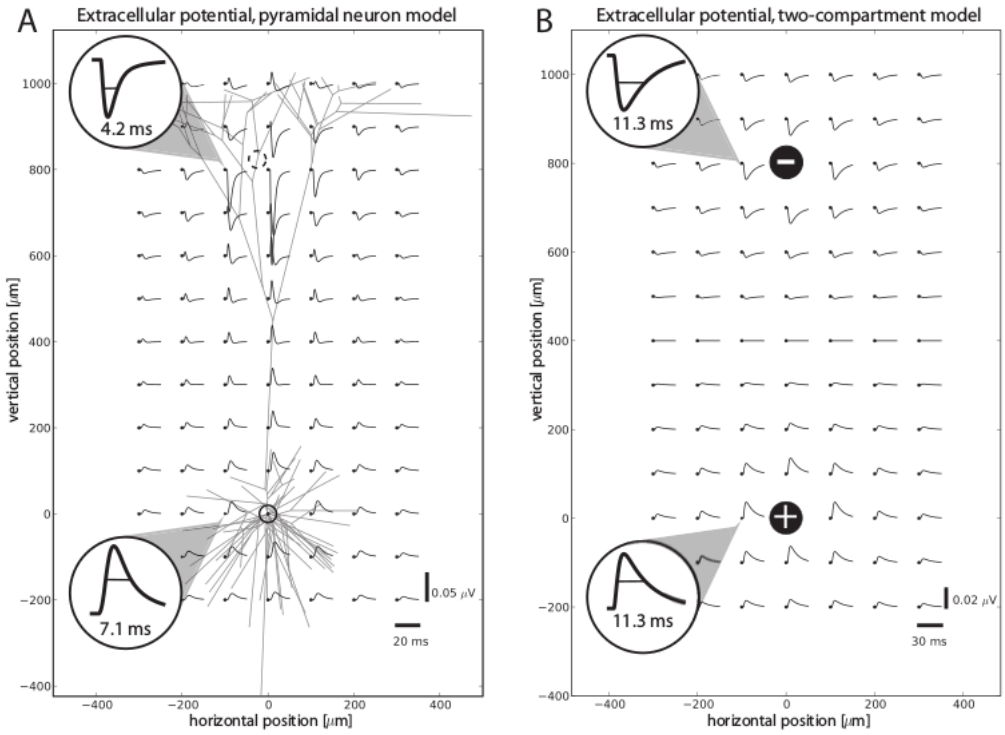

FIGURE 2.16 – Comparison of the LFP produced by a multi-compartmental pyramidal neuron (A) and an analogous two-compartmental model (B) following an excitatory synaptic input, adapted from [Pettersen et al., 2012].

contribute much more to the resulting LFP than contacts made onto interneurons.

Recently, another approach for the modelisation of LFP have also been developed, called hybrid LFP, which consists in first simulating a network's activity using time-saving, single-compartment neuron dynamics, and then use the generated spike trains to obtain the LFP through a model of multicompartmental neurons (see [Hagen et al., 2016]).

Once a LFP signal is obtained, it is often interpreted in the frequency domain using Fourier analysis.

In this context, sharp-wave ripple complexes are often detected by first filtering the LFP signals in the ripple (or sharp-wave) frequency range (and then in most cases computing the Root-Mean-Square (RMS) of the filtered signal). Then, a threshold is applied to only keep portions of the signal significantly above its baseline level. This is for example what is done in [Girardeau et al., 2009], [Roux et al., 2017], [Zylla et al., 2013], or [Taxidis et al., 2012]. Eventually, other criteria can be applied to remove unprobable sharp-wave ripples for example if they have an unrealistic duration, shape, or if they are too close to each other.

The detection of epileptic seizures or interictal spikes is usually done by studying several features of a signal (either in the temporal or frequency domain) before applying an automated classifier to separate portions of signal between healthy and pathological, or even using deep learning methods (see for example [Paul, 2018] for a review on seizure detection and [Gaspard et al., 2014] or [Antoniades et al., 2017] for interictal discharges detection).

2.4.2 Model analysis techniques

Knowing the differential equations defining a network, it is sometimes possible to predict its behavior without having to effectively simulate it. In two-dimensional single neurons and population models in particular, it is possible to perform phase plane analysis (explained in [Gerstner, 2014]) to mathematically find a system's equilibrium points as well as possible bifurcations. However, in more complex neural networks, such mathematical analysis is often impossible and other methods should be used. We will now present two techniques we used in this work to analyze the behavior of our neural network models.

Design of Experiments

To analyze the influence of a set of parameters on a model, a naive approach would consist in simply running a large number of simulations, sampling the parameter space regularly, to deduce the network behavior empirically. However, when the parameter space is too large or too high-dimensional, the time and computational resources needed to perform all these becomes unreasonably large as well. One solution to this issue consists in applying Design of Experiments (DOE) techniques to choose an optimal subset of simulations to run, and then fit a linear or polynomial function on the observed behaviors (see [Goupy and Creighton, 2013] for complete explanations on DOE).

In general, a DOE method will propose a set of experiments to run to be able to estimate a polynomial function f such that $y = f(x_1, x_2, ..., x_N)$., where $x_1, x_2, ..., x_N$ are N factors describing a multi-variate system and y is a relevant output of said system. In a first order description of the system, the output y will be estimated as a function of $N + 1$ coefficients $p_0, p_1, ..., p_N$:

$$y = p_0 + \sum_{j=1}^{N} p_j x_j. \tag{2.2}$$

With a matrix notation, if $Y = \begin{bmatrix} y_1 \\ y_2 \\ \vdots \\ y_k \end{bmatrix}$ are the observations of the output y in k experiments ($k > N$) obtained with the values of the factors $X = \begin{bmatrix} x_{1,1} & x_{1,2} & \dots & x_{1,N} \\ x_{2,1} & x_{2,2} & \dots & x_{2,N} \\ \vdots & & & \vdots \\ x_{k,1} & x_{k,2} & \dots & x_{k,N} \end{bmatrix}$, we will obtain the coefficient vector P such that $Y = XP$ (by using a least-square method).

Usually, the factors in the matrix X are normalized, so that each of them ranges between -1 and 1.

When the joint interactions of parameters need to be considered, products of two or more factors (terms of the form $x_i x_j$ or longer) can be added to the matrix X and the corresponding terms to the solution P. In other words, with such second order, the output of each experiment y_i ($i < k$) will be estimated as :

$$y_i = p_0 + \sum_{j=1}^{N} p_j x_{i,j} + \sum_{j=1}^{N} p_{jj} x_{i,j}^2 + \sum_{\substack{j=1 \\ l=1 \\ l \neq j}}^{N} p_{jl} x_{i,j} x_{i,l}. \tag{2.3}$$

The quality of the approximation of the output Y can be estimated by computing the coefficient of determination R^2, which represents the ratio of the explained variance of Y by the model by the total variance of Y. An example of linear and quadratic fitting on a simple 2D example is shown on Figure 2.17.

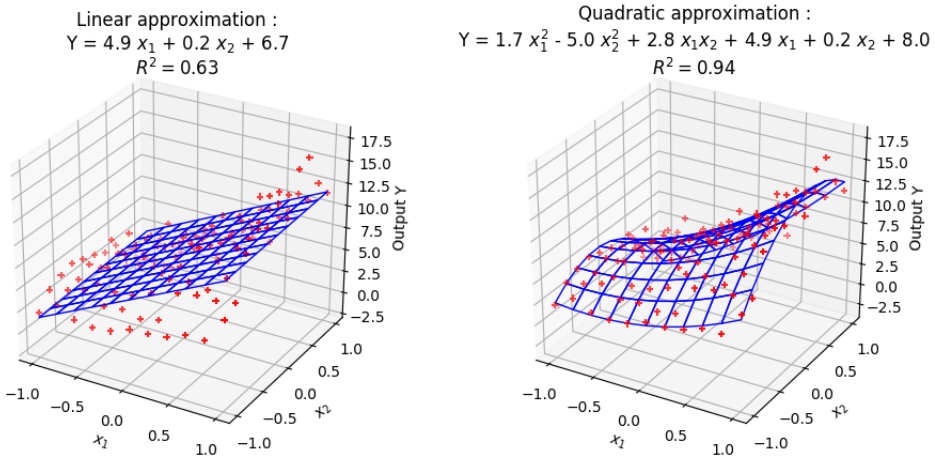

FIGURE 2.17 – Examples of linear and quadratic fitting on 2D data. The red stars indicate experimental points, while the blue surface is the approximated response, fitted with a least-square method.

Some of the most common types of DOE experiment matrices X are as follows (see Figure 2.18 for an illustration in a three-dimensional parameter space) :

— Factorial design : all the combinations of values with all $x_i = -1$ *or* 1 are explored, for

a total of 2^N experiments. The points studied are the corners of the hypercube defining parameter space.

— Fractional factorial design : in experiments where the high order interactions between parameters are negligible, some points in a factorial design can be removed while keeping a good estimation of y

— Box-Behnken design : proposed in 1960 by Box and Behnken ([Box and Behnken, 1960]), this design places the experimental points on the middle of the edges of the parameter space's hypercube, as well as points in the center of the cube (all factors set to 0). This design is made for obtaining quickly second-order modeling of the output y. It also has the interesting property that additional factors can be added to the model without loosing the results of the first experiments made.

— Doehlert design : in this design, the experimental points form are spread regularly in the parameter space following an hexagonal pattern. One of its advantages is that it makes it possible to extend the range of values to be studied for some parameters by simply extending the pattern, again without having to perform any new experiments inside the parameter subspace initially studied.

Overall, a DOE method can indicate which parameters may influence the most the output of a system, as these will be associated with high coefficients in the coefficient vector P. It can also help predict the values of the system in new experimental points x by simply computing the dot product of x and P for a linear system or by applying equation 2.3.

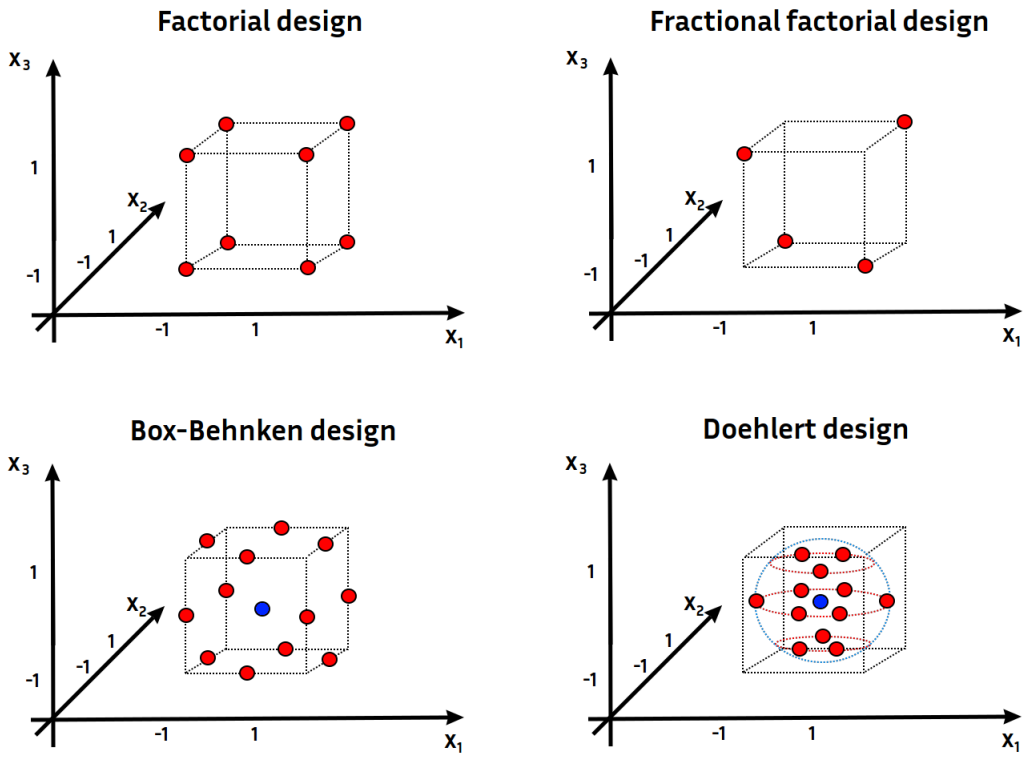

FIGURE 2.18 – Examples of matrices of experiments for a 3 factors DOE with different design methods.

Global sensitivity analysis

DOE techniques are useful to approximate the behavior of a system, but when the system is too complex, other methods such as global sensitivity analysis can give a more complete vision of the influence of each parameter on the output. Here we will focus on the Sobol' methods, as they do not require to make any assumption on the linearity or monotony of the model (these methods and others are described thoroughly in [Saltelli, 2008]).

Sobol' methods are variance analysis methods, meaning that they aim at estimating the contributions of each parameter x of the system to the variance of its output y (taken individually or jointly). The analysis yields, for each parameter, a so-called sensitivity index.

To better understand this approach, let us define D the total variance of the output y, D_i the variance of y obtained by varying the parameter x_i only, and more generally D_z the variance of y obtained by varying only the parameters in a subset z. The first order sensitivity index relative to the i-th parameter is then defined as $S_i = \frac{D_i}{D}$, and the sensitivity index relative to the subset z of parameters is defined as $S_z = \frac{D_z}{D}$.

The global sensitivity index S_i^{tot} of the i-th parameter represents the total influence of this parameter taken individually and jointly with other parameters on the output and is defined as the sum of S_i and all the S_z where $i \in z$. For example if the system has three variables, then $S_1^{tot} = S_1 + S_{12} + S_{13} + S_{123}$.

Having $S_i = S_i^{tot} = 0$ for a certain parameter x_i means that y does not depend on x_i. Conversely, $S_i = S_i^{tot} = 1$ means that y depends only on x_i.

Provided that the input parameters are independent and the output is square-integrable, the sensitivity index S_i of the output relative to the i-th parameter varied individually can be written as (see [Sobol', 2001]) :

$$S_i = \int_{[0,1]^N} \int_{[0,1]^{(N-1)}} y(x)y(x_i, x'_{\sim i})dxdx' - y_0^2, \tag{2.4}$$

where all the parameters are normalized in the $[0, 1]$ interval, $x = (x_1, ..., x_N) = (x_i, x_{\sim i})$ is a point of the parameter space, $x_i, x'_{\sim i}$ denotes a vector with same component x_i as in x (the other components being $x'_{\sim i}$), and y_0 is the mathematical expectation of y.

The sensitivity index S_z relative to any set of parameters z can be computed with a similar process :

$$S_z = \int_{[0,1]^N} \int_{[0,1]^{(N-|z|)}} y(x)y(z, x'_{\sim z})dxdz' - y_0^2. \tag{2.5}$$

The integrals in this expression can be approximated by using a Monte-Carlo or similar method, which gives the following estimation of S_i :

$$\hat{S}_i = \frac{1}{N_{sim}} \sum_{k=1}^{N_{sim}} y(x)y(x_i, x'_{\sim i}) - \hat{y}_0^2. \tag{2.6}$$

Usually, a quasi Monte-Carlo method called Sobol sequence is used to define the sequence of simulations to run to obtain a faster convergence.

As can be seen, the sensitivity of the system to one parameter is obtained by varying all the parameters simultaneously which is why this method is called a global sensitivity analysis, in opposition with a local sensitivity analysis.

2.5 Conclusions of the chapter

The hippocampus is a complex structure which plays a key role in memory formation and spatial navigation. Its functions are performed through neural oscillatory patterns in a broad range of frequencies, but the mechanisms underlying their generation are not yet fully understood, which makes it all the more difficult to understand and cure hippocampal pathologies such as temporal lobe epilepsies.

The literature on the anatomy and electrophysiology of the hippocampus as well as the existing computational models of this structure highlight different issues to be taken into account in our building of a model capable of reproducing all the variety of rhythms seen in the healthy and epileptic hippocampus over the sleep-wake cycle :

— Both theta-nested gamma oscillations and sharp-wave ripple complexes, as well as epileptic seizures are largely influenced by network connectivity, therefore large populations of neurons need to be modeled, and particular attention should be given to synaptic connectivity ;

— Sharp-wave ripple complexes require the communications of the CA3 and the CA1 region, and epilepsy often goes with mossy fiber sprouting in the DG. Finally, theta-nested gamma oscillations are thought to need the closed loop of the hippocampus with the EC. Therefore, our model should include the four following regions : the EC, the DG, CA3 and CA1 ;

— Theta rhythms occurring during wakefulness may require a specific ion channel (the CAN channel), and epilepsy is sometimes also associated with altered individual neuron dynamics, and so Hodgkin-Huxley modeling of the neurons would be needed to investigate these effects ;

Finally, as the human hippocampal data available to us comes from sEEG measurements, the model needs to include LFP modeling.

In the next section, we will now present our model handling all these issues and propose an analysis of its behavior.

Chapter 3

Structural and functional modeling of the healthy hippocampus

In this section, we will present our model of the hippocampus, and analyze the oscillations it produces depending on its structural and functional parameters. We will then show how these parameters can be tuned to reproduce sleep-wake cycle variations in the healthy hippocampus.

3.1 Description of the model

3.1.1 Neuron dynamics

The neurons in our network were simulated using a point conductance-based model derived from Hodgkin-Huxley's ([Hodgkin and Huxley, 1952]). The temporal evolution of each neuron membrane potential V_m followed a differential equation of the form :

$$C_m \frac{dV_m}{dt} = -I_{leak} - \sum I_{channel} - I_{syn_E} - I_{syn_I} + \eta, \tag{3.1}$$

where C_m is the membrane capacitance (proportional to the cell area), I_{leak} is a leakage current, each $I_{channel}$ is the membrane current associated with the ion channel *channel*, I_{syn_E} and I_{syn_I} are the excitatory and inhibitory synaptic inputs to the cell, respectively, and η is a random gaussian noise accounting for unknown entries.

Our principal excitatory neurons were pyramidal cells modelled with the following ion channels : fast sodium (I_{Na}), potassium (I_K), low-threshold calcium current (I_{Ca}), and potassium M-current (I_M). To some pyramidal cells, we also added Calcium-Activated-Nonspecific (CAN) cationic channels, which was found in hippocampal pyramidal neurons as well as in the entorhinal cortex (see [Yoshida et al., 2012]) and enables persistant activity during wakefulness in the theta band ([Giovannini et al., 2017]), with corresponding current I_{CAN}. In the following, these two types of pyramidal cells are referred to as non-CAN and CAN respectively. Interneurons were modelled with the following ion channels : fast sodium (I_{Na}), and potassium (I_K).

The complete expressions for all these ionic channel currents are taken from [Giovannini et al., 2017], and will be detailed below.

The leakage currents obey the following equation :

$$I_{leak} = (g_{leak} \times A) \times (V_m - E_{leak}), \tag{3.2}$$

where g_{leak} is the maximum leaking conductance, A is the area of the neuron membrane and E_{leak} is the channel reversal potential.

The I_K, I_M and I_{CAN} currents follow a set of equations of the form :

$$I_{channel} = (g_{channel} \times A) \times m^k \times (V_m - E_{channel}), \tag{3.3}$$

where m is a gating variable defined by :

$$\frac{dm}{dt} = \frac{m_\infty - m}{\tau_m}.$$

For I_K and I_{CAN}, the m_∞ and τ_m parameters depend on two functions α_m and β_m (themselves dependent on the membrane voltage V_m, see Table 3.1 and 3.2) :

$$m_\infty = \frac{\alpha_m}{\alpha_m + \beta_m},$$
$$\tau_m = \frac{0.2}{\alpha_m + \beta_m}.$$

Similarly, the I_{Na} and I_{Ca} currents follow a set of equations of the form :

$$I_{channel} = (g_{channel} \times A) \times m^k \times n \times (V_m - E_{channel}), \tag{3.4}$$

with two gating variables m and n, such as :

$$\frac{dm}{dt} = \frac{m_\infty - m}{\tau_m}, \qquad \frac{dn}{dt} = \frac{n_\infty - n}{\tau_n},$$
$$m_\infty = \frac{\alpha_m}{\alpha_m + \beta_m}, \qquad n_\infty = \frac{\alpha_n}{\alpha_n + \beta_n},$$
$$\tau_m = \frac{0.2}{\alpha_m + \beta_m}, \qquad \tau_n = \frac{0.2}{\alpha_n + \beta_n}.$$

Finally the gating variable α of the I_{CAN} current depends on the calcium concentration inside the neuron, $[Ca]_i^{2+}$, defined by :

$$\frac{d[Ca]_i^{2+}}{dt} = \gamma(I_{Ca}) + \frac{([Ca]_\infty^{2+} - [Ca]_i^{2+})}{\tau_{[Ca]^{2+}}},$$
$$\gamma(I_{Ca}) = \frac{-k_u \times I_{Ca}}{2 \times F \times depth \times A},$$

where $\tau_{[Ca]^{2+}} = 1s$ represents the rate of calcium removal from the cell, $[Ca]_\infty^{2+} = 0.24 mol/L$ is the calcium concentration if the calcium channel remains open for a duration $\Delta_T \to \infty$, $k_u = 10^4$ is a unit conversion constant, F is Faraday's constant and $depth = 1\mu m$ is the depth at which the calcium is stored inside the cell (as in [Giovannini et al., 2017]).

The amplitude of the noise η (Equation 3.1) simulating random unknown inputs to our network was set to $100pA$ for excitatory neurons and $10pA$ for inhibitory neurons, so as to obtain sporadic spikes in all of them in the absence of synaptic inputs.

The full expression of all the parameters defined here can be found in Table 3.1 and Table 3.2 for interneurons and excitatory neurons, respectively. The I-f curve of each type of neuron, describing their firing rate as a function of their input current, is shown on Figure 3.1.

TABLE 3.1 – Parameter values of interneurons

Parameter	Expression
A	$14 \cdot 10^3 cm^2$
g_{leak}	$0.1 mS/cm^2$
E_{leak}	$-90mV$
g_K	$9 mS/cm^2$
E_K	$-65mV$
k_K	4
$\alpha_{m,K}$	$0.01 \frac{V_M + 34mV}{1 - e^{-0.1(V_M + 34mV)}}$
$\beta_{m,K}$	$0.125\ e^{-\frac{V_M + 44mV}{80mV}}$
g_{Na}	$35 mS/cm^2$
E_{Na}	$55mV$
k_{Na}	3
$\alpha_{m,Na}$	$0.1 \frac{V_M + 35mV}{1 - e^{-0.1(V_M + 35mV)}}$
$\beta_{m,Na}$	$4\ e^{-\frac{V_M + 60mV}{18mV}}$
$\alpha_{n,Na}$	$0.07\ e^{-\frac{V_M + 58mV}{20mV}}$
$\beta_{n,Na}$	$\frac{1}{e^{1 - 0.1 * (V_M + 28mV)}}$

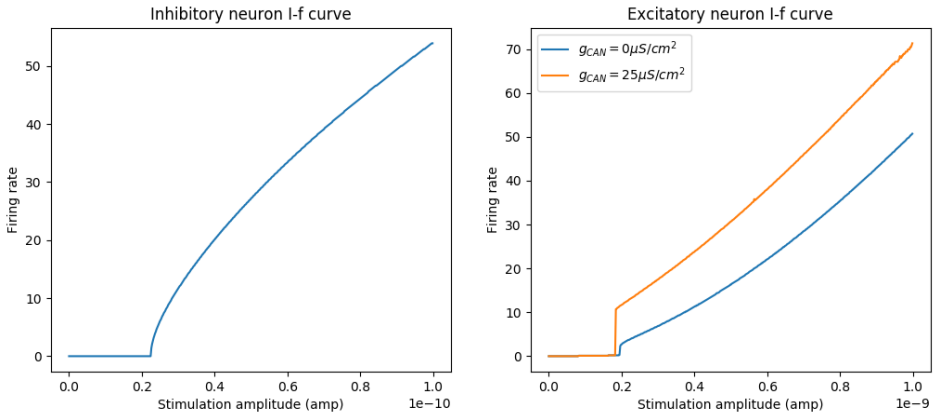

FIGURE 3.1 – I-f curves of the excitatory and inhibitory neurons used in the model.

TABLE 3.2 – Parameter values of pyramidal neurons

Parameter	Expression
A	$29 \cdot 10^3 cm^2$
g_{leak}	$0.01 mS/cm^2$
E_{leak}	$-70mV$
g_K	$5 mS/cm^2$
E_K	$-100mV$
k_K	4
$\alpha_{m,K}$	$-0.032 \frac{V_M+40mV}{e^{-1-0.2(V_M+40mV)}}$
$\beta_{m,K}$	$0.5\ e^{-\frac{V_M+45mV}{40mV}}$
g_{Na}	$50 mS/cm^2$
E_{Na}	$50mV$
k_{Na}	3
$\alpha_{m,Na}$	$-0.32 \frac{V_M+42mV}{e^{-\frac{V_M+42mV}{4mV}}-1}$
$\beta_{m,Na}$	$0.28 \frac{V_M+15mV}{e^{-\frac{V_M+15mV}{5mV}}-1}$
$\alpha_{n,Na}$	$0.128\ e^{-\frac{V_M+38mV}{18mV}}$
$\beta_{n,Na}$	$\frac{4}{1+e^{-\frac{V_M+15mV}{5mV}}}$
g_M	$90 \mu S/cm^2$
E_M	$-100mV$
k_M	1
$m_{\infty,M}$	$\frac{1}{1+e^{-\frac{V_M+35mV}{10mV}}}$
$\tau_{m,M}$	$\frac{1}{3.3e^{\frac{V_M+35mV}{20mV}}+e^{-\frac{V_M+35mV}{20mV}}}$
g_{Ca}	$0.1 mS/cm^2$
E_{Ca}	$120mV$
k_{Ca}	2
$\alpha_{m,Ca}$	$-0.055 \frac{V_M+27mV}{e^{-\frac{V_M+27mV}{3.8mV}}-1}$
$\beta_{m,Ca}$	$-0.94\ e^{\frac{V_M+75mV}{17mV}}$
$\alpha_{n,Ca}$	$-0.000457 e^{\frac{V_M+13mV}{50mV}}$
$\beta_{n,Ca}$	$\frac{0.0065}{e^{-\frac{V_M+15mV}{28mV}}+1}$
g_{CAN}	$0.5 \mu S/cm^2$
E_{CAN}	$-20mV$
k_{CAN}	2
$\alpha_{m,CAN}$	$0.0002 \cdot 3^{1.4} \frac{[Ca]_i^{2+}}{0.5 mol/L}$
$\beta_{m,CAN}$	$0.0002 \cdot 3^{1.4}$

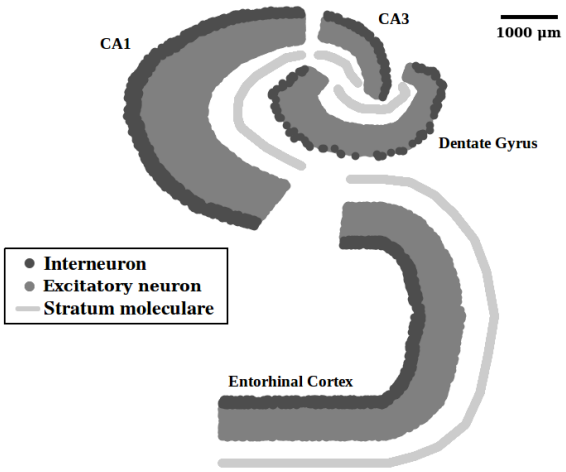

FIGURE 3.2 – Topology of the entorhinal cortex and the hippocampus used in the model.

3.1.2 Topology of the network

At the macroscopic level, our network is composed of two different structures : one representing the hippocampus, and the other representing the entorhinal cortex. The hippocampus proper itself is divided into three substructures : the dentate gyrus, CA3 and CA1 (the CA2 and CA4 regions are not modeled here due to their smaller size).

As our goal is to model realistically the population's extracellular recordings as obtained on human epileptic patients, the position of the entorhinal cortex and the hippocampal structures and the different types of neurons within them were chosen in accordance with human anatomy. A $15mm$-thick slice of the hippocampal formation was reproduced in this way, with excitatory neurons uniformly distributed within the stratum pyramidale for CA3, CA1 and the EC, or within the stratum granulosum for the dentate gyrus, and interneurons uniformly distributed within the stratum oriens. For each excitatory neuron, its projection on the stratum moleculare was also computed as an estimation of the position of its apical dendrites (Figure 3.2), and its projection on the stratum oriens as an estimation of the position of its basal dendrites, and thus the orientation of the (neural) elementary dipole used for generating the extracellular recordings. In other words, at the cellular level, the detailed geometry of the pyramidal neurons was simplified to simple current dipoles ([Pettersen et al., 2012]). Moreover, as interneurons contributions to the LFP are very small [Mazzoni et al., 2015], their microscopic geometry was neglected (point neurons). CAN neurons (see section 3.1.1) were used in the entorhinal cortex, CA3 and CA1, while non-CAN neurons were used in the dentate gyrus.

A 10 :1 ratio between pyramidal neurons and interneurons, as reported in [Jinno and Kosaka, 2010] for dorsal hippocampus, was respected in all regions but the dentate gyrus . The same 10 :1 ratio was used between the total number of neurons in CA1 and the total number of neurons in CA3, as reported in humans in [West and Gundersen, 1990].

As for the dentate gyrus, we considered a ratio 100 :1 ratio between the pyramidal cells and the interneurons, because of the higher proportion of excitatory cells compared to inhibitory cells in this structure ([Patton and McNaughton, 1995],[Jinno and Kosaka, 2010]).

As will be further explained in 3.3.1, the number of neurons in the smallest groups in the model, i.e. in the interneuron group in CA3 and in the DG, was set to 100, and neuron numbers in other regions were derived from it (see Table 3.3).

TABLE 3.3 – Number of excitatory neurons (N_E) and interneurons (N_I) in each region

Region	N_E	N_I
Entorhinal cortex	10000	1000
Dentate Gyrus	10000	100
CA3	1000	100
CA1	10000	1000

TABLE 3.4 – Parameter values of the biexponential synapses

Synapse Type	AMPA	GABA
Resting Potential (E)	0 mV	-80 mV
Time constant for rise (τ_g)	0.3 ms	1 ms
Time constant for decay (τ_h)	5 ms	10 ms
Maximum Conductance (g_{max}, see section 3.2.2)	60 pS	600 pS

3.1.3 Synapses model

The interactions between neurons were modelled as AMPA and GABA-A synapses, with I_{syn_E} and I_{syn_I} currents for excitatory and inhibitory connections respectively. These currents are described by the following bi-exponential differential equations :

$$\begin{aligned} I_{syn_{I,E}} &= g_{I,E}(V_m - E_{I,E}), \\ \frac{dg_{I,E}}{dt} &= (-g_{I,E} + h_{I,E})\frac{1}{\tau_{g_{I,E}}}, \\ \frac{dh_{I,E}}{dt} &= -h_{I,E}\frac{1}{\tau_{h_{I,E}}}. \end{aligned} \tag{3.5}$$

Whenever a pre-synaptic spike occurs, the value of h_I or h_E in the post-synaptic neuron is instantaneously increased by a fixed (impulse) conductance g_{max_e} or g_{max_i}.

The values of the synaptic resting potentials E_I and E_E, and the synaptic time constants of rise and decay τ_{g_E}, τ_{h_E}, τ_{g_I} and τ_{h_I} are given in Table 3.4. The maximum conductances g_{max_E} and g_{max_I} were chosen in accordance with the total number of neurons in each region so as to get a reasonable total synaptic input to them.

However it should be noted that different factors such as the varying concentration of neurotransmitters can modify these synaptic conductances. The effect of Acetylcholine in particular will be studied later on in this chapter.

3.1.4 Synaptic connection probabilities

As was also done in [Taxidis et al., 2012], the connection probability p between any two neurons within the same region in the model depends on the distance D between them, following a gaussian-like distribution : $p = A\, e^{-\frac{D^2}{2\sigma^2}}$. The width σ of this distribution was set to $2500\mu m$ for excitatory cells, in accordance with [Ropireddy et al., 2011] (which states that hippocampal pyramidal cells make half of their connections within 1.3-1.7mm), and to the value of $350\mu m$ for interneurons, in accordance with the values reported in [Freund and Buzsáki, 1998] for hippocampal basket cells (which states that the transverse extent of their axon is between 9mm and 1.3mm). The connection probability distributions for each region are then characterized by

TABLE 3.5 – Maximum probability A of the synaptic connectivity within each region. EC : Entorhinal Cortex, DG : Dentate Gyrus. Py : Pyramidal neuron, In : Interneuron (the first two letters indicates the presynaptic neuron type while the second one indicates the post-synaptic neuron type). Sources : [Couey et al., 2013], [Patton and McNaughton, 1995], [Taxidis et al., 2012], [Larimer and Strowbridge, 2008], [Debanne et al., 1995], [Knowles and Schwartzkroin, 1981]. Note that parameters come from physiological recordings on human or rat hippocampus depending on the availability of the data.

	Py-Py	Py-In	In-Py	In-In
EC	0	0.37	0.54	0
DG	0	0.06	0.14	0
CA3	0.56	0.75	0.75	0
CA1	0	0.28	0.3	0.7

the maximum probability A of two neurons within a distance D close to zero to be connected, summed up in Table 3.5.

Regarding the synaptic connections between different subregions, only excitatory connections were considered, as these are the most commonly reported ([Andersen et al., 2007]). The probability distribution is also gaussian-like among the septo-temporal axis, following the equation $p = A.e^{-\frac{\Delta_z^2}{2\sigma^2}}$, where Δ_z is the difference of z coordinates between the source and target neuron (i.e. the connection probability is higher between neurons in adjacent layers). As will be explained in section 3.2.2, the maximum value of the probability distribution on the trisynaptic pathway (i.e. for connections from the EC to the DG, from the DG to CA3, from CA3 to CA1 and from CA1 to the EC) was set to $p_{tri} = 0.45$, whereas for the monosynaptic pathway (i.e. connections made from the EC directly to CA3 and CA1), the maximum value was set to $p_{mono} = 0.3$. The width σ of the distribution was set to $50\mu m$ for all these connections, so as to have connections of neurons in close layers with little dispersion. Consequently, each excitatory neuron in the entorhinal cortex for example targets about 700 excitatory neurons and 70 inhibitory neurons in the dentate gyrus (7% of each population), 50 excitatory neurons and 5 inhibitory neurons in CA3 and 500 excitatory neurons and 50 inhibitory neurons in CA1 (5% of each population).

3.1.5 Simulations outputs

The analyzed output is the extracellular potential generated by the network, at a macroscopic scale.

The modelling of the LFP follows the approach proposed in [Mazzoni et al., 2015]. More precisely, the potential in every point in space was approximated by a weighted sum of the synaptic currents arriving at each pyramidal neuron, and neglecting the influence of the interneurons. Considering the neurons as dipoles, the contribution U of a neuron of length L to the extracellular potential at any point in space, at a distance r and an angle θ from the midpoint of the neuron (see Figure 3.3), writes as :

$$U = \frac{L\,cos\,\theta}{4\pi\sigma r^2}\,(I_{syn_E} + I_{syn_I}), \tag{3.6}$$

where $\sigma = 0.3\,S/m$ is the conductivity of the extracellular medium, which we considered homogeneous. One extremity of each neuronal dipole is set to its soma, while the other is set to either its approximated basal dendrite or apical dendrite position (see section 3.1.2), depending on the synapse type, according to the literature on this topic ([Andersen et al., 2007]).

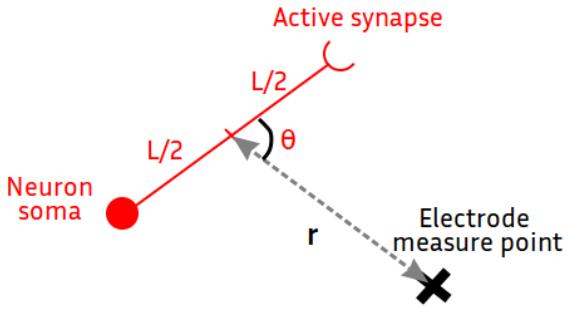

FIGURE 3.3 – Diagram of the parameters L, r and θ used to compute the contribution of single neuron to the LFP.

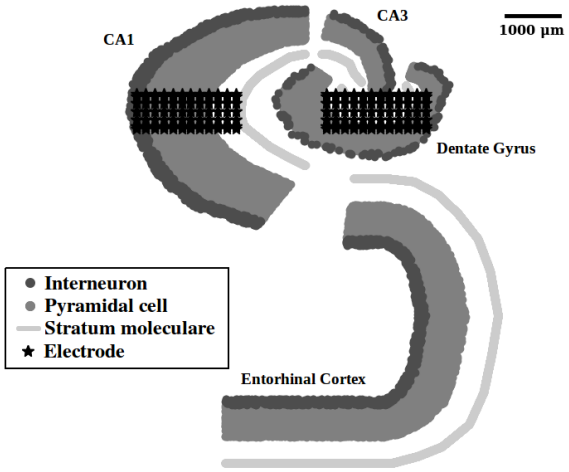

FIGURE 3.4 – Topology of the entorhinal cortex and the hippocampus used in the model, along with the two simulated electrode contacts.

The LFP at one point is the sum of the contributions from all the excitatory neurons in the entorhinal cortex and the hippocampus (dentate gyrus, CA3, and CA1) : LFP$= \sum U$. In order to model the signal recorded by the macroscopic electrode and to compare it with real patient recordings, we averaged the LFP on two sets of 144 points evenly distributed on a cylinder of diameter 0.8mm going through the network, each of them representing a 2mm-long contact, separated by 1.5mm, and computed the difference between the two resulting signals, as in a bipolar sEEG montage (see figure 3.4).

Similarly to what is done in the intracranial EEG recordings available to us (section 4.3.1), the simulated LFP was also bandpass filtered between 0.15Hz and 480Hz and downsampled to 1024Hz.

3.1.6 Parameters to be studied

The model described in the previous sections was built in accordance with the literature on the hippocampus in as many aspects as possible. However, there are parameters that needed to be tuned more arbitrarily, either because too little information was available in the literature or

due to computer resource constraints.

First, because our modeled hippocampus includes less neurons than a real human hippocampus, each of our modeled neurons receives less synaptic contacts from its surroundings. Therefore, in order for these synaptic inputs to properly drive neural activity, i.e. in order for each modeled neuron to receive the same overall synaptic current as a real hippocampal neuron, the amplitude of each synaptic current should be increased. This is done by increasing the maximum conductances of both excitatory and inhibitory synapses : $g_{max,e}$ and $g_{max,i}$.

Another parameter that needs to be set is the maximum connection probabilities between different subregions of our model, as little quantitative information can be found about it in the literature.

It has been shown that neurons from the entorhinal cortex can target both excitatory and inhibitory neurons in the dentate gyrus ([Amaral et al., 2007]) and in the CA regions ([Kiss et al., 1998]), and the same holds true for Schaffer collaterals (synaptic contacts from region CA3 to CA1, [Wittner et al., 2006]). In [Ursino et al., 2010], connections with different properties were modeled depending on whether the target neuron was excitatory or inhibitory in order to generate complex dynamics, but it is not the case in all models ([Taxidis et al., 2012], [Wendling et al., 2002]). Because such differentiated connections are not needed in our network in order to generate both fast and slow oscillatory rhythms, and in absence of strong experimental evidence proving so, we decided to keep our approach simple and have not changed connection probabilities depending on the type of neurons targeted.

Similarly, so as not to make the model more complex than needed, we only set one connection probability p_{tri} for all synaptic connections along the tri-synaptic loop (from the Entorhinal Cortex to the Dentate Gyrus, from the Dentate Gyrus to CA3, from CA3 to CA1, and from CA1 back to the Entorhinal Cortex), and one connection probability p_{mono} for synaptic connections made from the Entorhinal Cortex directly to CA3 and CA1.

Then, some functional parameters can also be changed which will help represent sleep-wake variations :

- As was mentioned before, the varying concentration of neurotransmitters like ACh between wakefulness and slow-wave sleep modulate the synaptic interactions between and within hippocampal subregions. More precisely, due to the presence of nicotinic and muscarinic receptors on hippocampal neurons, it has been shown that some synaptic connections are enhanced by a high ACh concentration, such as the inhibitory connections within the dentate gyrus and CA1 ([Jones and Yakel, 1997], [Frazier et al., 1998]), or the excitatory connections from the dentate gyrus ([Cheng and Yakel, 2013], [Gray et al., 1996]), while others are reduced, such as the excitatory connections from the entorhinal cortex ([Heys et al., 2012]) or CA3 ([Herreras et al., 1988]). To represent these changes, we define three gains that can be used to modify the synaptic conductances : G_e (increasing excitatory synaptic conductances in the DG), g_e (decreasing excitatory synaptic conductances in the EC and CA3), and G_i (increasing inhibitory synaptic conductances in the DG and CA1).
- As presented in [Yoshida et al., 2012], ACh also plays a key role in the activation of CAN currents in hippocampal pyramidal cells. Therefore, the conductance of this channel g_{CAN} will also be a parameter that we can change.

Finally, as neurons in the model do not fire in an organized manner on their own, an external stimulation has to be applied to perform a simulation. In order to assess the network behavior under a stereotypical input, it is possible to simply apply a positive current on each of the entorhinal cortex neurons (either excitatory or inhibitory). To study the response of our model to input variations, we chose to apply a square wave current I_{stim} starting at $t_0 = 250ms$ of

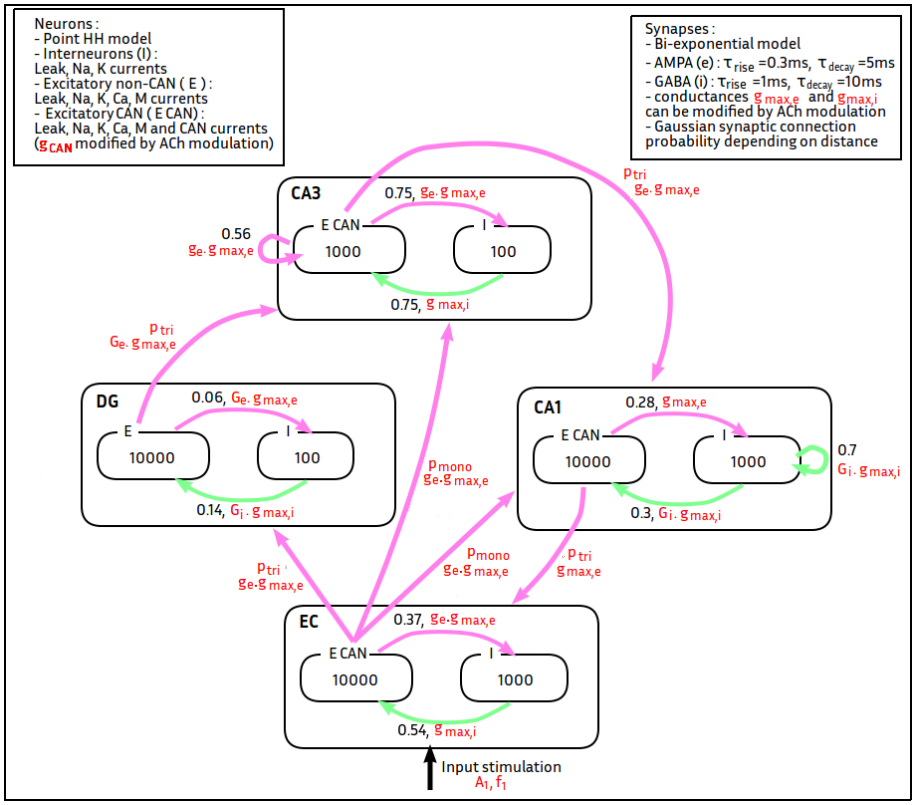

FIGURE 3.5 – Diagram of our model of the hippocampal formation, with the parameters to be studied appearing in red. The number of neurons of each type in each region is shown inside black boxes. Purple arrows represent AMPA synaptic interactions, and green arrows represent GABA synapstic interactions, with next to them the corresponding connection probability and the maximum synaptic conductance. The black arrow represents input stimulation given to the EC neural populations.

which we varied the maximum value A_1 ($A_1 > 0$) as well as the frequency f_1 across simulations :

$$I_{stim}(t) = \begin{cases} A_1 & \text{if } t > t_0 \text{ and } sin(2\pi f_1(t - t_0)) \geq 0, \\ 0 & \text{otherwise.} \end{cases} \tag{3.7}$$

A diagram of the model and its parameters are shown on Figure 3.5.

The influence of these 10 parameters ($g_{max,e}$, $g_{max,i}$, p_{tri}, p_{mono}, G_e, g_e, G_i, g_{CAN}, A_1 and f_1) will be analyzed in section 3.2.1.

Then in section 3.3, we will also discuss some other of our modeling choices, including the number of neurons, as well as the LFP approximation.

3.2 Exploration of the parameter space under stereotypical inputs

3.2.1 Parameter study with a Design of Experiments and Sobol' method

So as to get a first intuition on the behavior of the model, we conducted simulations following a Box-Benhken design matrix with our ten parameters (the simulation amplitude A_1, the

stimulation frequency f_1, the connection probability on the trisynaptic pathway p_{tri}, and monosynaptic pathway p_{mono}, the maximum conductance of excitatory synapses $g_{max,e}$, and inhibitory synapses $g_{max,i}$, the gain on the conductance of ACh-enhanced excitatory synapses G_e, on ACh-reduced excitatory synapses g_e, on ACh-enhanced inhibitory synapses G_i, and the conductance of the CAN channel g_{CAN}) normalized from the following ranges to the $[-1, 1]$ interval :

— A_1 : $[0.5nA, 1.5nA]$
— f_1 : $[0Hz, 10Hz]$
— p_{tri} : $[0.2, 0.7]$
— p_{mono} : $[0.1, 0.5]$
— $g_{max,e}$: $[50pS, 70pS]$
— $g_{max,i}$: $[500pS, 700pS]$
— G_e : $[1, 5]$
— g_e : $[1, 5]$
— G_i : $[1, 5]$
— g_{CAN} : $[0.5\mu S/cm^2, 25\mu S/cm^2]$

Because the hippocampus is able to produce both fast oscillations (gamma or ripple frequency range) and slow oscillations (delta to theta frequency range), we chose to interpret the following outputs of our model : the peak frequency of its spectrum in the 30-250Hz range (from gamma to ripple and higher) f_{fast} and the peak frequency of its spectrum in the 1-30Hz range (which includes the delta and theta frequency bands) f_{slow}.

We then used a least squares method to fit this data with a second order polynomial function of the parameters :

$$f_{fast} = a_0 + \sum_{i=1}^{10} a_i p_i + \sum_{i=1}^{10} a_{ii} p_i^2 + \sum_{\substack{i=1 \\ j=1 \\ i \neq j}}^{10} a_{ij} p_i p_j + E_{fast}, \tag{3.8}$$

$$f_{slow} = b_0 + \sum_{i=1}^{10} b_i p_i + \sum_{i=1}^{10} b_{ii} p_i^2 + \sum_{\substack{i=1 \\ j=1 \\ i \neq j}}^{10} b_{ij} p_i p_j + E_{slow}, \tag{3.9}$$

with $p_i, i \in [1, 10]$ the ten parameters of the network studied here, a and b the 65 coefficients defining the effects of each parameter on the fast and slow oscillations frequency respectively, and E the residuals of the model represented as a random variable.

This model reproduces the values of f_{fast} and f_{slow} with good accuracy (a coefficient of determination $R^2 = 0.88$ and $R^2 = 0.95$ respectively). Figure 3.6 shows the values of the coefficients relative to each parameter and combination of parameters. It can be seen that some factors have more influence (either positive or negative) on the resulting oscillations than others.

In the approximation of f_{slow}, a few parameters seem to stand out, mostly the frequency of the input f_1 as well as the product of parameters $f_1 \cdot g_e$. The approximation of f_{fast} on the other hand seems to involve more parameters, and the most important parameters are different than those for f_{slow}. It is possible to evaluate the significance of each of the factors used in this fitting with a Student's t-test, knowing that any coefficient β_k (where β stands for a or b) follows a t-distribution :

$$\frac{\hat{\beta_k} - \beta_k}{S\sqrt{[(XX')^{-1}]_{k,k}}} \sim T(n - p - 1), \tag{3.10}$$

with β_k the coefficient associated with the k-th factor in the description of one of the model's outputs (f_{fast} or f_{slow}), $\hat{\beta_k}$ is its estimation obtained with a least-square method from the simulations, S is an estimation of the variance of the studied output, X is the matrix containing all the factors used in the simulations, T is a Student's t-distribution, n is the number of simulations performed (here 170), and p is the number of factors studied (here 65).

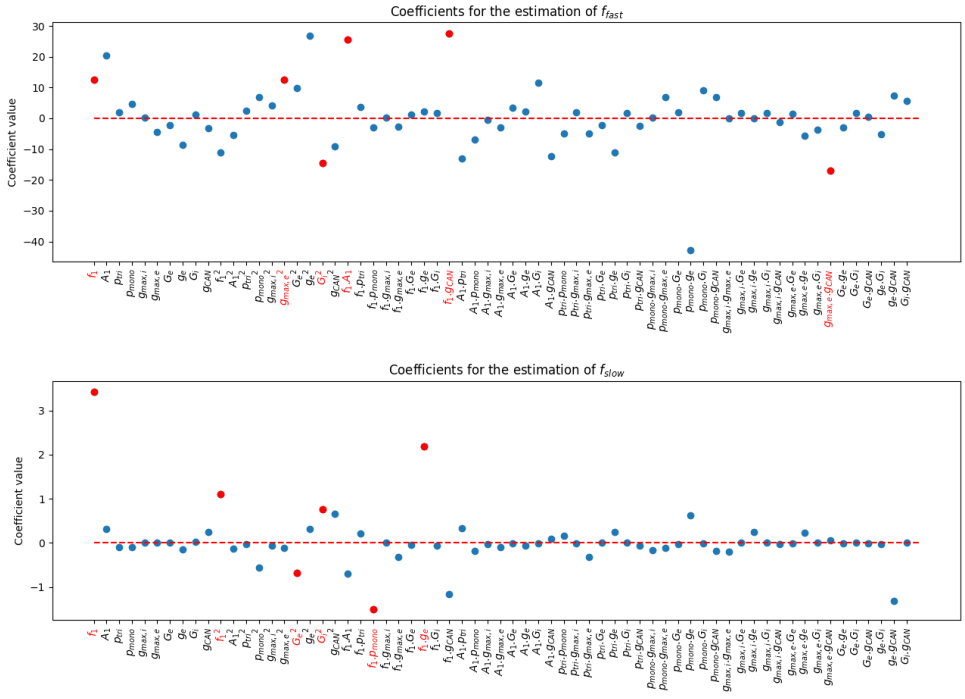

FIGURE 3.6 – Coefficients measuring the each parameter's individual, squared or joint influence in the modeling of f_{fast} and f_{slow}, from a Box-Behnken DOE. The significant coefficients ($p<0.01$) are shown in red.

To simplify the models of f_{fast} and f_{slow}, we tried to remove the least significant factors one by one and optimize the model iteratively (see Figure 3.7).

For approximating f_{slow}, keeping only four parameters is enough to keep a R^2 value above 0.8. These four factors are : f_1, $f_1 \cdot g_e$, $f_1 \cdot p_{mono}$, and f_1^2. In other words, the slow frequency of the oscillations mostly follows the frequency of the input, though other parameters also influence it to a lesser extent. However, f_{fast} appears as a more complex function of the network parameters as not less than 15 factors are needed to model it with a R^2 value above 0.8. These 15 factors include all of the initial ten parameters studied, except for $g_{max,i}$ and G_e.

To provide a better understanding of the parameters influencing the fast oscillations of the network in particular, we completed our previous analysis with a global sensitivity analysis following a Sobol' method.

After performing 2200 simulations sampling the whole parameter space, the first-order as well as global sensitivity indices obtained for the outputs f_{fast} and f_{slow} are shown on Figure 3.8. Once again, the frequency of the slow oscillations f_{slow} seems mostly influenced by the frequency of the input f_1. As for the fast oscillations frequency f_{fast}, even though A_1 looks like it is the only important factor in a first order approximation, global sensitivity indices reveal that other factors such as f_1, g_e and p_{mono} also carry a lot of information on the variance of

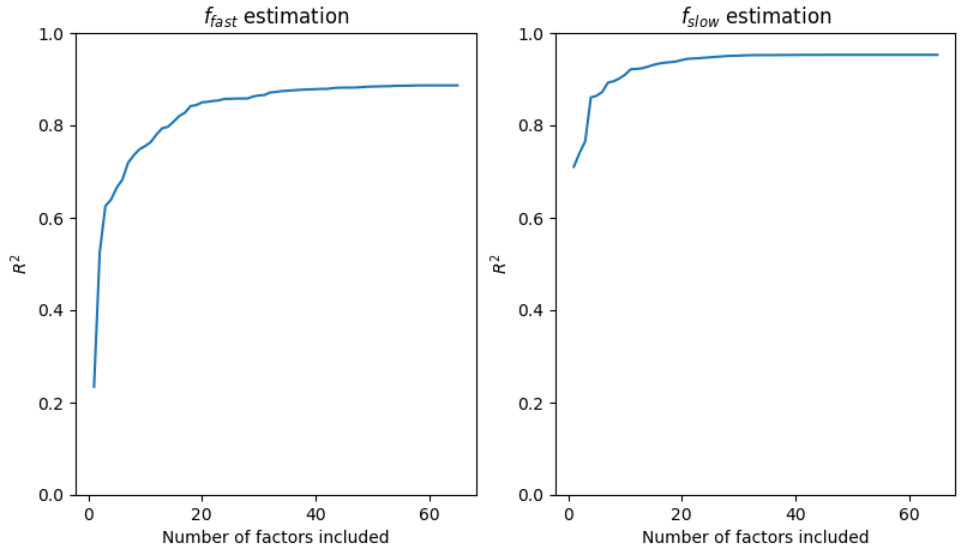

FIGURE 3.7 – R^2 values of the models of f_{fast} and f_{slow} obtained with different number of factors. Starting from the original model with all factors included, the least significant factor was removed iteratively.

this output. Surprisingly, the gain put on increased excitatory synaptic conductances G_e (in the dentate gyrus) and inhibitory synaptic conductances G_i (in the dentate gyrus and CA1) have much less influence on f_{fast} than the reduction of excitatory synaptic conductances g_e (in the entorhinal cortex and CA3), in accordance with the common hypothesis stating that sharp-wave ripples complexes are initiated by recurrent excitatory connections in CA3 ([Buzsáki, 2015]).

Overall it should be noted that the frequency of the slow oscillations of the network f_{slow} can have values within the whole range of $[0Hz, 10Hz]$ used to stimulate it, while the frequency of the fast oscillations f_{fast} varies between 30Hz (the minimum value of the range considered for f_{fast}) and 190Hz. Therefore, the model can only reproduce oscillations with frequency up to the ripple frequency band, and is not able to generate pathological high frequency oscillations (HFOs), without further modifications.

A quadratic model can also be fit on the results of these simulations as was done with the Box-Benhken DOE, which yields a coefficient of correlation R^2 of 0.70 for the estimation of f_{fast} and 0.93 for the estimation of f_{slow}. The coefficients of these quadratic fittings are shown on Figure 3.9.

Overall, the following factors are significantly ($p < 0.001$) linked to the outputs of the model :

— for f_{fast} : 7 single factors (f_1, A_1, p_{tri}, p_{mono}, $g_{max,i}$, $g_{max,e}$, and g_e), 6 squared factors (f_1^2, p_{tri}^2, p_{mono}^2, $g_{max,i}^2$, g_e^2 and g_{CAN}^2), and 17 products of two factors ($f_1 \cdot A_1$, $f_1 \cdot p_{mono}$, $f_1 \cdot g_e$, $f_1 \cdot G_i$, $f_1 \cdot g_{CAN}$, $A_1 \cdot p_{tri}$, $A_1 \cdot g_{max,i}$, $A_1 \cdot g_{max,e}$, $A_1 \cdot g_e$, $A_1 \cdot G_i$, $p_{tri} \cdot g_{CAN}$, $p_{mono} \cdot g_{max,e}$, $p_{mono} \cdot g_e$, $g_{max,i} \cdot g_e$, $g_{max,e} \cdot g_e$, $g_e \cdot G_i$, and $g_e \cdot g_{CAN}$).

— for f_{slow} : 3 single factors (f_1, $g_{max,e}$, and g_e), 2 squared factors (f_1^2 and g_e^2), and 16 products of two factors ($f_1 \cdot A_1$, $f_1 \cdot p_{tri}$, $f_1 \cdot p_{mono}$, $f_1 \cdot g_{max,i}$, $f_1 \cdot g_{max,e}$, $f_1 \cdot G_e$, $f_1 \cdot g_e$, $A_1 \cdot p_{mono}$, $A_1 \cdot g_{max,e}$, $A_1 \cdot g_e$, $A_1 \cdot g_{CAN}$, $p_{tri} \cdot g_{max,i}$, $p_{tri} \cdot g_e$, $p_{mono} \cdot g_{max,e}$, $p_{mono} \cdot g_e$, and $g_{max,e} \cdot g_e$).

Both f_{fast} and f_{slow} depend on the characteristics of the input A_1 and f_1, showing that our hippocampal model can have specific responses to stimuli from afferent structures or sensory

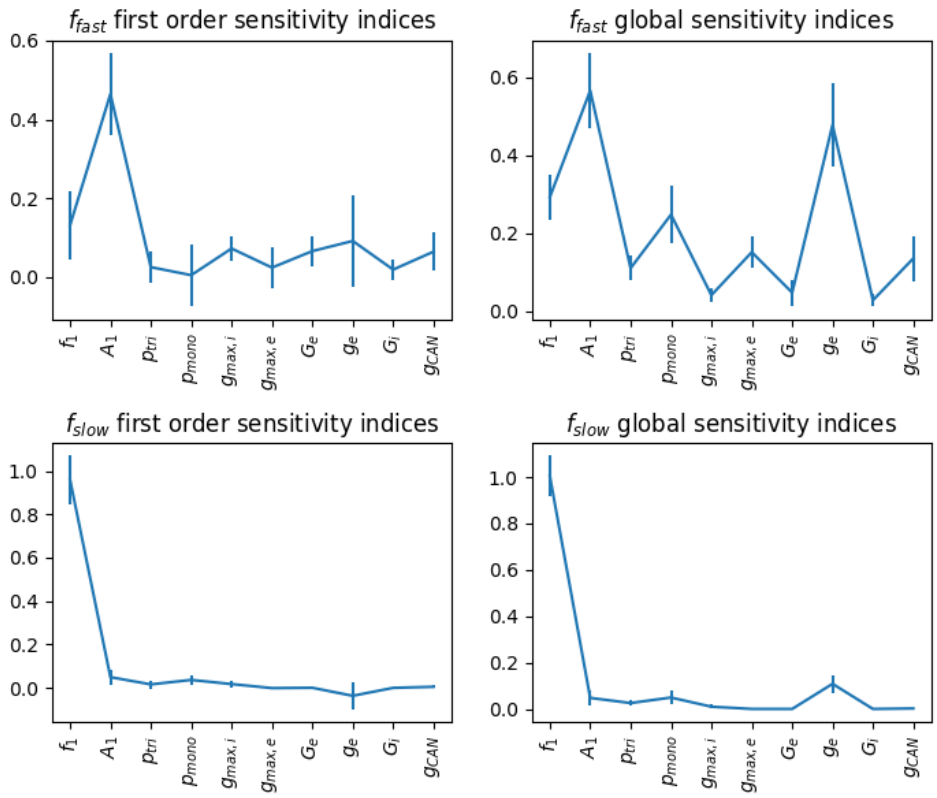

FIGURE 3.8 – Sobol' sensitivity indices (first order and global) for all our ten parameters for the study of f_{fast} and f_{slow}, with confidence intervals at 95%.

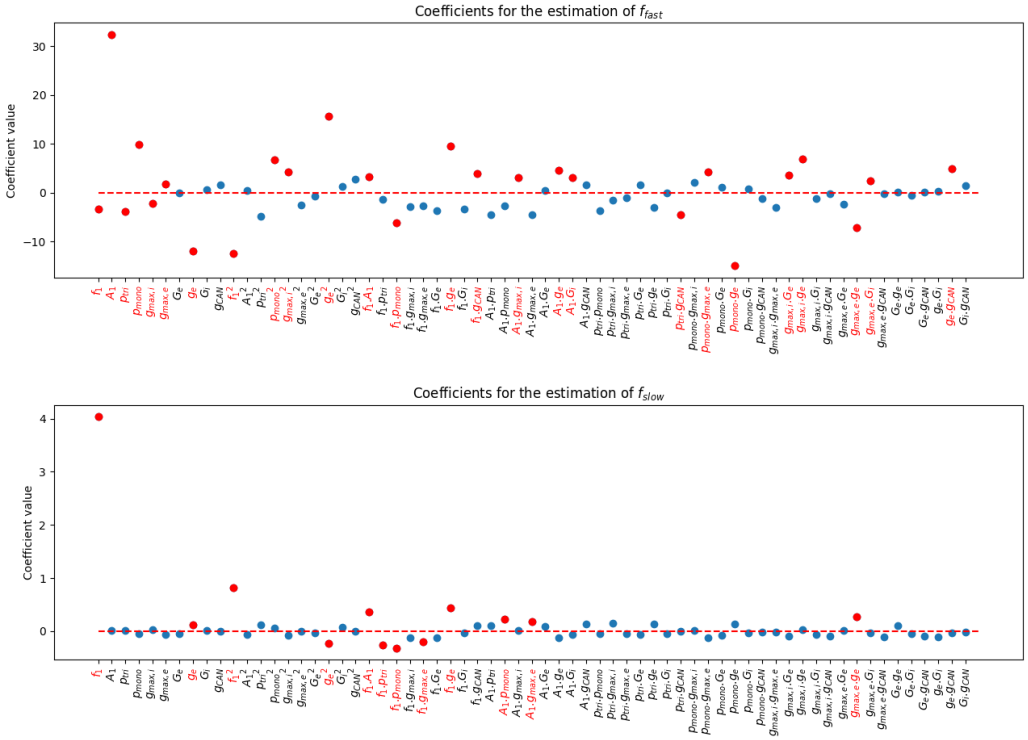

FIGURE 3.9 – Coefficients measuring the each parameter's individual, squared or joint influence in the modeling of f_{fast} and f_{slow}, obtained from 2200 simulations following a Sobol' sequence. The significant coefficients ($p<0.001$) are shown in red.

modalities in accordance with its biological function, but these outputs also depend on structural and functional properties of the network.

This analysis will help us find the appropriate set of parameters for reproducing either delta, theta, gamma or ripple oscillations, depending on the vigilance state. In the next section, we will first focus on non input-related parameters, before studying the influence of the input in more details in section 3.2.3.

3.2.2 Choices of parameters for representing wakefulness or slow-wave sleep states

Representing typical oscillations of the sleep-wake cycle can be done by choosing the appropriate sets of parameters so as to have f_{slow} in the theta range (5-10Hz) and f_{fast} in the gamma range (30-90Hz) for wakefulness and f_{slow} in the delta range (1-4Hz) and f_{fast} in the ripple range (130-200Hz) for slow-wave sleep respectively. We showed before the frequency f_{slow} is mostly determined by the frequency f_1 of the input, which is why this section will mostly be focused on the choice of parameters needed to obtain oscillations either in the gamma or ripple range.

Among the parameters that can be used to tune the network's behavior, some of them like g_e, G_e, g_i and g_{CAN} that reflect neurotransmitter concentrations could change their value to better reproduce either sleep or wakefulness oscillations. On the other hand, p_{tri} and p_{mono} represent the structural connectivity of the network, so they should not be changed between simulations once properly set. The same holds true for $g_{max,e}$ and $g_{max,i}$ which represent the basic conductances of synapses (i.e. without any synaptic plasticity or external neurotransmitter influence).

From the simulations performed in the previous section for the Sobol' sensitivity analysis, we classified the parameters depending on the frequency range of the output f_{fast} (into gamma, 30-90Hz, and ripple 130-200Hz frequency bands), and represented their distribution on Figure 3.10. Four parameters, p_{mono}, $g_{max,i}$, g_e and g_{CAN}, have a significantly different distribution between the gamma and ripple bands ($p<0.001$ in a Wilcoxon–Mann–Whitney test). Figure 3.11 shows the value of f_{fast} depending on these four parameters on all the 2200 simulations performed in the Sobol' analysis. Overall, a large set of parameters could be used to produce either sleep or wakefulness oscillations.

Because p_{tri} and $g_{max,e}$ have been shown (Figure 3.8) to have only limited influence on the output oscillations, we chose to keep them at the mean value of the previous studied range, that is : $p_{tri} = 0.45$ and $g_{max,e} = 60pS$. The value of $g_{max,i}$ is slightly more influential, but as shown on Figure 3.10 the mean value $g_{max,i} = 600pS$ is also appropriate to be able to reproduce both gamma and ripple oscillations.

The parameters G_e and G_i, which have very limited influence on f_{fast}, represent the possible increases of the synaptic conductances due to the presence of neurotransmitters such as Acetylcholine in the network. Therefore, we chose to have $G_e = G_i = 1$ to represent the slow-wave sleep state (that is, the absence of Acetylcholine), and $G_e = G_i = 3$ (the mean value of the range we studied) for the representation of the wakefulness state, for biological plausibility reasons.

Then, the three main parameters that remain to be chosen are p_{mono}, g_e and g_{CAN}. From Figure 3.11, it can be seen the fastest oscillations (i.e. in the ripple range) can be obtained roughly when g_e and g_{CAN} are low, and p_{mono} is rather high. Conversely, oscillations in the gamma range are obtained with higher g_e and g_{CAN} and low p_{mono}.

Because p_{mono} should be kept the same during wakefulness and slow-wave sleep, we chose to use the mean value of 0.3. For the other values, we chose to have g_{CAN} set to its minimal value to represent sleep ($0.5\mu S/cm^2$) and to its highest value during wakefulness ($25\mu S/cm^2$), and g_e

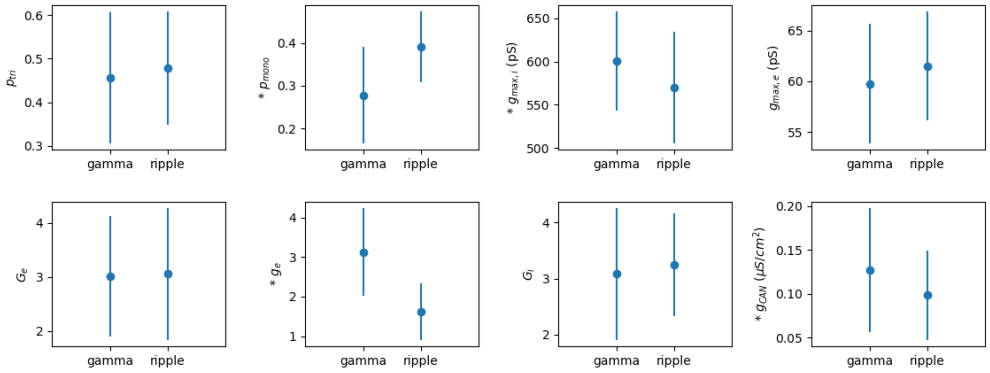

FIGURE 3.10 – Mean and standard deviation of the set of parameters yielding fast oscillations in the gamma (30-90Hz) and ripple (130-200Hz) frequency range respectively. A star (*) next to a parameter's name indicate that the gamma and ripple sets are statistically different ($p<0.001$ in a Wilcoxon–Mann–Whitney test).

to its lowest value during sleep ($g_e = 1$) and to its middle value ($g_e = 3$) during wakefulness to stay coherent with the other parameters representing the variation of synaptic conductances G_e and G_i. These values are also represented on Figure 3.11.

All these choices of parameters can be found in Table 3.6.

Parameter	Slow-wave sleep value	Wakefulness value
p_{tri}	0.4	
p_{mono}	0.3	
$g_{max,i}$	600pS	
$g_{max,e}$	60pS	
G_e	1	3
g_e	1	3
G_i	1	3
g_{CAN}	$0.5\mu S/cm^2$	$25\mu S/cm^2$

TABLE 3.6 – Choice of network parameters for the sleep and wakefulness state

3.2.3 Influence of the input

After having chosen the network's internal parameters, we can now study in more details the relation between its output and the input used to stimulate it.

We first stimulated our "sleep state" network with a step current ($f_1 = 0$ in Equation 3.7). When stimulated by a sufficiently high current (A_1 above 300pA), the network LFP presents a transient fast activity whose frequency, amplitude and duration depend on the value of the step current, resulting from a fast activity of CA1 pyramidal neurons. Increasing this current about 1nA makes the network start oscillating at a low frequency (about 2.5Hz), on which faster

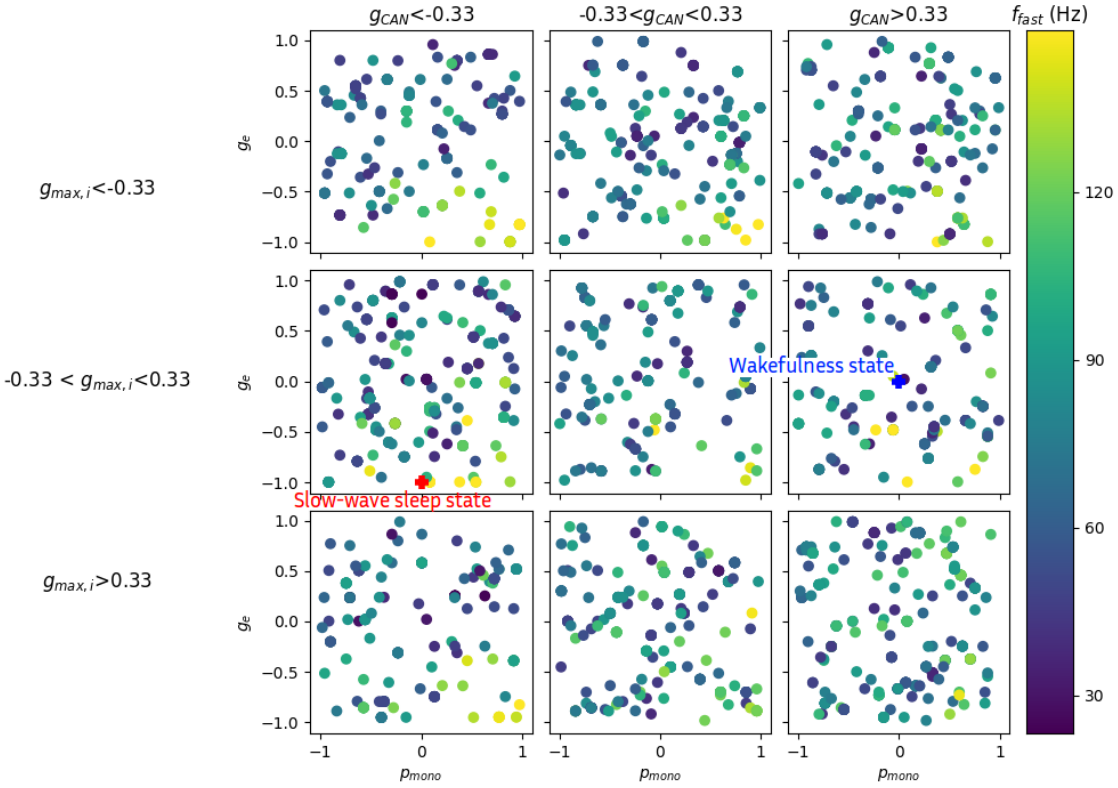

FIGURE 3.11 – Evolution of the f_{fast} oscillatory frequency depending on the parameters $g_{max,i}$, g_e, p_{mono} and g_{CAN} (normalized). The parameter values chosen to represent the slow-wave sleep and wakefulness states are shown with a red and blue cross respectively.

oscillations are superimposed (see Figure 3.12).

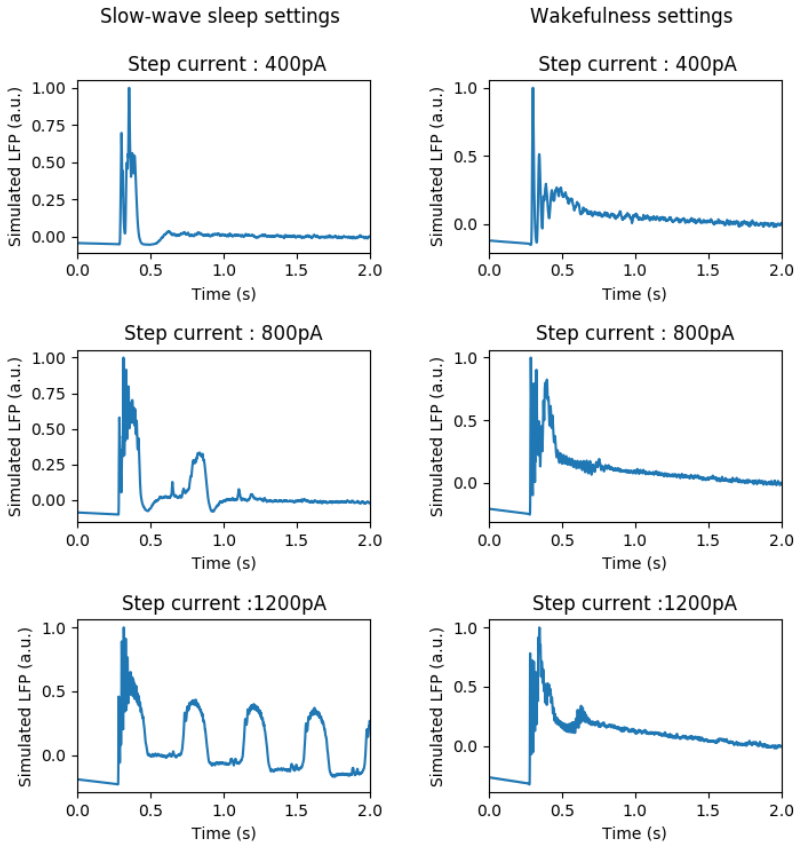

FIGURE 3.12 – Simulated LFP resulting from a step current stimulation starting at t=250ms, with values 400pA, 800pA and 1200pA, under slow-wave sleep and wakefulness conditions.

Applying a square wave stimulation with $f_1 > 0$ also makes the network produce coupled fast and slow oscillations, mostly synchronized with the input (Figure 3.13). The frequency of the slow oscillations f_{slow} increases with the frequency f_1 of the square waves before dropping at a value which depends on the stimulation current value A_1 (see Figure 3.14 - B), when the input isn't strong enough to elicit an activation of the whole network up to the CA1 region. On the other hand the frequency of the fast oscillations f_{fast} increases with the amplitude A_1 of the stimulation, and reaches its maximum value when the input frequency f_1 is close to 2.5Hz, the natural frequency of the oscillations occurring with a step input (Figure 3.14 - A).

With parameters set to the "wakefulness" state instead of the sleep one, similar patterns of the evolution of f_{slow} can be seen, except that no rhythmic slow activity appears for a step input stimulation. Furthermore, there is no strong resonance effect of f_{fast} around $f_1 = 2.5Hz$ as there was in slow-wave sleep, and overall slower f_{fast} values can be reached (Figure 3.15).

Whatever the parameters settings, stimulating only a small part of the entorhinal cortex neurons gives rise to oscillations in the corresponding layers of the other regions which shows that localized patterns of activation can be achieved (see the raster plots on Figure 3.16). The spread of this localized activity is limited to adjacent layers in excitatory cell groups but reaches neurons further away in interneuron groups.

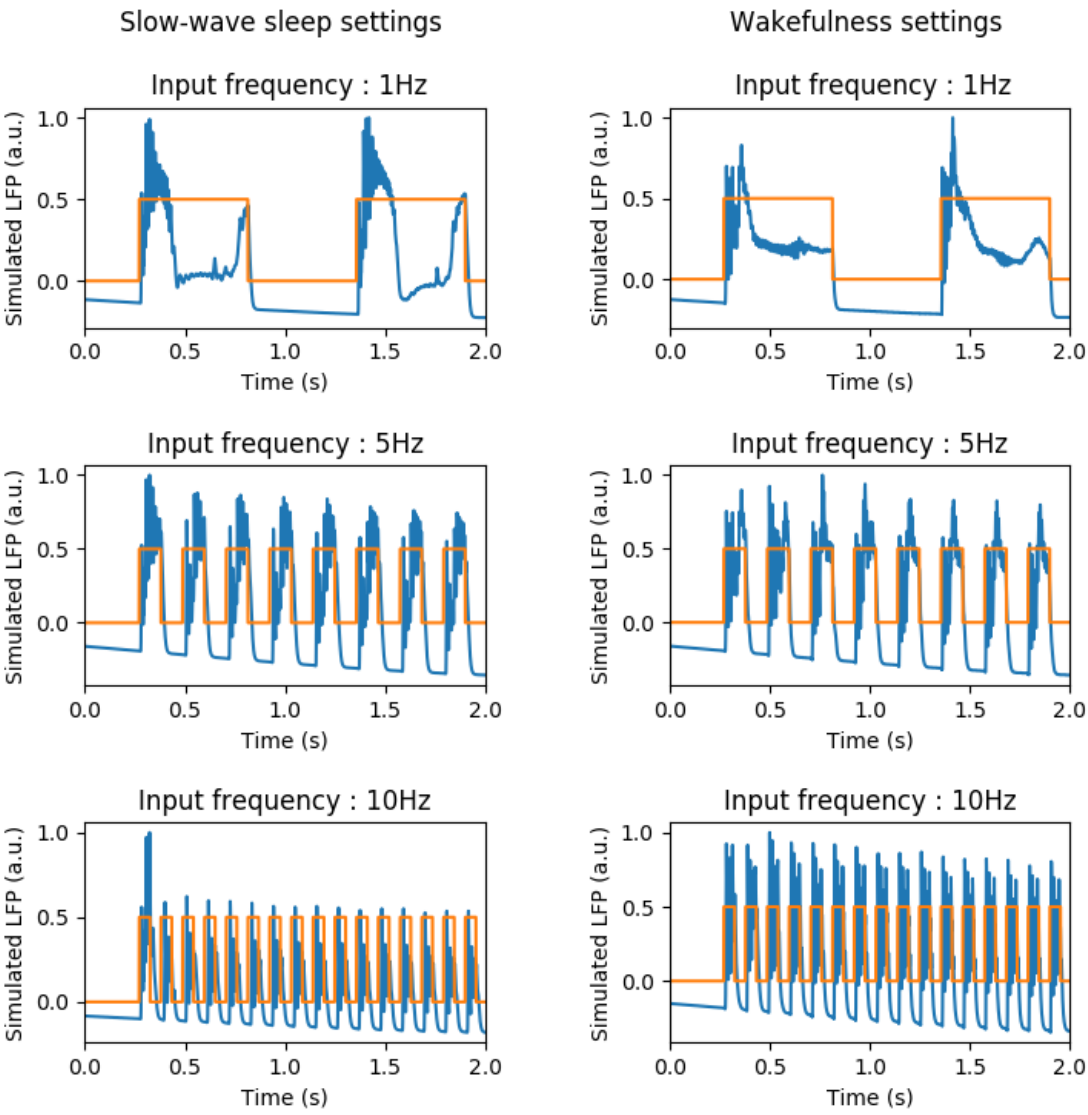

FIGURE 3.13 – Simulated LFP (in blue) resulting from a square current stimulation starting at t=250ms, with maximum value A_1=1nA and frequency 1Hz, 5Hz and 10Hz, under slow-wave sleep and wakefulness conditions. The corresponding input shape is shown in orange on each plot.

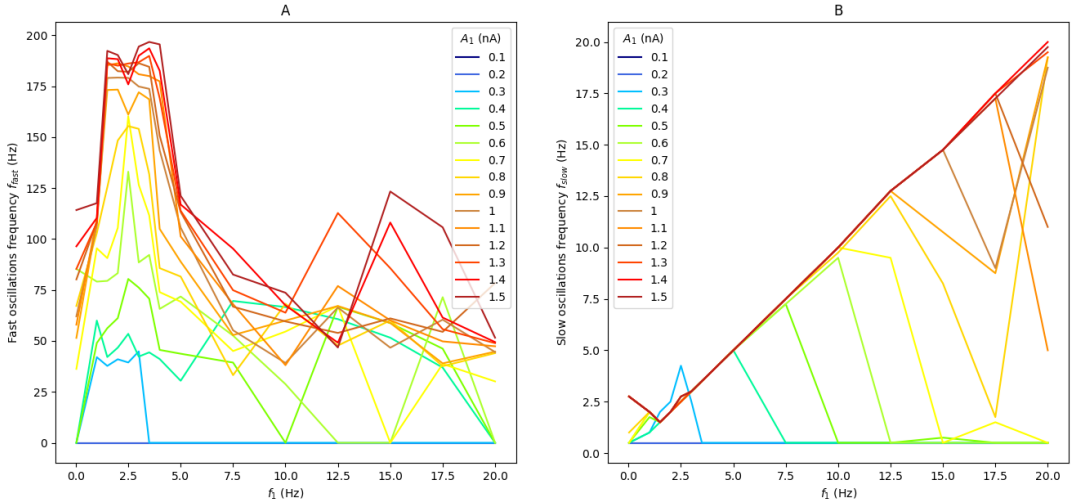

FIGURE 3.14 – Evolution of the network activity depending on the maximal amplitude A_1 and frequency f_1 of the input square wave current for a network with slow-wave sleep settings. A- Frequency of the fast oscillations, B- Frequency of the slow oscillations generated by the network.

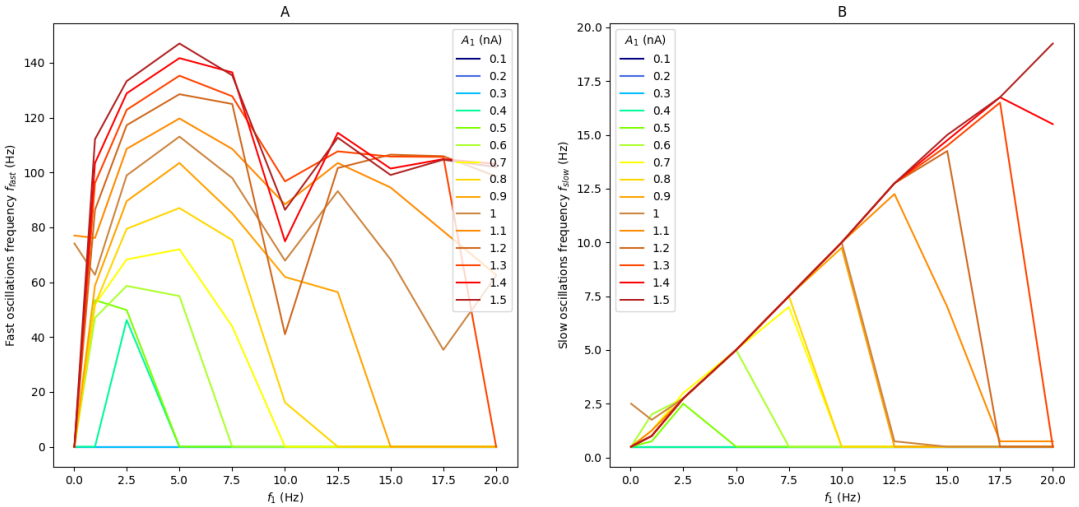

FIGURE 3.15 – Evolution of the network activity depending on the maximal amplitude A_1 and frequency f_1 of the input square wave current for a network with wakefulness settings. A- Frequency of the fast oscillations, B- Frequency of the slow oscillations generated by the network.

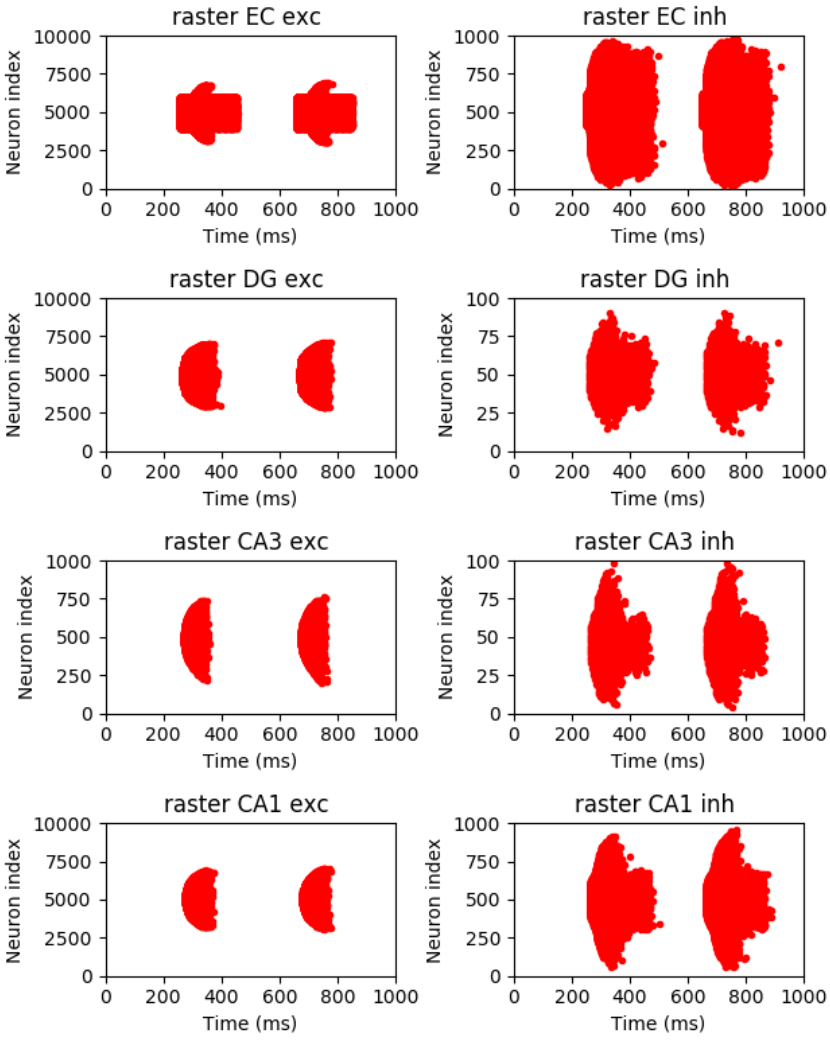

FIGURE 3.16 – Raster plots of the 4 subregions of the network with a localized input to the EC of frequency $f_1 = 2.5Hz$ and amplitude $A_1 = 1nA$, starting at $t = 250ms$, with slow-wave sleep settings. Neurons are indexed according to their position along the septo-temporal axis.

Overall, this study shows that in order to obtain delta and sharp-wave ripple oscillations in the sleep mode, an input with high amplitude A_1 and frequency f_1 in the delta range or below is needed, while to obtain theta-gamma oscillations in the wakefulness mode, input with f_1 in the theta range and lower A_1 should be applied. This last point is in accordance with the theory stating that an external pacemaker, such as the medial septum, induces hippocampal theta oscillations (see for example [Hangya et al., 2009], [Kang et al., 2015] or [Buzsáki, 2002]), however it should be noted that the inputs studied here have a very peculiar shape, and that inputs from regions afferent to the hippocampus, with a more complex, realistic spectrum, and at least a component in the theta range could also elicit theta oscillations. This realistic setup will be studied in the next chapters.

3.3 Other modeling choices

3.3.1 Number and types of neurons

The human hippocampus contains tens of millions of neurons. Simulating each of their individual dynamics through a Hodgkin-Huxley formalism would be impossible to do in a reasonable amount of time considering the current computing resources available to us, so the number of neurons had to be scaled down in our model.

Still, a minimum number of neurons is needed to obtain relevant results. More precisely, [Williamson et al., 2016] shows that group activity starts to arise in networks containing tens of neurons, while [Batista et al., 2014] shows that the dynamic range of a network activity increases with the number of neurons in it (starting from around 10dB for an individual Hodgkin-Huxley neuron, and stabilizing at around 30dB for networks with 80 or more neurons). Furthermore, as the synaptic connections in our network are random, and as the connection probabilities to the smallest neuron groups in our model can be as low as 6%, having too few neurons in any region could result in strong behavior variations depending on the initialization of the network.

Therefore, we chose to model 100 neurons in our smallest neuronal populations, i.e. CA3 and Dentate gyrus interneurons (however it should be noted that such scaling down of the neuron numbers could still affect the network dynamics, as shown in [van Albada et al., 2015] for example).

The Figure 3.17 below shows the resulting LFP obtained in simulations where the neuron numbers have been reduced tenfold compared to this value (and the synaptic conductance has been increased tenfold accordingly), and is to be compared with Figure 3.14. Though most of the features of the larger network are reproduced this way, there are still notable differences. Most notably, the stimulation frequency that is associated with the fastest oscillations increases with the stimulation intensity (instead of being stable at around 2.5Hz for the larger network), and the peak associated with this resonance effect also gets wider. Moreover, the network is able to follow fast frequency inputs even for a stimulation intensity as low as 0.7nA, which overall could indicate that under realistic slow-wave sleep inputs, a smaller network would generate more sharp-wave ripple complexes than a larger, more realistic one.

Figure 3.18 however demonstrates that having five times more neurons in the network compared to our base values doesn't change its behavior significantly, and therefore we kept these values in the following parts to keep the simulation time as low as possible.

The choice of the different types of neurons to be modeled was also based on computational simplicity. We simulated the behavior of the network when replacing all excitatory neurons in the Dentate Gyrus by smaller neurons (the size of the soma was divided by two), and by adding a different type of interneuron with half the usual membrane capacity in all the regions. As shown

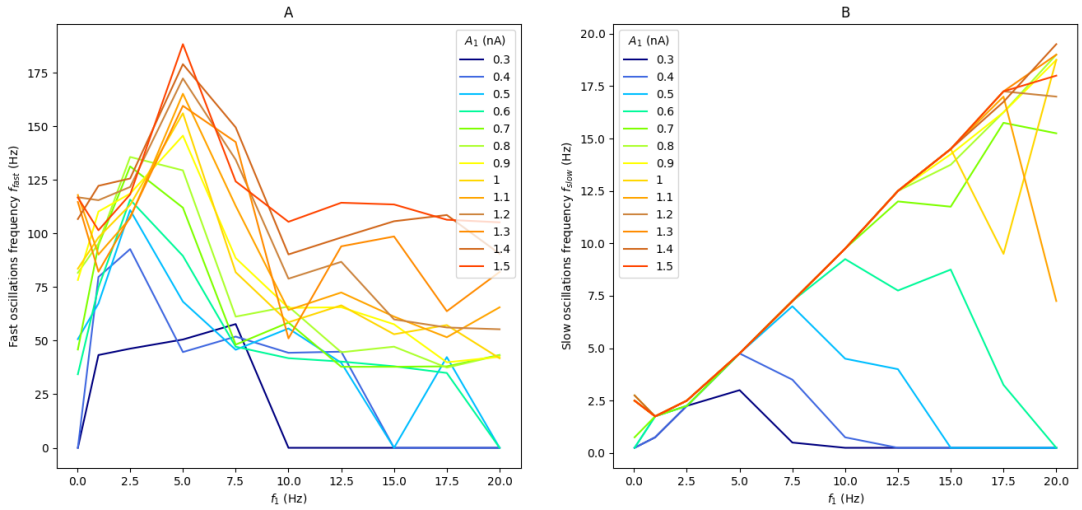

FIGURE 3.17 – Evolution of the network activity depending on the maximal amplitude A_1 and frequency f_1 of the input square wave current for a network with 10 neurons in the smallest population, under slow-wave sleep settings. A- Frequency of the fast oscillations, B- Frequency of the slow oscillations generated by the network.

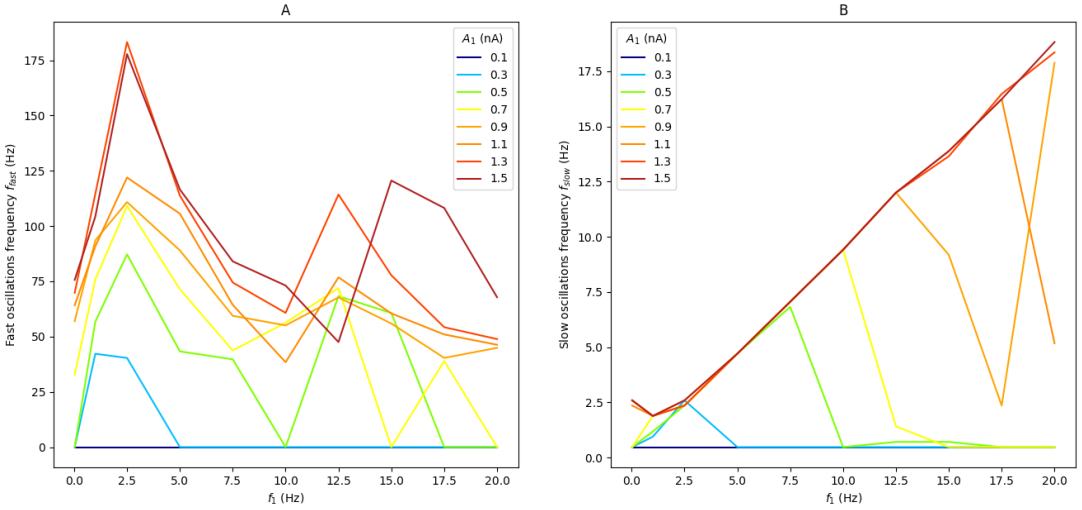

FIGURE 3.18 – Evolution of the network activity depending on the maximal amplitude A_1 and frequency f_1 of the input square wave current for a network with 500 neurons in the smallest population. A- Frequency of the fast oscillations, B- Frequency of the slow oscillations generated by the network.

on Figure 3.19, the behavior of this network under stereotypical inputs remains very similar to our previous results, which is why we chose to keep using only one type of excitatory and inhibitory neurons in the following chapters.

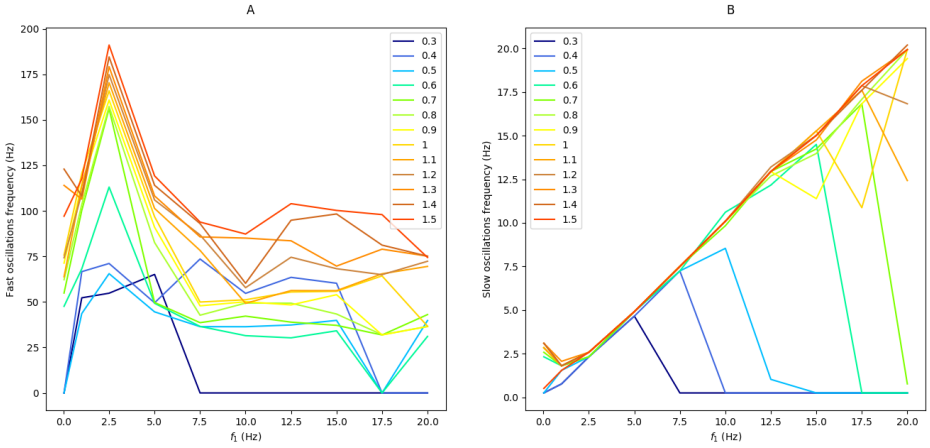

FIGURE 3.19 – Evolution of the network activity depending on the maximal amplitude A_1 and frequency f_1 of the input square wave current for a network with 10 neurons in the smallest population. A- Frequency of the fast oscillations, B- Frequency of the slow oscillations generated by the network.

3.3.2 LFP model

So as to reduce the computational resources needed to simulate our network dynamics, we chose to include only point Hodgkin-Huxley neurons instead of multicompartmental ones. As a consequence, the way we compute the LFP generated by each neuron is but an approximation of the real extracellular potentials. In particular, instead of being originated at a specific location on the neuron morphology, the synaptic currents in our modeled LFP are all located at a single point, representing either the apical or basal dendrites of the neuron.

However, because we are studying the LFP recorded by a macro-electrode, each neuron contribution is spatially average on its whole surface, and therefore the position of the origin of synaptic currents only has a limited effect on the resulting signal.

To verify this, we added a random component on the position of the dendrite of each neuron at each time step in the calculation of the LFP. More precisely, the position of the dendrite was uniformly drawned from a cylinder of diameter $50\mu m$, with axis the soma-dendrite vector used previously, as shown on Figure 3.20. As can be seen on Figure 3.21, the resulting LFP is highly similar both in the temporal and frequency domain to our previous LFP estimation (the correletion coefficient between the two is 0.97 on the example shown), which is why we kept using the latter in the rest of our work.

It should however be noted that other factors influencing the LFP, such as the contribution of other membrane potentials, were not considered here (see Appendix A for supplementary results including the influence of action potentials on the fast frequencies).

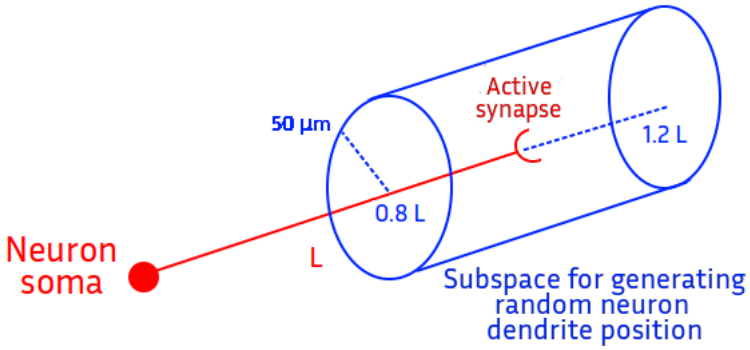

FIGURE 3.20 – Diagram of the subspace used to draw the position of the dendrite of neurons randomly in the approximation of the LFP.

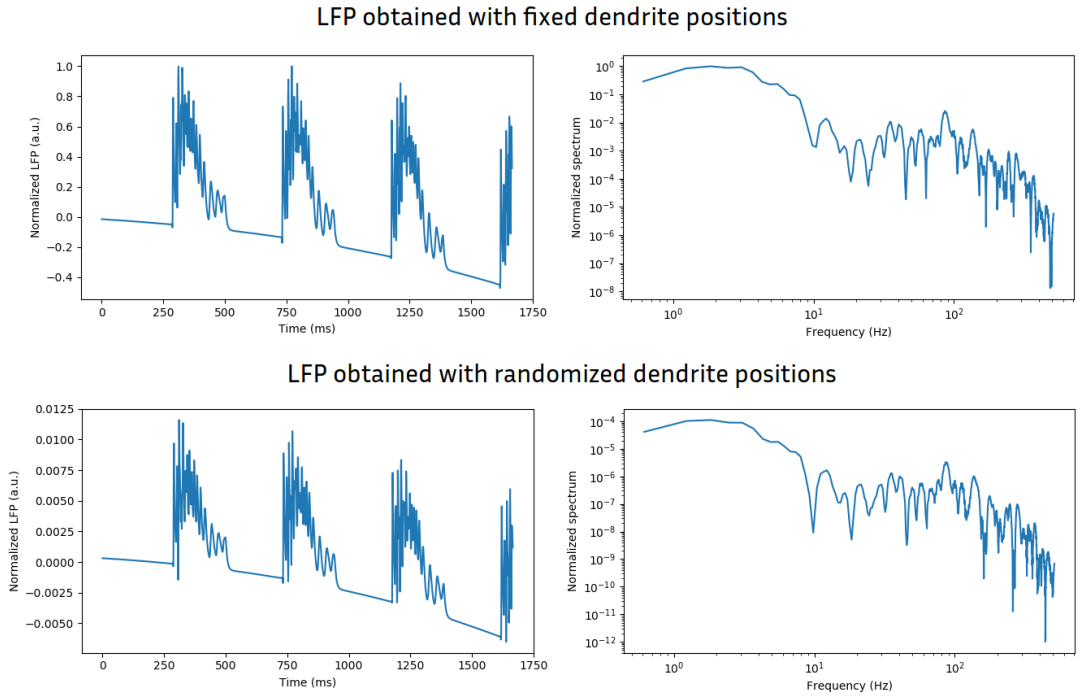

FIGURE 3.21 – Simulated LFP and its frequency spectrum with fixed dendrite positions (top) or randomized positions (bottom).

Chapter 4

Modeling of the sleep-wake cycle

In the previous section, we built a model of the hippocampus, capable of reproducing both wakefulness and sleep rhythms (i.e theta-nested gamma oscillations and sharp-wave ripple complexes), and other combinations of fast and slow rhythms as well. Different sets of parameters can lead to similar oscillations, however not all of the transitions between those sets would be plausible, biologically speaking, during the sleep-wake cycle.

Among the changes occurring in the hippocampus during the sleep-wake cycle, a focus will now be put on the role of Acetylcholine (ACh) on the functional connectivity as well as individual dynamics of hippocampal neurons. We will then compare our modeled network activity with intracerebral recordings in a more realistic setup.

We published our investigations on this chapter's questions in [Aussel et al., 2018] for the most part, on a previous version of our model. Therefore we will also present how the additions we have made since reinforce or qualify the results of this publication.

4.1 Parameters representing the sleep-wake cycle

In this section, we reduce our previous chapter's parameter study to only three parameters so as to test three main hypotheses for explaining the sleep/wake variations of the signals recorded inside the human hippocampal formation, two of which are directly linked to the concentration of ACh in the system. These three hypotheses are :

1. The role of the synaptic connectivity : The varying concentration of ACh between wakefulness and slow-wave sleep modulate the synaptic interactions between and within hippocampal subregions. According to [Hasselmo, 1999], high ACh concentration during wakefulness reduces synaptic interactions from CA3 to CA1 and back to the entorhinal cortex, thus promoting short-term memory storage in CA3, and conversely the low concentration of ACh during sleep strengthens these connections and promotes long-term memory formation in the neocortex. More precisely, due to the presence of nicotinic and muscarinic receptors on hippocampal neurons, it has been shown that some synaptic connections are enhanced by a high Ach concentration, such as the inhibitory connections within the dentate gyrus and CA1 ([Jones and Yakel, 1997], [Frazier et al., 1998]), or the excitatory connections from the dentate gyrus ([Cheng and Yakel, 2013], [Gray et al., 1996]), while others are reduced, such as the excitatory connections from the entorhinal cortex ([Heys et al., 2012]) or CA3 ([Herreras et al., 1988]). This effect was modeled by modulating the strength of synaptic interactions, multiplying or dividing by a gain $G = 3$ the conductance $g_{max,e}$ or $g_{max,i}$ of these synapses to represent higher ACh concentration

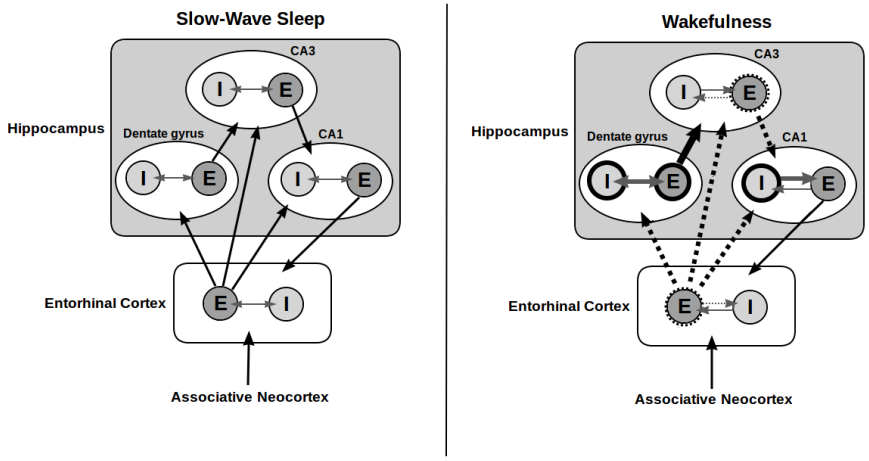

FIGURE 4.1 – Synaptic connectivity for slow-wave sleep and wakefulness. Bold lines indicate increased connectivity, and dotted lines indicate decreased connectivity during wakefulness compared to slow-wave sleep

during wakefulness (this factor G regroups the parameters called G_e, g_e and G_i used in the previous chapter). These two connectivity settings, summed up in Figure 4.1, will be called later on "slow-wave sleep connectivity" and "wakefulness connectivity". It is worth noting that other biological mechanisms apart from the varying concentration of ACh could also cause changes in the functional connectivity during the sleep-wake cycle, such as synaptic plasticity ([Tononi and Cirelli, 2006]) or differential activity of distinct interneurons subtypes ([Gan et al., 2017]).

2. The role of CAN currents : As presented in [Yoshida et al., 2012], ACh also plays a key role in the activation of CAN currents in hippocampal pyramidal cells. As was detailed in the previous chapter, to obtain wakefulness rhythms we chose a value of $g_{CAN} = 25\mu S/cm^2$, and to account for the low concentration of ACh during slow-wave sleep, we chose $g_{CAN} = 0.5\mu S/cm^2$. These two values will be referred to as "CAN off" and "CAN on" respectively in the following.

3. The role of the input : The last possible factor inducing sleep wake variations that we are investigating here is the (glutamatergic) input of the hippocampal network. Indeed, the inputs the hippocampal formation receives from its afferent structures also vary between wakefulness and sleep, as the whole brain exhibits different oscillatory rhythms. Therefore we chose to change the input stimulation to our network accordingly, by basing it on measured LFP signals measured in the patient's brain either during wakefulness or slow-wave sleep (see Section 4.3.1). Please note that cholinergic inputs (from the medial septum for example) are only represented by changing the two other settings (functional connectivity and CAN currents), and that other non-glutamatergic inputs are not directly modeled here.

4.2 Network response to stereotypical inputs

A first analysis can be done by stimulating the network with stereotypical inputs, defined as in the previous chapter by the application of a positive current to entorhinal cortex neurons.

Sleep inputs were represented as square inputs in the delta frequency band ($f_1 = 2.5Hz$) and large maximum value ($A_1 = 1.2nA$), while wakefulness inputs were represented as square inputs in the theta frequency band ($f_1 = 7.5Hz$) and smaller maximum value ($A_1 = 0.8nA$). The frequency of the resulting fast oscillations f_{fast} and slow oscillations f_{slow}, defined as in the previous chapter as the frequency of maximum energy in the power spectrum of the simulated LFP in the 30-250Hz and 0-30Hz bands respectively, are shown on Figure 4.2.

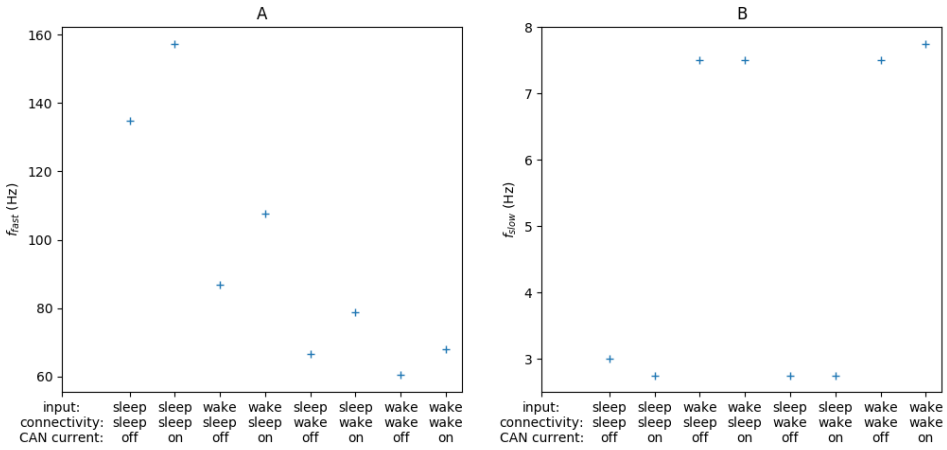

FIGURE 4.2 – Distribution of the frequencies f_{fast} (A) and f_{slow} (B) generated by the model under stereotypical inputs, with an input corresponding to sleep ($A_1 = 1.2nA$, $f_1 = 2.5Hz$) or wakefulness ($A_1 = 0.8nA$, $f_1 = 7.5Hz$), functional connectivity corresponding to sleep or wakefulness and presence or absence of CAN currents.

These simulations show that our three factors can all influence the fast oscillations frequency f_{fast}. In particular, both sleep input and connectivity are needed to achieve oscillations in the ripple frequency band, while wakefulness connectivity on its own drives the network in the gamma band instead (the other two factors being less influential in this situation).

On the other hand, the frequency of the slow oscillations f_{slow} generated by the network are almost only determined by the input given to the network, and does not seem to change when the connectivity and CAN currents are varied.

However, because the inputs received by the hippocampus in vivo are much more complex than stereotypical ones used here, and contain different frequency components, it is likely that the input-output relationships we observed before will be slightly different as well. Therefore, the next sections will focus on studying the behavior of the model under realistic inputs.

4.3 Inputs and outputs of the model to perform comparisons with real signals

4.3.1 Definition of realistic inputs

In the following sections, we apply a more realistic input than the one used previously, this time derived from sEEG measurements in human patients. The LFP data we used was obtained from patients suffering from refractory epilepsy, implanted with intracranial electrodes for surgery planning at the Neurology Service of the University Hospital (CHU) from Nancy, France. The patient gave his informed consent and the study was approved by the ethics committee

of the hospital. The sEEG electrodes (Dixi Medical®, France) had a diameter of 0.8mm, with 2mm-long contacts and 1.5mm inter-contact distance. The patient was notably implanted in the prefrontal cortex, the temporal lobe and the hippocampus (see Figure 4.3 for an MRI image of the implantation of an electrode in the hippocampus), but the epileptogenic zone was located in another region. The position of the electrodes in the patient's brain was automatically ascertained using a procedure described in [Hofmanis et al., 2011].

Signals were recorded using Micromed®, Italy acquisition system. The sampling frequency was 1024 Hz. All signals were labelled by a neurologist to identify the different stages of the sleep-wake cycle (based on EEG signal) as well as to exclude any epileptic phenomena from the data (interictal or seizures). Therefore we assumed that, when no seizure or epileptic spike occurred, the signals from these regions were similar to that of healthy people. We used data from either the slow-wave sleep or wakefulness state.

From the data recorded on the electrodes located in the prefrontal cortex, the lateral temporal lobe and the temporal pole, three groups of 10000 Poisson neurons were defined : each of their firing rates was obtained by first high-pass filtering the LFP from one of these regions above 5Hz, then taking its absolute value, and finally scaling it to a 0-200Hz range, so as to roughly follow its temporal evolution. Each of the Poisson neuron group was connected to the neurons of a different slice of the entorhinal cortex region with a uniform probability of 0.05 through excitatory synapses with the same conductance $g_{max,e}$ as within the network. The goal of this process was to provide uncorrelated inputs to the entorhinal cortex, with some temporal and frequential characteristics of clinically recorded brain signals.

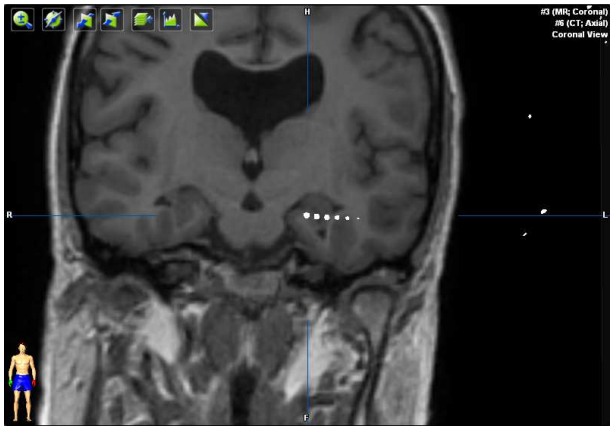

FIGURE 4.3 – Coregistered CT-MRI image of the implantation of an sEEG electrode in the patient's hippocampus (coronal view).

4.3.2 Sharp-Wave Ripples and gamma oscillations detection

Under realistic inputs, the spectrum of the generated LFP is much more complex than it was with stereotypical inputs, following a $1/f$ decrease in power typical of sEEG signals. Therefore the frequency of the fast and slow oscillations f_{fast} and f_{slow} have to be obtained in a different manner than previously.

Meaningful events were located in the simulated signals with a method close to that of ([Taxidis et al., 2012]). First, the root mean square (RMS) of the signal was computed using 10ms-long time windows with no overlap, and its standard deviation (SD) was derived from its whole length. Portions of signal where the RMS was greater than 4xSD, with a peak above 6xSD,

were considered as events. However, unlike in [Taxidis et al., 2012], RMS was applied to the raw signal and not to the signal filtered in the ripple frequency band, so as to be able to detect not only ripples, but other types of oscillations as well.

The spectrum of all the detected events was then analyzed to identify the type of oscillatory patterns : each of them was bandpass filtered between 30 and 250Hz with a Butterworth filter of order 2, and the frequency of maximum power was extracted (please note that in the rest of this work, all the filters applied to signals are Butterworth filters of order 2). The frequency of these fast oscillations is similar to the f_{fast} output obtained before.

The distribution of the peak frequencies in the different simulations performed were compared using Wilcoxon–Mann–Whitney tests (with the purpose of avoiding making assumptions on the shape of the distributions).

In the real sEEG signals, a similar procedure was used to detect SWR, except that the RMS was computed from the 120-250Hz bandpass filtered signal, and only events when the peak RMS was above 7xSD were considered.

On the other hand, the frequency of the slow oscillations was obtained by low-pass filtering the signals below 20Hz and looking at the highest frequency with an energy greater than half the maximum energy of the spectrum. This output is to be compared with the f_{slow} frequencies obtained before.

4.4 Network response to realistic inputs

4.4.1 Slow-wave sleep mode

Under realistic inputs, large amplitude events can be seen on the simulated electrode every few seconds (11 events in a typical one-minute-long simulation, with mean duration 156ms), as the one shown on Figure 4.4. Band-pass filtering them between 30 and 400Hz reveals an oscillatory pattern with peak frequency at 125Hz (SD : 20Hz) (see also Figure 4.10), which is consistent with the literature on sharp-wave ripple complexes for in vivo recordings ([Buzsáki, 2015]).

The ripples in the simulation also appear to happen with a timing close to that of the sharp-waves ripples in the LFP recorded in the patient's hippocampus, as shown in Figure 4.5. In ten one-minute-long signals, 216 SWR were found in the measured LFP and 211 in the corresponding simulations. 80% of the simulated events were located within 1 second of a SWR in the corresponding measured signal, the simulated SWRs occurring in average 265ms before a measured SWR (SD :2s).

Figure 4.6 shows the evolution of the firing rates of the excitatory and inhibitory neuron populations in CA3 and CA1 during a SWR. It can be seen that the sharp-wave activity follows the evolution CA1 interneurons firing rate, while ripple activity mostly comes from increased CA1 excitatory neurons firing rate. The event is preceded by strong CA3 inhibition. During the SWR, interneurons in CA3 then decrease their firing rate, and only get strongly activated again around 100ms later, possibly causing its termination. This pattern of activity of CA3 interneurons is similar to what has been reported for O-LM interneurons in particular (see [Somogyi et al., 2014]).

The direction of the propagation of the ripples in CA1, as well as their original location, varies between events, in accordance with [Patel et al., 2013]. However, about one third of all of the CA1 pyramidal neurons fire during each of the SWR events, which is more than what was reported in the literature, as in [Nádasdy et al., 1999].

The spectrum of the simulated signal is quite similar to that of the sEEG signal measured in the hippocampus during slow-wave sleep, though the simulated signal shows a slightly stronger power density in the ripple frequency band (see Figure 4.9). This could be explained by the fact that our simulated neurons only model a slice of the hippocampus where too many CA1 pyramidal cells get involved in the SWRs and synchronize, and therefore our simulations do not show enough noise and power in other frequency bands. Also, we do not include in our simulation the LFP generated by neighboring structures and propagated through the extracellular medium, which could increase the energy in the low frequencies of the LFP and therefore could compensate for the apparent high frequency peak that we observe in our simulations.

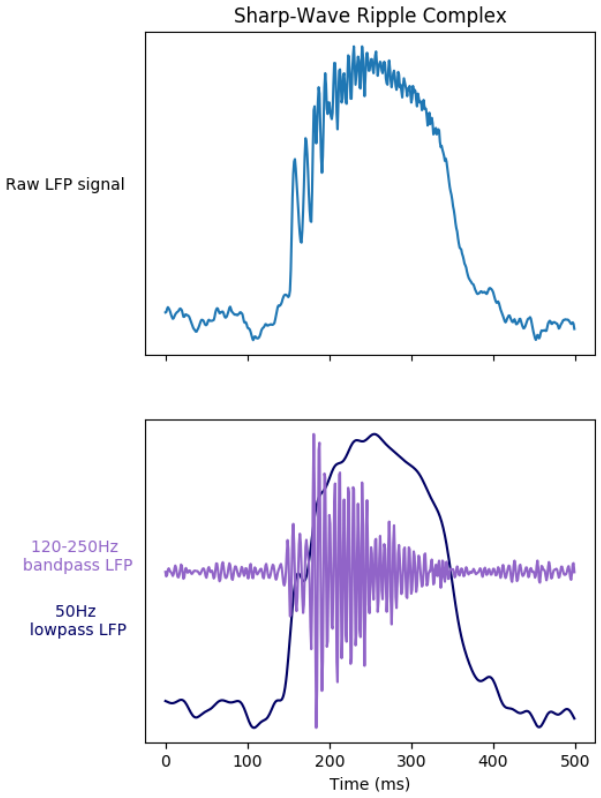

FIGURE 4.4 – LFP simulated at the electrode during a ripple, and corresponding 120-250Hz bandpass filtered and 50 Hz lowpass filtered signals.

4.4.2 Wakefulness mode

Switching the network parameters to the wakefulness ones gives rise to different oscillatory rhythms. Indeed, when applying a similar method of event detection as for slow-wave sleep, that is when looking for portions of the signal with RMS significantly above its standard deviation (see Section 4.3.2), it can be seen that the events' peak frequency is shifted towards the gamma range (90Hz, SD 31Hz). Also, the signal now presents lower frequency oscillations, with a peak in its power spectral density around 7Hz, which corresponds to the theta frequency band (see

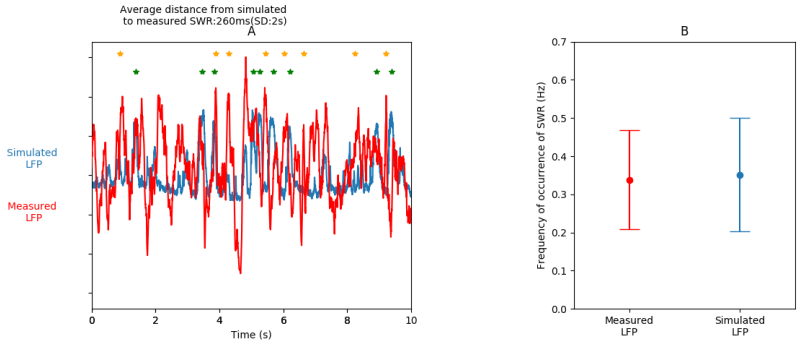

FIGURE 4.5 – A : Comparison between the position of sharp-wave ripples in the simulation (orange stars) and in the slow-wave sleep recordings of the hippocampus (green stars). The blue line corresponds to the simulated LFP, and the red line to the recorded one. B : Frequency of occurrence of the sharp-wave ripples in the measured and simulated LFP.

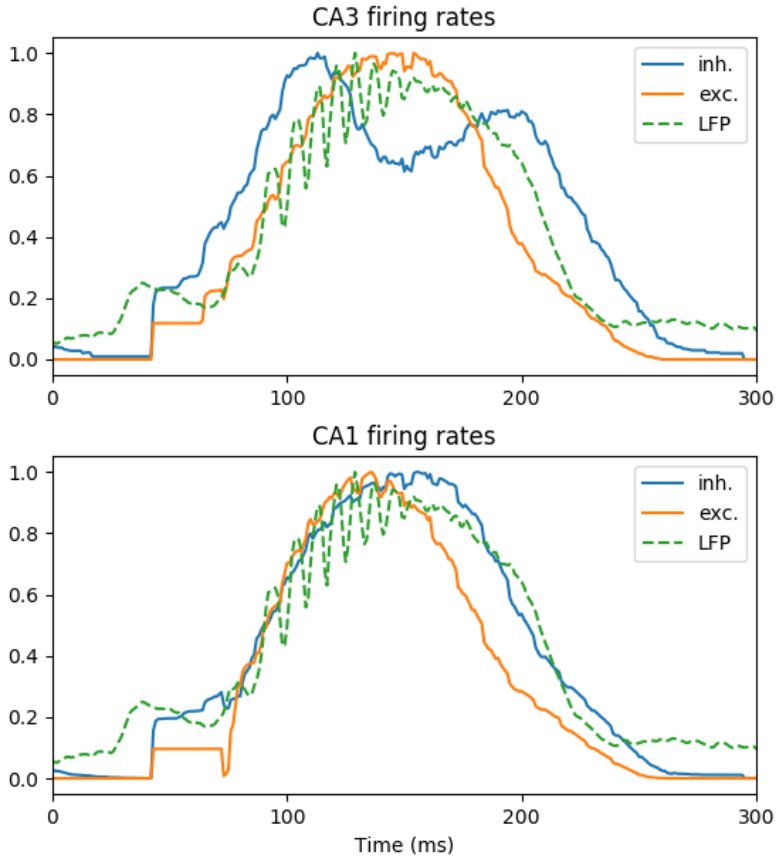

FIGURE 4.6 – Evolution of the firing rates of the CA3 (top) and CA1 regions (bottom) during a sharp-wave ripple, superimposed on the LFP. Orange : excitatory neurons firing rate, Blue : inhibitory neurons firing rate, Green : LFP (all normalized).

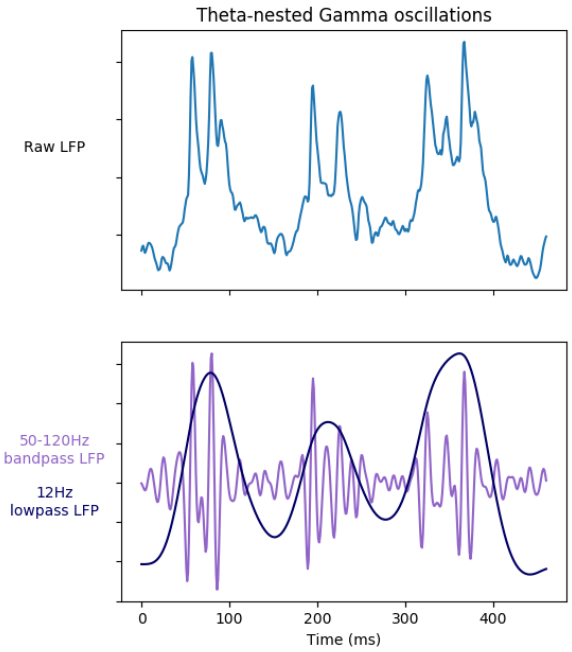

FIGURE 4.7 – LFP simulated at the electrode during theta-nested gamma oscillations, and corresponding 50-120Hz bandpass filtered and 12 Hz lowpass filtered signals.

Figure 4.7).

More precisely, power in the gamma frequency band (30-100Hz) is mostly located around the peak of the theta oscillations (see Figure 4.8). On the other hand, the frequency of the gamma oscillations doesn't change significantly depending on the phase of the theta oscillations.

4.5 Factors influencing the sleep-wake oscillatory rhythms

After having confirmed that slow-wave sleep and wakefulness parameters (input, CAN current and functional connectivity) were associated with sharp-wave ripples and theta-nested gamma oscillations respectively, we tried to modify each of them individually to analyze their influence. Note that among these parameters, two are continuously varying (functional connectivity gain G and CAN channel conductance g_{CAN}), while the third one is binary (sleep/wake input).

A first analysis can actually be done by binarizing all three factors. As we have determined the most plausible values that generate either sleep rhythms (i.e. SWR) or wake rhythms (theta-gamma oscillations), we can choose the respective values for the connectivity gain and the CAN conductance ($G = \{1,\ 3\}$ and $g_{CAN} = \{0.5,\ 25\}\mu S$). These values are designated in the following by sleep ($G = 1$, $g_{CAN} = 0.5$) and wake ($G = 3$, $g_{CAN} = 25$) respectively.

As it can be seen in Figure 4.10, the high frequency component of the oscillations depends mostly on the functional connectivity, with little effect from the CAN current and the input : slow-wave sleep connectivity produces events within ripple frequency range, while wakefulness connectivity produces peak frequencies within the gamma band. The input type (sleep/wake) does not significantly change these peak frequencies. The CAN conductance has a slightly more

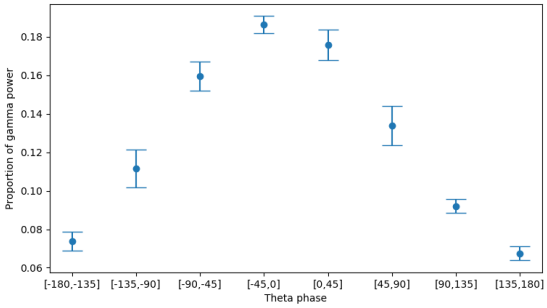

FIGURE 4.8 – Proportion of the power in the gamma frequency band depending on the phase of the theta oscillations, in ten one-minute-long simulations

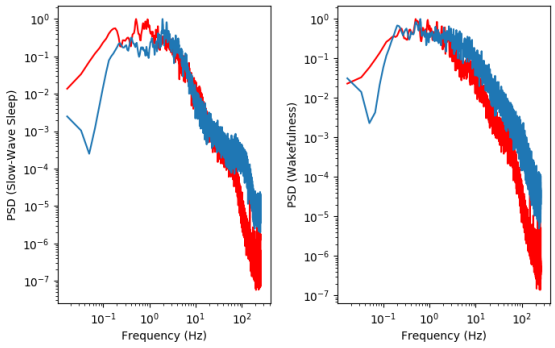

FIGURE 4.9 – Comparison between the power spectrum of the hippocampal LFP (red) and the corresponding simulated signal (blue), during slow-wave sleep (left) and wakefulness (right).

important effect, increasing the frequency of the oscillations. Similar results can also be seen on Figure 4.11, as whenever the slow-wave sleep connectivity increases the ripple to gamma band power ratio. The CAN currents increase the overall power in the signal in every parameter set, and also increase the frequency of occurrence of SWRs seen with slow-wave sleep connectivity, from 0.3Hz (SD 0.1Hz) to 1.6Hz (SD 0.1Hz) with sleep inputs and from 0.13Hz (SD 0.04Hz) to 1.25Hz (SD 0.4Hz) with wakefulness inputs (in each case the p-value is less than 0.01). The power of the signal is much higher with slow-wave sleep connectivity than with wakefulness connectivity, which may be due to the very high neuronal activity seen during our simulated SWRs.

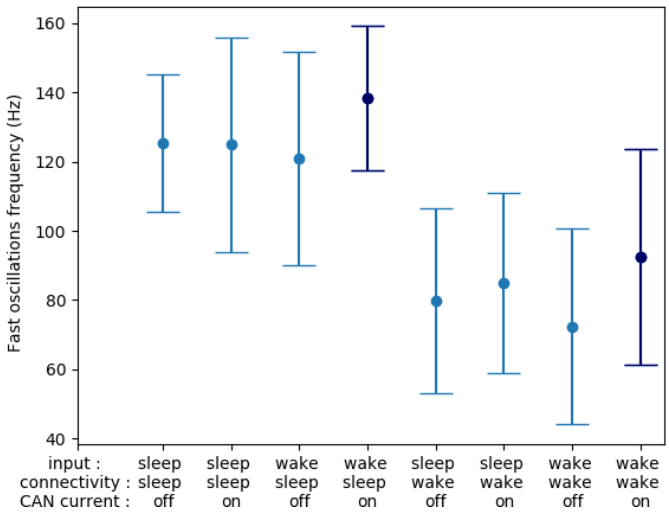

FIGURE 4.10 – Distribution of the fast oscillations frequencies of events in ten one-minute-long simulations with Sleep or Wakefulness stimulation, Sleep or Wakefulness connectivity, and presence or absence of CAN current, with mean and standard deviation. Whenever a different connectivity is used, the peak frequency is significantly different ($p < 10^{-3}$). The dark blue points correspond to the same set of parameters chosen for the study of the influence of the connectivity in Fig 4.12.

In order to asses more precisely the effect of the CAN conductance variations, we have also modified it gradually between the two extreme values (see Figure 4.14, left panel ; recall that the on/off CAN current labels in Figure 4.10 correspond to the most extreme cases in Figure 4.14).

Figure 4.10 indicates that functional connectivity is the most important factor for changing the peak frequency. The natural question which arises is if this change in the peak frequency is gradual when we vary the connectivity gain G or if there is a switch at some point. This is explored in Figure 4.12 (left panel). As it can be seen, the peak frequency decreases non-linearly as G is increased. Only the value $G = 1$ ensures the generation of ripples, while values greater than or equal to 1.5 lower the peak frequencies into the gamma band. For conciseness, we present here the dependency of the peak frequency with G for fixed values of the CAN conductance (to one of the extreme values, namely wake) and the input (wake also).

The low frequency part of the simulated signals seems to be influenced differently by these three factors. This slow oscillations frequency seems to be influenced by both the CAN current and functional connectivity, with smaller effect from the input type (see Figure 4.13). Increased CAN current (see Figure 4.14, right panel) increases the slow oscillations frequency, and so

does wakefulness connectivity (see Figure 4.12, right panel), but only up to the value $G = 3$, above which the slow oscillations frequency drops. Wakefulness connectivity also increases its standard deviation, meaning that different input signals of the same type can then induce very different oscillatory frequencies. High CAN current and wakefulness connectivity are both needed to achieve slow oscillations consistently in the theta band instead of the delta band.

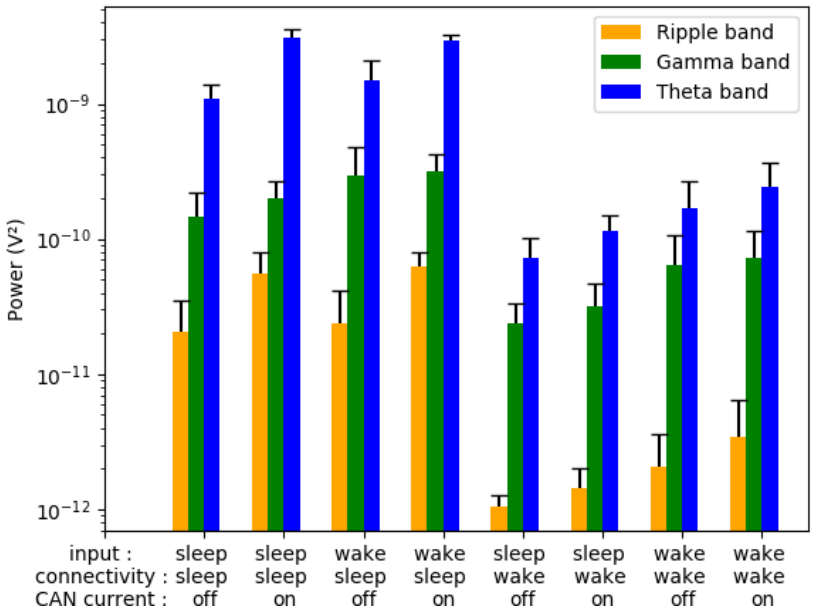

FIGURE 4.11 – Power in the oscillations in the Ripple (120-200Hz, yellow), Gamma (30-100Hz, green) and Theta (5-10Hz, blue) frequency bands in ten one-minute-long simulations with Sleep or Wakefulness stimulation, Sleep or Wakefulness connectivity, and presence or absence of CAN current, with mean and standard deviation.

4.5.1 Network topology and structural connectivity influences the resulting LFP

In [Aussel et al., 2018], we published similar results to the ones presented previously in this chapter. However, the biological plausibility of our model has been improved since then, notably by applying different inputs to three different layers of our modeled entorhinal cortex, and connecting the regions in our model with a connection probability decreasing with the distance between the source and target neurons along the septo-temporal axis.

These changes helped us obtain a simulated LFP closer to clinical recordings in the frequency domain. In particular in slow-wave sleep settings, the power spectrum of our current model is closer to sEEG measurements in the ripple band, as the synchronized groups of neurons during SWRs is smaller than in our previously published model (see Figure 4.15). It seems likely that applying more diverse inputs to the entorhinal cortex could lead to an even more realistic network activity.

The trends observed in the variation of the fast and slow oscillatory frequencies in our published model are mostly similar to those presented here (see Figure 4.16 and 4.17), with fast oscillations frequency being mostly influenced by functional connectivity and slow oscillations

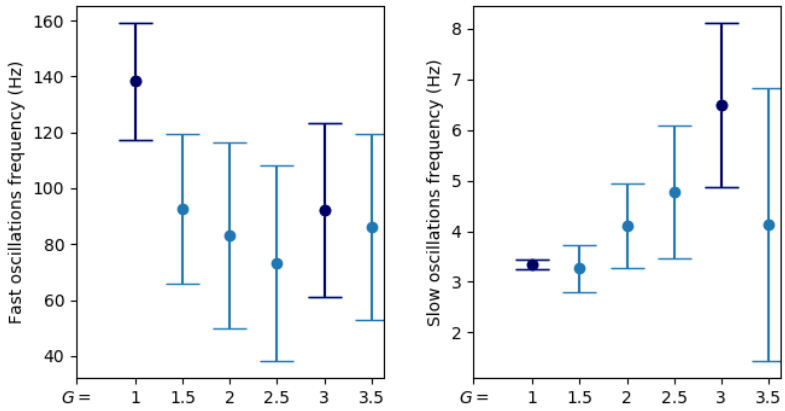

FIGURE 4.12 – Influence of the functional connectivity modification factor G, with wakefulness input and high CAN current. In dark blue, the value $G = 1$ corresponds to the sleep connectivity and $G = 3$ corresponds to the wakefulness one. Left : Distribution of the fast oscillations frequencies. Right : Distribution of the slow oscillations frequencies (ten simulations in each case).

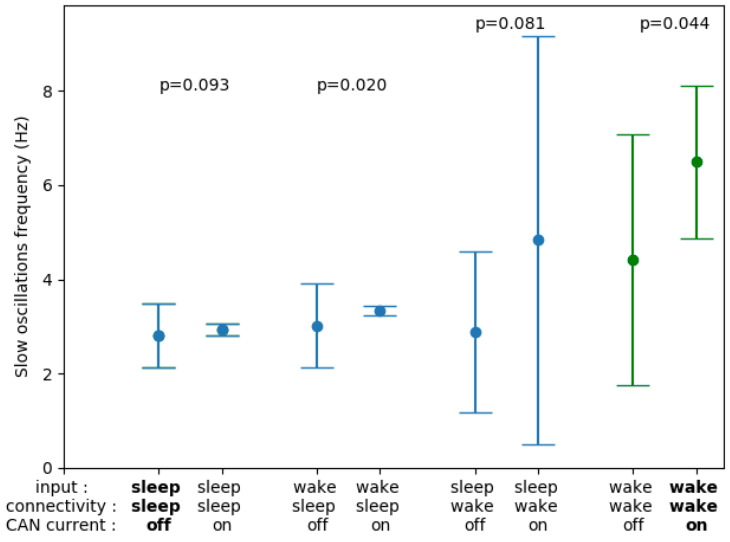

FIGURE 4.13 – Distribution of the slow frequency components of the neural oscillations in ten one-minute-long simulations with Sleep or Wakefulness stimulation, Sleep or Wakefulness connectivity, and presence or absence of CAN current. The p-values indicated correspond to the comparison of the signals with and without CAN in each situation. The green points correspond to the same set of parameters chosen for the study of the influence of the CAN channel conductance as in Fig 4.14.

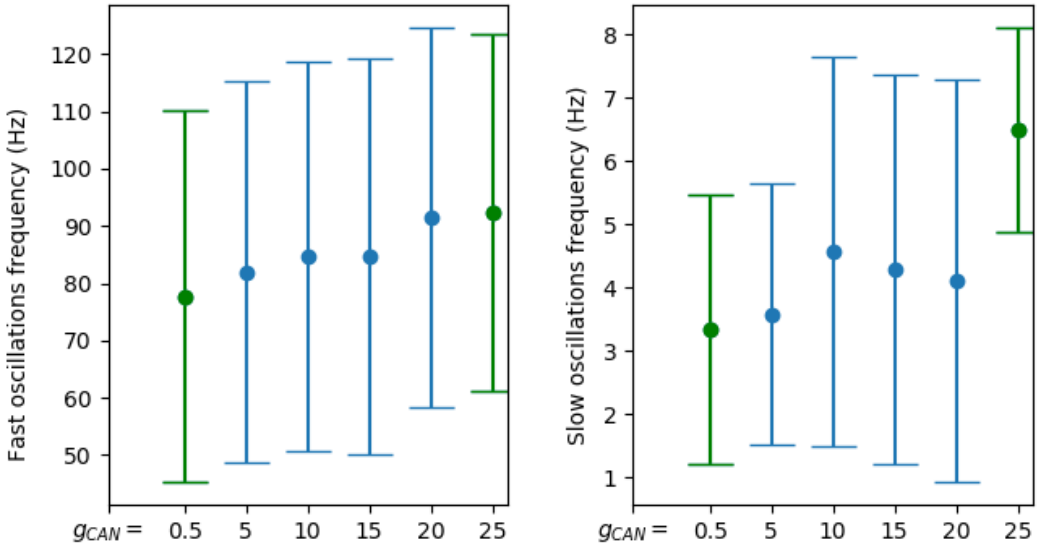

FIGURE 4.14 – Influence of the CAN channel conductance g_{CAN} (in $\mu S/cm^2$), with wakefulness input and connectivity. In green, the value $g_{CAN} = 0.5\mu S/cm^2$ corresponds to slow-wave sleep settings and $g_{CAN} = 25\mu S/cm^2$ corresponds to wakefulness. Left : Distribution of the fast oscillations frequencies. Right : Distribution of the slow oscillations frequencies (ten simulations in each case).

frequency being influenced by the CAN currents. However, our current more complex input and inter-region connectivity induce a more diverse response of the network along the septo-temporal axis, which tend to increase the variability in the fast oscillations frequency observed, as different oscillatory patterns can now appear at the same time in different neuron groups. As for the slow oscillations frequency, our current more complex model reveals that functional connectivity plays an important role in the production of theta oscillations (and not only CAN currents).

In our previous article [Aussel et al., 2018], one of the original contributions was the use of an approximation of the real anatomy of the simulated systems. Therefore, regardless and previous to any sleep/wake analysis, we also checked in this work what could be the benefits of using a anatomically realistic topology and connectivity compared to, say, a random one.

Figure 4.18 and Figure 4.19 present the simulated LFP with slow-wave sleep and wakefulness parameters respectively in 3 different networks : a first network with topology and connectivity as defined in the previous chapter, a second network with the same topology but a uniform rather than distance-related connectivity, and a third network where the connectivity was kept but where each structure's topology was replaced with a simple rectangular-shaped column. Other parameters were kept the same across simulations.

What can be seen is that both topology and connectivity influence the results of the simulations for slow-wave sleep parameters. Sharp-wave ripples-like events (see Section 4.4.1) can only be seen with a distance-related connectivity and not with uniform connectivity. The events obtained with the full topology are closer to the frequency of sharp-wave ripples reported in the literature (see [Buzsáki, 2015]), while those obtained with a simplified topology lie within the gamma band (and there is proportionally more power in the theta and gamma bands compared

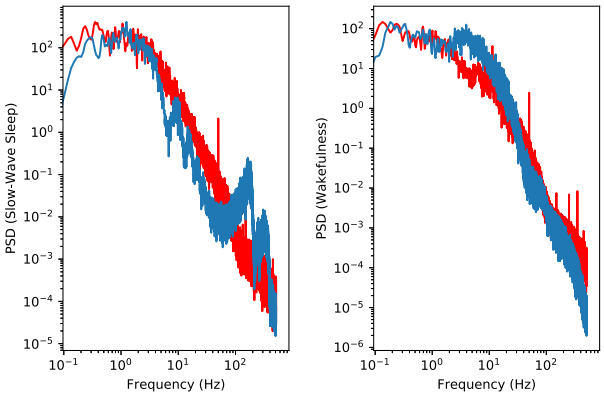

FIGURE 4.15 – Comparison between the power spectrum of the hippocampal LFP (blue) and the corresponding simulated signal (orange), during slow-wave sleep (left) and wakefulness (right), from the model published in [Aussel et al., 2018].

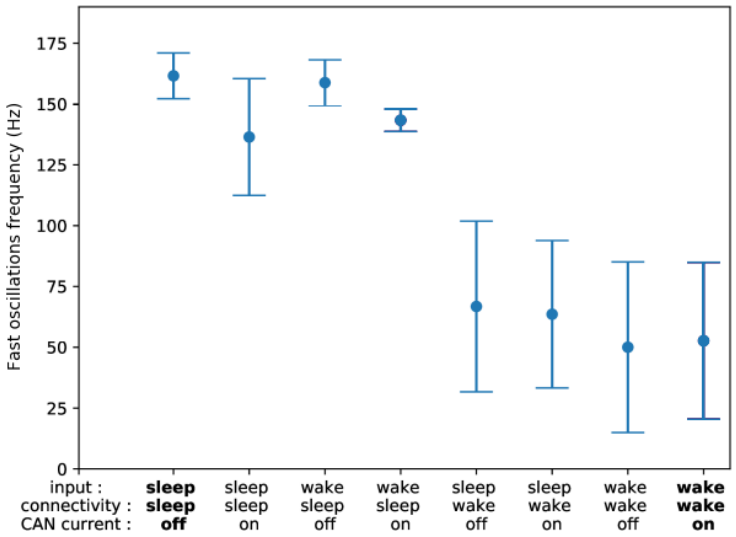

FIGURE 4.16 – Distribution of the fast oscillations frequencies in ten one-minute-long simulations with Sleep or Wakefulness stimulation, Sleep or Wakefulness connectivity, and presence or absence of CAN current, with mean and standard deviation, from the model published in [Aussel et al., 2018]. Whenever a different connectivity is used, the peak frequency is significantly different ($p < 10^{-3}$).

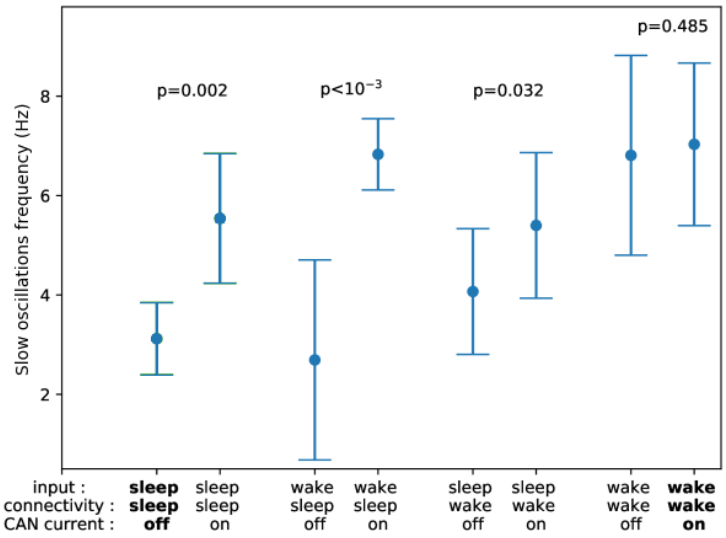

FIGURE 4.17 – Distribution of the slow frequency components of the neural oscillations in ten one-minute-long simulations with Sleep or Wakefulness stimulation, Sleep or Wakefulness connectivity, and presence or absence of CAN current, from the model published in [Aussel et al., 2018]. The p-values indicated correspond to the comparison of the signals with and without CAN in each situation.

to the ripple band in this case).

On the other hand, theta and gamma oscillations can be obtained with all the three networks, though the temporal aspect of the simulated signal is modified by changing either the connectivity or the topology.

A possible explanation as for why the topology and connectivity can affect so much the resulting simulations in the slow-wave sleep case is that it changes the number and sizes of interconnected neuronal clusters and therefore without a detailed topology it is hard to get the same kind of neural synchronization as seen during sharp-wave ripple complexes. To a lesser extent, changing the position of the neurons and their orientation when changing the topology also affects the resulting signal as it affects the way neural activities are summed up when computing the LFP seen by the electrode.

4.6 Discussion

Our results suggest that the high frequency component of hippocampal oscillations might be governed mostly by network connectivity, whereas the low frequency components could result from both individual neuron channel properties and network connectivity. A possible consequence of this idea is that higher frequency, pathological oscillations that are seen in the epileptic hippocampus for example (fast ripples or seizures) might also emerge from an abnormal functional connectivity of the system rather than individual neuron properties.

An interesting point to raise is that the glutamatergic inputs given to the network seemed to have little to no influence on the frequency of our model's oscillations, which could indicate that the hippocampus doesn't need an external "pacemaker" such as the medial septum to set its rhythms, but it has its own internal pacemaker, the CAN neurons (for more arguments

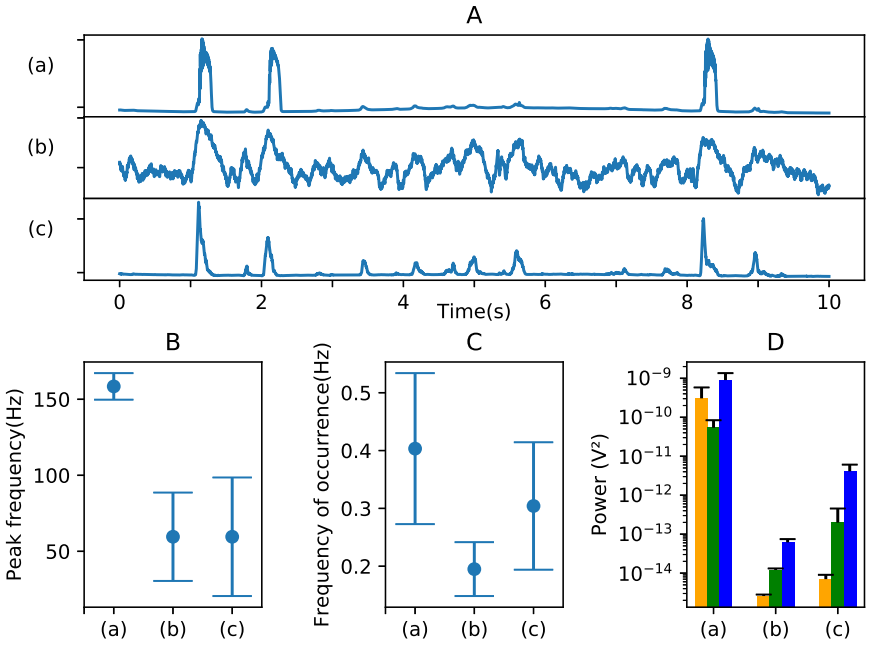

FIGURE 4.18 – Comparison of the simulated LFP for slow-wave sleep, with the following topology and connectivity : (a) full topology and distance-related connectivity, (b) full topology but uniform connectivity, and (c) simplified topology and distance-related connectivity. A : 10-second LFP traces for each conformation. B : Fast oscillations frequencies in each LFP simulation, for each conformation, with mean and SD. Statistical comparison shows significant difference between each case ($p < 10^{-3}$). C : Frequency of occurrence of the events for each conformation, with mean and SD. D : Power in in the oscillations in the Ripple (120-200Hz, yellow), Gamma (30-100Hz, green) and Theta (5-10Hz, blue) frequency bands, with mean and SD, for each conformation.

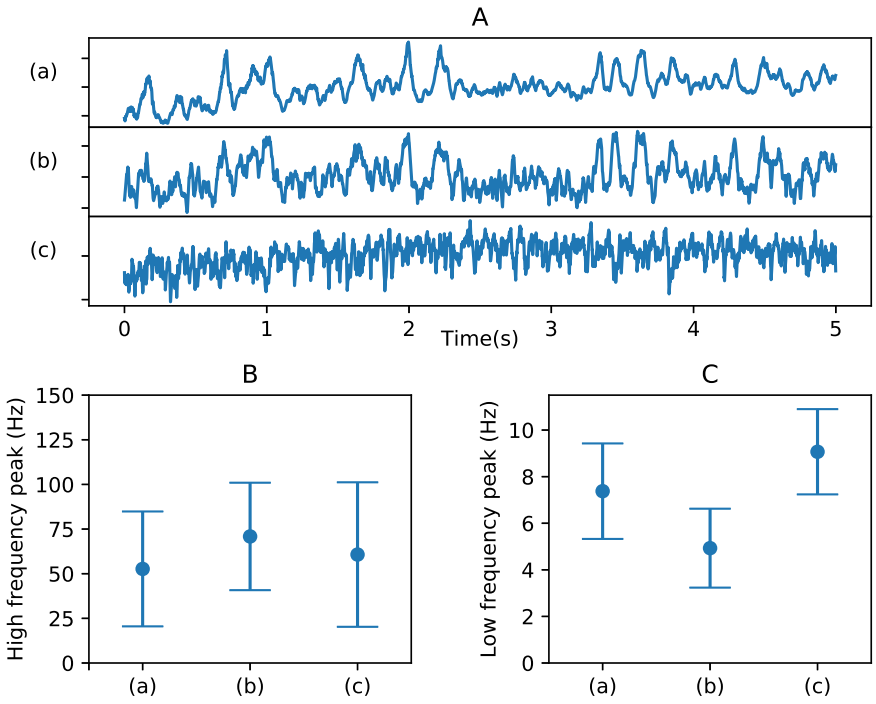

FIGURE 4.19 – Comparison of the simulated LFP for wakefulness, with the following topology and connectivity : (a) full topology and distance-related connectivity, (b) full topology but uniform connectivity, and (c) simplified topology and distance-related connectivity. A : 5-second LFP traces for each conformation. B : Fast oscillations frequencies in each LFP simulation, for each conformation, with mean and SD. Statistical comparison shows significant difference between each case ($p < 10^{-3}$). C : Peak frequency of the LFP filtered in the theta band (5-10Hz), for each conformation, with mean and SD.

on that topic, see for example [Hangya et al., 2009], [Kang et al., 2015] or [Buzsáki, 2002]). Still, the external influence cannot be excluded, as our model predicts that theta oscillations can also be generated by the correct combination of the inputs and functional connectivity, as seen under stereotypical inputs. On the other hand, the inputs seem to influence the timing at which oscillations are generated, which could account for signal encoding, particularly during wakefulness. On portions of the signals, the simulation even showed some similarities with the measurements in the temporal domain and not only in the frequency domain (see Figure 4.5).

Similarly to what have been proposed by [Taxidis et al., 2012], our model was able to reproduce different rhythms, and sharp-wave ripples in particular, by using only chemical synapses (and therefore no axo-axonic gap junctions). This further supports the idea that gap junctions may not be necessary for generating high frequency oscillations in the hippocampus.

Finally, our work suggests that the topology of the hippocampal formation should be taken into account in order to improve existing computational models. In particular, such methods could produce a realistic sEEG signal estimation while keeping the simulation complexity low, by solving the differential equations for point neurons only and considering them as dipoles for calculating local field potentials.

Chapter 5

Modeling of the epileptic hippocampus

After having built a convincing model of the healthy hippocampus and parametrized it for mimicking sleep and wakefulness, we will now extend it so as to study pathological epileptic rhythms. As in the previous sections, we will base our modeling choices on existing physiological knowledge of the epileptic hippocampus. In particular, we will study the effects of four common neuropathological changes on the oscillations generated by the network, in relation with the vigilance state.

5.1 Model changes to account for epilepsy

Among the different changes that can occur in an epileptic hippocampus, we chose to focus on four in particular : hippocampal sclerosis, mossy fiber sprouting, increased excitability and impaired inhibition.

Hippocampal sclerosis was modeled by reducing the number of excitatory neurons in each subregion of the model as a fraction *scl* of the maximum pyramidal cell and granule cell reduction observed in type 1 hippocampal sclerosis ([Blümcke et al., 2013]). More precisely, the number of excitatory neurons was set to :

— $10000 \cdot (1 - 0.75scl)$ in the entorhinal cortex
— $10000 \cdot (1 - 0.6scl)$ in the dentate gyrus
— $1000 \cdot (1 - 0.8scl)$ in CA3
— $10000 \cdot (1 - 0.8scl)$ in CA1

with *scl* varying between 0 (no sclerosis) and 1 (high sclerosis). The number of inhibitory neurons on the other hand was left unchanged. With $scl = 0$, the number of excitatory neurons in all regions is the same as in the healthy model.

Mossy fiber sprouting ([Noebels et al., 2012]) was represented by including recurrent excitatory connections in the dentate gyrus as well as increasing the number of connections from excitatory to inhibitory neurons in this region. A parameter *spr* varying between 0 (no sprouting) to 1 (high sprouting) was defined to modify the maximum synaptic connection probabilities to :

— $0.1 \cdot spr$ from excitatory to excitatory neurons, so that each excitatory neuron makes in average 300 synapses with $spr = 1$, in accordance with the maximum 500 new synapses reported in a pilocarpine epilepsy model in [Buckmaster et al., 2002]
— $0.06 \cdot (1 + spr)$ from excitatory to inhibitory neurons, so that each excitatory neuron forms about 1% of its new synapses with inhibitory interneurons.

Regarding the increased excitability of pyramidal cells, we chose to change the equilibrium potential E_K of their potassium channels, which could represent for example a channelopathy ([Lerche et al., 2012]) or impaired glial function ([Coulter and Steinhauser, 2015]). A healthy hippocampus is characterized with $E_K = -100mV$, and this value is increased to $-90mV$ or $-80mV$, increasing neuronal excitability, to represent epilepsy.

Finally, different mechanisms can alter synaptic inhibition in mesial temporal lobe epilepsy. The one we chose to model is the accumulation of chloride ions inside pyramidal cells changing the reversal potential of GABA synapses (see [Huberfeld et al., 2007]).

We propose to model chloride ion concentration in each excitatory neuron as a simple first order process :

$$\frac{d[Cl^-]}{dt} = -\frac{[Cl^-]}{\tau_{Cl}}, \tag{5.1}$$

with τ_{Cl} the decay rate of $[Cl^-]$. Whenever the excitatory neuron emits an action potential, the concentration $[Cl^-]$ is then increased by a fixed amount (set here to 0.2). A healthy hippocampus is characterized by a fast τ_{Cl} decay rate of $0.1s$, and this value is increased up to $0.5s$ or $1s$ to represent epilepsy.

The expression of the resting potential E_I of the inhibitory synaptic current received by the neuron is then modified to :

$$E_I = \begin{cases} -80mV & \text{if } [Cl^-] \leq 0.5, \\ 0mV & \text{otherwise.} \end{cases} \tag{5.2}$$

The threshold value 0.5 and increase to $[Cl^-]$ have been set to 0.5 and 0.2 respectively so that the threshold is scarcely exceeded in a simulation with parameters representing a healthy hippocampus.

To summarize, our epilepsy study introduces 4 new parameters in our hippocampal model, *scl*, *spr*, E_K and τ_{Cl}, representing respectively hippocampal sclerosis, mossy fiber sprouting, pyramidal cell hyperexcitability and impaired inhibition. These parameters are to be studied in relation with the vigilance state, which can be set to either slow-wave sleep and wakefulness.

Because the number of parameters is much smaller than in our initial study of the healthy hippocampus in Chapter 3, we will investigate their influence on the resulting LFP by sampling the parameter space regularly, without using a DOE or Sobol' analysis method.

5.2 Detection of epileptic oscillations in the modeled LFP

In clinical context, pathological oscillations such as seizures and interictal discharges (IEDs) are commonly detected by visual inspection of the EEG or sEEG signals by an expert. Their automated detection is still an active research field, and often relies on machine learning techniques to cluster the data into a physiological and epileptic set (see for example [Paul, 2018] for the detection of seizures or [Gaspard et al., 2014] for IEDs).

In this work, we chose to keep a rather simple approach for the detection of pathological oscillations in our simulated signals. Seizures were detected and characterized by an increase in the power in the theta to alpha band (4-10Hz), as was for example found out in intracranial recordings in [Naftulin et al., 2018].

Interictal spikes (IEDs), sharp-wave ripples and fast ripples were detected by first filtering our simulated LFP in the corresponding frequency bands (10-80Hz, 120-200Hz and 200-500Hz respectively), and computing the root mean square (RMS) of the resulting signals. Events were

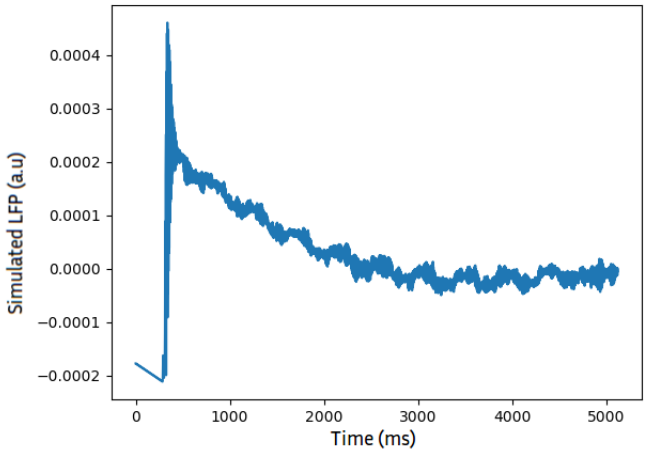

FIGURE 5.1 – Simulated LFP under a square current of amplitude 1nA, with $spr = 1$, $scl = 0$, $E_K = -100mV$ and $\tau_{Cl} = 0.1s$.

then defined as portions of LFP with RMS higher than its mean value and with a peak at least four times its standard deviation in at least one of the defined frequency band. IEDs were defined as events with a peak in the RMS of the 10-80Hz filtered signal but no peak in the ripple or fast ripple frequency ranges, ripples were defined as events with a peak in the RMS of the 120-200Hz filtered signal but no peak in the fast ripple frequency range, and fast ripples were defined as events with a peak in the RMS of the 200-500Hz filtered signal.

5.3 Influence of the parameter changes under stereotypical inputs

5.3.1 Model saturation

Certain parameters values cause the wakefulness network to saturate after a few seconds (see Figure 5.1), i.e. to produce continuous paroxystic neural spiking in all the regions of the model, which does not stop even after all external input to the network is removed. This abnormal activity first arises from CA3, which can be expected knowing that this region is the one with highest recurrent excitation. The LFP in this saturated state shows a peak in the fast ripple frequency band (above 200Hz) in its spectrum.

The emergence of such saturation states only depends on the mossy fiber sprouting level *spr* and the hippocampal sclerosis level *scl*. More precisely, it can be observed that the mossy fiber sprouting level *spr* promotes instability while the hippocampal sclerosis level *scl* reduces it (see Figure 5.2). This is consistent with an overall epileptogenic effect of sprouting ([Santhakumar et al., 2005]) compared to a protective effect of sclerosis ([Lopim et al., 2016]).

With high *spr* and low *scl*, this saturation effect arises even for very low input stimulation, meaning that it can develop from the internal noise put on all neurons and closed-loop excitation only. Also, E_K and τ_{Cl} do not change the sprouting and sclerosis levels generating this paroxystic activity, meaning that recurrent excitation, more than individual neurons hyperexcitability or reduced inhibition is needed to obtain such pathological oscillations.

The sleep-wake cycle does influence this phenomenon, as in slow-wave sleep settings it arises from a smaller subset of the parameters space than in wakefulness, that is with high pyramidal cell hyperexcitability ($E_K = -80mV$ or higher), very high sprouting ($spr = 0.8$ or higher), and

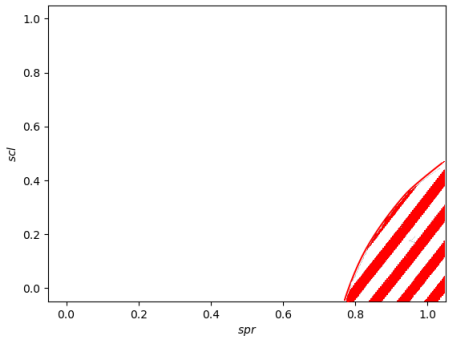

FIGURE 5.2 – Simple diagram showing the region of *spr* and *scl* parameters leading to network instability in hached red, under wakefulness settings.

no hippocampal sclerosis ($scl = 0$). In conditions where instability appears only in wakefulness, it seems to arise from the modified synaptic connectivity accompanying wakefulness (and the increased excitatory synaptic strength in the dentate gyrus in particular), and not from the increased CAN current (see Figure 5.3).

5.3.2 Pathological oscillations

The evolution of the fast oscillations mean frequency f_{fast} as a function of the four parameters *spr*, *scl*, E_K and τ_{Cl} is shown on Figure 5.4 for slow-wave sleep and wakefulness respectively. Each subplot of this figure shows in color the values of f_{fast} depending on *spr* and *scl*, for fixed values of E_K and τ_{Cl}, which correspond to the line and column at which the subplot appears. The point in the bottom-left corner of the bottom-left plot therefore corresponds to a healthy hippocampus model. This layout will be used again throughout this chapter for the representation of other model outputs.

In both the slow-wave sleep and wakefulness modes, high mossy fiber sprouting level comes with higher frequency fast oscillations compared to the healthy hippocampus. Reciprocally, high hippocampal sclerosis tends to reduce the frequency of the fast oscillations produced by the network.

The relationship between the fast oscillations frequency f_{fast} and our four parameters can be estimated with a second order polynomial function (with the same method as in Chapter 3, section 3.2.1) :

$$\begin{aligned} f_{fast} \quad = \quad & a_0 + a_1 spr + a_2 scl + a_3 E_K + a_4 \tau_{Cl} + a_{11} spr^2 + a_{22} scl^2 + a_{33} E_K^2 + a_{44} \tau_{Cl}^2 \\ & + a_{12} spr \cdot scl + a_{13} spr \cdot E_K + a_{14} spr \cdot \tau_{Cl} + a_{23} scl \cdot E_K + a_{24} scl \cdot \tau_{Cl} + a_{34} E_K \cdot \tau_{Cl} \\ & + E_{fast} \end{aligned} \tag{5.3}$$

with a coefficient of determination R^2 of 0.84 in the wakefulness mode and 0.77 in the slow-wave sleep one. In both slow-wave sleep and wakefulness, the most important parameters are the mossy fiber sprouting level *spr* and the sclerosis *scl*, followed by the potassium channel equilibrium potential E_K (see Figure 5.5). The value of f_{fast} also increases with the amplitude of the input A_1, especially under slow-wave sleep settings.

From this study, it seems that the fast ripple oscillations observed in epileptic hippocampus experimentally in wakefulness and slow-wave sleep could be obtained in our model with high

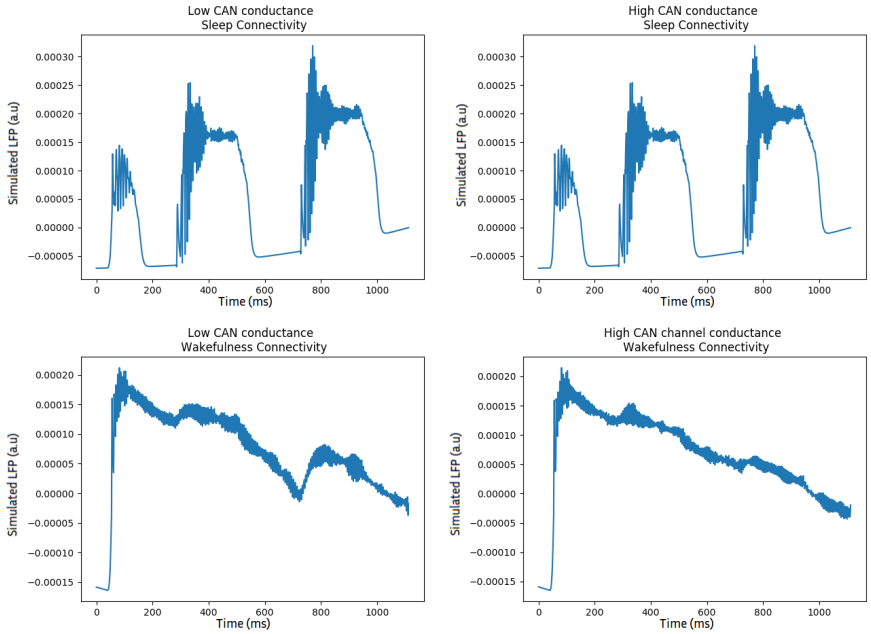

FIGURE 5.3 – Simulated LFP under a square current of amplitude 1nA, with $spr = 1$, $scl = 0.2$, $E_K = -100mV$ and $\tau_{Cl} = 0.01s$, with low or high CAN channel conductance and wakefulness or slow-wave sleep connectivity.

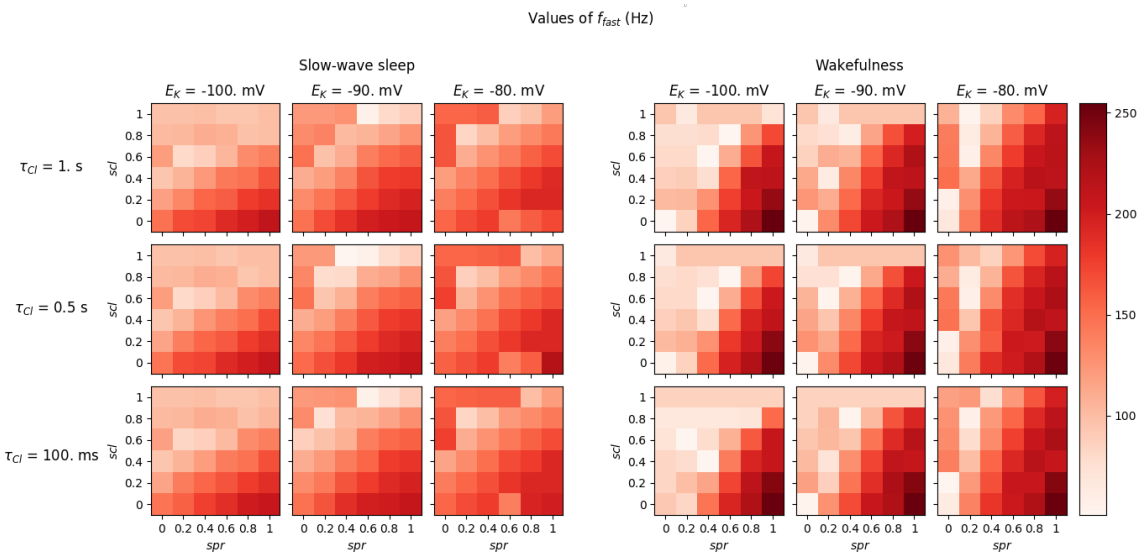

FIGURE 5.4 – Fast oscillation frequency f_{fast} of the simulated LFP for different values of spr, scl, E_K and τ_{Cl} (in Hz). Left : Slow-wave sleep settings. Right : Wakefulness settings. The input stimulation has frequency $f_1 = 2.5Hz$ and amplitude $A_1 = 1.2nA$ for slow-wave sleep and $A_1 = 0.8nA$ for wakefulness.

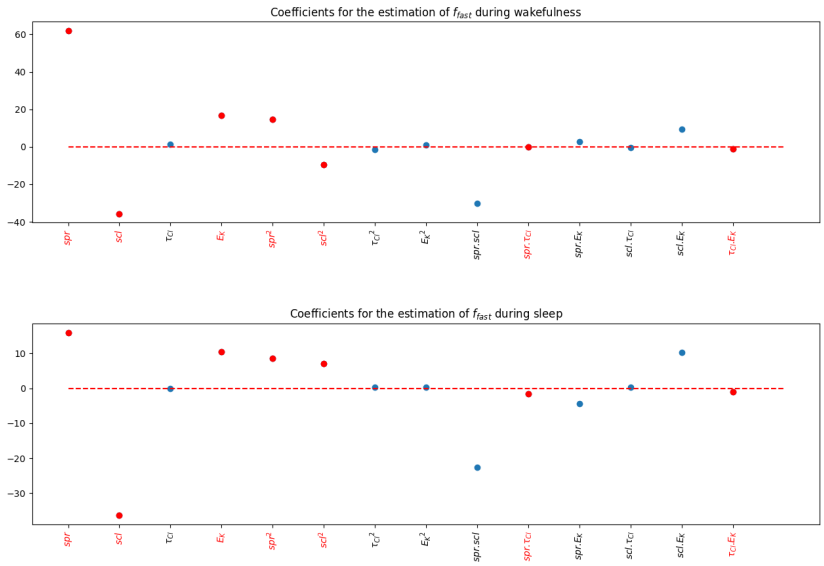

FIGURE 5.5 – Coefficients measuring each parameter's individual, squared or joint influence in the modeling of f_{fast} in the wakefulness and slow-wave sleep mode. The significant coefficients ($p<0.001$) are shown in red.

mossy fiber sprouting level and rather low sclerosis level. An hyperexcitability of the pyramidal neurons (controlled by the parameter E_K) would facilitate such pathological oscillations. As for slower epileptiform patterns such as interictal discharges, these could be obtained more easily with higher sclerosis levels and medium mossy fiber sprouting level. These hypothesis will be tested with realistic inputs in the next section.

It should also be noted that when presented with an input consisting of several stimulations with the same duration and amplitude, the network can respond at different frequencies, as can be seen on Figure 5.6, where the standard deviation of the f_{fast} frequency of the network activity emerging from successive stimulations is shown. This is especially true for intermediate to high values of all four parameters, that is when the network is at the limit between a healthy and a fast pathological behavior. The standard deviation of f_{fast} is also higher in the wakefulness compared to the slow-wave sleep state. Because no parameter was changed between successive stimulations, it is likely that the different oscillatory frequencies result from a different initial state of the network when the stimulation starts.

Epileptic features of the network influence the slow frequency of the oscillations f_{slow} as well, when the network is stimulated with a constant input (Figure 5.7). In particular, high sclerosis and sprouting enable the network to produce oscillations in the theta frequency band under constant input during wakefulness, and even in the alpha or beta band when potassium dynamics are altered. Our results from Chapter 3 indicate that our hippocampal network will respond preferentially (i.e with higher f_{fast} frequency) when stimulated with an input at this f_{slow} frequency, which may then lead to epileptic seizures.

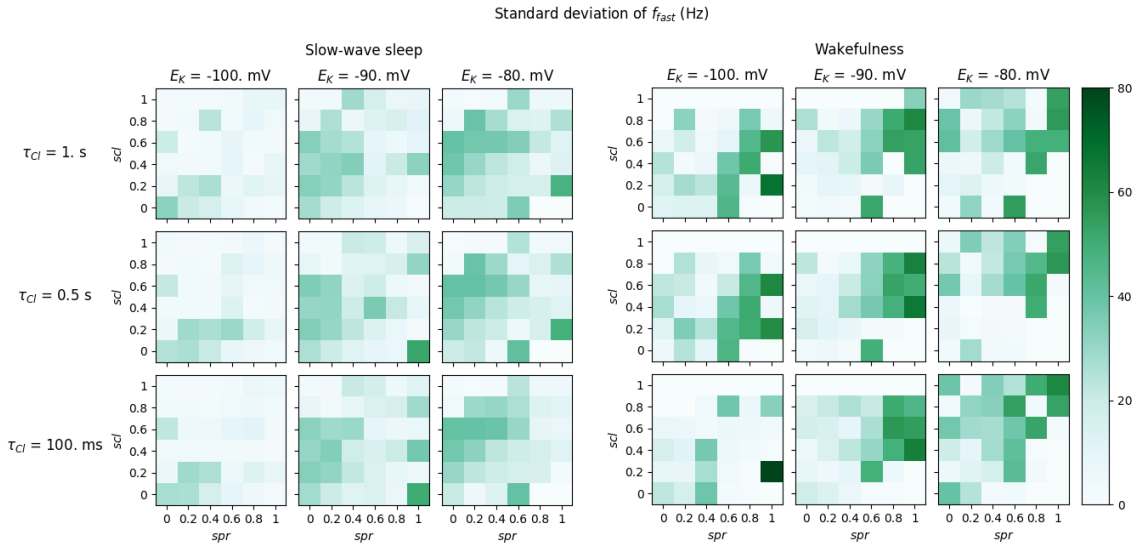

FIGURE 5.6 – Standard deviation of the fast oscillation frequency f_{fast} of the simulated LFP for different values of spr, scl, E_K and τ_{Cl} (in Hz). Left : Slow-wave sleep settings. Right : Wakefulness settings. The input stimulation has frequency $f_1 = 2.5Hz$ and amplitude $A_1 = 1.2nA$ for slow-wave sleep and $A_1 = 0.8nA$ for wakefulness.

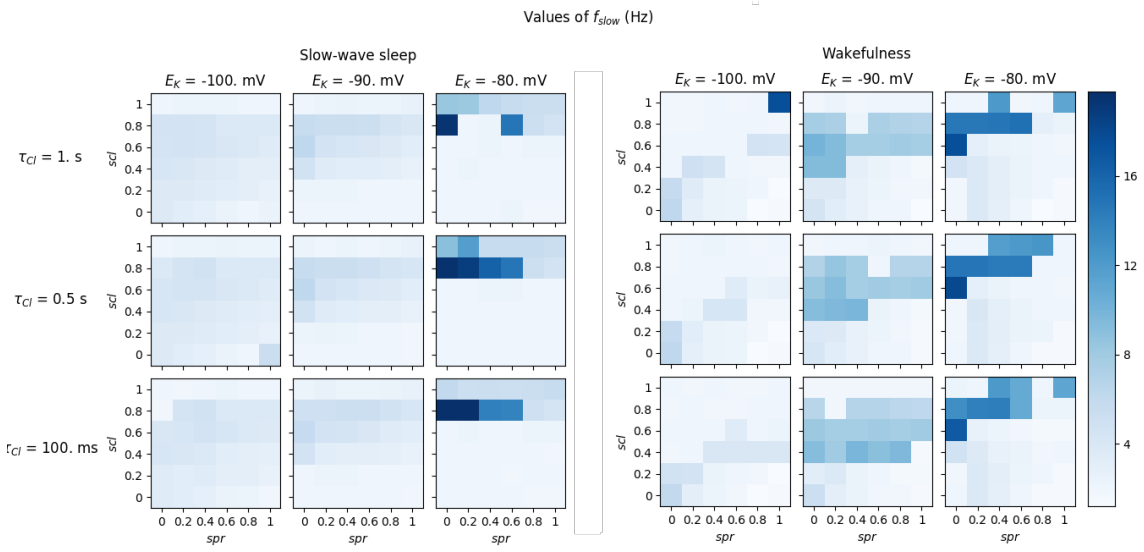

FIGURE 5.7 – Slow oscillation frequency f_{slow} of the simulated LFP for different values of spr, scl, E_K and τ_{Cl} (in Hz). Left : Slow-wave sleep settings. Right : Wakefulness settings. The input stimulation has frequency $f_1 = 0Hz$ and amplitude $A_1 = 0.8nA$.

5.4 Reproduction of epileptiform activity under realistic inputs

We next applied a realistic input to our network as defined in Section 4.3.1. In particular, we chose a portion of signal from an awake patient around a seizure episode for the wakefulness inputs and a portion of signal from another sleeping patient which included interictal discharges for the slow-wave sleep inputs.

5.4.1 Reproduction of seizure-like activity in wakefulness settings

Under wakefulness settings, it is possible for the model to reproduce seizures with similar timing and duration as in clinical measurements, as shown on Figure 5.8 - A, which goes with an increased power in the theta frequency band. Increasing the parameters *spr* or E_K, or decreasing the parameter *scl*, tends to make the seizure in the model last longer or even never stop (though it should be noted that our model does not include any internal seizure termination mechanisms), as well as it increases the amplitude and frequency of the discharges in it, as shown for example on Figure 5.8-B). Choosing parameters closer to a healthy state has the opposite effect, to a point where the seizure disappears. The longer seizures as the one on Figure 5.8-B show a slow increase in their theta band power at the beginning of the seizure similar to that of the real seizure. The seizure-like activity in the simulated LFP occurs when the input stimulation shows an increased power in the theta to beta frequency bands, in accordance with our previous results on stereotypical inputs. No significant change occur in the spectrum of the LFP before the beginning of the seizure.

The total power in the theta band in the whole seizure episode (Figure 5.9) is high for values of *scl* slightly below *spr*, and is strongly reduced at higher sclerosis levels. The neuronal hyperexcitability controlled E_K is slightly increasing the range of the *spr* and *scl* parameters enabling such high power in the theta band, thus making the network more prone to generate epileptiform activity.

Figure 5.10 shows the Peak Signal-to-Noise Ratio (SNR) of the simulated signal, computed here as the ratio of the maximum value to the standard deviation of the (raw) LFP : SNR = $\frac{\max(LFP)}{\mathrm{SD}(LFP)}$. With intermediate values of the parameters, seizures appear with a high SNR, that is with bursts of synchronized activity with an amplitude much higher than the background noise. When the parameters are changed towards a more epileptic state (high *spr*, E_K and τ_{Cl} and low *scl*), the SNR is reduced due to the augmentation of background noise, as synchronized activity becomes more prominent (and the seizure fails to stop), and when parameters are changed towards a healthy state the SNR is also reduced, this time due to the reduction of the maximum amplitude of the signal. The SNR value in the human seizure recordings we used is 9.98, which corresponds to a simulated signal with such intermediate values of the parameters, while the SNR value in the same patient in the contralateral hippocampus outside a seizure episode is 4.9, which is similar to the value of 5.9 obtained in the healthy model (*spr*=0, *scl*=0, E_K=-100mV, and τ_{Cl}=100ms).

5.4.2 Reproduction of interictal spikes and fast ripples in slow-wave sleep settings

Regarding slow-wave sleep settings and inputs, it is possible for the network to produce high amplitude, brief activity peaks similar to interictal discharges (IEDs) as shown on Figure 5.11. These IEDs tend to appear when a healthy network would produce large amplitude, slow oscillations (see Figure 5.12), and they become more numerous as the sclerosis level *scl* is increased

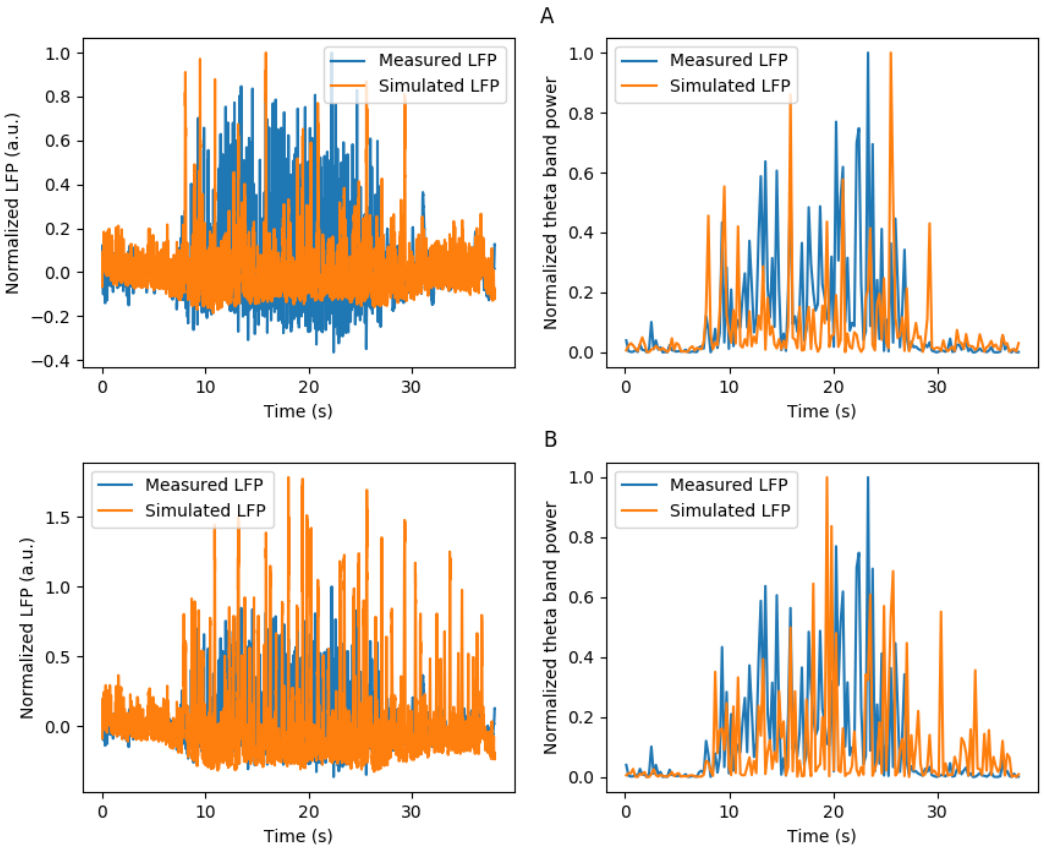

FIGURE 5.8 – Comparison of the measured hippocampal LFP and its theta band power around a seizure in a patient (blue) and the simulated LFP of the model (orange). A- With spr=0.6, scl=0.6, $E_K = -100mV$ and tau_{Cl}=0.1 second. B- With spr=0.6, scl=0.4, $E_K = -100mV$ and tau_{Cl}=0.1 second.

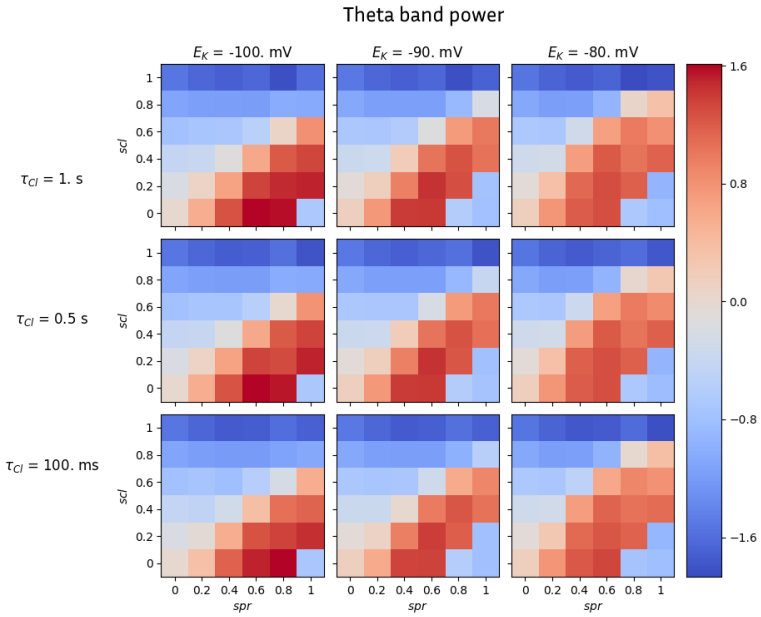

FIGURE 5.9 – Power in the theta band of the simulated LFP, depending on the values of *spr*, *scl*, E_K and τ_{Cl}, with wakefulness settings and input. The values shown are in log-scale, with the zero corresponding to the theta band power in healthy conditions (*spr*=0, *scl*=0, $E_K = -100mV$ and τ_{Cl}=0.1 second).

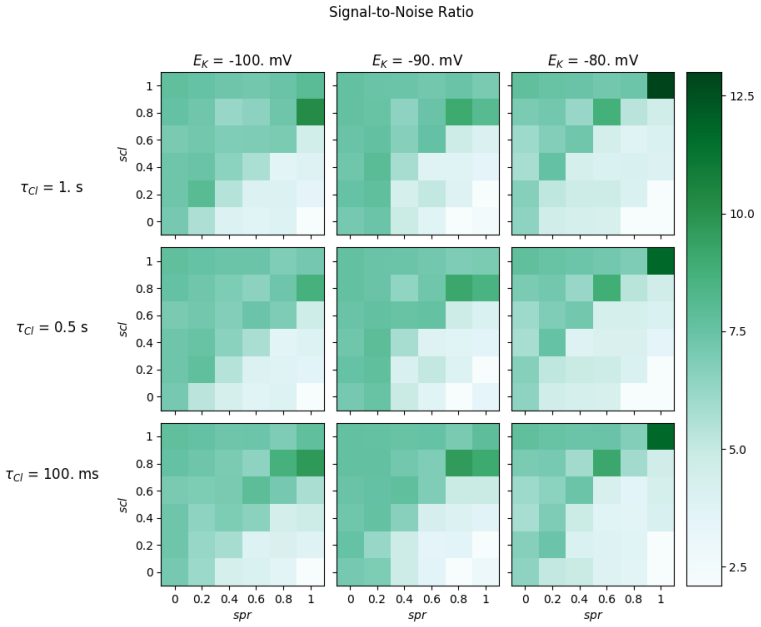

FIGURE 5.10 – Signal-to-Noise Ratio of the simulated LFP, computed as the ratio of the maximum value to the standard deviation of the signal, depending on the values of *spr*, *scl*, E_K and τ_{Cl}, with wakefulness settings and input.

and gets higher than the sprouting level *spr* (Figure 5.13). At high *scl* levels, the number of IEDs is also increased by either high E_K or τ_{Cl}, while it is reduced by the same two parameters in the $spr > scl$ region of the parameter space.

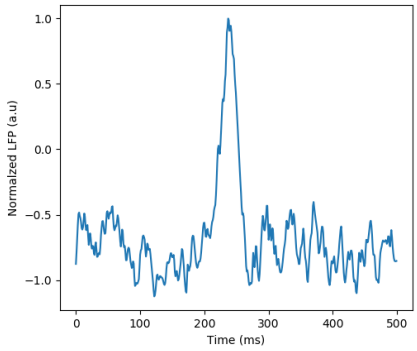

FIGURE 5.11 – Interictal discharge simulated with a network in a slow-wave sleep state with $spr = 0.6$, $scl = 0.6$, $E_K = -90mV$ and $\tau_{Cl} = 500ms$.

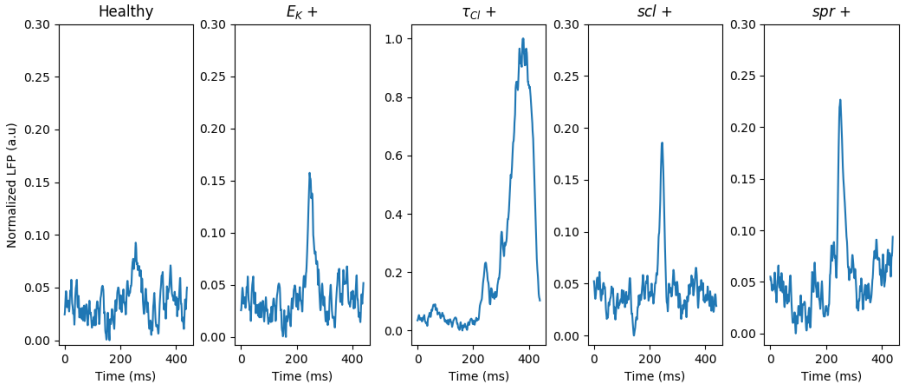

FIGURE 5.12 – Comparison of the LFP generated with a network in a slow-wave sleep state in five different conditions, under the same input stimulation. Healthy state : $spr = 0$, $scl = 0$, $E_K = -100mV$ and $\tau_{Cl} = 100ms$. E_K + state : $spr = 0$, $scl = 0$, $E_K = -90mV$ and $\tau_{Cl} = 100ms$. τ_{Cl} + state : $spr = 0$, $scl = 0$, $E_K = -100mV$ and $\tau_{Cl} = 500ms$. scl + state : $spr = 0$, $scl = 0.2$, $E_K = -100mV$ and $\tau_{Cl} = 100ms$. spr + state : $spr = 0.2$, $scl = 0$, $E_K = -100mV$ and $\tau_{Cl} = 100ms$.

The $spr > scl$ region of the parameter space also promotes the production of oscillations in the fast ripple range (200-500Hz), especially when either E_K or τ_{Cl} are high, as shown on Figure 5.14. In this figure, it should be noted that in the region where $E_K = -80mV$, *spr* is high and $scl = 0$, the network is in a saturated state and therefore no fast ripple events can be detected with our method. The three parameters *spr*, E_K and τ_{Cl} tend to turn physiological sharp-wave ripple complexes into fast ripples, while increased sclerosis reduce their frequency down to the gamma frequency band (see Figure 5.15).

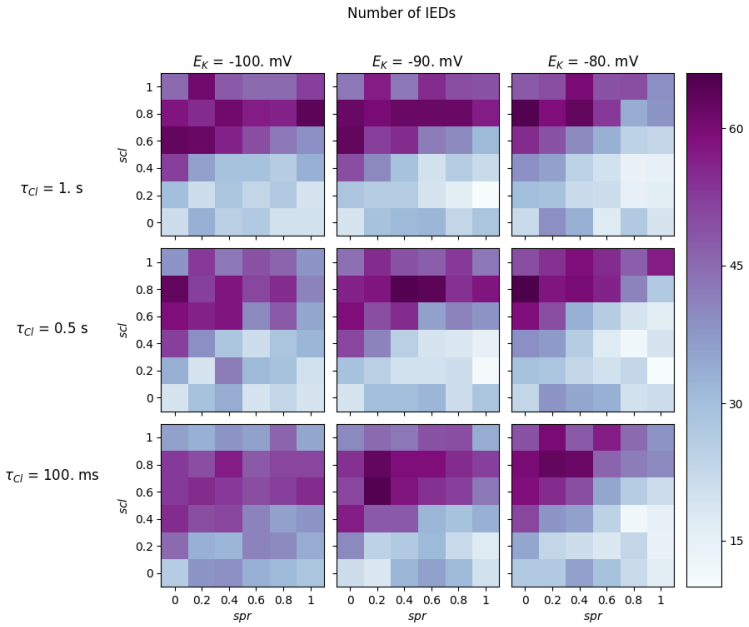

FIGURE 5.13 – Number of interictal discharges obtained with a network in slow-wave sleep state in a one-minute-long simulation for different values of *spr*, *scl*, E_K and τ_{Cl}.

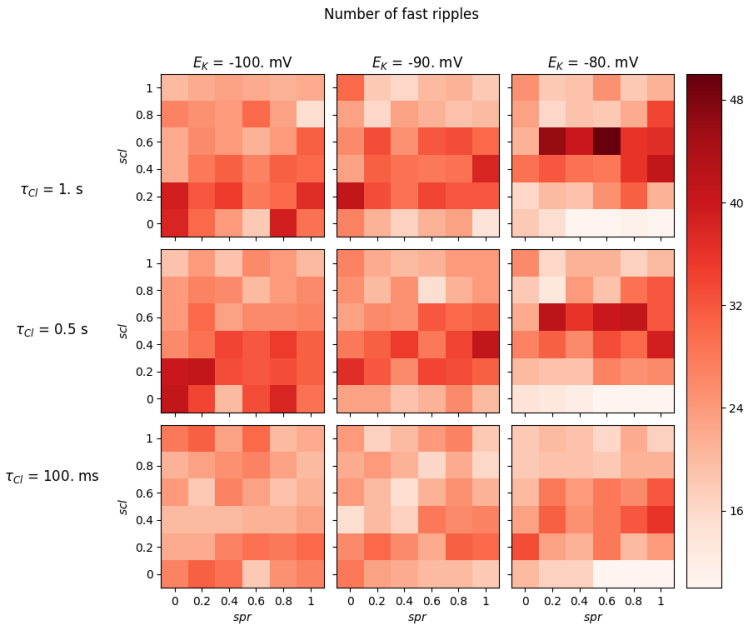

FIGURE 5.14 – Number of fast ripple oscillations obtained with a network in slow-wave sleep state in a one-minute-long simulation for different values of *spr*, *scl*, E_K and τ_{Cl}.

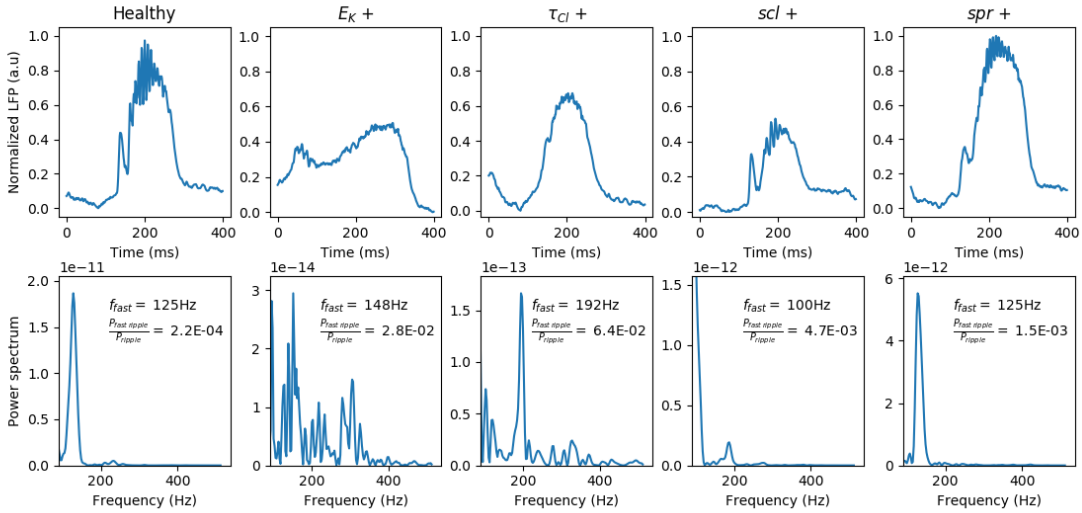

FIGURE 5.15 – Comparison of the activity generated with a network in a slow-wave sleep state in five different conditions, under the same input stimulation generating a sharp-wave ripple like event, in the temporal (top) and frequency domain (bottom). Healthy state : $spr = 0$, $scl = 0$, $E_K = -100mV$ and $\tau_{Cl} = 100ms$. E_K + state : $spr = 0$, $scl = 0$, $E_K = -90mV$ and $\tau_{Cl} = 100ms$. τ_{Cl} + state : $spr = 0$, $scl = 0$, $E_K = -100mV$ and $\tau_{Cl} = 500ms$. scl + state : $spr = 0$, $scl = 0.2$, $E_K = -100mV$ and $\tau_{Cl} = 100ms$. spr + state : $spr = 0.2$, $scl = 0$, $E_K = -100mV$ and $\tau_{Cl} = 100ms$.

5.5 Discussion

In this chapter, we have modified our previously developed hippocampal model so as to take into account four hippocampal abnormalities usually associated with epilepsy, that is hippocampal sclerosis (type I), mossy fiber sprouting, impaired potassium dynamics (leading to neuronal hyperexcitability), and impaired chloride dynamics (leading to impaired inhibition).

A study of the network's behavior under stereotypical inputs reveals that very fast oscillations, as well as paroxistic activity, can now be obtained. The wakefulness state enhances the capacity of the network to produce such saturated state, mostly due to the combined effect of mossy fiber sprouting and cholinergic modulation of synaptic currents. Impaired potassium dynamics also favor such abnormal activities, while hippocampal sclerosis has a rather protective effect.

When stimulated with a realistic input, the network can also reproduce epileptic seizures occurring during wakefulness, as well as interictal spikes and fast ripples occurring during slow-wave sleep. The timing of epileptic seizures in particular is determined by the power in the theta to beta frequency ranges in the stimulation input given to the network.

Epileptic seizures closest to the clinical recordings can be obtained when the degrees of sclerosis and mossy fiber sprouting are balanced. High mossy fiber sprouting with low hippocampal sclerosis leads to perpetual seizure-like activity, while high sclerosis with low sprouting suppresses the seizure. However, it should be noted that the model does not include any mechanism related to seizure termination (such as synaptic depletion for example), and therefore it is probable that high sprouting and low sclerosis could also enable realistic seizures, though longer than with a more balanced set of parameters. Interestingly, impaired potassium and chloride dynamics have little influence on the generation of seizures.

In the model, interictal spikes are more numerous in the presence of hippocampal sclerosis, impaired potassium dynamics or impaired chloride dynamics, but their number is reduced in the case of high mossy fiber sprouting. Fast ripples on the other hand are favored by high sprouting levels along with impaired chloride and potassium dynamics. One possible consequence of these results is that cognitive impairments seen in epileptic patients, and promoted by interictal spikes and fast ripples ([Kleen et al., 2013], [Krauss et al., 1997]), might be reduced by targeting such chloride and potassium mechanisms.

Overall, the $spr = scl$ hyperplane of the parameter space plays a very important role in the production of pathological oscillations. With high spr and scl, it is possible to reproduce realistic seizures, $scl > spr$ increases the number of interictal discharges while $spr > scl$ favors fast ripple oscillations instead. Impaired potassium and chloride dynamics mostly influence the generation of interictal discharges and fast ripples, but not the generation of seizures (at least in the parameter range we studied). Seizures are mostly the result of the abnormal structural connectivity induced by mossy fiber sprouting and modified functional connectivity of wakefulness.

Interestingly, our results suggest that though brain injury is often a cause of acquired epilepsy, the seizures may not be due to the neuronal loss itself, but to the mossy fiber sprouting it induces instead. Further hippocampal sclerosis could then take place to counterbalance mossy fiber sprouting and reduce seizure-like activity.

Chapter 6

Conclusions and Perspectives

This chapter provides a summary of the work described in this manuscript, the main contributions of each section as well as possible extensions that could be done in future works.

6.1 General conclusions

The hippocampus can exhibit different oscillatory rhythms within the sleep-wake cycle, each of them being involved in cognitive processes. For example, theta-nested gamma oscillations, consisting of the coupling of theta (4-12Hz) and gamma (40-100Hz) rhythms, are produced during wakefulness and are associated with spatial navigation and working memory tasks ([O'Keefe and Recce, 1993], [Axmacher et al., 2010]), whereas Sharp-Wave-Ripple (SWR) complexes, consisting of fast (120-200Hz) oscillatory events occurring during low frequency waves (≤ 0.5Hz), are produced during slow-wave sleep and quiet waking and play an important role in memory consolidation ([Girardeau and Zugaro, 2011], [Buzsáki, 2015]). Models exist to reproduce and explain the generation of each of these rhythms individually : for Sharp-Wave Ripples, see [Taxidis et al., 2012] or [Traub and Bibbig, 2000] and for theta-nested gamma oscillations, see [Pastoll et al., 2013], [Fukai, 1999], or [Bartos et al., 2007]. However, the mechanisms of generation and transition between all of these rhythms are not yet fully understood.

This question is all the more important that altered hippocampal rhythms are involved in drug-resistant mesial temporal lobe epilepsy, a form of epilepsy affecting about 0.6 person per 1000 people ([Asadi-Pooya et al., 2017]) and which cannot be controlled by existing pharmaceutical treatments. As for physiological rhythms, some models have also been previously developed to reproduce epileptic seizures (episodes of excessive neural activity, see the review from [Stefanescu et al., 2012]) or interictal discharges (brief peaks of synchronous activity, see for example [Demont-Guignard et al., 2009]), but these models cannot fully explain the links between neuropathological conditions of the hippocampus, physiological processes such as the sleep-wake cycle, and the resulting oscillations.

In this context, the main objective of this thesis was to provide better understanding of various hippocampal oscillations, both physiological and pathological, including theta-nested gamma oscillations, sharp-wave ripple complexes, epileptic seizures and interictal spikes. We did so by developing a computational model of the hippocampus regrouping many mechanisms previously described in separate works, and analyzing its oscillatory activity as we varied different parameters representing either structural or functional properties of the network, as well as pathological modifications typically observed in epilepsy, using well-defined techniques such as Design of Experiments and Sobol' analysis to quantitatively evaluate the importance of each

parameter. The model also includes a simulation of the Local Field Potential (LFP) generated by the neurons, so as to be comparable with clinical recordings.

Our results suggest that the network connectivity is crucial to control the frequency of hippocampal fast oscillations in particular. Moreover, regarding epilepsy, we showed that mossy fiber sprouting could have a strong epileptogenic effect, while hippocampal sclerosis could be rather protective. More details on the different parts of this work are given below. Overall, our work provides new insights into the mechanisms underlying the generation of various hippocampal oscillations, which could pave the way to future clinical applications.

6.2 Building of a healthy hippocampus model

6.2.1 Contributions

In the first part of our work, we designed a full model of the hippocampal formation including the entorhinal cortex, the dentate gyrus and the CA3 and CA1 regions, with in total more than thirty thousand Hodgkin-Huxley point neurons. This model includes a LFP estimation as measured by a macroscopic sEEG electrode so as to be more easily interpretable, obtained with a direct problem approach by considering each pyramidal neuron as a current dipole.

Our model was made biologically plausible by relying on existing literature on the anatomy and electrophysiological properties of the hippocampus. In particular, the position of the neurons as well as the connection probabilities within each hippocampal region was reproduced, which we later showed was important to reproduce its rhythms.

However, due to the model complexity, a lot of parameters needed to be tuned in order to obtain realistic behavior. Therefore, we performed a thorough study of the network's activity as a function of our parameters through a design of experiment method and a sobol' global sensitivity analysis method, and used this analysis to deduce the most appropriate parameters to reproduce either sleep or wakefulness typical oscillations.

In order to investigate the role of the input, we then studied how this hippocampal model responds to stereotypical inputs. In particular, we showed that under slow-wave sleep conditions, the network responds preferentially to inputs in the delta range, where it is able to generate sharp-wave ripple oscillations. Furthermore, under both slow-wave sleep or wakefulness conditions, the frequency of the slow oscillations of the network mostly follows that of the input, showing for example that a stimulation with at least a component in the theta band is needed to obtain this type of oscillations.

6.2.2 Future work

Improving the LFP estimation

The LFP approximation in our model relies on the hypothesis that each excitatory neuron can be seen as a current dipole, with the current source located at the soma and the sink located in the stratum moleculare at the neuron's supposed apical dendrites location, even though its dynamics are simulated only with point Hodgkin-Huxley equations. This approach has the advantage of not requiring too much computational resource, but a more accurate approximation of the LFP could be obtained by replacing the point excitatory neurons in our model by compartmental ones, more or less detailed.

Furthermore, our LFP approximation only takes into account synaptic currents, and not all membrane currents arising from neurons' action potentials. As we model the LFP seen by sEEG

electrodes inserted directly into the hippocampus, and therefore very close to some neurons, the contribution of action potentials might be significant ([Schomburg et al., 2012]), especially in highly synchronized activity like epileptic spikes and seizures. To address this issue, we started to work in collaboration with Harry Tran from the CRAN to develop a hybrid model of LFP where hippocampal dynamics and spike timings would be simulated with our model before being used to compute action potentials signatures in a more complex framework mimicking multi-compartmental neurons. A poster was presented at the CNS conference 2019 in Barcelona about this work, which is reproduced in Appendix A along with its abstract. The inclusion of action potentials in our LFP approximation could reveal other appropriate parameter choices for the generation of fast oscillations such as sharp-wave ripple complexes in particular.

Detailing or reducing the hippocampal model

Further knowledge of hippocampal oscillations could also be gained by either detailing or reducing our current network model.

On the one hand, our model could be made even more realistic, provided that enough computational resources are available, for example by adding more complex ion channel dynamics, different neuron types (as in [Santhakumar et al., 2005] or [Demont-Guignard et al., 2009]), as well as modeling the different layers of each region of the hippocampus and entorhinal cortex with their own structural and functional connectivity. Also, it could be interesting to add gap junctions (as in [Traub et al., 1999]) or ephaptic coupling to the regular synaptic interactions in the network to study their influence on the resulting hippocampal rhythms and fast oscillations in particular, as these mechanisms could induce neural synchrony at high frequency.

On the other hand, simplifying the neuron model could help study and predict the network behavior mathematically, and going through the process of model reduction could also help identify the key mechanisms that are necessary for the generation of each type of oscillations. Some work was done in this direction during and following our Master thesis, where we studied the activity of a simple ring-shaped Hopfield neural network (see Appendix B), and which we then started to extend so as to study the interaction of several ring populations.

6.3 Modeling of the hippocampus sleep-wake cycle

6.3.1 Contributions

After having defined the model and its sleep and wakefulness modes, we compared its activity under realistic input stimulation with intracranial recordings obtained in epileptic patients outside of seizure episodes and free from interictal discharges. Our model was able to reproduce both theta-nested gamma oscillations, typical of the awake state, and sharp-wave ripple complexes, typical of slow-wave sleep, with temporal and frequential similarities with the measured sEEG signals.

We linked the modification of some parameters of the network, that is the conductance of the CAN ion channels and the synaptic conductances, with cholinergic modulation, and showed how single neuron dynamics are mostly involved in the determination of the slow oscillations of the network (and the transition from delta to theta frequency band), while network functional connectivity influences both its slow and fast oscillations (and the transition from gamma to ripples).

Our results, published in [Aussel et al., 2018], also indicate that the reproduction of realistic hippocampal oscillations, and especially sharp-wave ripple complexes, can only be done with

realistic structural and functional connectivity patterns in the model. Gap junctions on the other hand are not needed to obtain fast oscillations in the ripple frequency band, in accordance with [Taxidis et al., 2012].

All the Python source files used for building our healthy hippocampus model and running the simulations are accessible on the ModelDB public repositories.

6.3.2 Future work

Adding explicit cholinergic inputs

Our model includes cholinergic modulation through their indirect effect on functional connectivity and CAN channel dynamics, however it could also be interesting to model the concentration of Acetylcholine explicitly and add cholinergic inputs from the medial septum to the network.

In particular, it would make our modeling of the wakefulness state more accurate. Making synaptic and CAN channel properties vary following a theta rhythm characteristic of awake septal inputs, instead of being fixed, could make the resulting oscillations change significantly. Acetylcholine can also have an excitatory effect on neurons that we did not take into account in this work.

Studying REM sleep and the transitions between sleep phases

Another interesting research direction could be to study hippocampal oscillations in other sleep stages, such as REM sleep or lighter stages of NREM sleep.

This could be done for example by introducing other neurotransmitters effects to the model, like serotonin or norepinephrine, whose concentration in the hippocampus vary within the sleep-wake cycle differently from acetylcholine ([Hasselmo, 1999]). The transitions between waking and sleep and between sleep stages could also be studied from our model by gradually changing the concentrations of these three (or more) neurotransmitters. It could then be useful to add the thalamocortical loop to our model.

Linking oscillatory rhythms to memory

The main hippocampal function usually associated with the sleep-wake cycle is the formation of short-term memories and their consolidation into long-term memory. Though this work was only focusing on the generation of sleep-wake oscillatory rhythms, as our collaborators from the CHRU Nancy now started to record signals from epileptic patients during and after spatial-like memory tasks, our model may be extended to study some aspects of memory function.

For example, it could be interesting to add synaptic plasticity dynamics to our network and study how they could affect the shape and timing of theta-gamma and sharp-wave ripple oscillations, in interaction with the cholinergic modulation currently present in the model, and see whether it would be possible to observe some replay of wakefulness activation patterns during slow-wave sleep ([Buzsáki, 2015]). Similarly, memory impairments could be studied from our model as altered hippocampal rhythms.

6.4 Modeling of the epileptic hippocampus

6.4.1 Contributions

We developed our model further to include four typical pathological modifications of the hippocampus seen in mesial temporal lobe epilepsies, that is hippocampal sclerosis ([Blümcke et al., 2013]), mossy fiber sprouting ([Noebels et al., 2012]), impaired potassium dynamics ([Lerche et al., 2012], [Coulter and Steinhauser, 2015]), and impaired chloride dynamics in pyramidal neurons (and its influence on inhibition, [Huberfeld et al., 2007]). Similarly to our sleep-wake cycle study, these modifications involve both network connectivity and single neuron dynamics. It should be noted that our "healthy" model of the hippocampus was unable to reproduce pathological outputs.

Following a similar methodology as for the healthy hippocampus, we first analyzed our model's behavior under stereotypical inputs, and studied how these four modifications can induce instability or modify oscillatory frequency. We also showed that the specific functional connectivity of wakefulness induced by cholinergic modulation could make this state more vulnerable to epilepsy-associated damage.

We then applied realistic stimulation to the network and were able to reproduce hippocampal seizure timing and duration with an appropriate choice of parameters under wakefulness settings, and interictal spikes and fast ripples under slow-wave sleep settings.

Our results suggest that mossy fiber sprouting is the main factor inducing epileptic seizure, which reinforces the idea that epilepsy is a "network disease", while hippocampal sclerosis shows a rather protective effect, but increases the variability in hippocampal response. Hippocampal sclerosis, though often at the origin of acquired epilepsy, would not be the cause of seizures themselves, but instead these would be caused by the mossy fiber sprouting induced by neuronal loss. Potassium and chloride dynamics have little influence on the generation of seizures, but increase the number of interictal discharges and fast ripples produced by the network, and thus could be involved in the cognitive impairments usually associated with hippocampal epilepsy.

6.4.2 Future work

Modeling the effect of antiepileptic drugs

Anti-epileptic drugs used to reduce seizures each have an effect on specific ion channels or synaptic receptors ([Chindo et al., 2016]), which could be included in our model's Hodgkin-Huxley dynamics.

Such work could make it possible to study the effectiveness of a drug depending on the four parameters characterizing an epileptic hippocampus in our model, thus helping to find out the types of patient it is the most likely to treat, or providing insights on the effect of new treatments before starting clinical trials.

Studying the propagation of seizures and ripples to other brain regions

Another main aspect of epilepsy that we did not study in this work is the propagation of seizures from the seizure onset zone to other brain regions.

For now, our model only includes the hippocampus and entorhinal cortex regions, but it would be possible to model an additional one, for example a cortical column, and study the conditions needed for an epileptic spike or seizure occurring in the hippocampus to cause pathological oscillations in this region too.

Hippocampo-cortical coupling in general could be an interesting direction to explore, as it has been shown to be involved in memory consolidation ([Maingret et al., 2016]), and its alteration is a cause of memory impairments in epilepsy ([Gelinas et al., 2016]). The issue of detecting and quantifying hippocampo-cortical coupling on human sEEG measurements has been investigated by Iris Dumeur, student at the Ecole des Mines de Nancy, during a student research project, and could be used to validate the model.

Studying other hippocampal pathologies

Finally, we have seen in the different parts of this work that our hippocampal network can generate many different oscillatory patterns. Here, we focused only on patterns related to the sleep-wake cycle and epilepsy, but information on other pathological rhythms could also be inferred from the simulations we performed when exploring the parameter space. It would also be possible to include other hippocampal abnormalities in the model so as to study other illnesses, such as Alzheimer's disease for example.

Annex A

Hybrid modeling of LFP

Extracellular synaptic and action potential signatures in the hippocampal formation: a modeling study

Amélie Aussel[1,2,3], Harry Tran[2,3], Laure Buhry[1,3], Steven Le Cam[2,3], Louis Maillard[2,4], Sophie Colnat-Coulbois[2,3,4], Valérie Louis-Dorr[2,3], and Radu Ranta[2,3]

[1]LORIA - UMR CNRS 7503 INRIA, [2]CRAN - UMR CNRS 7039, [3]Université de Lorraine, [4]Centre Hospitalier Universitaire de Nancy

Introduction

Local Field Potentials (LFPs) recorded with micro and/or macro-electrodes include a mixture of low frequency patterns, mainly attributed to the synaptic currents (SCs) and high-frequency components reflecting action potentials (APs) activity.

Simulating a realistic LFP is often based on detailed neural models and requires a high computational burden [1], but it is necessary to study phenomenons where the fast and slow components of neural activity are equally important, such as hippocampal oscillations [2].

In this work we propose a hybrid model to simulate large scale neural networks efficiently while computing a realistic approximation of the LFP signal including both SCs and APs signatures. We apply this method on a hippocampal network [3] and use it to infer their relative contributions on human intracranial measurements.

Methods

Simulation process :

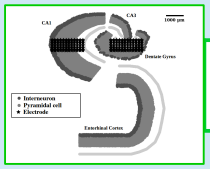

Computational model with simplified neuron morphology → LFP_SC

Raster plot

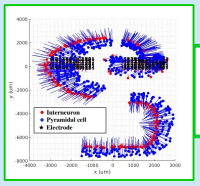

Extracellular Action Potentials model based on geometrical filtering and HH dynamics → LFP_AP

LFP_full=α LFP_AP+β LFP_SC

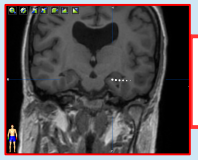

Comparison of the spectrums of the generated LFP and intracranial LFP measurement

More details on the computational model [3] :

- ≈30000 single compartment Hodgkin-Huxley neurons
- Realistic topology and connectivity of the hippocampus
- Able to reproduce sleep and wakefulness oscillatory patterns through cholinergic modulation

More details on the AP LFP model [4] :

- Mimicks multicompartmental neurons
- Extracellular action potentials obtained with a morphological filtering taking into account the neuron geometry and relative positions to the electrodes.
- Action potential signatures are convoluted with the raster plot obtained in the previous step

Final simulated LFP :

- Weighted average of SC and AP contributions over the surface of two sEEG electrodes
- Realistic intracranial recordings settings : 2 cylindrical contacts, 2mm-long, diameter 0.8mm, sampled with a regular grid

Results

We computed the difference between the spectrum of the real and simulated LFPs for different values of α and β in four frequency bands : delta (1-4Hz), theta (4-10Hz), gamma (30-100Hz) and ripple (120-250Hz)

During wakefulness : typical rhythms are theta and gamma. Theta oscillations are mostly due to SCs while gamma are mostly explained by APs.

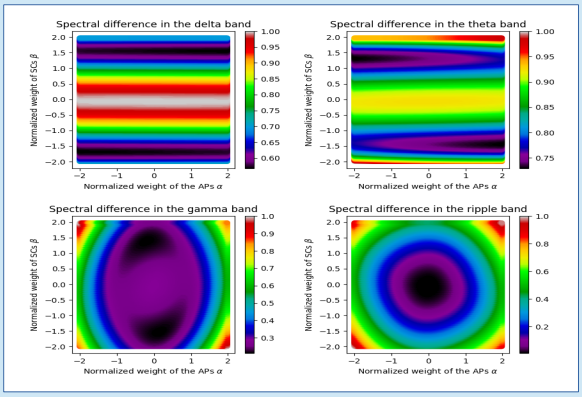

During slow-wave sleep : typical rhythms are delta and ripples. Delta oscillations only depend on SCs but ripples involve both APs and SCs.

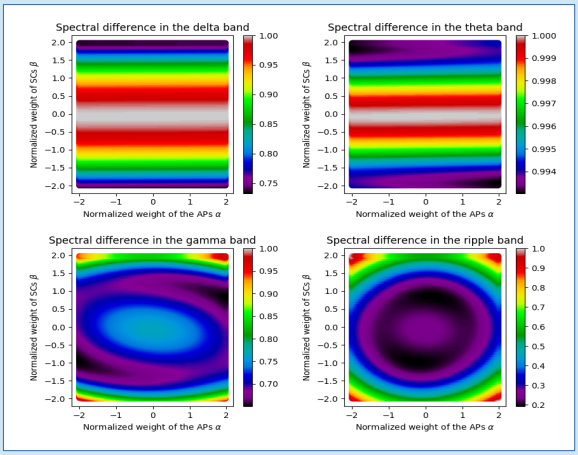

Conclusions

In this work, we present and analyze a computationally efficient way of calculating LFPs.

We show the importance of considering both action potentials and synaptic currents contributions to the LFP, even at rather low frequencies such as theta and gamma.

Our results suggest that, depending on the oscillatory pattern studied, these contributions could be balanced differently to better reproduce experimental findings.

References

[1] Einevoll GT, et al. Modelling and analysis of local field potentials for studying the function of cortical circuits. Nat. Rev. Neuroscience, 14(11), 770, 2013

[2]Schomburg EW, Anastassiou CA, Buzsáki G, Koch C. The spiking component of oscillatory extracellular potentials in the rat hippocampus. J Neurosci. 32(34):11798-811, 2012

[3] A. Aussel et al. A detailed anatomical and mathematical model of the hippocampal formation for the generation of sharp-wave ripples and theta-nested gamma oscillations. J Comput Neurosci 45: 207. https://doi.org/10.1007/s10827-018-0704-x, 2018

[4]H.Tran et al. Simulating extracellular signatures of actions potentials using single compartments neurons and geometrical filtering. In the 27th Computational Neuroscience Conf, Seattle, USA, 2018

Extracellular synaptic and action potential signatures in the hippocampal formation: a modelling study

Amélie Aussel[1,2], Harry Tran[1], Laure Buhry[2], Steven Le Cam[1], Louis Maillard[1,3], Sophie Colnat-Coulbois[1,4], Valérie Louis-Dorr[1], and Radu Ranta[1]

[1] Université de Lorraine, CNRS, CRAN, F-54000 Nancy, France

[2] Université de Lorraine, CNRS, Inria, LORIA, F-54000 Nancy, France

[3] Université de Lorraine, CHRU-Nancy, Service de neurologie, F-54000, France

[4] Université de Lorraine, CHRU-Nancy, Service de neurochirurgie, F-54000, France

Introduction

Simulating extracellular recordings of neuronal populations is a challenging task for understanding the nature of extracellular field potentials (LFPs), investigating specific brain structures and mapping cognitive functions. In general, it is assumed that extracellular recording devices (micro and/or macro-electrodes) record a mixture of low frequency patterns, mainly attributed to the synaptic currents and high-frequency components reflecting action potentials (APs) activity. Simulating such signals often require a high computational burden due to the multicompartmental neuron models used [1]. Therefore, different LFP proxies coexist in the litterature, most of them only reproducing some of the features of experimental signals [2]. This may be an issue in producing and validating computational models of phenomenons where the fast and slow components of neural activity are equally important, such as hippocampal oscillations [3]. In this work, we propose an original approach for simulating large scale neural networks efficiently while computing a realistic approximation of the LFP signal including both synaptic and action potentials extracellular signatures. We apply this method on a hippocampal network [4] and compare the simulated signal with intracranial measurements made on human patients.

Methods

Computational model. The first step of our method consists in simulating an anatomical and functional realistic hippocampal network, using the macroscopic hippocampal anatomy. The modelled hippocampal formation includes four of its areas (CA1, CA3, dentate gyrus and the entorhinal cortex) and contains more than 32.000 neurons placed in an anatomically realistic manner to be able to simulate various fast and slow oscillations rhythms. The neurons inside each of the 4 regions were simulated with minimal LFP producing morphologies (2 compartments, approximated thus by a dipole). Each neuron' dynamics was modelled using Hodgkin-Huxley type equations (a specific Calcium-Activated-Nonspecific / CAN channel was added for simulating a richer dynamics). The connections within and between the modelled régions d regions were set according to the available neurobiological literature or tuned in order to obtain realistic outputs (various fast and slow oscillatory rhythms, such as theta-nested gamma oscillations and sharp-wave ripple complexes). For details of this model, see [4].

The input of the model was modelled as a random (Poisson) process with variable intensity (firing rate). This intensity / firing rate was extracted from the enveloppes of real depth EEG recordings from cerebral areas projecting onto the Entorhinal cortex of human epileptic patients (recorded during presurgical evaluation in the Neurology Service of the Nancy University Hospital - CHU Nancy).

The output of the model was the LFP generated by the network on an sEEG electrode, to be compared with real depth intrahippocampal sEEG signals (see Figure 1 for the localization of the electrodes). It is described in more details in the next section.

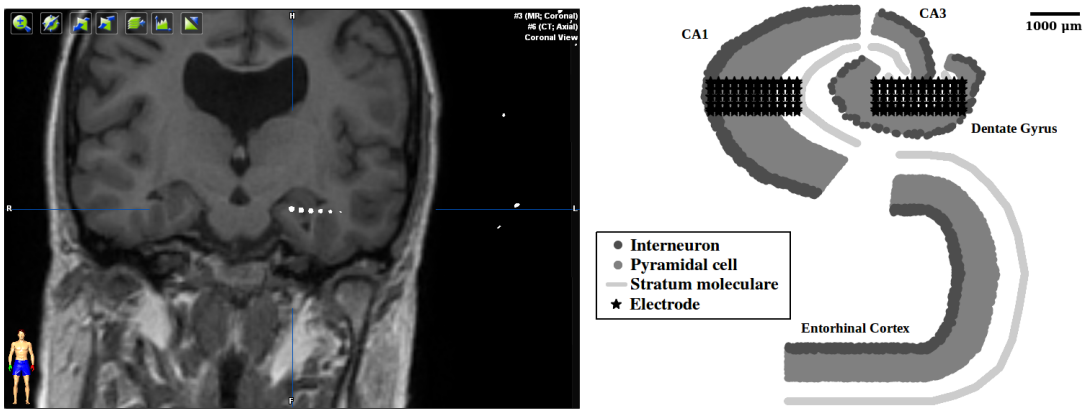

Figure 1 : Left - Coregistered CT-MRI image of the implantation of an SEEG electrode in the patient's hippocampus (coronal view). Right - Topology of the modeled hippocampal network.

LFP model. Realistic simulations of LFP imply compartmental neuron models with detailed morphologies. For a large population, these simulations are time consuming and need powerful computers. We propose to use a simpler approach. First, we modelled the extracellular potentials as a sum of synaptic and action potential related currents, assumed to be the main contributors [5]. Next, the contribution of synaptic currents was obtained by considering each pyramidal neuron as a fixed current dipole (between soma and dendrites). The generated electrical potentials (LFP) were computed at specific points in space, corresponding to the extracellular electrode positions, assuming that the propagation medium is homogeneous isotropic. We focused on the pyramidal neurons contributions, significantly higher than those of interneurons [2].

Concerning the extracellular waveforms of the action potentials, a realistic simulation might take into account several factors, such as the presence and density of specific ion channels for every compartment, the neuron morphology and the electrode position in relation to it [6]. Indeed, for compartmental models, the potential recorded by an extracellular electrode is a weighted sum of the membrane currents of all compartments, the weights depending on the medium conductivity and the distances between each compartment and the electrode (thus on the neuron geometry). For our population, we used the simplified model proposed previously [7] which consists of a lumped soma attached to an axon subdivided into fixed-length compartments. With this type of morphology, one can obtain the extracellular action potentials (EAP) using a fast morphological filtering approach [7]. The coefficients of the filter depend on the neuron morphology. Here, the axon diameter is set to 2 um for both types excitatory and inhibitory neurons and its length is 1000 um for the former and 400 um for latter. The axons of both populations for each hippocampus regions were oriented in a realistic manner. Having obtained the EAPs for every neuron, we next generated the total population contribution for each electrode by convolving the EAPs of each neuron with the raster plot given by the computational model described in the previous section and summing up.

The final simulated LFP, recorded by a finite electrode size, was obtained by a weighted average of synaptic and EAP contributions over the surface of the sEEG electrodes, sampled using a regular grid of 288 points.

Results and conclusions

To evaluate the how realistic our model is, we compared the frequency properties of our simulated signal and one recorded at the CHRU Nancy in an awake patient's hippocampus, presenting theta and gamma waves (see Figure 2 below). More precisely, we computed the norm of the difference between the real and simulated signal spectra on different frequency bands. By choosing a pair of weights balancing the contributions of the action potentials and the synaptic currents (called w_{AP} and w_{syn} respectively), it is possible to adapt our model so that it specifically reproduces either theta or

gamma oscillations.

It should be noted that though action potentials and synaptic currents play a similar role in determining the LFP in the gamma band, it is not true for lower frequencies, where the action potentials contribution is less significant.

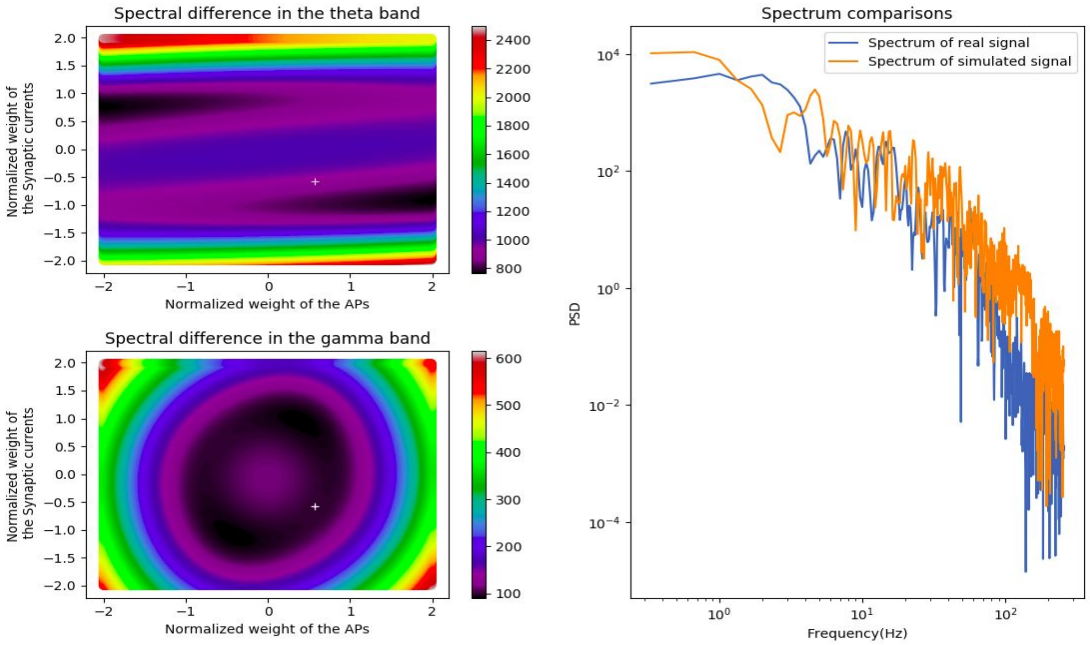

Figure 2 : Left - Observed difference in the frequency domain between the real and simulated signals, with varying contributions of the action potentials and synaptic currents, in the theta band (top) and gamma band (bottom). Right - Power spectrum of the real and simulated signals after optimal weighting of the AP and synaptic contributions to the LFP (w_{AP}=-$w_{syn,}$ white dot on the left images)

Overall, this work shows the importance of considering both action potentials and synaptic currents contributions to the LFPs, even in rather low frequency bands (such as gamma), while presenting a computationally efficient way of calculating them.

References :

[1] Einevoll GT, et al. **Modelling and analysis of local field potentials for studying the function of cortical circuits**. *Nat. Rev. Neuroscience*, 14(11), 770, 2013

[2] Mazzoni A, Lindén H, Cuntz H, Lansner A, Panzeri S, et al. **Computing the Local Field Potential (LFP) from Integrate-and-Fire Network Models**. *PLOS Computational Biology* 11(12): e1004584. https://doi.org/10.1371/journal.pcbi.1004584, 2015

[3] Schomburg EW, Anastassiou CA, Buzsáki G, Koch C. **The spiking component of oscillatory extracellular potentials in the rat hippocampus**. *J Neurosci*. 32(34):11798-811, 2012

[4] A. Aussel et al. **A detailed anatomical and mathematical model of the hippocampal formation for the generation of sharp-wave ripples and theta-nested gamma oscillations**. *J Comput Neurosci* 45: 207. https://doi.org/10.1007/s10827-018-0704-x, 2018

[5] Buzsáki G, Anastassiou CA, Koch C. **The origin of extracellular fields and currents--EEG, ECoG, LFP and spikes.** *Nat Rev Neuroscience*, 13(6):407-20, 2012

[6] Gold, C., et al. **On the origin of the extracellular action potential waveform: a modeling study**. *Journal of neurophysiology*. 95: 3113–3128, 2006

[7] H.Tran et al. **Simulating extracellular signatures of actions potentials using single compartments neurons and geometrical filtering**. In the *27th Computational Neuroscience Conf,* Seattle, USA, 2018

Annex B

On the stability of Hopfield neural networks

Before we started building a detailed model of the hippocampus including Hodgkin-Huxley neurons, we first performed a short work related to the stability of rate models such as those used to represent head-direction cells.

This work, though not directly related to the scope of our thesis, was published as a full length conference article at the IEEE Conference on Decision and Control 2017, which is reproduced thereafter.

Stability conditions of Hopfield ring networks with discontinuous piecewise-affine activation functions*

Amelie Aussel[1], Laure Buhry[2] and Radu Ranta[3]

***Abstract*— Ring networks, a particular form of Hopfield neural networks, can be used in computational neurosciences in order to model the activity of place cells or head-direction cells. The behaviour of these models is highly dependent on their recurrent synaptic connectivity matrix and on individual neurons' activation function, which must be chosen appropriately to obtain physiologically meaningful conclusions.**

In this article, we propose some simpler ways to tune this synaptic connectivity matrix compared to existing literature so as to achieve stability in a ring attractor network with a piecewise affine activation functions, and we link these results to the possible stable states the network can converge to.

I. INTRODUCTION

In the hippocampus and the entorhinal cortex, some neurons, such as place cells, grid cells and head-direction cells, are capable of firing at different rates depending on an animal's position ([10]). When organized in a network, these cells function as a "cognitive map" of one's environment, providing the basis of spatial orientation skills, but are also involved in short-term memory, as they can encode spatial information and retain it for some time even when all external stimuli are removed.

Different computational models have been developed to represent these structures, for examples see [9], mainly based on Hopfield-like neural networks ([4]). In Hopfield neural networks, each neuron's activity s_k is computed from the weighted sum of the activity of all the N neurons of the network, through an activation function ϕ. As the synaptic decay of biological neurons is known to have an exponential shape, we have the following differential equation:

$$\dot{s}_k = -\frac{1}{\tau}s_k + \phi(\sum_{i=0}^{N-1} w_{ki}s_i + b_k) \tag{1}$$

or, in a matrix format:

$$\dot{\mathbf{s}} = -\frac{1}{\tau}\mathbf{s} + \phi(\mathbf{W}\mathbf{s} + \mathbf{b}) \tag{2}$$

where $\mathbf{W}$ is called the (recurrent) synaptic connectivity matrix, τ is a synaptic time constant and $\mathbf{b}$ is the external input provided to the system (see [11]). The term $\mathbf{W}\mathbf{s} + \mathbf{b}$ can be interpreted as the total synaptic input received by the neurons, and the term $\phi(\mathbf{W}\mathbf{s} + \mathbf{b})$ as their firing rates (the number of action potentials they emit in one second).

In the first studies of the latter model, the synaptic connectivity matrix $\mathbf{W}$ was symmetric, and the activation function ϕ was $\mathcal{C}^1$ and strictly increasing (often a sigmoid function), which ensured the convergence of the system to a stable point for any stimulation $\mathbf{b}$ (as shown in [5]). However, when some of these constraints were lifted in order to account for more realistic networks, the stability analysis of the model became a much more complicated task (for a review, see [13]). In particular, a few authors have studied Hopfield-like neural networks with non-$\mathcal{C}^1$ activation functions ϕ, in order to establish the conditions for a unique stable point to exist (for example see [1]).

In [3], a necessary and sufficient condition for the stability of a system with a non-$\mathcal{C}^1$ activation functions ϕ was presented. More precisely, with $\phi(x) = \max(x, 0)$ it was shown that the system converges to an equilibrium point for all constant b and all initial conditions, if and only if the matrix $(\frac{1}{\tau}\mathbf{I} - \mathbf{W})$ is copositive; that is, $\mathbf{x}^T(\frac{1}{\tau}\mathbf{I} - \mathbf{W})\mathbf{x} > 0$ for all nonnegative $\mathbf{x}$, except $\mathbf{x} = \mathbf{0}$.

However, it is not clear how to apply this reasoning for a more complex activation function ϕ. Also, the copositivity of a matrix is not something easy to ensure when tuning the connectivity matrix $\mathbf{W}$. In addition, it provides no information about the form of the solution at the stable points.

Our point is that some other stability conditions can be obtained, which may be weaker than those developed in [3], but are also easier to verify when choosing the synaptic connectivity matrix $\mathbf{W}$. These conditions take advantage of the periodic structure that can be imposed on $\mathbf{W}$, when considering place cells or head-direction cells.

Indeed, because networks made of these cells have to be able to encode a continuum of positions, the associated model should also present a continuum of stable points, and such a continuous attractor dynamics is often achieved by choosing a synaptic connectivity matrix with some kind of periodicity (see [9]). This structure is coherent with experimental results, as it has been observed that hippocampal neurons are highly interconnected and tend to form associative networks (see [7]).

In Section II of the present article, we will detail the model we used, a ring-shaped, Hopfield-like neural network with a

*This work was not supported by any organization

[1]Amelie Aussel is with the Centre de Recherche en Automatique de Nancy (CRAN-CNRS UMR 7039 University of Lorraine, FRANCE), and the Laboratoire Lorrain de Recherche en Informatique et ses applications (LORIA UMR 7503, University of Lorraine-INRIA-CNRS, F-54506). amelie.aussel@loria.fr

[2]Laure Buhry is with the Laboratoire Lorrain de Recherche en Informatique et ses applications (LORIA UMR 7503, University of Lorraine-INRIA-CNRS, F-54506). laure.buhry@loria.fr

[3]Radu Ranta is with the Centre de Recherche en Automatique de Nancy (CRAN-CNRS UMR 7039 University of Lorraine, FRANCE). radu.ranta@univ-lorraine.fr

piecewise affine activation function ϕ, then we will present the results we obtained regarding its stability of the form of its stable states in Section III. Finally, in Section IV we will show how these results can apply on a simulation of a network with a gaussian synaptic connectivity matrix.

II. DEFINITION OF THE RING NETWORK MODEL

A. Network dynamics

We studied the stability of a network consisting of N identical neurons, which activity $\mathbf{s}$ followed the dynamics (2) with an activation function ϕ defined by:

$$\phi(x) = \begin{cases} \alpha x + \beta & if \quad x \geq 0 \\ 0 & if \quad x < 0 \end{cases} \tag{3}$$

where α and β are positive real constants.

The stimulation $\mathbf{b}$ is chosen strictly positive and uniform on all neurons ($\forall k \in [\![0; N-1]\!], b_k = b$).

This definition of ϕ ensures that neuronal firing rates are always positive, and it also represents the fact that neurons can only fire if the total input they receive is greater than a certain threshold. With $\alpha > 0$ and $\beta = 0$, the function ϕ represents the behaviour of type-I neurons (capable of firing at frequencies close to zero when excited with stimulus just above their threshold), and with $\alpha > 0$ and $\beta > 0$, it represents the behaviour of type-II neurons (that have a minimal firing rate).

It can be shown from equations (2) and (3) that, whatever the initial conditions, the network activity $\mathbf{s}$ will always become and remain non-negative after a certain amount of time, and therefore, for simplicity reason, we will only consider non-negative $\mathbf{s}$.

With our definition of the activation function ϕ (equation (3)), each neuron can follow two distinct linear differential equations, depending on the input it receives:

- On the one hand, if a neuron k receives an input that is greater than or equal to zero, it will be called "excited" and follow the equation: $\dot{s}_k = -\frac{1}{\tau} s_k + \alpha \sum_{i=0}^{N-1} w_{ki} s_i + \alpha b + \beta$
- On the other hand, if it receives an input that is less than zero, it will be called "inhibited" and follow the equation: $\dot{s}_k = -\frac{1}{\tau} s_k$

Therefore, at any instant t, our whole network can be described by one of 2^N different linear systems depending on which neurons are excited or inhibited. We can then consider our model as a switched system in the form:

$$\dot{\mathbf{s}}(t) = \left(-\frac{1}{\tau} \mathbf{I}_N + \alpha \mathbf{P}_{\Sigma(t)} \mathbf{W} \right) \mathbf{s}(t) + \mathbf{P}_{\Sigma(t)} (\alpha b + \beta) \mathbf{1} \tag{4}$$

where $\mathbf{I}_N$ is the identity matrix of size N-by-N, $\mathbf{1}$ is the N-by-1 all-ones vector and $\mathbf{P}_{\Sigma(t)}$ is a diagonal N-by-N matrix containing ones at indexes corresponding to the excited neurons at the instant t and zeros elsewhere.

B. The ring structure condition

In order to model structures such as head-direction cells, we considered ring-shaped, rotation invariant networks, which imposed some constraints on the synaptic connectivity matrix $\mathbf{W}$.

Each neuron was assigned a position so that they were all uniformly distributed on a circle: for k in $[\![0; N-1]\!]$ the angular position of neuron k was $\theta_k = -\pi + \frac{2k\pi}{N}$. Then, because all neurons were identical (same time constant τ, same activation function ϕ), the rotation invariance was obtained by connecting all neurons to their neighbours identically. In other words, the synaptic interaction between any two neurons does not depend on their position on the ring, but only on the angular distance between them ($w_{ij} = f(\theta_i - \theta_j)$). This imposes that $\mathbf{W}$ is Toeplitz. So that there was no discontinuity for $\theta_i - \theta_j = k\pi$, $\mathbf{W}$ was even chosen circulant (which means that any line of $\mathbf{W}$ can be obtained as a right-shift a the previous one).

We also chose to keep $\mathbf{W}$ symmetric, which means that the function f is even, and that the synaptic interaction associated with an angular distance is the same whether we go clockwise or anti-clockwise. Our synaptic connectivity matrix is therefore of the form:

$$\mathbf{W} = \begin{pmatrix} w_0 & w_1 & w_2 & \cdots & w_2 & w_1 \\ w_1 & w_0 & w_1 & \cdots & w_3 & w_2 \\ w_2 & w_1 & w_0 & \cdots & w_4 & w_3 \\ \vdots & & & \ddots & & \\ w_2 & w_3 & w_4 & \cdots & w_0 & w_1 \\ w_1 & w_2 & w_3 & \cdots & w_1 & w_0 \end{pmatrix} \tag{5}$$

The elements of $\mathbf{W}$ are all real values, but they can be either positive or negative. A positive coefficient represents an excitatory synapse and a negative one represents an inhibitory synapse.

C. Connectivity matrix and submatrices eigenvalues

In order to analyze the stability of the system in the next section, we had to determine the eigenvalues of the matrix $\mathbf{A}_\Sigma = (-\frac{1}{\tau}\mathbf{I}_N + \alpha \mathbf{P}_\Sigma \mathbf{W})$ for all possible matrices $\mathbf{P}_\Sigma$, as defined in II.

Let us consider a matrix $\mathbf{P}_\Sigma$ with k zeros along its diagonal (so that it corresponds to a system with k inhibited neurons), and let us consider $\mathbf{A}_\Sigma = (-\frac{1}{\tau}\mathbf{I}_N + \alpha \mathbf{P}_\Sigma \mathbf{W})$ and $\mathbf{A}_0 = (-\frac{1}{\tau}\mathbf{I}_N + \alpha \mathbf{W})$. The matrix $\mathbf{P}_\Sigma \mathbf{W}$ is obtained by replacing by zeroes all the k lines of $\mathbf{W}$ that corresponds to inhibited neurons. Therefore, as it is also explained in [3], by developing the determinant of $\mathbf{A}_\Sigma$ along these lines, we find that $\mathbf{A}_\Sigma$ has k eigenvalues equal to $-\frac{1}{\tau}$, and the other are the eigenvalues of the matrix $\tilde{\mathbf{A}}_\Sigma$, obtained by removing the rows and columns of $\mathbf{A}_0$ corresponding to inhibited neurons.

Because $\mathbf{W}$ is a real symmetric matrix, it is noteworthy that $\tilde{\mathbf{A}}_\Sigma$ is also a real symmetric matrix and therefore all the eigenvalues of the system are real. Moreover, we can infer from [6] (Cauchy interlacing theorem) that the eigenvalues of $\tilde{\mathbf{A}}_\Sigma$ all lie between the minimum and the maximum of the eigenvalues of $\mathbf{A}_0$.

As $\mathbf{W}$ is also circulant, its eigenvalues can be calculated as the discrete Fourier transform of its first row's coefficients: for all m in $[\![0; N-1]\!]$, the corresponding eigenvalue λ_m of $\mathbf{W}$ is equal to:

$$\lambda_m = \sum_{n=0}^{N-1} w_n e^{\frac{2mni\pi}{N}} \tag{6}$$

And the corresponding eigenvalue of $\mathbf{A}_0$ is:

$$\mu_m = \alpha\lambda_m - \frac{1}{\tau} \tag{7}$$

In the next section, we will now present our results regarding the stability of the system defined here, as well as the possible stable states it can reach.

III. STABILITY ANALYSIS

A. Form of the stable states

All the stable states of the system presented in section II can be seen as the equilibrium point of one of the subsystems defined by a combination of excited and inhibited neurons Σ:

$$\left(-\frac{1}{\tau}\mathbf{I}_N + \alpha\mathbf{P}_\Sigma\mathbf{W}\right)\mathbf{s} + \mathbf{P}_\Sigma(\alpha b+\beta)\mathbf{1} = \mathbf{0} \tag{8}$$

The equilibrium points of the different subsystems can be easily obtained.

The equilibrium point $\mathbf{s}_0$ of the subsystem with $\mathbf{P}_\Sigma = \mathbf{0}$ (all neurons inactive) is

$$\mathbf{s}_0 = \mathbf{0} \tag{9}$$

The equilibrium point $\mathbf{s}_{cons}$ of the subsystem with $\mathbf{P}_\Sigma = \mathbf{I}_N$ (all neurons active) is a state on which all neurons share the same activity, due to the circulant property of $\mathbf{W}$:

$$\mathbf{s}_{cons} = \frac{\alpha b+\beta}{\frac{1}{\tau}-\alpha\lambda_0}\mathbf{1} \tag{10}$$

The equilibrium point $\mathbf{s}^\Sigma$ of a system with $\mathbf{P}_\Sigma \neq \mathbf{I}_N, \mathbf{P}_\Sigma \neq \mathbf{0}$ (at least one active and one inactive neuron) verifies:

- For all inhibited neuron k, $s_k^\Sigma = 0$.
- As for the excited neurons, $\tilde{\mathbf{s}}^\Sigma = \tilde{\mathbf{A}}_\Sigma^{-1}(\alpha b+\beta)\mathbf{1}$ where $\tilde{\mathbf{s}}^\Sigma$ is the vector obtained by deleting all the elements corresponding to inhibited neurons from $\mathbf{s}^\Sigma$.

However, not all the equilibrium points of the different subsystems are also stable points for the whole system. For example, the state defined by $\mathbf{s}_0 = \mathbf{0}$ is the equilibrium point of the subsystem when all neurons are inactive, but it is not a stable point of the whole system, as is this state $\dot{\mathbf{s}}_0 = -\frac{1}{\tau}\mathbf{s}_0 + \phi(\mathbf{W}\mathbf{s}_0 + \mathbf{b}) = (\alpha b+\beta)\mathbf{1} \neq \mathbf{0}$ (because $b, \alpha > 0$, and $\beta \geq 0$).

In fact, an equilibrium point $\mathbf{s}^\Sigma$ of a subsystem defined by Σ is a stable point for the whole system if and only if it verifies:

$$\forall k \text{ active in } \Sigma,\ \mathbf{s}_k^\Sigma > 0 \text{ and } \mathbf{W}_k\mathbf{s}^\Sigma + \mathbf{b} \geq 0 \tag{11}$$

$$\forall k \text{ inactive in } \Sigma,\ \mathbf{s}_k^\Sigma = 0 \text{ and } \mathbf{W}_k\mathbf{s}^\Sigma + \mathbf{b} < 0 \tag{12}$$

where $\mathbf{W}_k$ denotes the k_{th} line of $\mathbf{W}$.

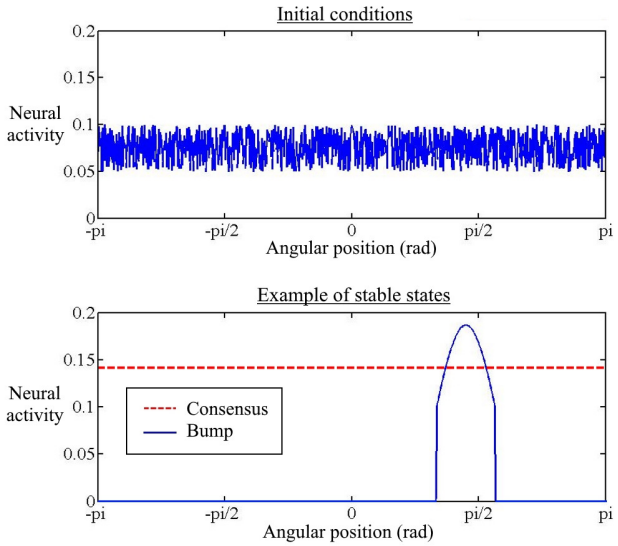

Fig. 1. Example of the two types of stable points for ring networks, achieved from the same initial conditions with two different synaptic connectivity matrices. Top plot: Initial conditions. Bottom plot: two stable states - consensus (red dashed line), and bump (blue solid line).

In this section, we will focus on the two following forms of the stable points of the whole system:

Definition 1: A stable state of the system is called a consensus if all the neurons share the same non-zero activity. A stable state which is not a consensus is called a bump.

An example of consensus and bump are shown on Fig.1.

It can be easily checked that the only possible consensus of the system is the state $\mathbf{s}_{cons}$ defined previously ((10)).

As ring network models are generally used to encode information in the form of localised activity around some angular position, we want to achieve an equilibrium point which is not a consensus.

B. Sufficient condition for stability

In [3], a necessary and sufficient condition for the stability of the system was presented. More precisely, with our notations and with $\beta = 0$, it can be shown that:

Theorem 1: The following statements are equivalent:

1) All positive eigenvectors of all submatrices of $-\mathbf{A}_0$ have positive eigenvalues.
2) The matrix $-\mathbf{A}_0$ is copositive; that is, $\mathbf{x}^T(-\mathbf{A}_0)\mathbf{x} > 0$ for all nonnegative $\mathbf{x}$, except $x = 0$.
3) For all constant b and all initial conditions, the dynamics converge to an equilibrium point.

However, we could not apply this reasoning with $\beta > 0$, and even with $\beta = 0$, the copositivity of the matrix $-\mathbf{A}_0$ is not something easy to ensure when tuning the connectivity matrix $\mathbf{W}$. What's more, it provides no information about the form of the solution at the stable points.

Then, let us first propose a sufficient condition for the stability of the system.

Theorem 2: If all the eigenvalues of $\mathbf{W}$ are strictly less than $\frac{1}{\alpha\tau}$, then the system converges to an equilibrium point,

for all constant b and all initial conditions. Under these conditions, the consensus $\mathbf{s}_{cons}$ is an equilibrium point of the system if and only if $\lambda_0 \geq -\frac{b}{\beta\tau}$.

Proof: Let us suppose that the connectivity matrix $\mathbf{W}$'s eigenvalues verify:

$$\forall m \in [\![0; N-1]\!], \lambda_m < \frac{1}{\alpha\tau}$$

Then all the eigenvalues μ_m of $\mathbf{A}_0$ are strictly negative. This also implies that all the possible matrices $\mathbf{A}_\Sigma = -\frac{1}{\tau}\mathbf{I}_N + \mathbf{P}_\Sigma\mathbf{W}$ defining our systems are negative definite. The function $V(\mathbf{x}) = \mathbf{x}^T\mathbf{x}$ is then a common Lyapunov function for all our subsystems, as we have $\mathbf{A}_\Sigma^T + \mathbf{A}_\Sigma$ negative definite for all possible $\mathbf{A}_\Sigma$. This ensures that the system converges to an equilibrium point, for all constant b and all initial conditions.

Let us now prove that in that case, the consensus $\mathbf{s}_{cons}$ is an equilibrium point of the system if and only if we also have $\lambda_0 \geq -\frac{b}{\beta\tau}$.

Let us consider a network that verifies $\forall m \in [\![0; N-1]\!], \lambda_m < \frac{1}{\alpha\tau}$, and the state $\mathbf{s}_{cons}$ in which for all neuron, the neural activity is equal to:

$$s_{cons} = \frac{\alpha b + \beta}{\frac{1}{\tau} - \alpha\lambda_0} > 0 \tag{13}$$

We can compute for each neuron k ($k \in [\![0; N-1]\!]$):

$$\mathbf{W}_k\mathbf{s}_{cons} + b = \left(\sum_{i=0}^{N-1} w_{ik}s_i\right) + b = s_{cons}\left(\sum_{i=0}^{N-1} w_{ik}\right) + b$$

As $\mathbf{W}$ is circulant, we have $\forall k \in [\![0; N-1]\!]$, $\sum_{i=0}^{N-1} w_{ik} = \lambda_0$. Therefore:

$$\mathbf{W}_k\mathbf{s}_{cons} + b = s_{cons}\lambda_0 + b = \frac{b + \beta\tau\lambda_0}{1 - \alpha\tau\lambda_0}$$

As explained in III-A, this state is a stable state for the system if and only if $\mathbf{W}_k\mathbf{s}_{cons} + b \geq 0$ for all k. Therefore the state $\mathbf{s}_{cons}$ is a stable state of the system if and only if $\lambda_0 \geq -\frac{b}{\beta\tau}$. ■

Summarizing this subsection, we have proposed a conservative sufficient for stability ($\lambda_i < 1/(\alpha\tau),\ \forall\ i$) corresponding to region 1 in figure 2 (splitted in two subregions depending on the type of equilibrium point). Moreover, we have defined strict necessary and sufficient conditions for the existence of a stable consensus (region 1a).

The next subsections partially tighten the stability conditions for the other possible equilibirum (bump), both analytically (subsection C) and numerically (section IV).

C. Necessary condition for stability

In this section we will prove the following statement:

Theorem 3: If $\lambda_0 \geq \frac{1}{\alpha\tau}$ then at least one neuron's activity diverges to infinity, for all constant b and all initial conditions (we will say that the system diverges).

Such a network, with neural activity that diverges to infinity, is of course highly unrealistic, so the region $\lambda_0 \geq \frac{1}{\alpha\tau}$ should be avoided when choosing the synaptic connectivity matrix.

Proof: From the definition of the activation ϕ (equation (3)), because α and β are positive, it is clear that:

$$\forall x \in \mathbb{R}, \phi(x) \geq \alpha x$$

Therefore, we can write the following inequality:

$$\sum_{k=0}^{N-1} \dot{s}_k \geq \sum_{k=0}^{N-1}\left(-\frac{1}{\tau}s_k + \alpha(\sum_{i=0}^{N-1} w_{ki} * s_i + b_k)\right) \tag{14}$$

Also, because the synaptic connectivity matrix $\mathbf{W}$ in circulant, we can show that:

$$\sum_{k=0}^{N-1}\sum_{i=0}^{N-1} w_{ki} * s_i = \left(\sum_{i=0}^{N-1} w_i\right)\left(\sum_{k=0}^{N-1} s_k\right) = \lambda_0\left(\sum_{k=0}^{N-1} s_k\right)$$

Then, we can deduce from (14) that:

$$\sum_{k=0}^{N-1} \dot{s}_k \geq \left(-\frac{1}{\tau} + \alpha\lambda_0\right)\left(\sum_{k=0}^{N-1} s_k\right) + N\alpha b$$

As all the neuronal activities s_k are positive, and the stimulation b is strictly positive, if the connectivity matrix $\mathbf{W}$ is such that $\lambda_0 \geq \frac{1}{\alpha\tau}$, at any given time we will have $\sum_{k=0}^{N-1} \dot{s}_k > 0$ which means that the system will diverge to infinity. ■

The eigenvalue λ_0 therefore plays a key role in the behaviour of the system, as it provides a necessary condition for stability of the system as well as necessary and sufficient condition for the existence of a consensus. As this eigenvalue is obtained from the sum of synaptic weights, it can be interpreted in terms of balance between excitation and inhibition in the network: stronger excitatory connections in the network (which increase λ_0) tend to make the network diverge, whereas stronger inhibitory connections (which decrease λ_0) tend to stabilize it and promote localized activity, as could be expected.

D. What about the remaining case ?

We will now focus on the case that was not addressed before, that is when $\mathbf{W}$ has at least one eigenvalue which is greater than $\frac{1}{\alpha\tau}$ and $\lambda_0 \leq \frac{1}{\alpha\tau}$.

Under these conditions, we could not find any more specific results regarding the stability of the system than those stated in Theorem 1, but we addressed the issue of the form of the solution when the system converges to an equilibrium point.

If $\lambda_0 \geq -\frac{b}{\beta\tau}$, as we also have $\lambda_0 \leq \frac{1}{\alpha\tau}$, then it can be easily shown that the consensus defined by $\mathbf{s}_{cons} = \frac{\alpha b+\beta}{\frac{1}{\tau}-\alpha\lambda_0}\mathbf{1}$ is an equilibrium point of the system (with a similar reasoning as in the proof for Theorem 2). However, as $\mathbf{W}$ has at least one eigenvalue that is strictly greater than $\frac{1}{\alpha\tau}$, it implies that $\mathbf{A}_0$ has at least one eigenvalue which is strictly greater than 0, and so this consensus is an unstable fixed point.

Therefore, when the system converges to an equilibrium point, if the initial state was not $\mathbf{s} = \mathbf{s}_{cons}$ with $\mathbf{s}_{cons}$ as defined in (10), or if $\lambda_0 \leq -\frac{b}{\beta\tau}$ then this equilibrium point must be a bump.

IV. APPLICATION WITH A GAUSSIAN SYNAPTIC CONNECTIVITY MATRIX

In order to verify our results, as well as tighten our stability conditions for the case $\lambda_0 \leq \frac{1}{\alpha\tau}$ but $\exists i \neq 0, \lambda_i > \frac{1}{\alpha\tau}$, we focused on studying a network in which the function used to generate the synaptic connectivity matrix $\mathbf{W}$ was known, and performed numerical simulations. Note that plausible synaptic connectivity matrices will usually have one mode (connection weights decrease monotonically with the distance). In this case, λ_1 will be the highest eigenvalue (corresponding to the lowest non null frequency revealed by the Fourier transform), which makes it possible to analyze the stability of the system regarding this eigenvalue only.

More precisely, the synaptic connectivity matrix $\mathbf{W}$ was built from a gaussian function as follows:

$$\begin{aligned} &\forall i \in [\![0; N-1]\!], \forall j \in [\![0; N-1]\!], \\ &\quad w_{ij} = f(\theta_i - \theta_j) + \mu \\ with \quad f : x \longmapsto &\begin{cases} e^{-\frac{x^2}{2\sigma^2}} & if \quad x \neq 0 \\ 0 & if \quad x = 0 \end{cases} \end{aligned} \tag{15}$$

This connectivity represents a ring in which all neurons are excitatory, with an excitatory synaptic interaction f decreasing as a gaussian of width σ with distance. Because neurons usually don't send synapses to themselves, the excitatory synaptic interaction is equal to zero for $i = j$. The presence of inhibitory interneurons with a uniform action on the network is represented by introducing effective inhibition as a global shift of $\mu < 0$ of the synaptic connectivity, as suggested in [2]. The connectivity matrix $\mathbf{W}$ can then be tuned by chosing only the two parameters σ and μ appropriately.

The parameters of the network were chosen as follows: N=1000, τ=10ms, α=2, β=10, b=1. The initial state of the network was chosen randomly, and the differential equations were solved using Euler method with a time step of 0.5ms.

All the simulations were performed using Matlab (MATLAB 8.1, The MathWorks Inc., Natick, MA, 2000).

With this synaptic connectivity matrix, for a large N, the eigenvalues of $\mathbf{W}$ can be approximated using the error function defined by $\text{erf}(x) = \frac{1}{\sqrt{\pi}} \int_{-x}^{x} e^{-t^2}\ dt$. More precisely, we have:

$$\lambda_0 \approx (N-1)\mu + \frac{N\sigma}{\sqrt{2\pi}} \text{erf}\left(\frac{\pi}{\sigma\sqrt{2}}\right) \tag{16}$$

and, among all the other eigenvalues of $\mathbf{W}$, the largest one is always:

$$\begin{aligned} \lambda_1 \approx \frac{N\sigma}{2\sqrt{2\pi}} e^{-\sigma^2} \Bigg(&\text{erf}\left(\frac{\pi}{\sigma\sqrt{2}} + i\frac{\sigma}{\sqrt{2}}\right) \\ &+ \text{erf}\left(\frac{\pi}{\sigma\sqrt{2}} - i\frac{\sigma}{\sqrt{2}}\right)\Bigg) + \mu \end{aligned} \tag{17}$$

We could then define the behaviour of the system in the following regions, depending on σ and μ:

- Region 1a ($\lambda_0 < \frac{1}{\alpha\tau}$, $\lambda_1 < \frac{1}{\alpha\tau}$ and $\lambda_0 \geq -\frac{b}{\beta\tau}$): the system converges to a consensus.

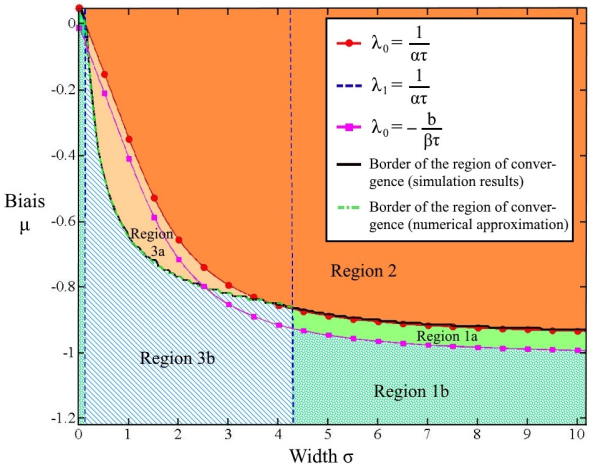

Fig. 2. Stability analysis of a neural network with a Gaussian connectivity matrix of parameters σ and μ. Red circled line: $\lambda_0 = \frac{1}{\alpha\tau}$; Blue dashed line: $\lambda_1 = \frac{1}{\alpha\tau}$; Magenta squared line: $\lambda_0 = -\frac{b}{\beta\tau}$; Black line: Border of the region of convergence, as obtained in simulations; Green dash-dot line: Border of the region of convergence, as predicted numerically.

- Region 1b ($\lambda_0 < \frac{1}{\alpha\tau}$, $\lambda_1 < \frac{1}{\alpha\tau}$ and $\lambda_0 < -\frac{b}{\beta\tau}$): the system converges to a bump.
- Region 2 ($\lambda_0 \geq \frac{1}{\alpha\tau}$): the system diverges to infinity.

As for Region 3, characterized by $\lambda_0 < \frac{1}{\alpha\tau}$ and $\lambda_1 \geq \frac{1}{\alpha\tau}$, even though we could not obtain theoretical results, we used numerical methods to predict the stability of the network as well as the exact form of the solution.

To do this for a given matrix $\mathbf{W}$, we considered all the different combinations of active and inactive neurons Σ on the ring (with regard to the rotation invariance of the network), such that $\tilde{\mathbf{A}}_\Sigma$ was negative definite (with $\tilde{\mathbf{A}}_\Sigma$ as defined in II-C). For each of these Σ, we computed the theoretical state $\mathbf{s}^\Sigma$ in which the network would be if it were to stabilize with active and inactive neurons as defined by Σ:

- for each inactive neuron k, $\mathbf{s}^\Sigma_k = 0$
- $\tilde{\mathbf{s}}^\Sigma = \tilde{\mathbf{A}}_\Sigma^{-1}(\alpha b + \beta)\mathbf{1}$, with $\tilde{\mathbf{s}}^\Sigma$ the vector obtained by selecting only the indices corresponding to active neurons in $\mathbf{s}^\Sigma$.

We then checked the nullity of $\dot{\mathbf{s}}^\Sigma$.

When no Σ could be found for which $\dot{\mathbf{s}}^\Sigma = 0$, we concluded that the network defined by $\mathbf{W}$ was unstable (Region 3a), whereas on the other case, we listed the possible forms in which the network could stabilize (Region 3b).

In Region 3b, our observations were that only one form of solution could be stable for a given matrix $\mathbf{W}$, and this form always corresponded to a Σ where all active neurons were grouped together on the ring, thus forming a single bump of activity on the ring.

With our simulations, we could then confirm our theoretical predictions and complement our numerical observations (as summed up in Fig.2):

- In Region 1a, the system converges to a consensus.
- In Region 1b, the system converges to a bump.
- In Region 2, the system diverges to infinity.
- In Region 3a, the system diverges to infinity.
- In Region 3b, the system converges to a bump of the predicted form.

In order to build a network that will converge to a bump, one should then choose the synaptic weight matrix parameters σ and μ corresponding to region 1b or 3b.

V. CONCLUSION

In this work, we studied the stability of ring neural networks with piecewise-affine, discontinuous activation functions. In comparison to existing literature, we obtained some simpler necessary conditions and sufficient conditions for convergence of the system depending on the eigenvalues of the synaptic connectivity matrix, and we were able to link them to the form of the solutions. When these theoretical conditions were not met, we were able to predict the behaviour of the system numerically on an example network. All of these results were then confirmed using simulations of a network with gaussian-like connectivity matrix.

Understanding the theoretical aspects of the behaviour of such systems could prove very useful in computational neurosciences, in order to build more complex models of place cells or head-direction cells, and easily tune them to resemble physiological networks.

As for future works, it would be interesting to see if the results of this study can be extended to activation functions with more than two affine regions (*e.g.*, with some saturation), to piecewise non-linear activation functions, or to systems with more complex dynamics (*e.g.*, with some noisy input, or with delays on the synaptic transmission). Another perspective would be to study this network in terms of memory, *i.e.*, how long the network can maintain accurate localized activity when the stimulation is removed.

REFERENCES

[1] M. Forti and P. Nistri, "Global Convergence of Neural Networks with Discontinuous Neuron Activations", *IEEE Transactions on Circuits and Systems I*, vol. 50, no. 11, November 2003.

[2] W. Gerstner, W. M. Kistler, R. Naud and L. Paninski, *Neuronal Dynamics, From single neurons to networks and models of cognition*, Cambridge University Press, ch. 16.3.2, 2014.

[3] Richard H. R. Hahnloser, H. S. Seung and J. Slotine, "Permitted and Forbidden Sets in Symmetric Threshold-Linear Networks", *Neural Computation*, vol.15, pp 621-638, 2003.

[4] J. J. Hopfield, "Neural networks and physical systems with emergent collective computational abilities", *PNAS*, vol. 79, pp 2554-2558, 1982.

[5] J. J. Hopfield, "Neurons with graded response have collective computational properties like those of two-states neurons", *PNAS*, vol. 81, pp 3088-3092, 1984.

[6] R. Horn and C. Johnson, *Matrix analysis*, Cambridge University Press, p189, 1990.

[7] C. Le Duigou, J. Simonnet, M. T. Telenczuk, D. Fricker and R. Miles, "Recurrent synapses and circuits in the CA3 region of the hippocampus: an associative network", *Frontiers in Cellular Neuroscience*, vol. 7, article 262, 2014.

[8] C. K. Machens and C. D. Brody, "Design of Continuous Attractor Networks with Monotonic Tuning Using a Symmetry Principle", *Neural Computation*, vol. 20, pp 452-485, 2008.

[9] B. L. McNaughton, F. P. Battaglia, O. Jensen, E. I. Moser and M. Moser, "Path integration and the neural basis of the 'cognitive map' ", *Nature Review Neuroscience*, vol. 7, pp 663-678, 2006.

[10] J. O'Keefe and L. Nadel, *The Hippocampus as a Cognitive Map*, Oxford University Press, 1978.

[11] F. J. Pineda, "Dynamics and Architecture for Neural Computation", *Journal of Complexity*, vol. 4, pp 216-245, 1988.

[12] S. V. Savchenko, "Normal matrices and their principal submatrices of co-order one", *Linear algebra and its applications*, vol. 419, pp 556-568, 2006.

[13] H. Zhang and D. Liu, "A Comprehensive Review of Stability Analysis in Continuous-Time Recurrent Neural Networks", *IEEE Transactions on Neural Networks and Learning Systems*, vol. 25, no. 7, July 2014.

Bibliography

[Abbott, 1999] Abbott, L. (1999). Lapicque's introduction of the integrate-and-fire model neuron (1907). *Brain Research Bulletin*, 50(5-6) :303–304.

[Adhikari et al., 2010] Adhikari, A., Topiwala, M. A., and Gordon, J. A. (2010). Synchronized activity between the ventral hippocampus and the medial prefrontal cortex during anxiety. *Neuron*, 65(2) :257–269.

[Agster and Burwell, 2013] Agster, K. L. and Burwell, R. D. (2013). Hippocampal and subicular efferents and afferents of the perirhinal, postrhinal, and entorhinal cortices of the rat. *Behavioural Brain Research*, 254 :50–64.

[Amaral et al., 2007] Amaral, D. G., Scharfman, H. E., and Lavenex, P. (2007). The dentate gyrus : fundamental neuroanatomical organization (dentate gyrus for dummies). In *The Dentate Gyrus : A Comprehensive Guide to Structure, Function, and Clinical Implications*, pages 3–790. Elsevier.

[Andersen et al., 2007] Andersen, P., Morris, R., Amaral, D., Bliss, T., and O'Keefe, J. (2007). *The hippocampus book*. Oxford University Press.

[Antoniades et al., 2017] Antoniades, A., Spyrou, L., Martin-Lopez, D., Valentin, A., Alarcon, G., Sanei, S., and Took, C. C. (2017). Detection of interictal discharges with convolutional neural networks using discrete ordered multichannel intracranial EEG. *IEEE Transactions on Neural Systems and Rehabilitation Engineering*, 25(12) :2285–2294.

[Asadi-Pooya et al., 2017] Asadi-Pooya, A. A., Stewart, G. R., Abrams, D. J., and Sharan, A. (2017). Prevalence and incidence of drug-resistant mesial temporal lobe epilepsy in the United States. *World Neurosurgery*, 99 :662–666.

[Aussel et al., 2018] Aussel, A., Buhry, L., Tyvaert, L., and Ranta, R. (2018). A detailed anatomical and mathematical model of the hippocampal formation for the generation of sharp-wave ripples and theta-nested gamma oscillations. *Journal of Computational Neuroscience*, 45(3) :207–221.

[Axmacher et al., 2010] Axmacher, N., Henseler, M. M., Jensen, O., Weinreich, I., Elger, C. E., and Fell, J. (2010). Cross-frequency coupling supports multi-item working memory in the human hippocampus. *Proceedings of the National Academy of Sciences*, 107(7) :3228–3233.

[Babb et al., 1989] Babb, T., Pretorius, J., Kupfer, W., and Crandall, P. (1989). Glutamate decarboxylase-immunoreactive neurons are preserved in human epileptic hippocampus. *The Journal of Neuroscience*, 9(7) :2562–2574.

[Bartos et al., 2007] Bartos, M., Vida, I., and Jonas, P. (2007). Synaptic mechanisms of synchronized gamma oscillations in inhibitory interneuron networks. *Nature reviews. Neuroscience*, 8(1) :45–56.

[Batista et al., 2014] Batista, C., Viana, R., Lopes, S., and Batista, A. (2014). Dynamic range in small-world networks of hodgkin–huxley neurons with chemical synapses. *Physica A : Statistical Mechanics and its Applications*, 410 :628–640.

[Bezaire and Soltesz, 2013] Bezaire, M. J. and Soltesz, I. (2013). Quantitative assessment of CA1 local circuits : Knowledge base for interneuron-pyramidal cell connectivity. *Hippocampus*, 23(9) :751–785.

[Bland and Bland, 1986] Bland, S. K. and Bland, B. H. (1986). Medial septal modulation of hippocampal theta cell discharges. *Brain Research*, 375(1) :102 – 116.

[Blümcke et al., 2013] Blümcke, I., Thom, M., Aronica, E., Armstrong, D. D., Bartolomei, F., Bernasconi, A., Bernasconi, N., Bien, C. G., Cendes, F., Coras, R., Cross, J. H., Jacques, T. S., Kahane, P., Mathern, G. W., Miyata, H., Moshé, S. L., Oz, B., Özkara, Ç., Perucca, E., Sisodiya, S., Wiebe, S., and Spreafico, R. (2013). International consensus classification of hippocampal sclerosis in temporal lobe epilepsy : A task force report from the ILAE commission on diagnostic methods. *Epilepsia*, 54(7) :1315–1329.

[Bouilleret et al., 1999] Bouilleret, V., Ridoux, V., Depaulis, A., Marescaux, C., Nehlig, A., and Salle, G. L. G. L. (1999). Recurrent seizures and hippocampal sclerosis following intrahippocampal kainate injection in adult mice : electroencephalography, histopathology and synaptic reorganization similar to mesial temporal lobe epilepsy. *Neuroscience*, 89(3) :717–729.

[Box and Behnken, 1960] Box, G. E. P. and Behnken, D. W. (1960). Simplex-sum designs : A class of second order rotatable designs derivable from those of first order. *The Annals of Mathematical Statistics*, 31(4) :838–864.

[Bragin et al., 1999] Bragin, A., Engel, J., Wilson, C. L., Fried, I., and Mathern, G. W. (1999). Hippocampal and entorhinal cortex high-frequency oscillations (100-500 hz) in human epileptic brain and in kainic acid-treated rats with chronic seizures. *Epilepsia*, 40(2) :127–137.

[Brette and Gerstner, 2005] Brette, R. and Gerstner, W. (2005). Adaptive exponential integrate-and-fire model as an effective description of neuronal activity. *Journal of Neurophysiology*, 94(5) :3637–3642.

[Brun, 2002] Brun, V. H. (2002). Place cells and place recognition maintained by direct entorhinal-hippocampal circuitry. *Science*, 296(5576) :2243–2246.

[Brunel and Wang, 2003] Brunel, N. and Wang, X.-J. (2003). What determines the frequency of fast network oscillations with irregular neural discharges ? I. Synaptic dynamics and excitation-inhibition balance. *Journal of Neurophysiology*, 90(1) :415–430.

[Buckmaster et al., 2002] Buckmaster, P. S., Zhang, G. F., and Yamawaki, R. (2002). Axon sprouting in a model of temporal lobe epilepsy creates a predominantly excitatory feedback circuit. *The Journal of Neuroscience*, 22(15) :6650–6658.

[Burgess et al., 2007] Burgess, N., Barry, C., and O'Keefe, J. (2007). An oscillatory interference model of grid cell firing. *Hippocampus*, 17(9) :801–812.

[Buzsaki, 2011] Buzsaki, G. (2011). *Rhythms of the Brain.* Oxford University Press.

[Buzsáki, 2015] Buzsáki, G. (2015). Hippocampal sharp wave-ripple : A cognitive biomarker for episodic memory and planning. *Hippocampus*, 25(10) :1073–1188.

[Buzsaki et al., 2012] Buzsaki, G., Anastassiou, C. A., and Koch, C. (2012). The origin of extracellular fields and currents - EEG, ECoG, LFP and spikes. *Nature Reviews Neuroscience*, 13(6) :407–420.

[Buzsáki, 2002] Buzsáki, G. (2002). Theta oscillations in the hippocampus. *Neuron*, 33(3) :325 – 340.

[Cavarsan et al., 2018] Cavarsan, C. F., Malheiros, J., Hamani, C., Najm, I., and Covolan, L. (2018). Is mossy fiber sprouting a potential therapeutic target for epilepsy ? *Frontiers in Neurology*, 9.

[Cavazos and Sutula, 1990] Cavazos, J. and Sutula, T. P. (1990). Progressive neuronal loss induced by kindling : a possible mechanism for mossy fiber synaptic reorganization and hippocampal sclerosis. *Brain Research*, 527(1) :1–6.

[Cheng and Yakel, 2013] Cheng, Q. and Yakel, J. L. (2013). Presynaptic $\alpha 7$ nicotinic acetylcholine receptors enhance hippocampal mossy fiber glutamatergic transmission via pka activation. *Journal of Neuroscience*, 34(1) :124–133.

[Cheung, 2008] Cheung, J. (2008). Neurons, nerve tissues, and the nervous system. Available at `http://biomedicalengineering.yolasite.com/neurons.php`.

[Chindo et al., 2016] Chindo, B. A., Adzu, B., and Gamaniel, K. S. (2016). Antiepileptic drug targets : An update on ion channels. In *Epileptology - The Modern State of Science*. InTech.

[Couey et al., 2013] Couey, J. J., Witoelar, A., Zhang, S.-J., Zheng, K., Ye, J., Dunn, B., Czajkowski, R., Moser, M.-B., Moser, E. I., Roudi, Y., et al. (2013). Recurrent inhibitory circuitry as a mechanism for grid formation. *Nature neuroscience*, 16(3) :318–324.

[Coulter and Steinhauser, 2015] Coulter, D. A. and Steinhauser, C. (2015). Role of astrocytes in epilepsy. *Cold Spring Harbor Perspectives in Medicine*, 5(3) :a022434–a022434.

[Crespel et al., 1998] Crespel, A., Baldy-Moulinier, M., and Coubes, P. (1998). The relationship between sleep and epilepsy in frontal and temporal lobe epilepsies : Practical and physiopathologic considerations. *Epilepsia*, 39(2) :150–157.

[Cressman et al., 2009] Cressman, J. R., Ullah, G., Ziburkus, J., Schiff, S. J., and Barreto, E. (2009). The influence of sodium and potassium dynamics on excitability, seizures, and the stability of persistent states : I. Single neuron dynamics. *Journal of Computational Neuroscience*, 26(2) :159–170.

[Csicsvari et al., 2003] Csicsvari, J., Jamieson, B., Wise, K. D., and Buzsáki, G. (2003). Mechanisms of gamma oscillations in the hippocampus of the behaving rat. *Neuron*, 37(2) :311 – 322.

[Debanne et al., 1995] Debanne, D., Guerineau, N. C., Gahwiler, B. H., and Thompson, S. M. (1995). Physiology and pharmacology of unitary synaptic connections between pairs of cells in areas CA3 and CA1 of rat hippocampal slice cultures. *Journal of Neurophysiology*, 73(3) :1282–1294. PMID : 7608771.

[Demont-Guignard et al., 2009] Demont-Guignard, S., Benquet, P., Gerber, U., and Wendling, F. (2009). Analysis of intracerebral EEG recordings of epileptic spikes : Insights from a neural network model. *IEEE Transactions on Biomedical Engineering*, 56(12) :2782–2795.

[Diba and Buzsáki, 2007] Diba, K. and Buzsáki, G. (2007). Forward and reverse hippocampal place-cell sequences during ripples. *Nature Neuroscience*, 10(10) :1241–1242.

[Doeller et al., 2010] Doeller, C. F., Barry, C., and Burgess, N. (2010). Evidence for grid cells in a human memory network. *Nature*, 463(7281) :657–661.

[Drexel et al., 2012] Drexel, M., Preidt, A. P., and Sperk, G. (2012). Sequel of spontaneous seizures after kainic acid-induced status epilepticus and associated neuropathological changes in the subiculum and entorhinal cortex. *Neuropharmacology*, 63(5) :806–817.

[Dyhrfjeld-Johnsen, 2008] Dyhrfjeld-Johnsen, J. (2008). Upregulated h-current in hyperexcitable CA1 dendrites after febrile seizures. *Frontiers in Cellular Neuroscience*, 2.

[Dyhrfjeld-Johnsen et al., 2007] Dyhrfjeld-Johnsen, J., Santhakumar, V., Morgan, R. J., Huerta, R., Tsimring, L., and Soltesz, I. (2007). Topological determinants of epileptogenesis in large-scale structural and functional models of the dentate gyrus derived from experimental data. *Journal of Neurophysiology*, 97(2) :1566–1587.

[Egorov et al., 2002] Egorov, A. V., Hamam, B. N., Fransén, E., Hasselmo, M. E., and Alonso, A. A. (2002). Graded persistent activity in entorhinal cortex neurons. *Nature*, 420(6912) :173–178.

[Eichenbaum, 2014] Eichenbaum, H. (2014). Time cells in the hippocampus : a new dimension for mapping memories. *Nature Reviews Neuroscience*, 15(11) :732–744.

[Einevoll et al., 2013] Einevoll, G. T., Kayser, C., Logothetis, N. K., and Panzeri, S. (2013). Modelling and analysis of local field potentials for studying the function of cortical circuits. *Nature Reviews Neuroscience*, 14(11) :770–785.

[Engel, 2001] Engel, J. (2001). Mesial temporal lobe epilepsy : What have we learned ? *The Neuroscientist*, 7(4) :340–352.

[Engel, 2014] Engel, J. (2014). Approaches to refractory epilepsy. *Annals of Indian Academy of Neurology*, 17(5) :12.

[Engel, 2012] Engel, J. J. (2012). *Seizures and Epilepsy (Contemporary Neurology Series)*. Oxford University Press.

[Engel et al., 2009] Engel, J. J., Bragin, A., Staba, R., and Mody, I. (2009). High-frequency oscillations : What is normal and what is not ? *Epilepsia*, 50(4) :598–604.

[Felix-Ortiz and Tye, 2014] Felix-Ortiz, A. C. and Tye, K. M. (2014). Amygdala inputs to the ventral hippocampus bidirectionally modulate social behavior. *Journal of Neuroscience*, 34(2) :586–595.

[Feng, 2001] Feng, J. (2001). Is the integrate-and-fire model good enough ?—a review. *Neural Networks*, 14(6-7) :955–975.

[Fiest et al., 2017] Fiest, K. M., Sauro, K. M., Wiebe, S., Patten, S. B., Kwon, C.-S., Dykeman, J., Pringsheim, T., Lorenzetti, D. L., and Jetté, N. (2017). Prevalence and incidence of epilepsy : A systematic review and meta-analysis of international studies. *Neurology*, 88(3) :296—303.

[Fisher et al., 2014] Fisher, R. S., Acevedo, C., Arzimanoglou, A., Bogacz, A., Cross, J. H., Elger, C. E., Engel, J., Forsgren, L., French, J. A., Glynn, M., Hesdorffer, D. C., Lee, B., Mathern, G. W., Moshé, S. L., Perucca, E., Scheffer, I. E., Tomson, T., Watanabe, M., and Wiebe, S. (2014). ILAE official report : A practical clinical definition of epilepsy. *Epilepsia*, 55(4) :475–482.

[Fisher et al., 2017] Fisher, R. S., Cross, J. H., French, J. A., Higurashi, N., Hirsch, E., Jansen, F. E., Lagae, L., Moshé, S. L., Peltola, J., Roulet Perez, E., Scheffer, I. E., and Zuberi, S. M. (2017). Operational classification of seizure types by the international league against epilepsy : Position paper of the ILAE commission for classification and terminology. *Epilepsia*, 58(4) :522–530.

[Foundation, 2013] Foundation, E. (2013). Diagnosing epilepsy. Available at `https://www.epilepsy.com/learn/diagnosing-epilepsy`.

[Frazier et al., 1998] Frazier, C. J., Rollins, Y. D., Breese, C. R., Leonard, S., Freedman, R., and Dunwiddie, T. V. (1998). Acetylcholine activates an α-bungarotoxin-sensitive nicotinic current in rat hippocampal interneurons, but not pyramidal cells. *Journal of Neuroscience*, 18(4) :1187–1195.

[Freund and Buzsáki, 1998] Freund, T. and Buzsáki, G. (1998). Interneurons of the hippocampus. *Hippocampus*, 6(4) :347–470.

[Freund et al., 1992] Freund, T., Ylinen, A., Miettinen, R., Pitkänen, A., Lahtinen, H., Baimbridge, K., and Riekkinen, P. (1992). Pattern of neuronal death in the rat hippocampus after status epilepticus. relationship to calcium binding protein content and ischemic vulnerability. *Brain Research Bulletin*, 28(1) :27–38.

[Fritschy et al., 1999] Fritschy, J.-M., Kiener, T., Bouilleret, V., and Loup, F. (1999). GABAergic neurons and GABAA-receptors in temporal lobe epilepsy. *Neurochemistry International*, 34(5) :435–445.

[Fukai, 1999] Fukai, T. (1999). Sequence generation in arbitrary temporal patterns from theta-nested gamma oscillations : a model of the basal ganglia–thalamo-cortical loops. *Neural Networks*, 12(7–8) :975 – 987.

[Gan et al., 2017] Gan, J., ming Weng, S., Pernía-Andrade, A. J., Csicsvari, J., and Jonas, P. (2017). Phase-locked inhibition, but not excitation, underlies hippocampal ripple oscillations in awake mice in vivo. *Neuron*, 93(2) :308 – 314.

[Gaspard et al., 2014] Gaspard, N., Alkawadri, R., Farooque, P., Goncharova, I. I., and Zaveri, H. P. (2014). Automatic detection of prominent interictal spikes in intracranial EEG : Validation of an algorithm and relationsip to the seizure onset zone. *Clinical Neurophysiology*, 125(6) :1095–1103.

[Gelinas et al., 2016] Gelinas, J. N., Khodagholy, D., Thesen, T., Devinsky, O., and Buzsáki, G. (2016). Interictal epileptiform discharges induce hippocampal–cortical coupling in temporal lobe epilepsy. *Nature Medicine*, 22(6) :641–648.

[Gerstner, 2014] Gerstner, W. (2014). *Neuronal Dynamics : From Single Neurons To Networks And Models Of Cognition*. Cambridge University Press.

[Giocomo et al., 2011] Giocomo, L. M., Moser, M.-B., and Moser, E. I. (2011). Computational models of grid cells. *Neuron*, 71(4) :589–603.

[Giovannini et al., 2017] Giovannini, F., Knauer, B., Yoshida, M., and Buhry, L. (2017). The can-in network : A biologically inspired model for self-sustained theta oscillations and memory maintenance in the hippocampus. *Hippocampus*, 27(4) :450–463.

[Girardeau et al., 2009] Girardeau, G., Benchenane, K., Wiener, S. I., Buzsáki, G., and Zugaro, M. B. (2009). Selective suppression of hippocampal ripples impairs spatial memory. *Nature Neuroscience*, 12(10) :1222–1223.

[Girardeau and Zugaro, 2011] Girardeau, G. and Zugaro, M. (2011). Hippocampal ripples and memory consolidation. *Current Opinion in Neurobiology*, 21(3) :452 – 459. Behavioural and cognitive neuroscience.

[Gloor, 1975] Gloor, P. (1975). Contributions of electroencephalography and electrocorticography to the neurosurgical treatment of the epilepsies. *Adv Neurol*, 8 :59–105.

[Gloveli et al., 2004] Gloveli, T., Dugladze, T., Saha, S., Monyer, H., Heinemann, U., Traub, R. D., Whittington, M. A., and Buhl, E. H. (2004). Differential involvement of oriens/pyramidale interneurones in hippocampal network oscillationsin vitro. *The Journal of Physiology*, 562(1) :131–147.

[Gonzalez-Sulser et al., 2012] Gonzalez-Sulser, A., Wang, J., Queenan, B. N., Avoli, M., Vicini, S., and Dzakpasu, R. (2012). Hippocampal neuron firing and local field potentials in the in vitro 4-aminopyridine epilepsy model. *Journal of Neurophysiology*, 108(9) :2568–2580.

[Goupy and Creighton, 2013] Goupy, J. and Creighton, L. (2013). *Introduction aux plans d'expériences - 5e Ed. - Toutes les techniques nécessaires à la conduite d'une étude*. DUNOD.

[Gray et al., 1996] Gray, R., Rajan, A. S., Radcliffe, K. A., Yakehiro, M., and Dani, J. A. (1996). Hippocampal synaptic transmission enhanced by low concentrations of nicotine. *Nature*, 383(6602) :713.

[Hagen et al., 2016] Hagen, E., Dahmen, D., Stavrinou, M. L., Lindén, H., Tetzlaff, T., van Albada, S. J., Grün, S., Diesmann, M., and Einevoll, G. T. (2016). Hybrid scheme for modeling local field potentials from point-neuron networks. *Cerebral Cortex*, 26(12) :4461–4496.

[Hangya et al., 2009] Hangya, B., Borhegyi, Z., Szilágyi, N., Freund, T. F., and Varga, V. (2009). GABAergic neurons of the medial septum lead the hippocampal network during theta activity. *Journal of Neuroscience*, 29(25) :8094–8102.

[Hasselmo, 1999] Hasselmo, M. E. (1999). Neuromodulation : acetylcholine and memory consolidation. *Trends in Cognitive Sciences*, 3(9) :351 – 359.

[Heinemann et al., 2000] Heinemann, U., Gabriel, S., Jauch, R., Schulze, K., Kivi, A., Eilers, A., Kovacs, R., and Lehmann, T.-N. (2000). Alterations of glial cell function in temporal lobe epilepsy. *Epilepsia*, 41(s6) :S185–S189.

[Herreras et al., 1988] Herreras, O., Solís, J., Herranz, A., del Río, R. M., and Lerma, J. (1988). Sensory modulation of hippocampal transmission. II. Evidence for a cholinergic locus of inhibition in the schaffer-ca1 synapse. *Brain Research*, 461(2) :303 – 313.

[Heys et al., 2012] Heys, J. G., Schultheiss, N. W., Shay, C. F., Tsuno, Y., and Hasselmo, M. E. (2012). Effects of acetylcholine on neuronal properties in entorhinal cortex. *Frontiers in behavioral neuroscience*, 6.

[Hindmarsh and Rose, 1984] Hindmarsh, J. L. and Rose, R. M. (1984). A model of neuronal bursting using three coupled first order differential equations. *Proc. R. Soc. Lond., B, Biol. Sci.*, 221(1222) :87–102.

[Hirtz et al., 2007] Hirtz, D., Thurman, D. J., Gwinn-Hardy, K., Mohamed, M., Chaudhuri, A. R., and Zalutsky, R. (2007). How common are the "common" neurologic disorders ? *Neurology*, 68(5) :326–337.

[Hodgkin and Huxley, 1952] Hodgkin, A. L. and Huxley, A. F. (1952). A quantitative description of membrane current and its application to conduction and excitation in nerve. *The Journal of Physiology*, 117(4) :500–544.

[Hofmanis et al., 2011] Hofmanis, J., Caspary, O., Louis-Dorr, V., and Maillard, L. (2011). Automatic depth electrode localization in intracranial space. In *4th International Conference on Bio-inspired Systems and Signal Processing, Biosignals 2011*, page CDROM, Rome, Italy.

[Huberfeld et al., 2007] Huberfeld, G., Wittner, L., Clemenceau, S., Baulac, M., Kaila, K., Miles, R., and Rivera, C. (2007). Perturbed chloride homeostasis and GABAergic signaling in human temporal lobe epilepsy. *Journal of Neuroscience*, 27(37) :9866–9873.

[Huh et al., 2010] Huh, C. Y. L., Goutagny, R., and Williams, S. (2010). Glutamatergic neurons of the mouse medial septum and diagonal band of Broca synaptically drive hippocampal pyramidal cells : Relevance for hippocampal theta rhythm. *Journal of Neuroscience*, 30(47) :15951–15961.

[Izhikevich, 2003] Izhikevich, E. (2003). Simple model of spiking neurons. *IEEE Transactions on Neural Networks*, 14(6) :1569–1572.

[Jacobs et al., 2013] Jacobs, J., Weidemann, C. T., Miller, J. F., Solway, A., Burke, J. F., Wei, X.-X., Suthana, N., Sperling, M. R., Sharan, A. D., Fried, I., and Kahana, M. J. (2013). Direct recordings of grid-like neuronal activity in human spatial navigation. *Nature Neuroscience*, 16(9) :1188–1190.

[Janca et al., 2014] Janca, R., Jezdik, P., Cmejla, R., Tomasek, M., Worrell, G. A., Stead, M., Wagenaar, J., Jefferys, J. G. R., Krsek, P., Komarek, V., Jiruska, P., and Marusic, P. (2014). Detection of interictal epileptiform discharges using signal envelope distribution modelling : Application to epileptic and non-epileptic intracranial recordings. *Brain Topography*, 28(1) :172–183.

[Jansen and Rit, 1995] Jansen, B. H. and Rit, V. G. (1995). Electroencephalogram and visual evoked potential generation in a mathematical model of coupled cortical columns. *Biological Cybernetics*, 73(4) :357–366.

[Jinno and Kosaka, 2010] Jinno, S. and Kosaka, T. (2010). Stereological estimation of numerical densities of glutamatergic principal neurons in the mouse hippocampus. *Hippocampus*, 20(7) :829–840.

[Jirsch, 2006] Jirsch, J. D. (2006). High-frequency oscillations during human focal seizures. *Brain*, 129(6) :1593–1608.

[Jiruska et al., 2010] Jiruska, P., Csicsvari, J., Powell, A. D., Fox, J. E., Chang, W. C., Vreugdenhil, M., Li, X., Palus, M., Bujan, A. F., Dearden, R. W., and Jefferys, J. G. R. (2010). High-frequency network activity, global increase in neuronal activity, and synchrony expansion precede epileptic seizures in vitro. *Journal of Neuroscience*, 30(16) :5690–5701.

[Jones and Yakel, 1997] Jones, S. and Yakel, J. L. (1997). Functional nicotinic ach receptors on interneurones in the rat hippocampus. *The Journal of Physiology*, 504(3) :603–610.

[Kang et al., 2015] Kang, D., Ding, M., Topchiy, I., Shifflett, L., and Kocsis, B. (2015). Theta-rhythmic drive between medial septum and hippocampus in slow-wave sleep and microarousal : a granger causality analysis. *Journal of Neurophysiology*, 114(5) :2797–2803. PMID : 26354315.

[Kazilek, 2011] Kazilek (2011). Brain regions. Available at `https://askabiologist.asu.edu/brain-regions`.

[Keeley et al., 2017] Keeley, S., Fenton, A. A., and Rinzel, J. (2017). Modeling fast and slow gamma oscillations with interneurons of different subtype. *Journal of Neurophysiology*, 117(3) :950–965.

[Kiss et al., 1998] Kiss, J., Buzsaki, G., Morrow, J. S., Glantz, S. B., and Leranth, C. (1998). Entorhinal cortical innervation of parvalbumin-containing neurons (basket and chandelier cells) in the rat ammon's horn. *Hippocampus*, 6(3) :239–246.

[Klausberger and Somogyi, 2008] Klausberger, T. and Somogyi, P. (2008). Neuronal diversity and temporal dynamics : The unity of hippocampal circuit operations. *Science*, 321(5885) :53–57.

[Kleen et al., 2013] Kleen, J. K., Scott, R. C., Holmes, G. L., Roberts, D. W., Rundle, M. M., Testorf, M., Lenck-Santini, P.-P., and Jobst, B. C. (2013). Hippocampal interictal epileptiform activity disrupts cognition in humans. *Neurology*, 81(1) :18–24.

[Knowles and Schwartzkroin, 1981] Knowles, W. and Schwartzkroin, P. (1981). Local circuit synaptic interactions in hippocampal brain slices. *Journal of Neuroscience*, 1(3) :318–322.

[Krauss et al., 1997] Krauss, G. L., Summerfield, M., Brandt, J., Breiter, S., and Ruchkin, D. (1997). Mesial temporal spikes interfere with working memory. *Neurology*, 49(4) :975–980.

[Larimer and Strowbridge, 2008] Larimer, P. and Strowbridge, B. W. (2008). Nonrandom local circuits in the dentate gyrus. *Journal of Neuroscience*, 28(47) :12212–12223.

[Lerche et al., 2012] Lerche, H., Shah, M., Beck, H., Noebels, J., Johnston, D., and Vincent, A. (2012). Ion channels in genetic and acquired forms of epilepsy. *The Journal of Physiology*, 591(4) :753–764.

[Lisman and Jensen, 2013] Lisman, J. and Jensen, O. (2013). The theta-gamma neural code. *Neuron*, 77(6) :1002 – 1016.

[Lopim et al., 2016] Lopim, G. M., Campos, D. V., da Silva, S. G., de Almeida, A. A., Lent, R., Cavalheiro, E. A., and Arida, R. M. (2016). Relationship between seizure frequency and number of neuronal and non-neuronal cells in the hippocampus throughout the life of rats with epilepsy. *Brain Research*, 1634 :179–186.

[Maingret et al., 2016] Maingret, N., Girardeau, G., Todorova, R., Goutierre, M., and Zugaro, M. (2016). Hippocampo-cortical coupling mediates memory consolidation during sleep. *Nature Neuroscience*, 19(7) :959–964.

[Malmivuo, 2011] Malmivuo, J. (2011). Comparison of the properties of EEG and MEG in detecting the electric activity of the brain. *Brain Topography*, 25(1) :1–19.

[Manford, 1992] Manford, M. (1992). The national general practice study of epilepsy. *Archives of Neurology*, 49(8) :801.

[Mazzoni et al., 2015] Mazzoni, A., Lindén, H., Cuntz, H., Lansner, A., Panzeri, S., and Einevoll, G. T. (2015). Computing the local field potential (lfp) from integrate-and-fire network models. *PLOS Computational Biology*, 11(12) :1–38.

[McHugh et al., 2004] McHugh, S. B., Deacon, R. M. J., Rawlins, J. N. P., and Bannerman, D. M. (2004). Amygdala and ventral hippocampus contribute differentially to mechanisms of fear and anxiety. *Behavioral Neuroscience*, 118(1) :63–78.

[Mendelson, 2012] Mendelson, Y. (2012). Chapter 10 - biomedical sensors. In Enderle, J. D. and Bronzino, J. D., editors, *Introduction to Biomedical Engineering (Third Edition)*, Biomedical Engineering, pages 609 – 666. Academic Press, Boston, third edition edition.

[Miller et al., 2015] Miller, C. B., Kyle, S. D., Melehan, K. L., and Bartlett, D. J. (2015). Methodology for the assessment of sleep. In *Sleep and Affect*, pages 65–90. Elsevier.

[Morgan and Soltesz, 2008] Morgan, R. J. and Soltesz, I. (2008). Nonrandom connectivity of the epileptic dentate gyrus predicts a major role for neuronal hubs in seizures. *Proceedings of the National Academy of Sciences*, 105(16) :6179–6184.

[Morris and Lecar, 1981] Morris, C. and Lecar, H. (1981). Voltage oscillations in the barnacle giant muscle fiber. *Biophys. J.*, 35(1) :193–213.

[Muñoz and Insausti, 2005] Muñoz, M. and Insausti, R. (2005). Cortical efferents of the entorhinal cortex and the adjacent parahippocampal region in the monkey (macaca fascicularis). *European Journal of Neuroscience*, 22(6) :1368–1388.

[Murray and al., 2012] Murray, C. J. L. and al. (2012). Disability-adjusted life years (dalys) for 291 diseases and injuries in 21 regions, 1990–2010 : a systematic analysis for the global burden of disease study 2010. *The Lancet*, 380(9859) :2197 – 2223.

[Nádasdy et al., 1999] Nádasdy, Z., Hirase, H., Czurkó, A., Csicsvari, J., and Buzsáki, G. (1999). Replay and time compression of recurring spike sequences in the hippocampus. *Journal of Neuroscience*, 19(21) :9497–9507.

[Nadel et al., 2000] Nadel, L., Samsonovich, A., Ryan, L., and Moscovitch, M. (2000). Multiple trace theory of human memory : Computational, neuroimaging, and neuropsychological results. *Hippocampus*, 10(4) :352–368.

[Nadel et al., 2007] Nadel, L., Winocur, G., Ryan, L., and Moscovitch, M. (2007). Systems consolidation and hippocampus : two views. *Debates in Neuroscience*, 1(2-4) :55–66.

[Naftulin et al., 2018] Naftulin, J. S., Ahmed, O. J., Piantoni, G., Eichenlaub, J.-B., Martinet, L.-E., Kramer, M. A., and Cash, S. S. (2018). Ictal and preictal power changes outside of the seizure focus correlate with seizure generalization. *Epilepsia*, 59(7) :1398–1409.

[Nagumo et al., 1962] Nagumo, J., Arimoto, S., and Yoshizawa, S. (1962). An active pulse transmission line simulating nerve axon. *Proceedings of the IRE*, 50(10) :2061–2070.

[National Institute of Neurological Disorders and Stroke, 2019] National Institute of Neurological Disorders and Stroke (2019). Brain basics : Understanding sleep. Available at `https://www.ninds.nih.gov/Disorders/Patient-Caregiver-Education/Understanding-Sleep`.

[Netoff, 2004] Netoff, T. I. (2004). Epilepsy in small-world networks. *Journal of Neuroscience*, 24(37) :8075–8083.

[Noebels et al., 2012] Noebels, J. L., Avoli, M., Rogawski, M. A., Olsen, R. W., Delgado-Escueta, A. V., and Buckmaster, P. S. (2012). *Jasper's Basic Mechanisms of Epilepsies*. Oxford University Press.

[O'Keefe and Dostrovsky, 1971] O'Keefe, J. and Dostrovsky, J. (1971). The hippocampus as a spatial map. preliminary evidence from unit activity in the freely-moving rat. *Brain Research*, 34(1) :171–175.

[O'Keefe and Recce, 1993] O'Keefe, J. and Recce, M. L. (1993). Phase relationship between hippocampal place units and the EEG theta rhythm. *Hippocampus*, 3(3) :317–330.

[Omura et al., 2015] Omura, Y., Carvalho, M. M., Inokuchi, K., and Fukai, T. (2015). A lognormal recurrent network model for burst generation during hippocampal sharp waves. *Journal of Neuroscience*, 35(43) :14585–14601.

[Osorio et al., 2016] Osorio, I., Zaveri, H., Frei, M., and Arthurs, S. (2016). *Epilepsy : The intersection of neurosciences, biology, mathematics, engineering, and physics*. CRC Press.

[Partridge and Swandulla, 1988] Partridge, L. and Swandulla, D. (1988). Calcium-activated nonspecific cation channels. *Trends in Neurosciences*, 11(2) :69–72.

[Pastoll et al., 2013] Pastoll, H., Solanka, L., van Rossum, M., and Nolan, M. (2013). Feedback inhibition enables theta-nested gamma oscillations and grid firing fields. *Neuron*, 77(1) :141 – 154.

[Patel et al., 2013] Patel, J., Schomburg, E. W., Berényi, A., Fujisawa, S., and Buzsáki, G. (2013). Local generation and propagation of ripples along the septotemporal axis of the hippocampus. *Journal of Neuroscience*, 33(43) :17029–17041.

[Patton and McNaughton, 1995] Patton, P. E. and McNaughton, B. (1995). Connection matrix of the hippocampal formation : I. The dentate gyrus. *Hippocampus*, 5(4) :245–286.

[Paul, 2018] Paul, Y. (2018). Various epileptic seizure detection techniques using biomedical signals : a review. *Brain Informatics*, 5(2).

[Pettersen et al., 2012] Pettersen, K. H., Lindén, H., Dale, A. M., and Einevoll, G. T. (2012). Extracellular spikes and CSD. *Handbook of neural activity measurement*, 1 :92–135.

[Picot et al., 2008] Picot, M.-C., Baldy-Moulinier, M., Daurès, J.-P., Dujols, P., and Crespel, A. (2008). The prevalence of epilepsy and pharmacoresistant epilepsy in adults : A population-based study in a western european country. *Epilepsia*, 49(7) :1230–1238.

[Quiroga et al., 2002] Quiroga, R. Q., Kreuz, T., and Grassberger, P. (2002). Event synchronization : A simple and fast method to measure synchronicity and time delay patterns. *Physical Review E*, 66(4).

[Raisman et al., 1966] Raisman, G., Cowan, W. M., and Powell, T. P. S. (1966). An Experimental Analysis of the Efferent Projection of the Hippocampus. *Brain*, 89(1) :83–108.

[Rasch and Born, 2013] Rasch, B. and Born, J. (2013). About sleep's role in memory. *Physiological Reviews*, 93(2) :681–766.

[Rastogi et al., 2014] Rastogi, P., Venkatesh, D., Chandra, M., Zhao, F., Kang, H., and You, L. (2014). Neuropsychological deficits in temporal lobe epilepsy : A comprehensive review. *Annals of Indian Academy of Neurology*, 17(4) :374.

[Rempel-Clower et al., 1996] Rempel-Clower, N. L., Zola, S. M., Squire, L. R., and Amaral, D. G. (1996). Three cases of enduring memory impairment after bilateral damage limited to the hippocampal formation. *The Journal of Neuroscience*, 16(16) :5233–5255.

[Ropireddy et al., 2011] Ropireddy, D., Scorcioni, R., Lasher, B., Buzsáki, G., and Ascoli, G. A. (2011). Axonal morphometry of hippocampal pyramidal neurons semi-automatically reconstructed after in vivo labeling in different ca3 locations. *Brain Structure and Function*, 216(1) :1–15.

[Roux et al., 2017] Roux, L., Hu, B., Eichler, R., Stark, E., and Buzsáki, G. (2017). Sharp wave ripples during learning stabilize the hippocampal spatial map. *Nature Neuroscience*, 20(6) :845–853.

[Saltelli, 2008] Saltelli, A. (2008). *Global sensitivity analysis : the primer*. John Wiley, Chichester, England Hoboken, NJ.

[Santhakumar et al., 2005] Santhakumar, V., Aradi, I., and Soltesz, I. (2005). Role of mossy fiber sprouting and mossy cell loss in hyperexcitability : A network model of the dentate gyrus incorporating cell types and axonal topography. *Journal of Neurophysiology*, 93(1) :437–453.

[Scharfman et al., 2003] Scharfman, H. E., Sollas, A. L., Berger, R. E., and Goodman, J. H. (2003). Electrophysiological evidence of monosynaptic excitatory transmission between granule cells after seizure-induced mossy fiber sprouting. *Journal of Neurophysiology*, 90(4) :2536–2547.

[Schmeiser et al., 2017] Schmeiser, B., Li, J., Brandt, A., Zentner, J., Doostkam, S., and Freiman, T. M. (2017). Different mossy fiber sprouting patterns in ILAE hippocampal sclerosis types. *Epilepsy Research*, 136 :115–122.

[Schomburg et al., 2012] Schomburg, E. W., Anastassiou, C. A., Buzsaki, G., and Koch, C. (2012). The spiking component of oscillatory extracellular potentials in the rat hippocampus. *Journal of Neuroscience*, 32(34) :11798–11811.

[Schwartz and Roth, 2008] Schwartz, J. and Roth, T. (2008). Neurophysiology of sleep and wakefulness : Basic science and clinical implications. *Current Neuropharmacology*, 6(4) :367–378.

[Scoville and Milner, 1957] Scoville, W. B. and Milner, B. (1957). Loss of recent memory after bilateral hippocampal lesions. *Journal of Neurology, Neurosurgery & Psychiatry*, 20(1) :11–21.

[Sedigh-Sarvestani et al., 2014] Sedigh-Sarvestani, M., Thuku, G. I., Sunderam, S., Parkar, A., Weinstein, S. L., Schiff, S. J., and Gluckman, B. J. (2014). Rapid eye movement sleep and

hippocampal theta oscillations precede seizure onset in the tetanus toxin model of temporal lobe epilepsy. *Journal of Neuroscience*, 34(4) :1105–1114.

[Sendrowski and Sobaniec, 2013] Sendrowski, K. and Sobaniec, W. (2013). Hippocampus, hippocampal sclerosis and epilepsy. *Pharmacological Reports*, 65(3) :555–565.

[Simoncelli et al., 2004] Simoncelli, E., P Paninski, J., W. Pillow, J., and Schwartz, O. (2004). Characterization of neural responses with stochastic stimuli. *The cognitive neurosciences*, 3.

[Sirven, 2011] Sirven, J. (2011). *Atlas of Video-EEG Monitoring*. McGraw-Hill Professional.

[Sloviter et al., 2005] Sloviter, R. S., Zappone, C. A., Harvey, B. D., and Frotscher, M. (2005). Kainic acid-induced recurrent mossy fiber innervation of dentate gyrus inhibitory interneurons : Possible anatomical substrate of granule cell hyperinhibition in chronically epileptic rats. *The Journal of Comparative Neurology*, 494(6) :944–960.

[Sobol', 2001] Sobol', I. (2001). Global sensitivity indices for nonlinear mathematical models and their Monte Carlo estimates. *Mathematics and Computers in Simulation*, 55(1-3) :271–280.

[Somogyi et al., 2014] Somogyi, P., Katona, L., Klausberger, T., Lasztóczi, B., and Viney, T. J. (2014). Temporal redistribution of inhibition over neuronal subcellular domains underlies state-dependent rhythmic change of excitability in the hippocampus. *Philosophical Transactions of the Royal Society of London B : Biological Sciences*, 369(1635).

[Spencer et al., 2005] Spencer, S. S., Berg, A. T., Vickrey, B. G., Sperling, M. R., Bazil, C. W., Shinnar, S., Langfitt, J. T., Walczak, T. S., and and, S. V. P. (2005). Predicting long-term seizure outcome after resective epilepsy surgery : The multicenter study. *Neurology*, 65(6) :912–918.

[Staba et al., 2007] Staba, R. J., Frighetto, L., Behnke, E. J., Mathern, G. W., Fields, T., Bragin, A., Ogren, J., Fried, I., Wilson, C. L., and Engel, J. (2007). Increased fast ripple to ripple ratios correlate with reduced hippocampal volumes and neuron loss in temporal lobe epilepsy patients. *Epilepsia*, 48(11) :2130–2138.

[Staba et al., 2002] Staba, R. J., Wilson, C. L., Bragin, A., Fried, I., and Engel, J. (2002). Quantitative analysis of high-frequency oscillations (80–500 hz) recorded in human epileptic hippocampus and entorhinal cortex. *Journal of Neurophysiology*, 88(4) :1743–1752.

[Stark et al., 2014] Stark, E., Roux, L., Eichler, R., Senzai, Y., Royer, S., and Buzsáki, G. (2014). Pyramidal cell-interneuron interactions underlie hippocampal ripple oscillations. *Neuron*, 83(2) :467–480.

[Stefanescu et al., 2012] Stefanescu, R. A., Shivakeshavan, R., and Talathi, S. S. (2012). Computational models of epilepsy. *Seizure*, 21(10) :748–759.

[Steriade, 2003] Steriade, M. (2003). *Neuronal substrates of sleep and epilepsy*. Cambridge University Press, Cambridge New York.

[Stickgold, 2005] Stickgold, R. (2005). Sleep-dependent memory consolidation. *Nature*, 437(7063) :1272–1278.

[Sullivan et al., 2011] Sullivan, D., Csicsvari, J., Mizuseki, K., Montgomery, S., Diba, K., and Buzsaki, G. (2011). Relationships between hippocampal sharp waves, ripples, and fast gamma oscillation : Influence of dentate and entorhinal cortical activity. *Journal of Neuroscience*, 31(23) :8605–8616.

[Taxidis et al., 2012] Taxidis, J., Coombes, S., Mason, R., and Owen, M. R. (2012). Modeling sharp wave-ripple complexes through a CA3-CA1 network model with chemical synapses. *Hippocampus*, 22(5) :995–1017.

[Tiesinga et al., 2001] Tiesinga, P. H., Fellous, J.-M., José, J. V., and Sejnowski, T. J. (2001). Computational model of carbachol-induced delta, theta, and gamma oscillations in the hippocampus. *Hippocampus*, 11(3) :251–274.

[Tononi and Cirelli, 2006] Tononi, G. and Cirelli, C. (2006). Sleep function and synaptic homeostasis. *Sleep Medicine Reviews*, 10(1) :49 – 62.

[Traub et al., 1999] Traub, R., Schmitz, D., Jefferys, J., and Draguhn, A. (1999). High-frequency population oscillations are predicted to occur in hippocampal pyramidal neuronal networks interconnected by axoaxonal gap junctions. *Neuroscience*, 92(2) :407–426.

[Traub and Bibbig, 2000] Traub, R. D. and Bibbig, A. (2000). A model of high-frequency ripples in the hippocampus based on synaptic coupling plus axon–axon gap junctions between pyramidal neurons. *Journal of Neuroscience*, 20(6) :2086–2093.

[Ullah et al., 2008] Ullah, G., Jr., J. R. C., Barreto, E., and Schiff, S. J. (2008). The influence of sodium and potassium dynamics on excitability, seizures, and the stability of persistent states : II. network and glial dynamics. *Journal of Computational Neuroscience*, 26(2) :171–183.

[Ursino et al., 2010] Ursino, M., Cona, F., and Zavaglia, M. (2010). The generation of rhythms within a cortical region : Analysis of a neural mass model. *NeuroImage*, 52(3) :1080–1094.

[Uslu et al., 2019] Uslu, S. C., Yuksel, B., Tekin, B., Sariahmetoglu, H., and Atakli, D. (2019). Cognitive impairment and drug responsiveness in mesial temporal lobe epilepsy. *Epilepsy & Behavior*, 90 :162–167.

[van Albada et al., 2015] van Albada, S. J., Helias, M., and Diesmann, M. (2015). Scalability of asynchronous networks is limited by one-to-one mapping between effective connectivity and correlations. *PLOS Computational Biology*, 11(9) :1–37.

[Vertes, 2015] Vertes, R. P. (2015). Major diencephalic inputs to the hippocampus. In *The Connected Hippocampus*, pages 121–144. Elsevier.

[Victor and Purpura, 1997] Victor, J. D. and Purpura, K. P. (1997). Metric-space analysis of spike trains : theory, algorithms and application. *Network : Computation in Neural Systems*, 8(2) :127–164.

[Vismer et al., 2015] Vismer, M. S., Forcelli, P. A., Skopin, M. D., Gale, K., and Koubeissi, M. Z. (2015). The piriform, perirhinal, and entorhinal cortex in seizure generation. *Frontiers in Neural Circuits*, 9.

[Wainer et al., 1985] Wainer, B. H., Levey, A. I., Rye, D. B., Mesulam, M.-M., and Mufson, E. J. (1985). Cholinergic and non-cholinergic septohippocampal pathways. *Neuroscience Letters*, 54(1) :45–52.

[Wang, 2010] Wang, X.-J. (2010). Neurophysiological and computational principles of cortical rhythms in cognition. *Physiological Reviews*, 90(3) :1195–1268. PMID : 20664082.

[Wang and Buzsáki, 1996] Wang, X.-J. and Buzsáki, G. (1996). Gamma oscillation by synaptic inhibition in a hippocampal interneuronal network model. *Journal of Neuroscience*, 16(20) :6402–6413.

[Weiss et al., 2015] Weiss, S. A., Alvarado-Rojas, C., Bragin, A., Behnke, E., Fields, T., Fried, I., Engel, J., and Staba, R. (2015). Ictal onset patterns of local field potentials, high frequency oscillations, and unit activity in human mesial temporal lobe epilepsy. *Epilepsia*, 57(1) :111–121.

[Wendling et al., 2002] Wendling, F., Bartolomei, F., Bellanger, J. J., and Chauvel, P. (2002). Epileptic fast activity can be explained by a model of impaired GABAergic dendritic inhibition. *European Journal of Neuroscience*, 15(9) :1499–1508.

[West et al., 1994] West, M., Coleman, P., Flood, D., and Troncoso, J. (1994). Differences in the pattern of hippocampal neuronal loss in normal ageing and alzheimer's disease. *The Lancet*, 344(8925) :769 – 772. Originally published as Volume 2, Issue 8925.

[West and Gundersen, 1990] West, M. J. and Gundersen, H. J. G. (1990). Unbiased stereological estimation of the number of neurons in the human hippocampus. *The Journal of Comparative Neurology*, 296(1) :1–22.

[West and Slomianka, 1998] West, M. J. and Slomianka, L. (1998). Total number of neurons in the layers of the human entorhinal cortex. *Hippocampus*, 8(1) :69–82.

[Williamson et al., 2016] Williamson, R. C., Cowley, B. R., Litwin-Kumar, A., Doiron, B., Kohn, A., Smith, M. A., and Yu, B. M. (2016). Scaling properties of dimensionality reduction for neural populations and network models. *PLOS Computational Biology*, 12(12) :e1005141.

[Williamson et al., 2015] Williamson, R. S., Sahani, M., and Pillow, J. W. (2015). The equivalence of information-theoretic and likelihood-based methods for neural dimensionality reduction. *PLOS Computational Biology*, 11(4) :e1004141.

[Wilson and Cowan, 1972] Wilson, H. R. and Cowan, J. D. (1972). Excitatory and inhibitory interactions in localized populations of model neurons. *Biophys. J.*, 12(1) :1–24.

[Wilson and McNaughton, 1994] Wilson, M. and McNaughton, B. (1994). Reactivation of hippocampal ensemble memories during sleep. *Science*, 265(5172) :676–679.

[Wittner et al., 2006] Wittner, L., Henze, D., Záborszky, L., and Buzsáki, G. (2006). Hippocampal CA3 pyramidal cells selectively innervate aspiny interneurons. *European Journal of Neuroscience*, 24(5) :1286–1298.

[Wulff et al., 2009] Wulff, P., Ponomarenko, A. A., Bartos, M., Korotkova, T. M., Fuchs, E. C., Bahner, F., Both, M., Tort, A. B. L., Kopell, N. J., Wisden, W., and Monyer, H. (2009). Hippocampal theta rhythm and its coupling with gamma oscillations require fast inhibition onto parvalbumin-positive interneurons. *Proceedings of the National Academy of Sciences*, 106(9) :3561–3566.

[Yoshida et al., 2012] Yoshida, M., Knauer, B., and Jochems, A. (2012). Cholinergic modulation of the CAN current may adjust neural dynamics for active memory maintenance, spatial navigation and time-compressed replay. *Frontiers in neural circuits*, 6.

[Zielinski et al., 2016] Zielinski, M. R., , McKenna, J. T., and McCarley, R. W. (2016). Functions and mechanisms of sleep. *AIMS Neuroscience*, 3(1) :67–104.

[Zylla et al., 2013] Zylla, M. M., Zhang, X., Reichinnek, S., Draguhn, A., and Both, M. (2013). Cholinergic plasticity of oscillating neuronal assemblies in mouse hippocampal slices. *PLoS ONE*, 8(11) :e80718.

Résumé

L'hippocampe peut présenter différents rhythmes oscillatoires au cours du cycle veille-sommeil, chacun étant impliqué dans des processus cognitifs. Par exemple, des oscillations theta-gamma sont produites pendant la veille et sont associés à la navigation spatiale et la mémoire à court terme, tandis que des complexes sharp-wave-ripples, produits durant les périodes de sommeil lent profond, jouent un rôle important dans la consolidation de la mémoire. Des modèles existent pour reproduire chacun de ces rythmes, cependant les mécanismes impliqués dans leur génération et les transitions entre eux ne sont pas encore parfaitement compris.

Cette question est d'autant plus importante qu'une altération des rythmes hippocampiques est impliquée dans l'épilepsie du lobe temporal médian phamaco-résistante, une forme courante d'épilepsie qui ne peut pas être contrôlée par les traitements médicamenteux existants. Des modèles ont aussi été développés pour reproduire des crises d'épilepsie ou des pointes intercritiques, mais ces modèles ne parviennent pas à expliquer entièrement les liens entre les conditions neuropathologiques de l'hippocampe, des processus physiologiques comme le cycle veille-sommeil, et les oscillations qui en résultent.

Dans ce contexte, l'objectif principal de cette thèse est d'apporter une meilleure compréhension de diverses oscillations hippocampiques, tant physiologiques que pathologiques.

Pour ce faire, nous développons tout d'abord un modèle computationnel de l'hippocampe sain incluant au total plus de trente mille neurones Hodgkin-Huxley, représentés par des dizaines de millers d'équations différentielles résolues numériquement, et comprenant une estimation du potentiel extracellulaire (LFP) généré par les neurones dipolaires tel que mesuré par une électrode macroscopique afin d'être plus facilement interprété. Nous effectuons ensuite une étude complète de l'activité de notre réseau basée sur des plans d'expérience afin d'étudier le rôle des paramètres intrinsèques du modèle et l'importance de la stimulation en entrée dans la production de différents rythmes couplés.

Par la suite, notre modèle est évalué dans un contexte réaliste : l'activité qu'il génère quand il est soumis à des entrées réalistes est comparée avec des enregistrements intracérébraux obtenus sur des patients épileptiques. Nous montrons ainsi que notre modèle est capable de générer des oscillations de veille ou de sommeil similaires aux signaux cliniques sur le plan temporel et fréquentiel. Nous relions les modifications de paramètres du modèle (gains synaptiques et conductances de canaux ioniques) à une modulation cholinergique, et montrons comment les dynamiques des neurones influencent principalement les oscillations basse fréquence, tandis que la connectivité fonctionnelle contrôle les oscillations haute fréquence.

Enfin, nous détaillons davantage notre modèle afin d'inclure quatre modifications de l'hippocampe observées dans les cas d'épilepsies du lobe temporal médian, à savoir la sclérose hippocampique, le bourgeonnement des fibres moussues, et une altération des dynamiques potassiques et chloriques (qui se traduisent par des modifications de la connectivité du réseau ou des paramètres des neurones individuels), et montrons comment ces mécanismes peuvent intéragir avec le cycle veille-sommeil décrit précédemment pour donner lieu à des synchronisations et rythmes pathologiques.

En conclusion, nous proposons dans cette thèse un modèle unique de l'hippocampe regroupant divers mécanismes précédemment décrits dans des travaux séparés, et analysons son activité oscillatoire tandis que nous varions différents paramètres représentant les propriétés structurelles et fonctionnelles du réseau, ainsi que des modifications pathologiques observées en épilepsie. Nos résultats apportent un nouvel éclairage sur les mécanismes impliqués dans la génération des oscillations hippocampiques, qui pourraient ouvrir la voie à de futures applications cliniques.

Mots-clés: hippocampe, cycle veille-sommeil, modélisation, traitement du signal, epilepsie.

Abstract

The hippocampus can exhibit different oscillatory rhythms within the sleep-wake cycle, each of them being involved in cognitive processes. For example, theta-nested gamma oscillations, consisting of the coupling of theta and gamma rhythms, are produced during wakefulness and are associated with spatial navigation and working memory tasks, whereas sharp-wave-ripple complexes, consisting of fast oscillatory events occurring during low frequency waves, are produced during slow-wave sleep and quiet waking and play an important role in memory consolidation. Models exist to reproduce and explain the generation of each of these rhythms, yet the mechanisms involved in their generation and the transitions between them are not yet fully understood.

This question is all the more important that altered hippocampal rhythms are involved in drug-resistant mesial temporal lobe epilepsy, a common form of epilepsy which cannot be controlled by existing pharmaceutical treatments. Some models have also been previously developed to reproduce epileptic seizures (episodes of excessive neural activity) or interictal discharges (brief peaks of synchronous activity), but these models cannot fully explain the links between neuropathological conditions of the hippocampus, physiological processes such as the sleep-wake cycle, and the resulting oscillations.

In this context, the main objective of this thesis is to provide better understanding of various hippocampal oscillations, both physiological and pathological.

To do so, we first design a full computational model of the healthy hippocampal formation including the entorhinal cortex, the dentate gyrus and the CA3 and CA1 regions. This model includes more than thirty thousand Hodgkin-Huxley point neurons, reprensented by tens of thousands differential equations to be solved numerically, as well as an estimation of the extracellular potentials (LFP) generated by the dipolar neurons as measured by a macroscopic electrode, so as to be more easily interpretable. We perform a thorough study of our model's activity based on design of experiments techniques to identify the role of each of its intrinsic parameters and the importance of input stimulation in the production coupled oscillatory outputs.

We then evaluate our model in a realistic context : its activity under realistic input stimulation is compared with intracranial recordings obtained in epileptic patients. We demonstrate that our model is able to reproduce both sleep and wakefulness oscillations with temporal and frequential similarities with the clinically measured signals. We link the modification of some parameters of the model (synaptic gains and ion channel conductances) with cholinergic modulation, and show how single neuron dynamics are mostly responsible for the frequency of slow oscillations of our network, while network functional connectivity controls its fast oscillations.

Finally, we detail our model further to include four pathological modifications of the hippocampus seen in mesial temporal lobe epilepsies, that is hippocampal sclerosis, mossy fiber sprouting, and impaired potassium and chloride dynamics in pyramidal neurons (which are modeled by changing the network connectivity or the parameters of individual neuron dynamics), and show how these mechanisms can interact with the previously described sleep-wake cycle and lead to pathological synchrony and rhythms such as seizures, interictal spikes and fast ripples.

In conclusion, we propose in this thesis a unique model of the hippocampus regrouping many mechanisms previously described in separate works, and analyze its oscillatory activity as we vary different parameters representing either structural or functional properties of the network, as well as pathological modifications observed in epilepsy. Our results provide new insights into the mechanisms underlying the generation of various hippocampal oscillations, which could open the way to future clinical applications.

Keywords: hippocampus, sleep-wake cycle, modeling, signal processing, epilepsy.